The Madden-Julian Oscillation and Nonlinear Moisture Modes

by

Masahiro Sugiyama

Submitted to the Department of Earth, Atmospheric, and Planetary Sciences
in partial fulfillment of the requirements for the degree of

Doctor of Philosophy in Climate Physics and Chemistry

at the

MASSACHUSETTS INSTITUTE OF TECHNOLOGY

February 2008

Author .....
Department of Earth, Atmospheric, and Planetary Sciences
September 14, 2007

Certified by .....
Peter H. Stone
Professor of Climate Dynamics
Thesis Supervisor

Accepted by .....
Maria T. Zuber
E.A. Griswold Professor of Geophysics
Head, Department of Earth, Atmospheric, and Planetary Sciences

The Madden-Julian Oscillation and Nonlinear Moisture Modes

by

Masahiro Sugiyama

Submitted to the Department of Earth, Atmospheric, and Planetary Sciences
on September 14, 2007, in partial fulfillment of the
requirements for the degree of
Doctor of Philosophy in Climate Physics and Chemistry

Abstract

The Madden-Julian oscillation (MJO), the dominant tropical intraseasonal variability with widespread meteorological impacts, continues to puzzle the climate research community on both theoretical and modeling fronts. Motivated by a recent interest in the role of humidity in tropical dynamics, this thesis hypothesizes that the MJO is a nonlinear moisture mode whose existence depends on moisture-convection feedback (the feedback between deep convection and environmental free-tropospheric humidity), and that weak moisture-convection feedback in general circulation models accounts for their deficiencies with the MJO simulations.

Moisture modes are found to exist in a large class of linear primitive equation models on the equatorial beta-plane. For models with standard quasi-equilibrium parameterizations, perturbation expansion analyses demonstrate that the weak temperature gradient (WTG) approximation of Sobel et al. describes the small-scale limit of the moisture mode accurately, with the small expansion parameter being the ratio between temperature tendency and adiabatic cooling. Under the WTG balance, the only leading order variables are humidity and vertical motion. Analyses of three models in the literature show that a moisture mode is unstable if moist static energy (MSE) sources such as cloud radiative forcing or gust-enhanced surface heat flux exceed the MSE export.

Numerical calculations of a single-column model under the WTG configuration show that a realistic convective scheme can reproduce moisture mode instability. Sensitivity tests on the strength of moisture-convection feedback in the Emanuel scheme indicate that such a feedback is essential for moisture mode instability, confirming the prediction from simple models.

To explore the nonlinear regime of a moisture mode, numerical calculations of a simplified Quasi-equilibrium Tropical Circulation Model on the equatorial beta-plane have been performed. A classical Gill model augmented with a prognostic humidity variable can capture nonlinear dynamics of the moisture mode. In particular, nonlinear advection of dry air by Rossby gyres is found to move the moisture mode eastward.

Notwithstanding progress made in the present thesis, numerous difficulties abound. The

most significant issue is that moisture mode instability favors the smallest scale in the linear regime. The author suggests that scale interaction and its effect on the humidity budget might be an important research topic.

Thesis Supervisor: Peter H. Stone
Title: Professor of Climate Dynamics

Acknowledgments

First of all, I would like to thank my advisor and committee members. Peter Stone's rigor always improved my mathematical analyses, both in this thesis and in my work on the runaway greenhouse. Without his generosity, I would not have been able to pursue another degree in MIT's Technology and Policy Program and spend an entire summer on the internship in Washington D.C.

Kerry Emanuel has been a source of inspiration. I owe most of my knowledge about the tropics to him. He also inspired one of the key analyses in this thesis, the systematic derivation of the WTG system through perturbation expansion.

Alan Plumb was keenly interested in my work, and his enthusiasm was always a great encouragement for me. And it was Alan Plumb's comment that led to the Gill model interpretation of the nonlinear moisture mode.

Tony Del Genio focused me on the link between general circulation models and theoretical work. In the modern age, such a link is very important but often neglected in the theoretical community.

My thinking was not conceptually clear until Zhiming Kuang's suggestion that moisture mode dynamics have two parts, linear and nonlinear. I also learned a great deal from the reading class with him, which was one of the best I attended.

Outside the committee, I am grateful to all the faculty members for the department's intellectual atmosphere. Among them, I learned a great deal from Lodovica Illari about synoptic meteorology, and it was fun to work with her on a poster on the potential vorticity map.

I would also like to mention my appreciation of my advisor in the Technology and Policy Program, Jake Jacoby. The sea-level rise project was challenging but certainly broadened my perspective.

Richard Moss, Peter Schultz, and Jim Titus all deserve credits for taking care of me during my stay at the U.S. Climate Change Science Program. They not only gave me nice projects but also provided me ample opportunities to explore the process of science policy, which was an extremely valuable experience.

Obviously thanks also go to many people who shared the same time with me. It was encouraging to have such wonderful studymates as Elke, Mike, and Vikram, in the months leading up to the generals. I always had interesting and stimulating discussions with Bill, Roberto, and Yang. Chatting with Taka and Shin was always fun and stimulating. I cannot but thank my initial mentor, Mitch, who essentially brought me to MIT. I thank Mary for being helpful for anything (literally) and improving my English writing.

And I cannot finish this note without thanking my family. Dad, Mom, Tetsuya, and Katsuhiko: thank you!

This research was supported in part by the NASA Goddard Space Flight Center under Cooperative Agreement NNG04GF12A with MIT, and in part by MIT's Joint Program on the Science and Policy of Global Change.

Contents

Chapter 1

Physics of the Madden-Julian oscillation

1.1 Context

The Madden-Julian oscillation (hereafter MJO), also called intraseasonal oscillation or 30-60- or 40-50-day oscillation, is the dominant variability in the tropical atmosphere on timescales shorter than a season (Madden and Julian 1971, 1972). It is a planetary-scale eastward propagating oscillation, manifesting itself in various meteorological fields and oceans in the tropics. It is closely related with active and break phases of monsoon (e.g., Yasunari 1979; Krishnamurti and Subrahmanyam 1982; Goswami 2005, for more recent progress). The MJO modulates tropical cyclone activity (Maloney and Hartmann 2000), and some MJO events seem to trigger or terminate El Niño-Southern Oscillation (ENSO) events (e.g., Takayabu et al. 1999; Bergman et al. 2001; Lau 2005, for more recent updates). In addition to its tropical influences, the MJO affects midlatitude circulations (Ferranti et al. 1990); its near-global impact even on rainfall has been statistically demonstrated (Donald et al. 2006). Understanding the mechanisms of the MJO is important not only for tropical weather and climate prediction but also for extratropical weather forecasts.

In spite of its importance and active research, the climate community is still struggling with the MJO (e.g., Bretherton in press). Most of the IPCC (Intergovernmental Panel on Climate Change)-class global climate models (or general circulation models; hereafter GCMs) still suffer from poor simulations of the MJO (Lin et al. 2006). Even when a model

shows a relatively good MJO, it is not straightforward to trace back where the improvement came from, inhibiting the transfer of success of one model to another. Although many theories have been proposed, they cannot explain why GCMs have a hard time simulating the MJO, nor why some GCMs began to show reasonable simulations. As noted by Zhang (2005), filling such a knowledge gap between theory and modeling should be among the highest priorities for MJO research.

My thesis attempts to make a contribution to our understanding of the MJO, and to connect the understanding and modeling of the MJO. I take a rather theoretical approach here, although my work does not provide a successful theory for the MJO. However, it illuminates the link between the MJO problem in GCM simulations and another common GCM problem: moisture-convection feedback. Indeed, only recently has the interplay between moist convection and free-tropospheric humidity been explored thoroughly, both in modeling and theoretical studies. To describe the importance of the interaction between moist convection and humidity above the boundary layer, I borrow various physical ideas from previous studies. The natural starting point of my thesis is thus a literature review on the MJO and related physical processes.

The literature on the MJO is extensive and there are excellent reviews on the MJO. Zhang (2005) provided a succinct review of the MJO. Lau and Waliser (2005) is a book dedicated to intraseasonal variability in the tropics, and the MJO is a theme of many chapters in the book. Wang's (2005) reviews theory, Slingo et al.'s (2005) summarizes modeling, and there are many other chapters. Older reviews include Hayashi and Golder (1993) and Lin et al. (2000) for theory; Madden and Julian (1994) for observation. The following gives a brief overview of the literature, with a special emphasis on theories.

1.2 MJO review: Observations

For observations, the focus here is on the average picture of the large-scale circulations associated with the MJO. In actuality, each MJO has a different appearance and influence. For example, some MJO events are strong enough to be involved in termination of an

ENSO event as documented by Takayabu et al. (1999). Nevertheless, the following gives the general behavior of the MJO, providing a context for theory and modeling.

The MJO is characterized by timescales of 30-60 days (Madden and Julian 1994). Its dynamical fields have horizontal scales of zonal wavenumber 1-3 (Hendon and Salby 1994; Salby and Hendon 1994), though the horizontal scale of deep convection extends from wavenumber 1 to 5 (Wheeler and Kiladis 1999). It manifests itself in many atmospheric fields, but propagation characteristics differ for each variable. Regression analyses show that convective activity as measured by outgoing longwave radiation (OLR) is limited mostly to the region from the Indian Ocean to the western Pacific with a phase speed of 5 m/s, whereas the upper tropospheric zonal winds travel around the whole globe and accelerates to about 10 m/s beyond the dateline (e.g., Hendon and Salby 1994). Similarly, spectral analyses show a difference in periods, with dynamical fields having periods of about 30-60 days (Madden and Julian 1994) and OLR about 30-95 days (Salby and Hendon 1994; Wheeler and Kiladis 1999).

Although the descriptions above might lead readers to believe that the MJO is like a sinusoidal wave, a closer examination shows otherwise: each MJO episode is more like a discrete disturbance than a sinusoidal wave, with active phase of convection narrower than the calm period. The name "oscillation" might thus be misleading in light of this pulse-like nature of the MJO (Salby and Hendon 1994; Yano et al. 2004; Zhang 2005).

Figure 1-1 is a schematic from Madden and Julian (1972) and describes the MJO as a global circulation pattern of predominant zonal wavenumber one structure. Zonal winds have much more coherent structures than meridional winds. During development of deep convection in the Indian Ocean, the region of descent propagates to the east, which Bantzer and Wallace (1996) characterized as a Kelvin wave front. Once developed, enhanced convection leaves the Indian Ocean and stops at around the central Pacific. The circulation pattern continues to travel and completes the whole circumference of the globe. The circulation exhibits a first baroclinic mode-like structure (Madden and Julian 1972, and others), but the winds in the lower troposphere tend to lose distinct characteristics beyond the date line. A similar picture emerges from more recent studies such as Hendon and Salby (1994)

and Kiladis et al. (2005). Although often characterized as a propagating disturbance, a closer inspection of Figure 1-1 shows that at the initial stages (F and G in the figure), the convective signal seems to be stationary while the dynamic signal propagates to the east. One can see the initial, quasi-stationary development of deep convection also in other analyses such as Wheeler and Hendon's 2004 (see their Figs. 8 and 9).

Wheeler and Kiladis (1999) performed a power spectral analysis of OLR and identified the MJO along with convectively coupled equatorial waves. Figure 1-2 presents one of their results, comparing the theoretically predicted dispersion relationship by Matsuno (1966) and power spectra of OLR. The diagram shows the ratio between power spectrum and background red noise. There is a striking correspondence between peaks of OLR power and theoretical dispersion relation curves. In addition, the figure suggests that the tropical atmosphere possesses an equivalent depth of 12-50 m, which is much shorter than 200 m, a value expected for a dry atmosphere. In fact, using dynamical fields, Wheeler and Kiladis (1999) did illustrate that the tropical atmosphere also has waves with h = 200 m. There appears to be a strong MJO signal for periods of 30-90 days and wavenumber 1–5. An interesting feature of this figure is that the MJO and Kelvin waves lie on different places in the wavenumber-frequency space: whereas convectively coupled Kelvin waves exhibit phase speeds of $11 - 22\mathrm{m/s}$ ($h \approx 12 - 50\mathrm{m}$), the MJO has a phase speed of about 5 m/s. Nevertheless, the MJO and Kelvin waves overlap slightly with each other, resulting in a complex structure.

Figure 1-2 also shows that there are other modes in the intraseasonal band. For example, part of the Kelvin wave and equatorial Rossby waves are longer than synoptic timescales, namely 5 days to a week. It is also important to note that some regions, such as the Indian continent, do exhibit the 10–20 mode in addition to the 30–60 day mode (Goswami 2005). Thus, the MJO is the dominant variability but there are other significant and physically important modes.

Building upon the spectral analysis of Wheeler and Kiladis (1999), Kiladis et al. (2005) obtained the four dimensional structure of the MJO. They defined the MJO index as the OLR at a reference point as filtered with the characteristics frequencies and wavelengths in

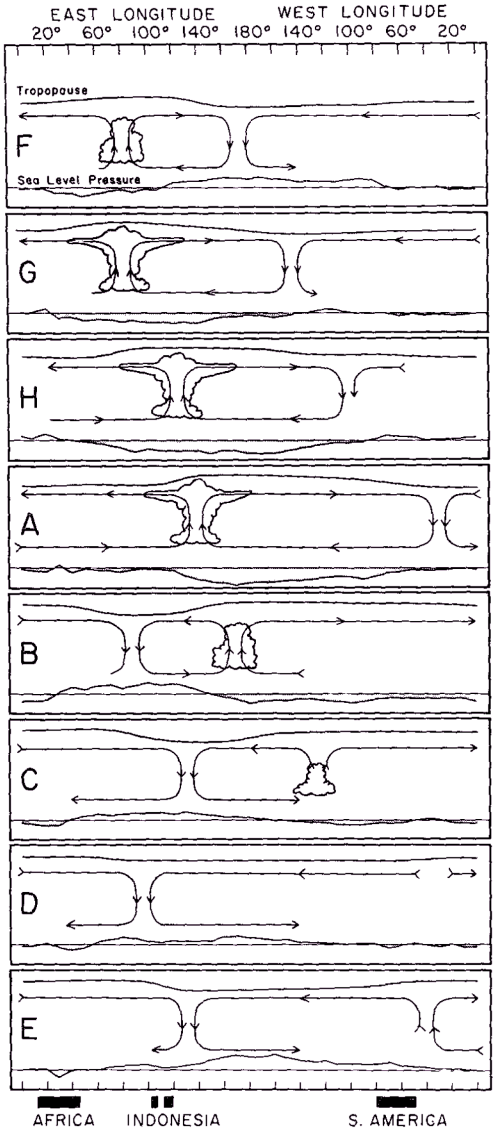

Figure 1-1: Schematic of different development stages of the MJO along the equator. Cloud symbols indicate the center of deep convective activity, and arrows represent zonal circulations, and curves above and below cloud symbols signify tropopause height and sea-level pressure perturbations, respectively. Figure 16 of Madden and Julian (1972).

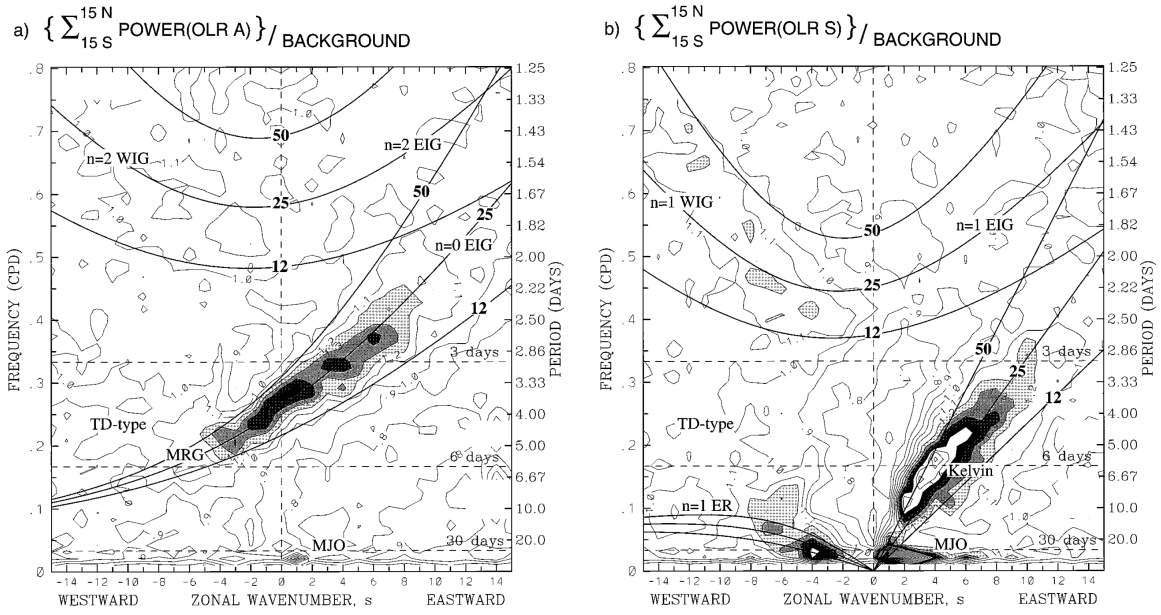

Figure 1-2: (a) The antisymmetric OLR power divided by the background power. Here symmetry is defined with respect to the equator. Contour interval is 0.1, and shading begins at a value of 1.1 for which the spectral signatures are statistically significantly above the background at the 95% level. Superimposed are the dispersion curves of the even meridional mode-numbered equatorial waves for the three equivalent depths of h = 12, 25, and 50 m. (b) Same as in panel (a) except for the symmetric component of OLR and the corresponding odd meridional mode-numbered equatorial waves. Figure 3 of Wheeler and Kiladis (1999).

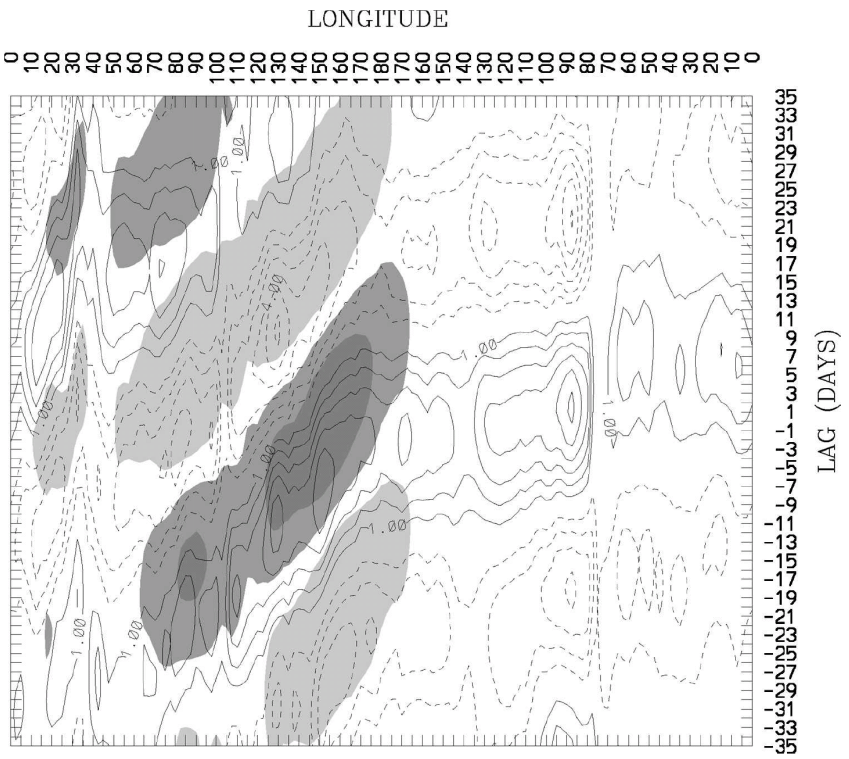

Figure 1-3: Hovmöller diagram of perturbation 850-hPa specific humidity (contours) and OLR (shading) averaged from 10°S to 10°N. Regression coefficients are multiplied by a $-40\mathrm{W/m^2}$ in OLR at the 0°N, 155°E on day 0 in this figure after the MJO filtering has been applied. The contour interval is $1.0{\cdot}10^{-1}$ g/kg with negative values dashed. The dark (darkest) shading denotes OLR anomalies less than $-16\mathrm{W/m^2}$ ($-18\mathrm{W/m^2}$) and the light shading represents anomalies greater than +16 $\mathrm{W/m^2}$. Adapted from Kiladis et al. (2005).

Figure 1-2, and then regressed OLR, specific humidity, and other variables onto the MJO index. Figure 1-3 shows the lag regression of the OLR and specific humidity at 850 hPa. This provides another confirmation that deep convection is restricted to the Indian Ocean and the west Pacific, as indicated in Figure 1-1. This figure clearly illustrates acceleration of the circulation propagation beyond the date line (from about 5 m/s to 10 m/s).

The early studies of the MJO regarded it as some sort of Kelvin wave because of dominance of zonal winds and eastward propagation. However, in addition to a Kelvin response east of convection, a number of studies have identified upper-tropospheric (typically 200hPa) anticyclonic circulations to the west of the enhanced convection (e.g., Knutson and Weickmann 1987; Kiladis and Weickmann 1992; Hendon and Salby 1994; Sperber et al.

1997). The spatial feature is consistent with what one would expect for a forced Kelvin-Rossby mode (Gill 1980). This is somewhat puzzling since the Gill model requires strong momentum damping for the entire troposphere. Whereas the boundary layer turbulence is the cause for strong damping for the lower troposphere (Neelin 1989), such strong friction usually cannot be justified for the upper troposphere. Interestingly Lin et al. (2005) found such strong friction in the upper troposphere, at least in the reanalyses they analyzed. Nonlinear advection and convective momentum transport combine to act like strong damping.

Recent studies provide even stronger confirmation for the Gill pattern-like structure, and find lower tropospheric cyclonic circulations as well. Figure 1-4 presents a regression analysis by Kiladis et al. (2005), depicting cyclonic circulations in the lower troposphere and anticyclonic circulations in the upper troposphere, to the west of enhanced convection. These studies have also found upper-tropospheric cyclones east of convection, presumably a response to suppressed convection. Although there are numerous subtleties in the structure depicted here, to the first order, the MJO's horizontal structure may be summarized as that of the Gill model.

The MJO shows a westward vertical tilt in various fields. Murakami and Nakazawa (1985) revealed a westward vertical tilt in zonal winds. Lin et al. (2004) have demonstrated that the anomalous heating profile of the MJO is tilted westward with height because of stratiform precipitation and cloud radiative forcing. Wheeler et al. (2000) noted a westward vertical tilt of temperature for a convectively coupled equatorial Kelvin wave. For a dry Kelvin wave, the westward vertical tilt in phase denotes downward energy flux (Holton 2004, for example). Care must be taken in interpreting these results, however, because in the present case the dynamics is strongly influenced by the interaction with convection. A more proper interpretation might be that heating due to shallow convection is inducing a second-baroclinic mode response.

Recent studies unraveled the humidity structure of the MJO. Maloney and Hartmann (1998) showed that moisture builds up before the core of deep convection arrives because of frictional convergence, and that the atmosphere rapidly dries after the passage of deep convection. Kemball-Cook and Weare (2001) confirmed preconditioning before the core

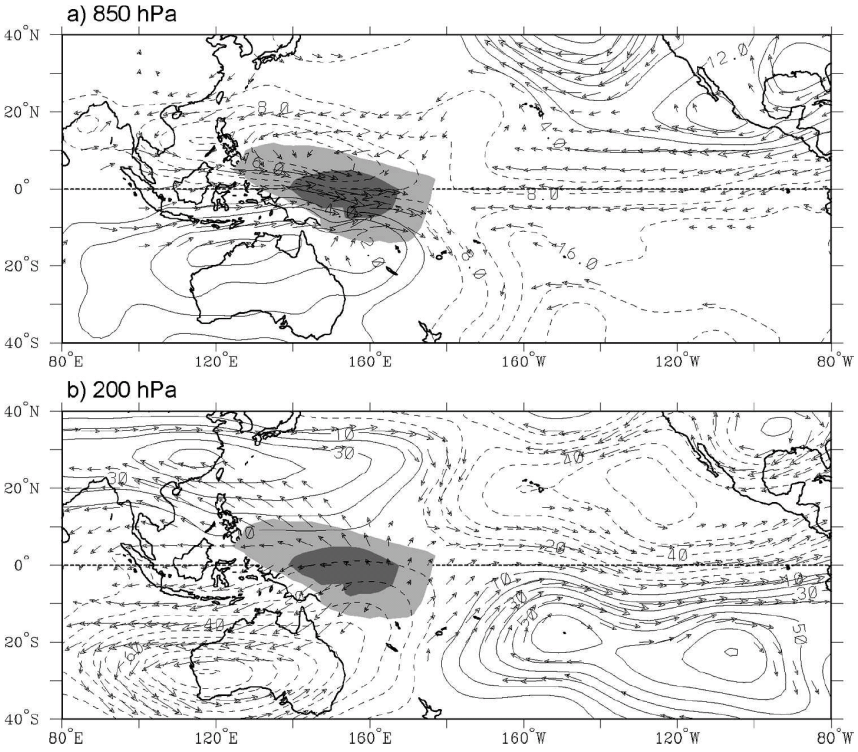

Figure 1-4: Anomalous OLR and circulation regressed on the MJO-filtered OLR at the equator, 155°E, with all seasons included. (a) 850 and (b) 200 hPa. Dark (light) shading denotes OLR perturbations less than $-32\mathrm{W/m^2}$ ($-16\mathrm{W/m^2}$). Streamfunction contour interval is (a) $4 \cdot 10^5$ $\mathrm{m^2/s}$ and (b) $10 \cdot 10^5$ $\mathrm{m^2/s}$. Only winds that are statistically significant at the 95% level are shown. The largest wind vectors are about 2 m/s in (a) and around 5m/s in (b). Figure 2 from Kiladis et al. (2005).

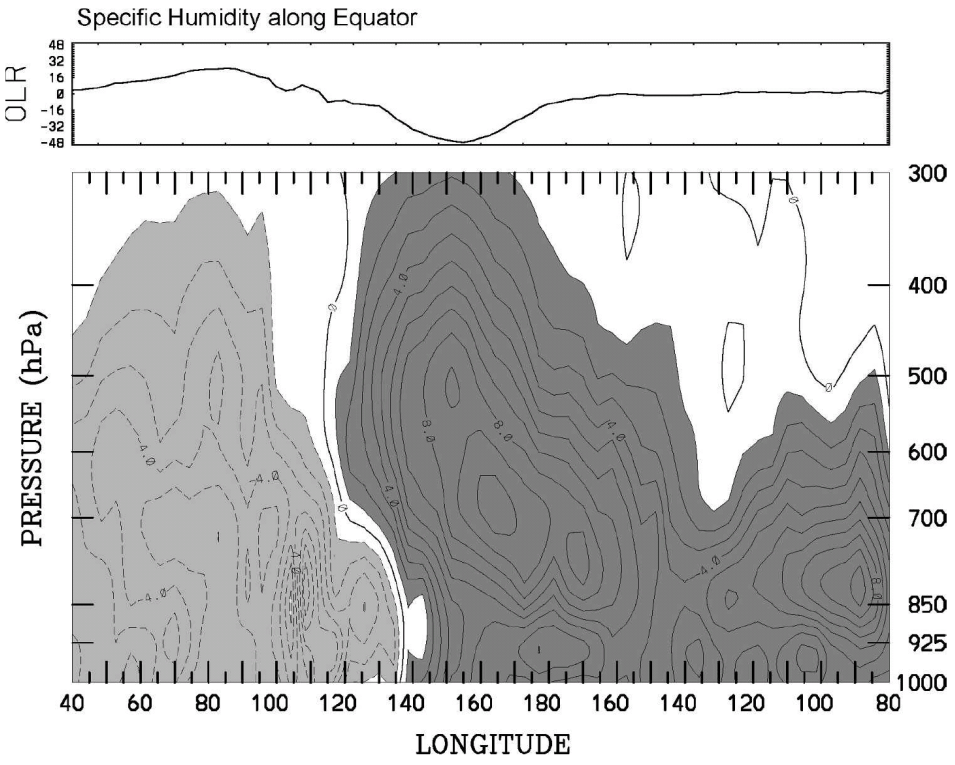

Figure 1-5: Longitude-height section of specific humidity anomaly along the equator associated with the pattern shown in Figure 4. The contour interval is $1{\cdot}10^{-1}$ g/kg. Figure 9 of Kiladis et al. (2005).

of convection, although they found that frictional convergence cannot explain the moisture buildup away from the equator.

Applying Wheeler and Kiladis's (1999) tempo-spatial filter to OLR, Kiladis et al. (2005) performed a linear regression analysis on the MJO. They confirmed most findings of the previous research and, in addition, identified detailed structures of specific humidity (Figure 1-5). Humidity build-up precedes deep convection, probably induced by shallow convection. Deep convection coincides with a humid middle troposphere. The atmosphere dries up rapidly after the core of deep convection passes. Analyzing the data from the Atmospheric Infrared Sounder (AIRS), Tian et al. (2006) also found a strong relationship between free tropospheric humidity and precipitation. Other studies corroborate the basic physical picture (Sperber 2003; Myers and Waliser 2003; Kikuchi and Takayabu 2004; Weare 2005; Agudelo et al. 2006).

There has been active research on the air-sea interaction in the MJO. Figure 1-6, taken from Zhang (2005), summarizes key observations. In the suppressed phase, precipitation reaches a very low value ($\sim$ 1.5 mm/day) and deep convection becomes very sporadic. Weak winds decrease evaporation, which, along with increased shortwave flux, increases SST. In the active phase, a strong westerly causes surface stress and enhances evaporation. Evaporation either lags or is collocated with the center of precipitation.

From the quasi-equilibrium standpoint, revealing the phasing between precipitation and evaporation is a prerequisite of theoretical understanding since evaporation is one of the key determinants of deep convection (e.g., Emanuel et al. 1994). Zhang (2005) compared the different phase relations between precipitation and evaporation that are found in models and observations, and elaborated on the theoretical implications. But the reason for such a difference might be quite simple, as argued by Hendon (2005). If evaporation perturbation is dominated by the wind-induced surface heat exchange (WISHE) effect, and if one assumes that the Gill (1980) model captures the first-order dynamic behavior of the MJO, a symmetric heating on the equator creates evaporation lagging precipitation, whereas an antisymmetric heating causes precipitation and evaporation to be in phase.

Numerous researchers have looked into the relation between the MJO and monsoons. I cannot do justice to the huge literature on this subject, and have included only minimal information. Yasunari (1979) found a dominant periodicity of about 40 days in the cloudiness over the Asian monsoon area, indicating a relation between the MJO and active and break phases of the monsoon. Krishnamurti and Subrahmanyam (1982) presented northward migration of troughs and ridges at 850 hPa at periods of 30-50 days over India. Not all the intraseasonal variability in monsoon regions is associated with the MJO, however. In the case of Indian monsoon, Goswami (2005) summarized in a chapter of a review book that although a fraction of the intraseasonal variability is associated with the MJO, other independent northward moving disturbances represent a significant portion (up to 50%) of the variability.

It is well known that tropical convective systems such as the MJO present multiscale organization. Nakazawa (1988) analyzed the satellite infrared data and found supercloud

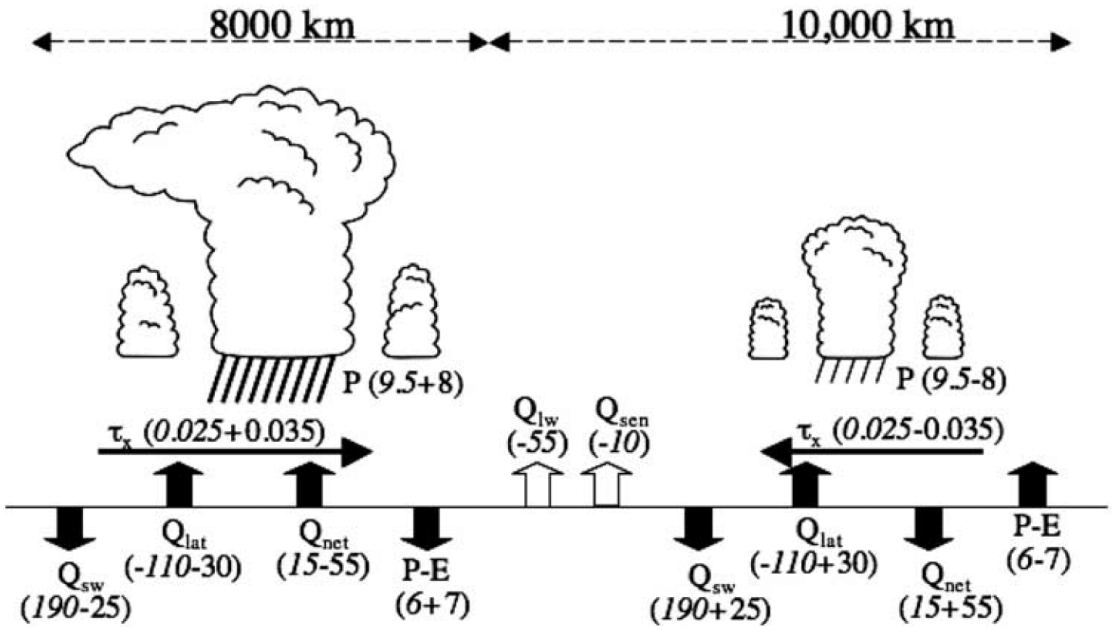

Figure 1-6: Schematic illustrating magnitudes of surface fluxes of the MJO. The format is (mean value plus/minus intraseasonal perturbation). Variables shown here are: shortwave flux (Q_{sw}), evaporation (Q_{lat}), net heat flux (Q_{net}), precipitation (P), net precipitation ($P-E$), and zonal stress (τ_x). Deep clouds on the left indicate the active period while the shallow clouds represent inactive phase. Intraseasonal perturbations in longwave flux and sensible heat flux are small and neglected here. Units are $\mathrm{W/m^2}$ for fluxes, mm/day for precipitation and net precipitation, and $\mathrm{N/m^2}$ for wind stress. Figure 15 of Zhang (2005), who complied observations from Zhang (1996), Cronin and McPhaden (1997), Shinoda et al. (1998), and Zhang and McPhaden (2000). Note that the zonal extent of the convectively active region has been corrected from 800 km to 8000 km, the value used in Shinoda et al. (1998).

clusters that propagate eastward at $10-15\mathrm{m/s}$ and are encompassed in an MJO. Each supercloud cluster further consists of cloud clusters traveling westward whose lifetime is $1-2$ days. These supercloud clusters are now considered to be convectively coupled Kelvin waves (Wheeler and McBride 2005). Other observational studies (e.g., Masunaga et al. 2006) find that equatorial Rossby waves are also collocated with the MJO. Nevertheless, the nature and physics of multi-scale convective organization is not yet clear.

In summary, we can describe the first-order picture of the MJO as follows:

Propagation characteristics Initially convection develops in the Indian Ocean, and then travels to the Pacific at about 5 m/s. It then dissipates around the dateline whereas the wind patterns continue to proceed at $\sim$ 10 m/s.

Scale The scale of convection is about wavenumber 2 although power spectral analysis shows a signal for wavenumber for 1 - 5.

Horizontal structure The Gill (1980) model describes the horizontal structure with Rossby gyres to the west and a Kelvin wave response to the east.

Vertical structure The first baroclinic mode dominates; a small but significant trace of the second baroclinic mode is also found. The superposition of two modes causes a westward tilt in winds and temperature.

Evaporation The phase relationship between precipitation and evaporation can be explained by the WISHE effect. However, the observed phasing differs from that of the linear WISHE as envisioned by Emanuel (1987) and Neelin et al. (1987).

Free-tropospheric humidity A humid troposphere is correlated with convection for both shallow and deep convection.

I take the physical depiction here as a benchmark against which modeling and theory should be evaluated. Having established an observational picture, the next section focuses on modeling.

1.3 MJO review: Modeling

A number of modeling studies have also been dedicated to the MJO. Hayashi and Sumi (1986) performed an aquaplanet numerical run of a GCM with a Kuo (1974)-type cumulus parameterization based on conditional instability of second kind (CISK), and found organized convection propagating eastward. The period was, however, 30 days and shorter than observed. After a decade, Slingo et al. (1996) examined the MJO simulations in 15 atmospheric GCMs as a diagnostic subproject of Atmospheric Model Intercomparison Project (AMIP), and found that although a few models exhibit a fairly good MJO, a closer investigation revealed that simulated MJOs have weaker amplitude, shorter periods, and different seasonality than observed. As noted at the beginning of this chapter, the model intercomparison study by Lin et al. (2006) found that the IPCC-class GCMs still suffer from poor simulations of the MJO and convectively coupled equatorial waves.

Since the interaction between large-scale dynamics and moist convection is considered to be at the heart of the MJO dynamics, numerous papers examined the implications of the choice of convective schemes. Chao and Lin (1994) performed numerical experiments of the two-dimensional GCM with four schemes, and found that the simulation of organized convection is highly sensitive to which scheme is used. Slingo et al. (1996) note that models using a convection scheme closed on buoyancy rather than moisture convergence tend to better simulate the MJO. Maloney and Hartmann (2001) tested three convective parameterizations in the NCAR Community Climate Model version 3.6, finding that MJO simulation can be improved by changing the standard scheme of Zhang and McFarlane to the relaxed Arakawa-Schubert scheme with cloud microphysics. They also found that removal of reevaporation of convection precipitation in unsaturated downdrafts reduces the amplitude of the simulated MJO because it changes the mean tropical circulation. More recently, among the models investigated by Lin et al. (2006), arguably the two best GCMs have convection schemes with some sort of moisture convergence closure or triggering, a result in contrast with that of Slingo et al. (1996).

Some modeling studies (Chao and Lin 1994; Chao and Deng 1996) suggest that the MJO is driven by supercloud clusters such as those identified by Nakazawa (1988) or em-

phasize the role of scale interaction between the planetary disturbance and smaller-scale organized convection. Motivated by the possibility of multi-scale organization, some studies examined cloud-resolving models (CRMs) in detail. Using a two-dimensional CRM of the equatorial channel, Grabowski and Moncrieff (2002) found that inclusion of the cloud-radiation interaction induces diabatic circulation, and that the MJO-like disturbance is less coherent than in a similar study but without cloud-radiation interaction by Grabowski and Moncrieff (2001).

There is an increasing interest in moisture-convection feedback. A particularly interesting approach is superparameterization, which attempts to embed a two-dimensional CRM in a grid point of the large model. Grabowski (2004) demonstrated that using a superparameterization leads to an improved simulation of the MJO-like disturbance. Khairoutdinov et al. (2005) applied a superparameterization to the NCAR Community Atmosphere Model (CAM) and found that such a modification ameliorates the MJO simulation in the model. Raymond (2001) and Grabowski and Moncrieff (2004) showed that models with enhanced moisture-convection feedback produce disturbances like the MJO, as with the super-parameterization approach. In a GCM experiment where they imposed an SST pattern that slowly moved eastward, Woolnough et al. (2001) discovered that tropospheric humidity is important in regulating the magnitude of the atmospheric response to the SST forcing.

Grabowski and Moncrieff's (2004) work is particularly noteworthy. They modified a cloud microphysical parameter in the Emanuel (1991) scheme, and demonstrated that a conventional parameterization is capable of reproducing moisture-convection feedback. They also argued that a simple scaling analysis focused on the subsidence region supports the importance of moisture-convection feedback on the intraseasonal timescale.

Some modeling studies investigated cloud-radiation interaction in detail. Slingo and Madden (1991) found that in NCAR Community Climate Model, removing cloud-longwave radiation interaction reduces the amplitude but does not change the period of the MJO. In Lee et al.'s (2001) aquaplanet GCM, cloud-radiation interaction actually contaminates the MJO-like mode, inducing small-scale westward disturbances. Although

they recovered MJO by modifying the cloud scheme, the resulting mean radiative balance had deteriorated. In Zurovac-Jevtić et al.'s (2006) two-dimensional GCM, cloud-radiation interaction slows down the large-scale mode while exciting small-scale westward advective disturbances. They also discovered that moisture-convection feedback tends to diminish advective waves.

With the increasing computation capacity, some attempted to explicitly simulate convection in a global model using a global CRM (Tomita et al. 2005; Natsuno et al. 2007) and a new approach such as DARE (Diabatic Acceleration and REscaling) (Kuang et al. 2005). These approaches are generally successful at capturing convectively coupled equatorial waves, but seem not be good at simulating the MJO. This topic will be taken up in the last chapter.

As discussed at the beginning of this chapter, part of the problem with modeling studies lies in the lack of an adequate theory that would guide model development. The state of the theoretical work is the topic of the next section.

1.4 MJO review: Theories

Hayashi and Golder (1993) present a review of theories and modeling up to their date. Lin et al. (2000) give a concise review of the proposed theories. The most up-to-date review is that of Wang (2005) but his main topic is a frictional wave-CISK model that he and his colleagues developed. Zhang (2005) provides a more balanced review. I briefly summarize their reviews and supplement with recent developments.

According to Zhang (2005), there are two classes of theories: instability theories and forced response theories. I first describe instability theories.

1.4.1 Slow propagation, instability, and scale selection

Early studies characterized the MJO as a Kelvin-like wave that is modified by moist convection. This was because the original studies by Madden and Julian (1971, 1972) emphasized the dominance of zonal winds, and the MJO propagates eastward. These two characteris-

tics match those of a Kelvin wave. However, getting the correct phase speed and scale from various instability mechanisms proved to be tough.

To illustrate, I consider a linear shallow water equation with vanishing meridional wind to represent the first baroclinic mode with a generic form of precipitation as follows.

$$\frac{\partial u}{\partial t} = -\frac{\partial T}{\partial x}, \tag{1.1}$$

$$\beta y u = -\frac{\partial T}{\partial y}, \tag{1.2}$$

$$\frac{\partial T}{\partial t} + c_0^2 \frac{\partial u}{\partial x} = Q, \tag{1.3}$$

where u is the zonal wind (with the sign representing upper-tropospheric directions), T is the temperature or geopotential height for the first baroclinic mode, Q represents precipitation that depends on other variables, $\beta = df/dy$, $c_0^2 = gh$, and h is the equivalent depth. Equivalent depth is a separation constant connecting the linear shallow water equations and the vertical structure equation for a resting atmosphere (Fulton and Schubert 1985; Lindzen 1990; Wheeler et al. 2000, for review).

This set of equations is augmented by a humidity equation:

$$\frac{\partial q}{\partial t} - a^2 \frac{\partial u}{\partial x} = -Q + E, \tag{1.4}$$

where a^2 represents the gross moisture stratification (see Chapter 2). Aside from notations, this system is almost identical to those considered by Emanuel (1987) and Neelin et al. (1987), and quite analogous to the QTCM considered in Chapter 2. For consistency of units, thermodynamic variables are in energy units; see Chapter 2 for the example of such a treatment.

Suppose that the MJO is one kind of Kelvin wave, which has no meridional wind ($v = 0$). We then realize that the MJO's phase speed is much slower than a dry Kelvin wave ($Q = 0$). For a dry Kelvin wave, the phase speed is given as $c_0 = \sqrt{gh}$. A dry atmosphere would have an equivalent depth of 200 m, which implies a phase speed of 44 m/s. This can be contrasted with the MJO's phase speed of 5-10 m/s. One thus needs to

invoke moist processes to account for slow propagation. It is also worth noting that observed convectively coupled equatorial waves, including Kelvin waves, have an estimated equivalent depth of 12-50 m (Takayabu 1994; Wheeler and Kiladis 1999). The MJO seems to be distinct from Kelvin waves.

Because of clear convective signals in the MJO, investigators have utilized theories of interactions between convection and large-scale dynamics to explain the slow phase speed such as wave-CISK (conditional instability of second kind) (e.g., Lau and Peng 1987) and statistical equilibrium thinking (Neelin et al. 1987; Emanuel et al. 1994). For both cases, presence of convection alters the effective static stability for waves, although the mechanism is different.

Another important question is what maintains the MJO against dissipation, and why it exhibits a predominance of low zonal wavenumbers. Wave-CISK and WISHE have been utilized as an instability mechanism. In both cases, the simplest formulations lead to largest growth rate at smallest scales available (Lindzen 1974; Emanuel 1987; Neelin et al. 1987) but methods to circumvent these difficulties have been proposed, including positive-only heating (Lau and Peng 1987) and frictional convergence (Salby et al. 1994) for wave-CISK, and wave leakage into the stratosphere (Yano and Emanuel 1991) and convective time lag for WISHE (Emanuel 1993).

In the next subsection, I focus on the two major theories, WISHE and wave-CISK, followed by a review of other proposed mechanisms.

1.4.2 Wave-CISK (Conditional Instability of Second Kind)

Wave-CISK theory (Hayashi 1970; Lindzen 1974) maintains that the tropical atmosphere has large convectively available potential energy (CAPE) and this is released through low-level (moisture) convergence due to wave dynamics rather than frictional convergence in the original formulation by Charney and Eliassen (1964). In the aforementioned simple model, one may parameterize precipitation as

$$Q = a^2 \frac{\partial u}{\partial x}, \tag{1.5}$$

where evaporation is neglected. Because of the sign convention here, $\partial u/\partial x$ denotes lower-level convergence (or more precisely, the upper-level divergence). The growth rate is

$$\sigma = \pm k\sqrt{a^2 - c_0^2}. \tag{1.6}$$

For an instability to happen, we need $a > c_0$, which I assume here. Note that $\sigma \to \infty$ as $k \to \infty$, a phenomenon called a CISK catastrophe. That is, linear wave-CISK predicts the fastest growth rate at smallest wavelength, and the growth rate tends to infinity. A nonlinear wave-CISK theory might overcome this difficulty (e.g., Lau and Peng 1987). A possible remedy is to invoke the asymmetry of heating:

$$Q = \begin{cases} a^2 \partial u/\partial x & \partial u/\partial x > 0 \\ 0 & \partial u/\partial x \leq 0 \end{cases} \tag{1.7}$$

Actually positive-only heating is unphysical if the basic state is taken as radiative-convective equilibrium (RCE) with a non-zero precipitation rate. Negative precipitation anomaly is of course possible. In any event, Crum and Dunkerton (1992) examined this model and sought a stationary solution that grows exponentially by dividing the domain into convecting and non-convecting regions. They found that the growth rate increases indefinitely as the scale of the convecting region contracts. They also examined more general cases, reaching a conclusion that positive-only heating might modify the normal wave-CISK catastrophe but does not necessarily eliminate it. To be sure, there are other remedies to avoid CISK catastrophe, including second-order diffusion and viscous processes.

Other forms of wave-CISK have been proposed. Wang and Rui (1990) and Salby et al. (1994) suggested that "frictional" wave-CISK in which frictional surface convergence helps selection for large waves. Hendon and Salby (1994) provided observational support for this theory, but Sperber et al. (1997) question the actual role of friction. Moskowitz and Bretherton (2000) have pointed out that the drag coefficient used by Wang and Rui (1990) was unrealistically large, but still found a modest destabilizing role of friction in a quasi-

equilibrium model.

At the more fundamental level, the CISK perspective has been called into question (e.g., Emanuel et al. 1994). Observations suggest that the tropical atmosphere does not have CAPE that is large enough to induce large-scale instabilities, but are almost neutral to a moist adiabatic ascent with condensate loading included (Xu and Emanuel 1988). Admittedly there are subtleties that change the magnitude of CAPE, such as whether to include latent heat of fusion in CAPE calculations (Williams and Rennó 1993) and the extent to which condensate loading equals the adiabatic value, but the CISK perspective went out of favor among most of the tropical dynamicists (Bretherton 2003).

1.4.3 WISHE (Wind-Induced Surface Heat Exchange)

The alternative to the CISK-type approach is quasi-equilibrium thinking (Emanuel et al. 1994), which serves as the basis for WISHE theory. First proposed by Arakawa and Schubert (1974), this school of thought argues that moist convection is instability in an atmospheric column and rapidly consumes convective available potential energy, and that without moist static energy sources like evaporation and cloud forcing, moist convection cannot cause instability of the large-scale circulations. My thesis also is premised on the quasi-equilibrium approach.

WISHE theory, advanced by Emanuel (1987) and Neelin et al. (1987), argues that in mean easterlies, enhanced easterly to the east of the upward motion causes enhanced evaporation and sensible heat flux. This brings about instability since low-level easterlies are collocated with warm temperature anomaly in the troposphere in an eastward propagating wave. Evaporation-induced precipitation is correlated with a warm temperature anomaly, increasing eddy potential energy.

In the present context, we may parameterize $E = Au$, and assume a zero tendency for the humidity equation:

$$-a^2\frac{\partial u}{\partial x} = -Q + E \quad \text{or} \quad Q = a^2\frac{\partial u}{\partial x} + Au. \tag{1.8}$$

The key difference from CISK is that now $a < c_0$. This is the model of Neelin et al. (1987) without damping, which is mathematically identical to Emanuel (1987) except that Emanuel took $a = c_0$. The dispersion relationship for $a < c_0$ is

$$\sigma = \pm\sqrt{-(c_0^2 - a^2)k^2 - ikA} \rightarrow \pm i\sqrt{c_0^2 - a^2}k \mp \frac{1}{2}\frac{A}{\sqrt{c_0^2 - a^2}} \qquad (k \rightarrow \infty). \qquad (1.9)$$

Note that on an equatorial β-plane, the condition of boundedness at infinity rejects the westward propagating mode. The growth rate for the unstable solution asymptotes to $(1/2)A/\sqrt{c_0^2 - a^2}$ in the small-scale limit. Although the smallest scale is still chosen, the growth rate is bounded, rather than indefinitely increasing.

Although linear perturbation analyses and modeling studies indicate that WISHE is capable of maintaining an MJO-like mode in some models (e.g., Neelin et al. 1987), beginning with Wang (1988), some researchers have cast doubts on the role of WISHE in the MJO. In fact, observational studies show that evaporation is suppressed to the east of active convection and enhanced to the west, a phase relationship opposite to that expected from linear WISHE theory (e.g., Lin and Johnson 1996; Hendon and Glick 1997; Sperber et al. 1997; Lau and Sui 1997; Woolnough et al. 2000).

And yet, nonlinear WISHE theory might be able to conquer these challenges. A quasi-linear WISHE model by Xie et al. (1993) with a resting basic state exhibits convective heating in regions of amplified westerlies. Maloney and Sobel (2004) performed a numerical experiment of a modified version of the National Center for Atmospheric Research (NCAR) Community Atmosphere Model 2.0.1. In their model, suppressing the WISHE effect greatly weakens the MJO, corroborating the importance of WISHE. Moreover, they find enhanced evaporation to the west of convection, consistent with observations.

1.4.4 Coupling of Kelvin and Rossby modes

Because the MJO has a dominant signal in zonal winds and propagates eastward, numerous theories characterized the MJO as a Kelvin-like mode of low zonal wavenumber that arises from interaction between convection and large-scale dynamics (Lindzen 1974; Emanuel

1987; Neelin et al. 1987, among others). Some argued, however, that because there are statistically significant anticyclonic circulations in the upper troposphere following active convection, the MJO should be regarded as a coupled Kelvin-Rossby mode (e.g., Hayashi and Sumi 1986) similar to Gill's (1980) pattern.

Some studies further distinguish between the behavior in the eastern hemisphere and that in the western hemisphere, and characterize the former as a Kelvin-Rossby forced response and the latter as a Kelvin-type radiating response (Salby et al. 1994).

Though earlier observational studies did not provide the horizontal structure of the MJO, newer ones depict it as a moving Gill (1980) pattern. That is, although the disturbance propagates, its dynamical structure can be understood by a stationary, damped response to a localized heating. One may symbolically write

$$\varepsilon \mathbf{v} + \beta y \mathbf{k} \times \mathbf{v} = -\nabla T, \tag{1.10}$$

$$\varepsilon_T T + c_0^2 \nabla \cdot \mathbf{v} = Q(x,y,t), \tag{1.11}$$

where $\mathbf{v} = (u,v,0)^T$ is the horizontal wind vector, ε is the Rayleigh damping coefficient and ε_T is the Newtonian cooling coefficient. If Q is prescribed, the above set gives a nice description of the MJO dynamics. However, this formulation does not answer what determines Q. As this form is not easily dealt in linear analysis, many researchers have assumed that the MJO is a coupled Kelvin-Rossby wave.

The literature suggests, unfortunately, that such coupling is rather difficult and seems to require Ekman convergence (Wang and Rui 1990; Moskowitz and Bretherton 2000) or nonlinearity (Lau and Peng 1987; Hendon 1988). Building on previous work, Chapter 7 presents an argument that Kelvin-Rossby coupling is unlikely in models with usual quasi-equilibrium parameterizations. The issue of Kelvin-Rossby coupling thus remains elusive in the theoretical context.

1.4.5 East-west asymmetry

Even if one succeeds in coupling Kelvin and Rossby waves, there still exists another problem: east-west asymmetry. In a review paper, Wang (2005) contrasted frictional wave-CISK and observations in one of his figures. His focus was on the air-sea interaction but the figure illuminates the pervasive difficulty with east-west asymmetry.

In Wang's figure, the observed MJO exhibits east-west asymmetry just like the standard Gill pattern, with surface westerlies much stronger than easterlies. The modeled Kelvin-Rossby mode, however, does not show such behavior. East-west symmetry of the model mode is a simple consequence of seeking an exponential solution $\sim \exp(ikx - i\omega t)$. To resolve this issue, we have to either invoke the coupling of different wavenumbers or nonlinearity. Since the wave is generally dispersive in the presence of moist convection, wavenumber coupling is quite difficult.

1.4.6 Other proposed maintenance mechanisms

Lin et al. (2000) categorizes previous theories on maintenance of the MJO against dissipation into five kinds. In addition to WISHE and wave-CISK reviewed above, they include (1) midlatitude excitation in the troposphere, (2) stochastic forcing like convective variance, and (3) self-excited oscillatory heat sources. Furthermore, there are studies that rely on still different mechanisms (excitation of supercloud clusters, for instance) to explain the MJO.

Similarly, Zhang (2005) classified theories into forced response theories and instability theories, which comprise wave-CISK and WISHE. For the forced response theories, he lists (1) tropical intraseasonal stationary forcing, (2) tropical stochastic forcing, (3) lateral forcing. He then examines other factors: (1) radiation, (2) water vapor, (3) sea surface temperature, (4) scale interaction, and (5) heating profile.

Some studies note extratropical influences on the MJO. Liebmann and Hartmann (1984) have found wintertime correlation between extratropical 500 hPa heights and tropical infrared data, indicating a possible influence of the midlatitude. Using the European Centre

for Medium-Range Weather Forecasts (ECMWF) model, Ferranti et al. (1990) have tested extratropical and tropical predictability and found that constraining one to the observed state improves the other, illustrating a link between the two. Straus and Lindzen's (2000) spectral analysis has demonstrated that low zonal wavenumber modes dominate upper tropospheric zonal winds in the phase speed range of 1-10 m/s and in the period range of 30-60 days. They hypothesized that the MJO is driven by planetary-scale baroclinic instability in the subtropics. Lin et al. (2000) have found that the MJO is greatly weakened in their Quasi-equilibrium Tropical Circulation Model (QTCM) when midlatitude cyclones are suppressed, although they caution that baroclinic storms in their model are more regular than observed and exhibit some unrealistic characteristics.

Stochastic forcing that stems from subgrid-scale convective variance has been suggested as a possible source of maintenance of the MJO. For example, Yu and Neelin's (1994) model results show that white noise thermal forcing feeds back onto low-frequency, low-wavenumber modes. On the other hand, Salby et al. (1994) included red-noise stochastic forcing in their model of frictional wave-CISK.

An oscillating heat source is another candidate for the MJO mechanism. From this perspective, one does not have to elaborate on interactions between convection and large-scale dynamics; essentially the influence is one-direction from the heating source. Extending Gill's (1980) model to include an oscillatory heating, Yamagata and Hayashi (1984) examined the thermally forced stationary waves. The resulting structure resembles the observed MJO but after the heating was turned off, they found westward propagating Rossby modes that are absent in the observations. At a more fundamental level, such a heating source has not yet been identified. Hu and Randall (1994) have found self-excited low-frequency oscillations due to interactions among convection, radiation, and surface fluxes in their radiative-convective model, although Brown and Bretherton (1995) did not find the same mechanism operating in their model, a result implying that Hu and Randall's mechanism is not a universal feature. Besides, Hu and Randall's oscillation had a very small amplitude (Sobel and Bretherton 2000).

Recently many papers have been devoted to scale interaction. In particular, Majda

and Biello (2004) and Biello and Majda (2005) developed a model of scale interaction between synoptic convectively coupled equatorial waves and the MJO. Eddy flux feeds onto the MJO, making the large-scale heating profile more top-heavy than the tropical mean profile. The model also captures the detailed dynamical features of the MJO. Nevertheless, they specified the large-scale oscillatory heating and did not address where the oscillatory heating originates from. Majda et al. (2007) attempt to answer this question, modifying the model of the convectively equatorial coupled wave. Since their model assumed a $v = 0$ solution, however, it remains to be seen whether their model can explain Rossby gyres.

1.5 MJO review: summary

Observational studies have provided a clearer physical picture of the MJO. To the first order, it is characterized by organized deep convection that propagates eastward at about 5 m/s from the Indian Ocean to the western Pacific, accompanied by a planetary scale Gill response. Recent observational analyses illuminated both air-sea interaction and moist processes. Shallow convection, perhaps induced by frictional convergence of moisture, precedes the center of deep convection. Deep convection coincides with moist free troposphere. Extensive areas of anvils follow anomalous precipitation.

In contrast with observations, the climate community has confronted numerous challenges on the modeling and theory sides. Theoreticians contributed a huge volume of the literature, but a satisfactory theoretical understanding is yet to emerge. IPCC-class GCMs still cannot simulate the MJO well, and often researchers cannot decipher why one model looks better over another.

It is rather curious that a vast number of theoretical studies are yet to explain the model deficiencies about the MJO. Presumably some physical processes have escaped attention of scientists for a long time because of lack of observations. There are some possible candidates, but my thesis focuses on a particular process called moisture-convection feedback. But before describing moisture-convection feedback, I review the weak temperature gradient (WTG) approximation, a recently developed theoretical tool. In fact, the WTG will

allow us to focus on the role of free-tropospheric humidity, a key ingredient of moisture-convection feedback.

1.6 Physics with recent developments

1.6.1 Weak temperature gradient approximation

One of the problems with the MJO theories is that tropical meteorology has not enjoyed a simplified dynamical system like the quasigeostrophic potential vorticity equation, a standard model for mid-latitude dynamicists and physical oceanographers (Charney and Stern 1962; Holton 2004, for a basic treatment). The balance equation in the tropics is complicated and is not amenable to simple analyses. Moreover, the key determinant of tropical dynamics is certainly moist convection; thermodynamics is at the heart of the problem. If so, one might ask, can we simplify dynamics so that we can focus on thermodynamics? Against this background, Sobel and Bretherton (2000) and Sobel et al. (2001) have proposed a method called the weak temperature gradient (WTG) approximation.

In the tropics where the Coriolis parameter is small and the Rossby deformation radius tends to infinity ($R_d = NH/f \to \infty$, where N is buoyancy frequency, H is the height scale, and f is the Coriolis parameter), gravity waves efficiently remove temperature gradient above the boundary layer (Bretherton and Smolarkiewicz 1989) and the horizontal temperature gradient is weak (Charney 1963). Various authors invoked such a notion to simplify their analyses (Schneider 1977; Held and Hou 1980; Lindzen and Nigam 1987).

Figure 7 shows the January climatological distributions of temperature at 500 hPa, SST, and precipitation. The datasets used are the National Centers for Environmental Prediction/National Center for Atmospheric Research (NCEP/NCAR) reanalysis (Kalnay et al. 1996), the Reynolds SST dataset (Reynolds and Smith 1994), and the CPC Merged Analysis of Precipitation (CMAP; Xie and Arkin 1997). Sobel (2002) provided an almost identical figure. Precipitation distribution roughly follows that of SST, but it has more fine-scale structures. Relative to the SST, temperature is almost constant for the entire tropics. For example, the zonal SST difference in the Pacific is 4 K, whereas that of midtropospheric

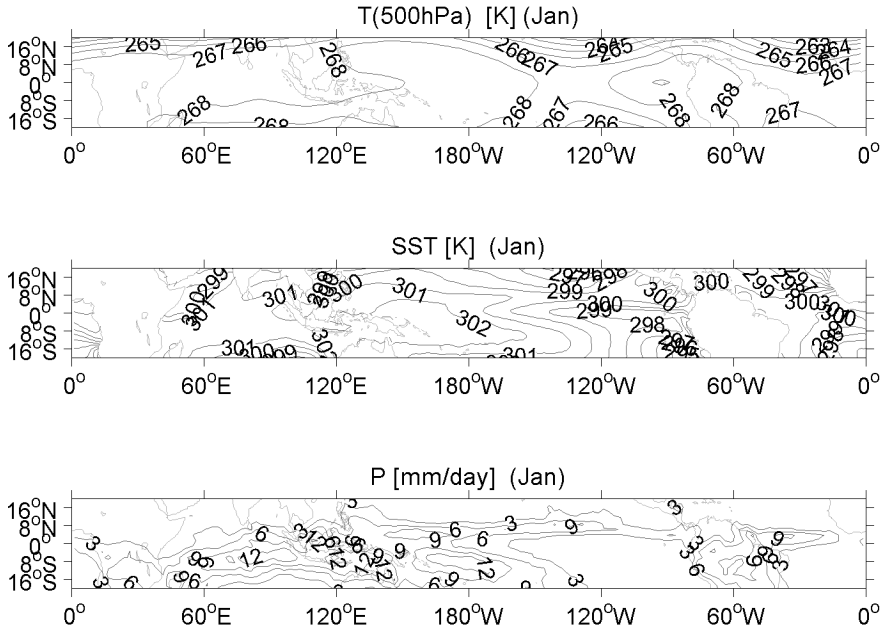

Figure 1-7: Climatological January distributions of (upper panel) temperature at 500 hPa in K, (middle panel) SST in K, and (lower panel) precipitation in mm/d. This is almost identical to Figure 1 of Sobel (2002), except for contour intervals.

temperature is < 1K.

The primary consequence of this dynamical constraint is that the temperature equation can be approximated by

$$w\frac{\partial \theta}{\partial z} \simeq Q_{net} \tag{1.12}$$

where w is vertical velocity, θ is potential temperature, and Q_{net} is net heating. Another way of saying this is that in the absence of heating, tropical circulations tend to be non-divergent (Charney 1963). Although many previous studies utilized this approximation in many ways, it was Sobel and Bretherton (2000) and Sobel et al. (2001) who advocated utilizing this relation as a formal approximation. Since these two papers, the weak temperature gradient (WTG) approximation has been applied to the Gill (1980) problem (Bretherton and Sobel 2003), Hadley circulation (Polvani and Sobel 2002; Burns et al. 2006), moist teleconnection (Chiang and Sobel 2002), the Walker circulation (Bretherton and Sobel 2002;

Peters and Bretherton 2005), and tropical intraseasonal variability (Sobel and Gildor 2003). Majda and Klein (2003) considered a systematic approach to derive various WTG systems, using a rigorous single-timescale multiple-spatial scale perturbation expansion.

Sobel and Bretherton (2000) proposed a new approach of using a single-column model (SCM), in which, unlike a traditional radiative-convective model, temperature is not calculated but specified, but vertical motion is diagnosed from the temperature equation. In other words, their formulation was simply to impose (1.12) on an SCM. In this configuration, the model is not meant to represent the horizontal average of the tropics but rather a limited area within the tropics. The weak tropical temperature gradient on the large scale is the justification for such a treatment. This method was later termed WTG approximation by Sobel et al. (2001).

When applied to systems like a shallow water model, the WTG is a filtering approximation for balanced dynamics in the tropics. The key difference from previous scaling is that diabatic heating enters at the leading order. As with the quasigeostrophic approximation for the extratropics, the WTG approximation filters out gravity waves (i.e. inertio-gravity waves and Kelvin waves), leaving only Rossby waves and moistures modes (Sobel et al. 2001; Bretherton and Sobel 2003). This is sometimes problematic since WTG removes the Kelvin wave, which propagates through gravity wave dynamics. In fact, the Gill (1980) model on the β-plane has a singularity at the WTG limit (Bretherton and Sobel 2003). Also some implementations cause problems like non-conservation of mass (Sobel and Bretherton 2000). Nonetheless, the WTG approximation is very powerful and is the central tool in my thesis.

Although various forms of scaling have been explored, in the following, I provide a very simple scaling argument, based on Sobel and Gildor (2003). Note that Sobel and Gildor (2003) included a mixed layer ocean but it is neglected here. Also I use the shallow water notation rather than the QTCM employed by them.

Our choice here is the familiar convectively coupled Kelvin-like wave that is composed of (1.1), (1.2), (1.3), and (1.4). Assuming $\sim \exp(ikx + \sigma t)$, and noting $\sigma u = -ikT$, (1.3)

and (1.4) become

$$i\frac{\sigma^2 u}{k} + c_0^2 iku = Q, \tag{1.13}$$

$$\sigma q - a^2 iku = -Q + E. \tag{1.14}$$

If $|\sigma^2/(c_0^2 k^2)| \ll 1$, the left-hand side of the temperature equation is dominated by the second term. The behavior of such a mode can be approximated by

$$c_0^2 iku = Q, \tag{1.15}$$

$$\sigma q - a^2 iku = -Q + E, \tag{1.16}$$

where temperature (geopotential) should be dropped in the formulations of Q and E. Now the model is independent of k aside from the formulation of Q and E.

At the first look, the condition $|\sigma^2/(c_0^2 k^2)| \ll 1$ appears difficult to satisfy. A perfect counter example is a dry gravity wave, which shows $|\sigma^2/(c_0^2 k^2)| = 1$. However, this condition is satisfied because of the prognostic humidity equation. For example, if we neglect evaporation and assume $(q-T)/\tau$, then

$$\frac{\partial q}{\partial t} = -\frac{c_0^2 - a^2}{c_0^2}\frac{q}{\tau} \quad \text{or} \quad \sigma = -\frac{c_0^2 - a^2}{c_0^2}\frac{1}{\tau}. \tag{1.17}$$

Different notations aside, the result here represents a moisture mode found by Sobel et al. (2001).

It is instructive to rewrite the condition as

$$L \ll 2\pi |c_0/\sigma|, \tag{1.18}$$

where $L \equiv 2\pi/k$. This means that the condition of WTG is that the length scale of a disturbance is much smaller than the distance a gravity wave can travel for a characteristic timescale. For timescales of several days ($\sigma \sim 2 \times 10^{-6}\mathrm{s}^{-1}$), assuming a dry gravity wave speed of 50 m/s, we have $L \ll O(100\ 000\mathrm{km})$, a condition easily met for the earth's

tropics. In reality, rotation sets a stricter constraint than this but WTG remains valid in many applications.

Some note on the naming is in order. It sounds somewhat strange to apply the weak temperature *gradient* approximation to an SCM, since an SCM *cannot* have gradient. Thus it is necessary to keep in mind that if used in a WTG configuration, an SCM would represent a limited area in the tropics where, as a whole, the temperature gradient is weak.

As Sobel et al. (2001) demonstrated and the simple analysis above indicates, the WTG renders water vapor central to balanced dynamics. For example, they discovered a moisture mode, as was found by other studies like Fuchs and Raymond (2002, 2005, 2007). Importance of tropospheric humidity, as opposed to boundary layer humidity, has gained interest recently. This is the topic of the next section.

1.6.2 Moisture-convection feedback

Deep convection is naturally associated with a moist free troposphere since convection is the primary source of humidity (Emanuel and Pierrehumbert 1996; Held and Soden 2000), but is convection affected by humidity? The answer seems to be yes, and what is important appears to be humidity in the low to mid-troposphere. As explained above, some authors contend that the lack of moisture-convection feedback is a cause of deficient GCM simulations of the MJO.

A number of recent observational studies show that a moist low to mid-troposphere favors deep convection and dry tropospheric air inhibits deep convection (Numaguti et al. 1995; Brown and Zhang 1997; Sherwood 1999; Sherwood and Wahrlich 1999; Bretherton et al. 2004; Sobel et al. 2004; Peters and Neelin 2006; Biasutti et al. 2006)

Brown and Zhang (1997) analyzed the data from the Tropical Ocean Global Atmosphere Coupled Ocean Atmosphere Response Experiment (TOGA COARE; Webster and Lukas 1992) and found a bimodal distribution of free tropospheric humidity. Deep convection was found to be associated with a moist free troposphere. Sobel et al. (2004) found a similar relationship between humidity and deep convection for a different observation campaign called the Kwajalein Experiment (KWAJEX). Sherwood (1999) compared pos-

sible convective precursors over the western Pacific and discovered that the dominant factor was low- to mid-tropospheric relative humidity (above the boundary layer). Biasutti et al. (2006) concluded that humid troposphere tends to lead deep convection in the Atlantic as well.

Bretherton et al.'s (2004) work is particularly illuminating. Using the data from Special Sensor Microwave Imager (SSM/I), they revealed that precipitation is an exponential function of column relative humidity, and that the functional form is universal across different ocean basins. The result has been replicated by Biasutti et al. (2006) and Peters and Neelin (2006). Moreover, Peters and Neelin (2006) discovered a power-law relation between precipitable water and precipitation beyond the exponential range considered by Bretherton et al. (2004).

Modeling studies also lend support to sensitivity of deep convection to free tropospheric humidity (Tompkins 2001; Redelsperger et al. 2002; Takemi et al. 2004). Tompkins (2001) used a CRM and in one simulation, explored the effect of a "hot spot"-like warm sea surface temperature (SST) anomaly. He found that convection does not spontaneously initiate over a newly established "hot spot" because of dryness of the atmosphere. Instead, the model atmosphere waits for the arrival of a convective system.

What is the physics behind the sensitivity of moist convection to mid-tropospheric humidity? Several ideas have been proposed, but the answer seems to be entrainment. Brown and Zhang (1997) showed that air parcels originating from the boundary layer loses buoyancy by entrainment. Kuang and Bretherton (2006) examined CRM simulations and found that undiluted air parcels that would cause a very high cloud height are too infrequent.

Since tropospheric moisture is provided by convection, such sensitivity of moist convection suggests a feedback between moist convection and environmental humidity. Held et al. (1993) and Tompkins (2001) found that moist convection tends to organize itself because of the effect of free-tropospheric humidity. More recently, Bretherton et al. (2005) showed an extreme example. Their CRM simulation demonstrated that self-aggregation in the model led to a warmer and drier atmosphere than the RCE, with a maximum precipitation rate of near 100 mm/day.

There are an increasing number of theoretical studies on moisture-convection feedback. Raymond (2000) explored the effect of making precipitation inversely proportional to saturation deficit, finding that convective timescale is a function of moisture. Sobel et al. (2001), and Fuchs and Raymond (2002, 2005, 2007) examined moisture modes (also called by slow moisture waves by Fuchs and Raymond 2002, 2005). Although it was not their primary focus, Yu and Neelin (1994) also found moisture modes in their model with a Betts-Miller parameterization.

The mode identified by these authors is actually equivalent to the damped moisture mode described in the previous section. Indeed, in the previous section WTG made humidity the sole prognostic variable, leaving only moisture mode (Sobel et al. 2001; Fuchs and Raymond 2007).

Fuchs and Raymond (2006) noted that the moisture mode might play a role in the MJO. Bretherton et al. (2005) argued that self-aggregation in a CRM, whose physics is analogous to that of moisture mode, might be related to the MJO. This is also the starting point of the hypothesis in my thesis. Upon closer inspection, however, difficulties in interpretation abound. For instance, the moisture mode is almost stationary and propagates through linear WISHE. Its spatial features resemble those of a Kelvin wave, not of a Kelvin-Rossby coupled mode. To be unstable it requires negative effective gross moist stability, with cloud radiative forcing exceeding MSE transport. Moreover, the moisture mode fails in scale selection. How can such a mode explain the MJO, a large-scale eastward propagating disturbance?

The hypothesis that the MJO is related to the moisture mode is attractive at least in one aspect. As Derbyshire et al. (2004) reported, a vast majority of convective parameterizations show only weak sensitivity to free-tropospheric humidity. In other words, GCMs with these convective schemes have very weak moisture-convection feedback. The lack of moisture-convection feedback would naturally imply the absence of the moisture mode, and hence poor simulations of the MJO.

1.7 Hypothesis

To ameliorate the deficiencies with moisture mode instability theory, I propose the following hypothesis, composed of three parts:

- The initial stage of the MJO, as depicted in the first two rows of Figure 1, can be explained as a linear moisture mode. It does not necessarily require negative effective gross moist stability because of enhanced gustiness. Moisture mode nonlinearly saturates via higher MSE export or weakening MSE sources;

- Once it reaches nonlinear saturation, its spatial features can be described by linear dynamics augmented by a nonlinear humidity equation. Scale selection and eastward movement occur through moist processes, including nonlinear WISHE, nonlinear advection, and boundary-layer convergence;

- The reason for poor simulations of the MJO by GCMs has to do with poor representation of moisture-convection feedback in GCMs. In other words, moisture mode instability requires moisture-convection feedback.

One novelty of the hypothesis is nonlinearity in the humidity equation. Tuyl (1987) demonstrated that nonlinear terms in the momentum and temperature equations are not significant for a disturbance like the MJO. This may not be the case, however, with humidity, which is more like a tracer advected around by large-scale wind field. In fact, observations of dry intrusion show that advection of dry air suppresses deep convective activity, suggesting its potential impact in tropical dynamics. Theoretically Sobel et al. (2001) explored the consequence of humidity spatial gradient, and found waves propagating because of humidity gradient in the WTG approximation. Although what they examined was *linear* humidity advection, this again implies a potentially important role of moisture advection. More recently Benedict and Randall (2007) discovered that the immediate drying after the active phase of the MJO is due to horizontal, nonlinear advection of dry air. Such an effect has yet to be explored in a theoretical context.

Another new aspect of this study is introduction of downdraft-enhanced gustiness. Although small relative to WISHE effect, the gust is always in phase with deep convection at the large-scale (at smaller scale, gustiness is not in phase since gust fronts spread out). Downdraft-enhanced gustiness thus constitutes another source of the column MSE. The two-step process described above is similar to the finding of Hendon (1988). He utilized a wave-CISK parameterization with interactive static stability and found that in the linear regime, the mode was stationary. Once the mode entered the nonlinear regime, the spatial structure resembled that of the Gill (1980) model, and began to progress. The Rossby response to the west of convection preferentially enhances static stability there, resulting in eastward movement of convection. Nonetheless, his study relied on a CISK parameterization, and was problematic with this regard.

1.8 Thesis organization

The organization of this thesis is as follows. Chapter 2 focuses on the initial, linear regime of the moisture mode. By analyzing a simplified QTCM, it sets the stage for the later chapters.

Results on tropical dynamics are dependent on the choice of a convective scheme, and always subject to some doubt. Given this consideration, Chapters 3, 4, and 5 all attempt to make the case for moisture mode stronger, investigating the model of Bony and Emanuel (2005), the QTCM with boundary layer developed by Sobel and Neelin (2006), and the SCM of Bony and Emanuel (2001), respectively. Indeed, the moisture mode is found in all of the four models examined in this thesis, and their characteristics are similar across different models.

The topic of Chapter 6 is the second, nonlinear regime of the moisture mode. Numerical calculations are performed with a simplified QTCM, showing that nonlinearly saturated moisture modes evolve with time through moist processes such as nonlinear WISHE and nonlinear advection. Although it fails to provide a successful theory for the MJO, it elucidates the behavior of the moisture mode on the equatorial β-plane.

Chapter 7 turns to the linear regime again, but this time I attempt to generalize the conditions for the existence of the moisture mode. In fact, the analysis shows that moisture modes exist in a large class of simple, linear primitive equation models with quasi-equilibrum convective parameterizations.

Lastly, Chapter 8 summarizes the key findings and discusses limitations of the present thesis.

Chapter 2

Moisture modes in QTCM

2.1 Introduction

Chapter 1 described my hypothesis that the MJO can be characterized as a nonlinear moisture mode. I hypothesize that the MJO dynamics is a two-step process: the linear regime, where a stationary moisture mode grows over the Indian Ocean until nonlinear saturation, and the nonlinear regime, in which the saturated nonlinear mode commences moving eastward through nonlinear moist processes.

The topic of this chapter is the initial linear stage of the MJO. I explore moisture modes in the Quasi-equilibrium Tropical Circulation Model (QTCM; Neelin and Zeng 2000), which is one of the simplest models. The chapter begins with QTCM derivation, and then examines linear stability for a Kelvin-like mode as an illustration of moisture modes, which is followed by analyses using linear and nonlinear weak temperature gradient (WTG) approximation.

Fuchs and Raymond (2002, 2005) extensively studied a QTCM-like model. Their formulation is mathematically equivalent to that of QTCM in the WTG limit. This chapter builds on their analyses, adding gustiness and performing a perturbation expansion to rigorously obtain the WTG limit.

The analyses presented in this chapter show that QTCM has an unstable moisture mode, which nonlinearly saturates because of thermodynamic limiting processes. While illumi-

nating the physical processes underlying the moisture mode, the results here raise numerous questions. For example, while the key to moisture mode instability seems to be the sensitivity of deep convection to free-tropospheric humidity, QTCM cannot address whether or not this is indeed the case since it does not separate boundary layer humidity and free-tropospheric humidity. Questions such as this will be taken up in later chapters.

2.2 Derivation of QTCM

Neelin and Zeng (2000) gave an elegant derivation of the QTCM, including all nonlinear terms. Here the purpose is to illustrate the concepts behind the QTCM, rather than giving technical details. Attention is thus restricted to a simple case. Readers interested in technicalities are referred to their original paper.

Besides nonlinearities, the original QTCM has another significant feature. It has many parameterizations of physical mechanisms, taken from general circulation model counterparts. However, the analysis presented here avoids sophisticated physical representations in the interest of simplicity.

2.2.1 Prognostic equations

The linear primitive equations around the horizontally homogeneous radiative-convective equilibrium (RCE) on an equatorial β-plane with a rigid lid and bottom may be written as

$$\frac{\partial \mathbf{v}}{\partial t} + \beta y \mathbf{k} \times \mathbf{v} = -\nabla \varphi - \frac{\mathbf{v}}{\tau_m}, \tag{2.1}$$

$$\frac{\partial T}{\partial t} + \omega \frac{\partial \bar{s}}{\partial p} = Q_c + Q_R + g \frac{\partial F_T}{\partial p}, \tag{2.2}$$

$$\frac{\partial \varphi}{\partial p} = -\kappa \frac{T}{p}, \tag{2.3}$$

$$\nabla \cdot \mathbf{v} + \frac{\partial \omega}{\partial p} = 0. \tag{2.4}$$

Here $\mathbf{v} = (u, v)^T$ is the horizontal wind vector, φ is the geopotential, T is the temperature, ω is the pressure velocity, s is the dry static energy ($s = T + \varphi$), $\beta = df/dy$ and f is the

Coriolis parameter, τ_m is the Rayleigh damping timescale, Q_c is convective heating, Q_R is radiative cooling, F_T is turbulent vertical eddy heat flux whose boundary condition is sensible heat flux ($F_T(p_s) = H$), and $\kappa = R_d/c_p$, R_d is the gas constant for dry air, and c_p is the specific heat of dry air at constant pressure. Note that temperature T is expressed in energy units; T here actually represents c_pT in usual notation.

Strictly speaking, it is necessary to distinguish the mean RCE state and perturbations. As the mean state is horizontally homogeneous, however, I can carry all the derivation without making this distinction. The following assumes that all variables are a sum of the horizontally homogeneous RCE and perturbations from it: for instance, $Q_c(x,y,p,t) = \overline{Q}_c(p) + Q'_c(x,y,p,t)$, where the overbar denotes the RCE mean state and the prime implies the perturbation from it.

For humidity, it turns out that nonlinearity is of central importance. For the moment, I proceed with the following equation.

$$\frac{\partial q}{\partial t} + \nabla \cdot (q\mathbf{v}) + \frac{\partial (q\omega)}{\partial p} = Q_q + g\frac{\partial F_q}{\partial p} + K_q \nabla^2 q, \tag{2.5}$$

where q is the specific humidity, Q_q is convective source term of humidity, F_q is vertical turbulent eddy humidity flux, and K_q is the horizontal eddy diffusion coefficient for specific humidity. As with temperature, specific humidity q is in energy units; q in my notation implies $L_v q$ in common notation. The boundary condition of F_q is evaporation: $F_q(p_s) = E$.

The idea behind the QTCM is to exploit the fact that the tropical temperature fluctuation tends to follow that of a moist adiabat, since moist convection keeps a quasi-equilibrium state with the large-scale forcing (Arakawa and Schubert 1974; Emanuel et al. 1994). Since hydrostaticity directly relates temperature with geopotential, moist convective quasi-equilibrium yields a dynamical constraint. There is an increasing recognition of the importance of small departures from the moist adiabat. That is, although first-baroclinic mode is usually quite large in amplitude, the second-baroclinic mode also plays an essential role as well (e.g., Mapes 2000). The original QTCM neglects it, however.

Ideally I would like to expand humidity just like temperature. Although expansion of a humidity using a single variable is rather dubious, it allows for a model that is straightfor-

ward to interpret.

To simplify the derivation, I define the following operators:

$$\langle \quad \rangle \equiv (\hat{\ }) \equiv \frac{1}{\Delta p}\int_{p_t}^{p_s}(\quad)dp', \tag{2.6}$$

$$(\quad)^{\dagger} \equiv \frac{1}{\Delta p}\int_{p}^{p_s}(\quad)d\ln p', \tag{2.7}$$

where Δp is the pressure depth of the troposphere, p_s is the surface pressure, p_t is the pressure at the tropopause. Neelin and Zeng (2000) wrote each field as the following, using a Galerkin expansion up to first-order:

$$\mathbf{v}(x,y,p,t) = V_0(p)\mathbf{v}_0 + V_1(p)\mathbf{v}_1 = \mathbf{v}_0 + V_1(p)\mathbf{v}_1, \tag{2.8}$$

$$T(x,y,p,t) = T_r(p) + a_1(p)T_1(x,y,t), \tag{2.9}$$

$$q(x,y,p,t) = q_r(p) + b_1(p)q_1(x,y,t). \tag{2.10}$$

Here x is the horizontal coordinate, y is the meridional coordinate, p is pressure and the vertical coordinate, t is time, V_0 is the basis function for the barotropic mode, $\mathbf{v}_0$ is the horizontal wind vector for the barotropic mode, V_1 is the basis function for the first baroclinic mode, and $\mathbf{v}_1$ is the first baroclinic component. The barotropic mode here is defined as the vertical average, and its basis function is simply a constant: $V_0(p) = 1$. T_r is the reference temperature profile, a_1 is the temperature basis function, T_1 is the amplitude of the temperature component associated with a_1, q_r is the reference profile of specific humidity, b_1 is the humidity basis function, q_1 is the specific humidity amplitude associated with b_1. T_r and q_r are taken from a typical tropical sounding.

Note that the "first baroclinic mode" here is not a normal mode of the troposphere in the sense of Fulton and Schubert (1985). It is easy to show that if the temperature follows a moist adiabat (or some characteristic profiles), the vertical motion field is one-signed and has a peak around the middle troposphere (Emanuel et al. 1994), as shown in Chapter 3. Since such a profile mimics the first baroclinic normal mode, I call it the "first baroclinic mode."

The basis function for velocity comes from the temperature basis function. Combining the vertical expansion of temperature and hydrostaticity yields

$$\nabla\varphi = \nabla\varphi_s + \nabla\int_p^{p_s} \kappa T d\ln p' = \nabla\varphi_s + a_1^\dagger(p)\kappa\nabla T_1, \tag{2.11}$$

where φ_s is the surface geopotential. This suggests that $V_1 \sim a_1^\dagger$. To ensure $\langle V_1 \rangle = 0$, I take

$$V_1 = a_1^\dagger - \left\langle a_1^\dagger \right\rangle. \tag{2.12}$$

Given this, the vertical pressure velocity may be written as

$$\omega = -\Omega_1(p)\nabla\cdot\mathbf{v}_1, \tag{2.13}$$

where $\Omega_1 \equiv \int_{p_s}^{p} V_1 dp'$ and $\partial_p\Omega_1 = V_1$.

The moisture basis function is chosen such that

$$b_1(p) = \frac{q_r(p)}{q_r(p_s)}, \tag{2.14}$$

which avoids a potential problem of having negative humidity.

Figure 2-1 displays basis functions for QTCM, created by the procedure described above and using a typical tropical sounding. The parameters and soundings are for version 2.3 of QTCM taken from the website.[1] As noted earlier, the temperature variation follows that of the moist adiabat, unlike conventional normal mode analysis. A_1 and B_1 are described in the subsection on diagnostic equations.

Noting $\nabla\varphi = \nabla\varphi_s + a_1^\dagger(p)\kappa\nabla T_1$ and $\mathbf{v} = \mathbf{v}_0 + V_1\mathbf{v}_1$, applying the vertical averaging op-

[1] Available online at http://www.atmos.ucla.edu/~csi/qtcm_frm.html. There are some issues associated with this figure, although none of them are fatal to the arguments presented in this chapter. One issue is the height of the tropopause, which is set at 150hPa here. However, the QTCM's standard implementation assumes the tropospheric depth of 800hPa. Also, a careful reading of the code shows that T_r and q_r are not used to calculate M_{sr} and M_{qr}, respectively.

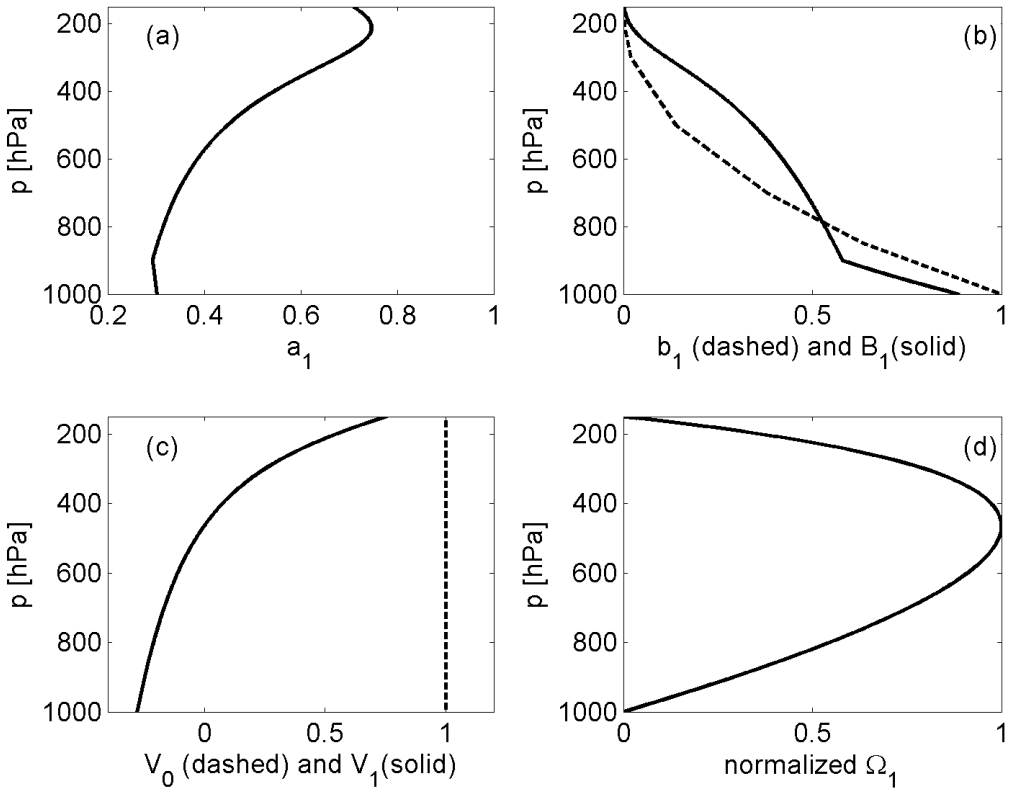

Figure 2-1: Basis functions for QTCM. (a) Temperature basis function $a_1(p)$. (b) Humidity basis function $b_1(p)$ and basis function for the humidity relaxation profile $B_1(p)$. (c) Velocity basis functions $V_0(p) = 1$ and $V_1(p)$. (d) Pressure velocity basis function $\Omega_1(p)$.

erator $\langle \quad \rangle$ to (2.1) and using the continuity equation yield the barotropic vorticity equation

$$\frac{\partial \zeta_0}{\partial t} + \beta v_0 = -\frac{\zeta_0}{\tau_m}, \tag{2.15}$$

where $\zeta_0 \equiv \partial_x v_0 - \partial_y u_0$. On the other hand, multiplying by V_1 and taking the vertical average of (2.1) result in

$$\frac{\partial \mathbf{v}_1}{\partial t} + \beta y \mathbf{k} \times \mathbf{v}_1 = -\kappa \nabla T_1 - \frac{\mathbf{v}_1}{\tau_m}, \tag{2.16}$$

where $\left\langle V_1 a_1^\dagger \right\rangle = \left\langle V_1^2 \right\rangle$ has been used.

In the following, I focus on the cases where friction takes the form of Rayleigh damping. This essentially decouples the baroclinic mode from the barotropic mode. Although the barotropic mode advects humidity around, it is simply damped and therefore neglected below. Invoking $\omega = -\Omega_1 \nabla \cdot \mathbf{v}_1$ and taking the vertical average simplifies the temperature equation (2.2) as

$$\hat{a}_1 \frac{\partial T_1}{\partial t} + M_{sr} \nabla \cdot \mathbf{v}_1 = \langle Q_c \rangle + \langle Q_R \rangle + \frac{H}{\Delta p / g}, \tag{2.17}$$

where $M_{sr} \equiv \left\langle -\Omega_1 \partial_p s_r \right\rangle$. For the humidity equation, the same procedure gives

$$\hat{b}_1 \frac{\partial q_1}{\partial t} + \hat{b}_1 \mathbf{v}_0 \cdot \nabla q_1 - M_{qr} \nabla \cdot \mathbf{v}_1 - M_{qp} \nabla \cdot (q_1 \mathbf{v}_1) = \left\langle Q_q \right\rangle + \frac{E}{\Delta p / g} + K_q \hat{b}_1 \nabla^2 q_1, \tag{2.18}$$

where $M_{qr} \equiv -\langle q_r V_1 \rangle$ and $M_{qp} \equiv -\langle b_1 V_1 \rangle$. It is straightforward to demonstrate

$$M_{qr} = -\langle q_r V_1 \rangle = \left\langle \Omega_1 \partial_p q_r \right\rangle, \tag{2.19}$$

$$M_{qp} = -\langle b_1 V_1 \rangle = \left\langle \Omega_1 \partial_p b_1 \right\rangle. \tag{2.20}$$

If the basic state consists of nonzero q_1 which is homogeneous in space, I can rewrite the equation as

$$\hat{b}_1 \frac{\partial q_1'}{\partial t} + \hat{b}_1 \mathbf{v}_0 \cdot \nabla q_1' - \overline{M}_{q1} \nabla \cdot \mathbf{v}_1 - M_{qp} \nabla \cdot (q_1' \mathbf{v}_1) = \left\langle Q_q \right\rangle + \frac{E}{\Delta p / g} + K_q \hat{b}_1 \nabla^2 q_1', \tag{2.21}$$

where $\overline{M}_{q1} \equiv M_{qr} + M_{qp}\overline{q}_1$. In what follows, I use (2.21) in favor of (2.18).

Had I included the nonlinear term (such as $\mathbf{v}\cdot\nabla T$) in the temperature equation (2.2), there appears a term equivalent to $M_{qp}\nabla\cdot(q_1\mathbf{v}_1)$ in the temperature equation, which allows the static stability to be a function of temperature itself. The contribution of this term is linear, and therefore in what follows, I replace M_{sr} in the temperature equation with $\overline{M}_{s1} \equiv M_{sr} + M_{sp}\overline{T}_1$, where $M_{sp} \equiv -\left\langle \Omega_1(\partial_p[\partial_p a_1 + \kappa a_1/p])\right\rangle$.

2.2.2 Diagnostic equations

Deep convection is parameterized as a linear variant of the Betts-Miller scheme (Betts 1986; Betts and Miller 1986). In a spirit similar to moist convective adjustment of Manabe and Strickler (1964), the Betts-Miller scheme relaxes temperature toward a moist adiabat. The adjustment however occurs over a finite time period as opposed to the instantaneous adjustment assumed by Manabe and Strickler. Observations do support convective adjustment for temperature, bringing it close to a moist adiabat. However, there is no universal target profile for humidity (Emanuel et al. 1994), and this exposes the lack of physical basis for the Betts-Miller scheme for humidity. Nevertheless, the choice is not completely useless as it captures moisture-convection feedback, albeit in a very crude way.

In general, the Betts-Miller parameterization takes the form

$$Q_c = \frac{T^c - T}{\tau_c} \quad \text{and} \quad Q_q = \frac{q^c - q}{\tau_c}. \tag{2.22}$$

Here the superscript c denotes the target reference profile, and τ_c is the timescale over which temperature and humidity are relaxed toward the reference profile. For a truncated model like QTCM, variables of interest are vertically averaged quantities like $\langle Q_c\rangle$ and $\left\langle Q_q\right\rangle$. Note that the enthalpy conservation dictates

$$\varepsilon_c(\hat{T}^c - \hat{T}_r - \hat{a}_1 T_1) + \varepsilon_c(\hat{q}^c - \hat{q}_r - \hat{b}_1 q_1) = 0, \tag{2.23}$$

where $\varepsilon_c \equiv 1/\tau_c$ if precipitation is positive and zero otherwise. In the spirit of the linear

scheme, one might formulate the reference temperature as

$$T^c = T_r^c + A_1 T_1^c, \tag{2.24}$$

where A_1 is the basis function for the reference temperature profile. In a similar vein, if the reference humidity profile comes from a fixed reference relative humidity, one could take

$$q^c = q_r^c + B_1 T_1^c. \tag{2.25}$$

With these assumptions, it is possible to solve the enthalpy conservation equation for the reference temperature. The result is

$$T_1^c = \frac{\hat{a}_1 T_1 + \hat{b}_1 q_1 - (\hat{T}_r^c - \hat{T}_r) - (\hat{q}_r^c - \hat{q}_r)}{\hat{A}_1 + \hat{B}_1}. \tag{2.26}$$

In the simplest case of $\hat{A}_1 = \hat{a}_1$, $\hat{B}_1 = \hat{b}_1$, $\hat{T}_r^c = \hat{T}_r$, and $\hat{q}_r^c = \hat{q}_r$, it further simplifies, yielding

$$\varepsilon_c \langle T^c - T \rangle = \frac{\hat{a}_1 \hat{b}_1}{\hat{a}_1 + \hat{b}_1} \varepsilon_c (q_1 - T_1). \tag{2.27}$$

Absorbing the coefficient $\hat{a}_1 \hat{b}_1 / (\hat{a}_1 + \hat{b}_1)$ in the convective timescale, I arrive at the desired expression for precipitation (2.28), which is actually used in the standard QTCM.

$$P = \frac{\Delta p}{g} \langle Q_c \rangle = \max \left(\frac{\Delta p}{g} \frac{q_1 - T_1}{\tau_c}, 0 \right). \tag{2.28}$$

Here P is precipitation in energy units (W/m^2) and ε_c is converted to the maximum operator.

The linear Betts-Miller convective scheme developed here certainly contains numerous problems. There is, however, at least one advantage with this scheme. Recall that Chapter 1 discussed the finding of Bretherton et al. (2004), who found an exponential relationship between precipitation and precipitable water:

$$P \sim \exp(aW/W^*), \tag{2.29}$$

where W is precipitable water, the asterisk denotes saturation, and a is a suitable constant coefficient. As reviewed in Chapter 1, Peters and Neelin (2006) and Biasutti et al. (2006) also confirmed a similar relationship from different datasets. The exponential relation suggests that for a small perturbation with negligible temperature anomaly, precipitation anomaly is $P' \propto W'$, where $W' = (\Delta p/g) \cdot \hat{b}_1 q_1'$. Indeed, this is exactly found in the convective parameterization derived here:

$$P' \propto q_1' \propto W'. \tag{2.30}$$

It is, of course, questionable whether one could elevate the observed correlation between precipitable water and rainfall to causality. The linear Betts-Miller approach used in this chapter is definitely not the best way. Nevertheless, the model at least would show the outcome of using the link between P and W found by Bretherton et al. (2004), Peters and Neelin (2006), and Biasutti et al. (2006).

The observations further indicate that the adjustment for humidity is on the order of 12 h to 16 h Bretherton et al. (2004), which is in contrast with an oft-cited timescale of 2-3 h in the Betts-Miller scheme. My choice for the reference value is τ_c = 12 h in accordance with observations.

Sensible heat flux and evaporation are parameterized using the bulk aerodynamic formula:

$$H = \rho_a C_E V_s (T_s - T_{rs} - a_{1s} T_1), \tag{2.31}$$

$$E = \rho_a C_E V_s (q_s^* - q_{rs} - b_{1s} q_1), \tag{2.32}$$

where ρ_a is the surface air density, C_E is the enthalpy transfer coefficient, V_s is the surface wind speed, T_s is the sea surface temperature, $T_{rs} \equiv T_r(p_s)$, $a_{1s} \equiv a_1(p_s)$, q_s^* is the saturation specific humidity at the surface, $q_{rs} \equiv q_r(p_s)$, and $b_{1s} \equiv b_1(p_s)$. The surface wind speed is defined as

$$V_s = \sqrt{(U + V_{1s} u_1)^2 + V_{1s}^2 v_1^2 + v_g^2 + v_{bg}^2}. \tag{2.33}$$

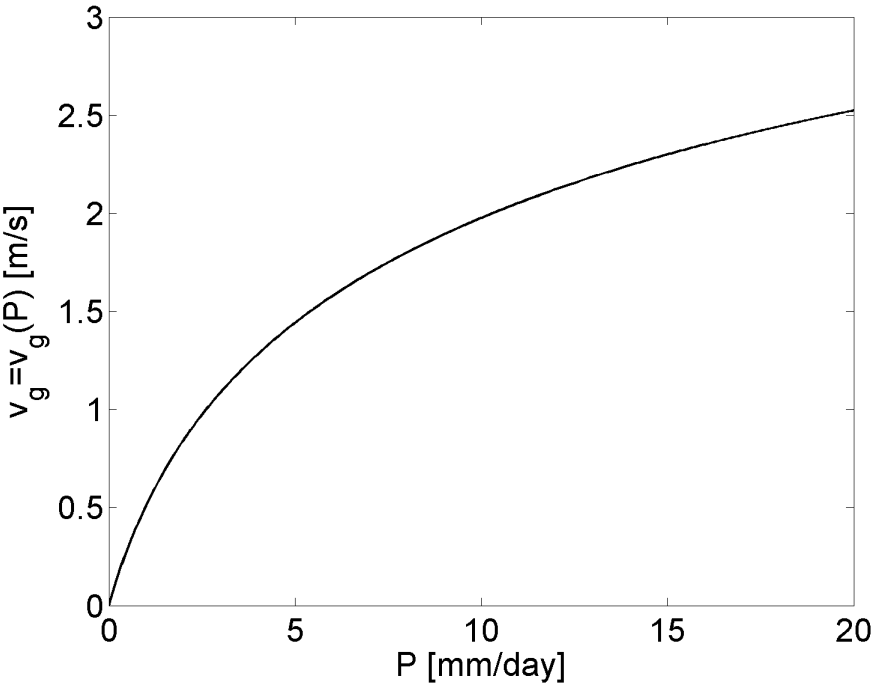

Figure 2-2: Gustiness as a function of precipitation as defined in (2.34.

Here U is the barotropic zonal mean wind, $V_{1s} = V_1(p_s)$, v_g is the downdraft-enhanced gust, and v_{bg} is the background gustiness independent of deep convective activity.

Redelsperger et al. (2000) proposed a parameterization for downdraft-enhanced gustiness as a function of precipitation. They compared outputs from a cloud-resolving model (CRM) with observations form TOGA COARE (Tropical Ocean Global Atmosphere Coupled Ocean Atmosphere Response Experiment), and correlated gustiness due to downdrafts in deep convection with precipitation, finding (2.34).

$$v_g(\tilde{P}) = \begin{cases} \ln(1 + 0.669\tilde{P} - 0.00476\tilde{P}^2) & \tilde{P} < 70.3 \\ 3.20 & \tilde{P} \geq 70.3 \end{cases} \tag{2.34}$$

Here $\tilde{P}$ is precipitation in mm/day (whereas P is in W/m^2). Figure 2-2 shows the gustiness function (2.34). Gustiness increases monotonically with rainfall rate. It is generally small and for typical values of precipitation, v_g is smaller than 2 m/s.

Clear-sky radiation is specified in the RCE calculation. For subsequent calculations, it

is parameterized as a Newtonian cooling. Cloud-radiative forcing follows (2.35), the form proposed by Bretherton and Sobel (2002) and Su and Neelin (2002), and subsequently utilized by Sobel and Gildor (2003) and Peters and Bretherton (2005).

$$\left\langle Q_{R,cld} \right\rangle = r \left\langle Q_c \right\rangle . \tag{2.35}$$

Here r is an empirical constant for cloud radiative forcing as a function of precipitation.

From the annual data of the International Satellite Cloud Climatology Project (ISCCP; Rossow and Schiffer 1991) and Xie and Arkin (1997) precipitation datasets, Peters and Bretherton reported a value of $0.16-0.17$ for r, excluding any points with a climatological precipitation of 50 W/m^2 (1.8 mm/day) or less. Similarly, Bretherton et al. (2005) found $r = 0.17$ in their CRM study. Any parameterization on clouds contains a significant uncertainty, and the scheme does not escape from this common problem. With some caution, the reference value here is taken to be 0.17.

Fuchs and Raymond (2002, 2005) considered a very similar formulation but parameterized cloud forcing as a function of humidity anomaly while Fuchs and Raymond (2007) adopted the same approach as used here. Since both in QTCM and their model precipitation is proportional to precipitable water anomaly, the two approaches are equivalent, and becomes the same form under the WTG balance.

2.3 Linear analysis of QTCM

2.3.1 RCE calculation

The RCE equations consist of

$$0 = \hat{a}_1 \frac{dT_1}{dt} = (1+r)\frac{q_1 - T_1}{\tau_c} + \left\langle Q_{R,clear} \right\rangle + \frac{H}{\Delta p/g}, \tag{2.36}$$

$$0 = \hat{b}_1 \frac{dq_1}{dt} = -\frac{q_1 - T_1}{\tau_c} + \frac{E}{\Delta p/g}. \tag{2.37}$$

Here (2.31) and (2.32) calculate H and E, respectively, and v_g is from (2.34). To calculate the RCE, I specify the sea-surface temperature (SST) and clear-sky radiative cooling $\left\langle Q_{R,clear} \right\rangle$. The two ordinary equations are integrated in a time-stepping manner until they reach a steady-state solution.

The parameters used and results are summarized in Tables 2.1 and 2.2. The background surface wind is specified as mean easterly, but one may interpret it as gustiness if linear WISHE (wind-induced surface heat exchange) is neglected. When interpreted as background gustiness, however, this value is excessively large. With some caution, I proceed with this choice.

There are some issues with the RCE solution. In particular, the large gap between the surface air temperature and SST, which inevitably has increased the mean sensible heat flux, is troublesome. However, this should not affect the stability and nonlinear analysis, since the gap affects sensible heat flux, whose fluctuation is secondary for dynamics, especially in the context of moisture mode under the WTG balance.

2.3.2 Linearization

The equations derived above are primarily linear and the only nonlinearity resides in advection of humidity and evaporation. As I assume a homogeneous background state, advection does not enter the linear problem. Evaporation and sensible heat flux linearize to

$$\frac{E'}{\Delta p/g} = -\frac{b_{1s} q_1'}{\tau_E} + c_s \frac{P'}{\Delta p/g} + c_u u_1', \tag{2.38}$$

$$\frac{H'}{\Delta p/g} = -\frac{a_{1s} T_1'}{\tau_E} + c_{hs} \frac{P'}{\Delta p/g} + c_{hu} u_1', \tag{2.39}$$

where

$$\frac{1}{\tau_E} \equiv \frac{\rho_a C_E \overline{V}_s}{\Delta p/g}, \tag{2.40}$$

$$c_s \equiv \overline{E} \frac{\overline{v}_g}{\overline{V}_s^2} \frac{0.669 - 0.00952\overline{\tilde{P}}}{1 + 0.669\overline{\tilde{P}} - 0.00476\overline{\tilde{P}}^2} \frac{86400}{L_v}, \tag{2.41}$$

Table 2.1: Parameters for QTCM and other basic parameters. Note that stability parameters are different from those from Neelin and Zeng (2000). Other parameters are either the same as before or directly taken from the manual of QTCM version 2.3 (available online at http://www.atmos.ucla.edu/~csi/qtcm_man/v2.3/online/qtcm_man.html, retrieved on December 2, 2006).

Parameter	Symbol	Reference value
Specific heat of dry air at constant pressure	c_p	1004 J/kg/K
Latent heat of vaporization at 30°C	L_v	$2.43 \cdot 10^6$ J/kg
Ratio of gas constant to specific heat at constant pressure	$\kappa = R_d/c_p$	287/1004
Acceleration due to gravity	g	9.8 m/s^2
Depth of troposphere	Δp	800 hPa
Pressure level of the surface	p_s	1000 hPa
Air density at surface	ρ_a	1.2 kg/m^3
Drag coefficient	C_E	$1.2 \cdot 10^{-3}$
Tropospheric average of temperature basis function	$\hat{a}_1 \equiv \langle a_1 \rangle$	0.4593
Tropospheric average of humidity basis function	$\hat{b}_1 \equiv \langle b_1 \rangle$	0.3157
Surface value of temperature basis function	$a_{1s} \equiv a_1(p_s)$	0.3020
Surface value of humidity basis function	$b_{1s} \equiv b_1(p_s)$	1
Surface value of baroclinic velocity basis function	V_{1s}	-0.245
Surface value of reference temperature profile	T_{rs}	302 c_p
Surface value of reference humidity profile	q_{rs}	$(51.96/c_p) \cdot L_v$
Static stability	$\overline{M}_{s1}$	$3.5 \cdot 10^3$ J/kg
Gross moisture stratification	$\overline{M}_{q1}$	$3.0 \cdot 10^3$ J/kg
Rayleigh damping timescale	τ_m	30 d
Newtonian cooling timescale	τ_R	30 d
Convective timescale	τ_c	12 h
Evaporation relaxation timescale	τ_E	15.7 d
Cloud-radiation interaction parameter	r	0.17
Gustiness parameter for evaporation	c_s	0.048
Gustiness parameter for sensible heat flux	c_{hs}	0.0083
WISHE parameter for evaporation	c_u	0.00072
WISHE parameter for sensible heat flux	c_{hu}	0.00012
Eddy diffusion coefficient for humidity	K_q	10^4 m^2/s

Table 2.2: Forcing parameters and output values for RCE. Clear-sky radiative forcing was taken from Peters and Bretherton (2005).

Forcing			
	Sea surface temperature	T_s	29.5°C
	Clear-sky radiative cooling	$\langle Q_{R,clear} \rangle$	140 W/m^2
	Mean wind or background gustiness	$-U$ or v_{bg}	4 m/s
Output			
	Surface air temperature	$T_{rs} + a_{1s}\overline{T}_1$	26.5°C
	Surface specific humidity	$q_{rs} + b_{1s}\overline{q}_1$	18.5 g/kg
	Surface relative humidity	$(q_{rs} + b_{1s}\overline{q}_1)/q_s^*$	72.2 %
	Precipitation/evaporation	$\overline{P} = \overline{E}$	3.71 mm/day = 104.3 W/m^2
	Sensible heat flux	$\overline{H}$	17.9 W/m^2
	Cloud radiative forcing	$r\overline{P}$	17.7 W/m^2
	Surface wind speed	$\overline{V}_s$	4.18 m/s
	Downdraft-driven gust	$v_g(\overline{P})$	1.23 m/s

$$c_u \equiv \frac{\overline{E}}{\Delta p/g}\frac{U}{\overline{V}_s^2}V_1(p_s), \tag{2.42}$$

$$(c_{hs}, c_{hu}) \equiv \frac{\overline{H}}{\overline{E}}(c_s, c_u). \tag{2.43}$$

Recall $P' = P - \overline{P} = (\Delta p/g)(q_1' - T_1')/\tau_c$.

Figure 2-3 displays gustiness as a function of precipitation along with the gustiness parameter c_s, which is a function of the basic state surface wind speed (which includes gustiness) and precipitation. The gustiness parameter increases as the fraction of gustiness in the mean surface wind speed increases. Its sensitivity on the precipitation rate is rather small. In a CRM, Bretherton et al. (2005) found a large value of $c_s + c_{hs} = 0.12$, presumably because they did not impose a large-scale mean surface wind. Note the difference in notation between their work and this thesis. c_s in their terminology represents the sum $c_s + c_{hs}$ in my notation.

As customary in tropical dynamics (Neelin and Yu 1994; Fuchs and Raymond 2002, among others), the primary target of my analysis is the Kelvin-like mode that has a vanishing meridional wind, $v = 0$. Formally such a system is isomorphic to a 1-dimensional wave equation without rotation, aside from the meridional structure equation. The QTCM prog-

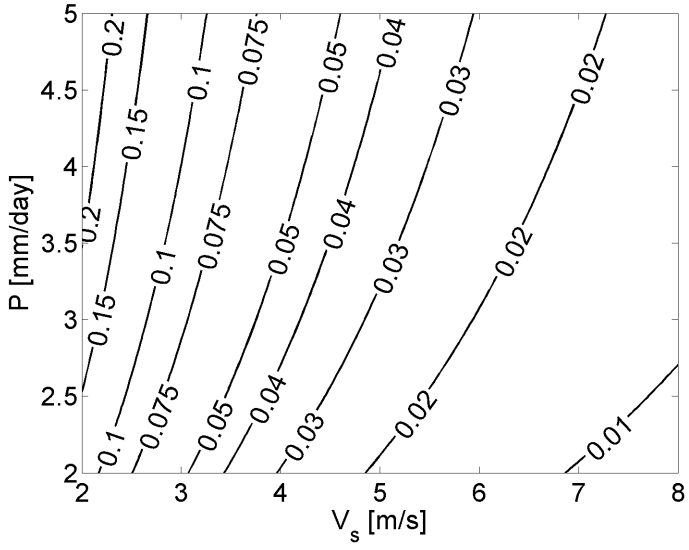

Figure 2-3: Contour plot of c_s as a function of surface speed and precipitation, as described in (2.41). Note that Bretherton et al. (2005) estimated $c_s = 0.12$ from their CRM simulation. The reference value in this paper is 0.04.

nostic equations linearized about the RCE in the reference frame with mean flow consist of the next three equations.

$$\frac{\partial u_1'}{\partial t} = -\kappa \frac{\partial T_1'}{\partial x} - \frac{u_1'}{\tau_m}, \tag{2.44}$$

$$\hat{a}_1 \frac{\partial T_1'}{\partial t} + \overline{M}_{s1} \frac{\partial u_1'}{\partial x} = (1 + r + c_{hs}) \frac{q_1' - T_1'}{\tau_c} - \frac{a_{1s} T_1'}{\tau_E} + c_{hu} u_1' - \hat{a}_1 \frac{T_1'}{\tau_R}, \tag{2.45}$$

$$\hat{b}_1 \frac{\partial q_1'}{\partial t} - \overline{M}_{q1} \frac{\partial u_1'}{\partial x} = c_s \frac{q_1' - T_1'}{\tau_c} - \frac{b_{1s} q_1'}{\tau_E} + c_u u_1' - \frac{q_1' - T_1'}{\tau_c} + \hat{b}_1 K_q \frac{\partial^2 q_1'}{\partial x^2}. \tag{2.46}$$

The geostrophic balance in the meridional momentum equation determines the meridional structure:

$$\beta y u_1' = -\kappa \frac{\partial T_1'}{\partial y}. \tag{2.47}$$

Here I have included eddy diffusion in the humidity equation. In reality eddy diffusion should take the form $\sim (\partial_x^2 + \partial_y^2)$. However, such a form would prohibit a simple Kelvin-like mode by changing the meridional structure from a Gaussian function, and force me to solve the dispersion relationship numerically. Nevertheless, the diffusion term is included to crudely assess the impact of eddy diffusion. Alternatively, if one regards the system

(2.44), (2.45), and (2.46) as a model of non-rotating fluid, the inconsistency is avoided. In any event, diffusion is suppressed for most of the calculations below.

2.3.3 Nondimensionalization

The next step is to nondimensionalize the system. The following definitions facilitate the procedure.

$$
\begin{aligned}
(t, \tau_c, \tau_m, \tau_R, \tau_E) &= \mu\,(\tilde{t}, \tilde{\tau}_c, \tilde{\tau}_m, \tilde{\tau}_R, \tilde{\tau}_E)\,, && (2.48)\\
x &= \mu c_{dry}\tilde{x}, && (2.49)\\
u_1' &= c_{dry}\tilde{u}, && (2.50)\\
(T_1', q_1', \overline{M}_{s1}, \overline{M}_{q1}) &= \frac{c_{dry}^2}{\kappa}(\tilde{T}, \tilde{q}, \hat{a}_1, \hat{b}_1\tilde{M}_q), && (2.51)\\
(c_{hu}, c_u) &= \frac{c_{dry}}{\mu}\left(\frac{\hat{a}_1}{\kappa}\tilde{c}_{hu}, \frac{\hat{b}_1}{\kappa}\tilde{c}_u\right), && (2.52)\\
K_q &= c_{dry}^2\mu\tilde{K}_q. && (2.53)
\end{aligned}
$$

Here the dry gravity wave speed is defined as

$$
c_{dry} \equiv \sqrt{\frac{\kappa\overline{M}_{s1}}{\hat{a}_1}}. \tag{2.54}
$$

The nondimensionalization here differs from that of Matsuno (1966) for time and length scales. He used the equatorial Rossby radius of deformation as the length scale, and estimated the timescale using the deformation radius and the speed of dry gravity wave. Here the timescale comes from a characteristic timescale of a disturbance of interest (a few to several days), and the length scale is determined by the timescale and the gravity wave speed. This scaling is consistent with Sobel and Gildor (2003).

The resulting nondimensional set is

$$
\frac{\partial\tilde{u}}{\partial\tilde{t}} = -\frac{\partial\tilde{T}}{\partial\tilde{x}} - \frac{\tilde{u}}{\tilde{\tau}_m}, \tag{2.55}
$$

$$\frac{\partial \tilde{T}}{\partial \tilde{t}} + \frac{\partial \tilde{u}}{\partial \tilde{x}} = \frac{\tilde{q}-\tilde{T}}{\tilde{\tau}_{c1}} - \frac{\tilde{T}}{\tilde{\tau}_{E1}} + \tilde{c}_{hu}\tilde{u}, \tag{2.56}$$

$$\frac{\partial \tilde{q}}{\partial \tilde{t}} - \tilde{M}_q \frac{\partial \tilde{u}}{\partial \tilde{x}} = -\frac{\tilde{q}-\tilde{T}}{\tilde{\tau}_{c2}} - \frac{\tilde{q}}{\tilde{\tau}_{E2}} + \tilde{c}_u\tilde{u} + \tilde{K}_q \frac{\partial^2 \tilde{q}}{\partial \tilde{x}^2}, \tag{2.57}$$

where

$$\frac{1}{\tilde{\tau}_{c1}} \equiv \frac{1+r+c_h}{\tilde{\tau}_c}, \tag{2.58}$$

$$\frac{1}{\tilde{\tau}_{E1}} \equiv \frac{1}{\tilde{\tau}_E}\frac{a_{1s}}{\hat{a}_1} + \frac{1}{\tau_R}, \tag{2.59}$$

$$\frac{1}{\tilde{\tau}_{c2}} \equiv \frac{1}{\tilde{\tau}_c}\frac{\hat{a}_1}{\hat{b}_1}(1-c_s), \tag{2.60}$$

$$\frac{1}{\tilde{\tau}_{E2}} \equiv \frac{b_{1s}}{\hat{b}_1}\frac{1}{\tau_E}. \tag{2.61}$$

2.3.4 Linear stability analysis

The geostrophic balance of the meridional momentum equation determines the meridional structure whereas other equations form a dispersion relationship. Assuming a solution of the form $\sim \exp(\tilde{\sigma}\tilde{t} + i\tilde{k}\tilde{x})$ leads to the dispersion relationship

$$\tilde{A}_3\tilde{\sigma}^3 + \tilde{A}_2\tilde{\sigma}^2 + \tilde{A}_1\tilde{\sigma} + \tilde{A}_0 = 0, \tag{2.62}$$

where

$$\tilde{A}_3 = 1, \tag{2.63}$$

$$\tilde{A}_2 = \frac{1}{\tilde{\tau}_m} + \frac{1}{\tilde{\tau}_{c1}} + \frac{1}{\tilde{\tau}_{E1}} + \frac{1}{\tilde{\tau}_{c2}} + \frac{1}{\tilde{\tau}_{E1}} + \tilde{K}_q\tilde{k}^2, \tag{2.64}$$

$$\begin{aligned}\tilde{A}_1 = {} & \left(\frac{1}{\tilde{\tau}_m} + \frac{1}{\tilde{\tau}_{c1}} + \frac{1}{\tilde{\tau}_{E1}}\right)\left(\frac{1}{\tilde{\tau}_{c2}} + \frac{1}{\tilde{\tau}_{E2}} + \tilde{K}_q\tilde{k}^2,\right) \\ & + \frac{1}{\tilde{\tau}_m}\left(\frac{1}{\tilde{\tau}_{c1}} + \frac{1}{\tilde{\tau}_{E1}}\right) + i\tilde{k}\tilde{c}_{hu} + \tilde{k}^2 - \frac{1}{\tilde{\tau}_{c1}\tilde{\tau}_{c2}},\end{aligned} \tag{2.65}$$

$$\begin{aligned}\tilde{A}_0 = {} & \left[\frac{1}{\tilde{\tau}_m}\left(\frac{1}{\tilde{\tau}_{c1}} + \frac{1}{\tilde{\tau}_{E1}}\right) + i\tilde{k}\tilde{c}_{hu} + \tilde{k}^2\right]\left(\frac{1}{\tilde{\tau}_{c2}} + \frac{1}{\tilde{\tau}_{E2}} + \tilde{K}_q\tilde{k}^2\right) \\ & + \frac{1}{\tilde{\tau}_{c1}}\left(i\tilde{k}\tilde{c}_u - \tilde{M}_q\tilde{k}^2 - \frac{1}{\tilde{\tau}_m\tilde{\tau}_{c2}}\right)\end{aligned} \tag{2.66}$$

Figure 2-4 shows dimensional growth rates and phase speeds for three modes without diffusion ($K_q = 0$). As usual, only eastward propagating modes are allowed in the presence of β because of the condition of boundedness at infinity; this mode is included here for completeness.

The model has three modes: two gravity waves and one quasi-stationary moisture mode. Gravity waves can be identified since they asymptote to dry gravity waves in the small-scale limit. The moisture mode (Neelin and Yu 1994; Yu and Neelin 1994; Sobel et al. 2001; Fuchs and Raymond 2002, 2005; Bony and Emanuel 2005; Fuchs and Raymond 2007) is characterized by predominance of the humidity variable over other variables. It is the only unstable mode in this model. As Figure 2-6 shows, it has growth rates that asymptote to a constant value as $n \to \infty$; unlike linear wave-CISK, the growth rate is bounded. Nonetheless, the growth rate is highest at the smallest scale.

Curiously, cloud forcing, gustiness, and linear WISHE do not destabilize gravity waves, regardless of wavenumber. This finding is consistent with Fuchs and Raymond (2002) but contrary to conventional analyses (see Emanuel et al. 1994, for a review). Gravity waves are damped because heating lags ascent, correlating with the cold phase of temperature, which Figure 2-5 confirms by showing the difference in the growth rates and phase speeds between the case shown in Figure 2-4 and the limit of no damping ($\tau_m, \tau_R, \tau_E \to \infty$). As differences are quite small, the negative growth rates for gravity waves are chiefly due to moist convective damping (Emanuel et al. 1994).

Another peculiar aspect is that for small n, all modes, including even gravity waves, are stationary in the absence of WISHE. Fuchs and Raymond (2002) reached a similar result, though the reason is not clear.

As Fuchs and Raymond (2007) noted, the WTG limit gives greater insight into the moisture mode. Figure 2-6 compares the growth rates and phase speeds of the moisture mode with those in the WTG limit. Before focusing on WTG limits, it is instructive to inspect the mode in detail. The effect of linear WISHE is intuitive. The moisture mode propagates only when linear WISHE is turned on, and linear WISHE makes the large-scale wave most unstable. Regardless of linear WISHE, the moisture mode has an asymptotic

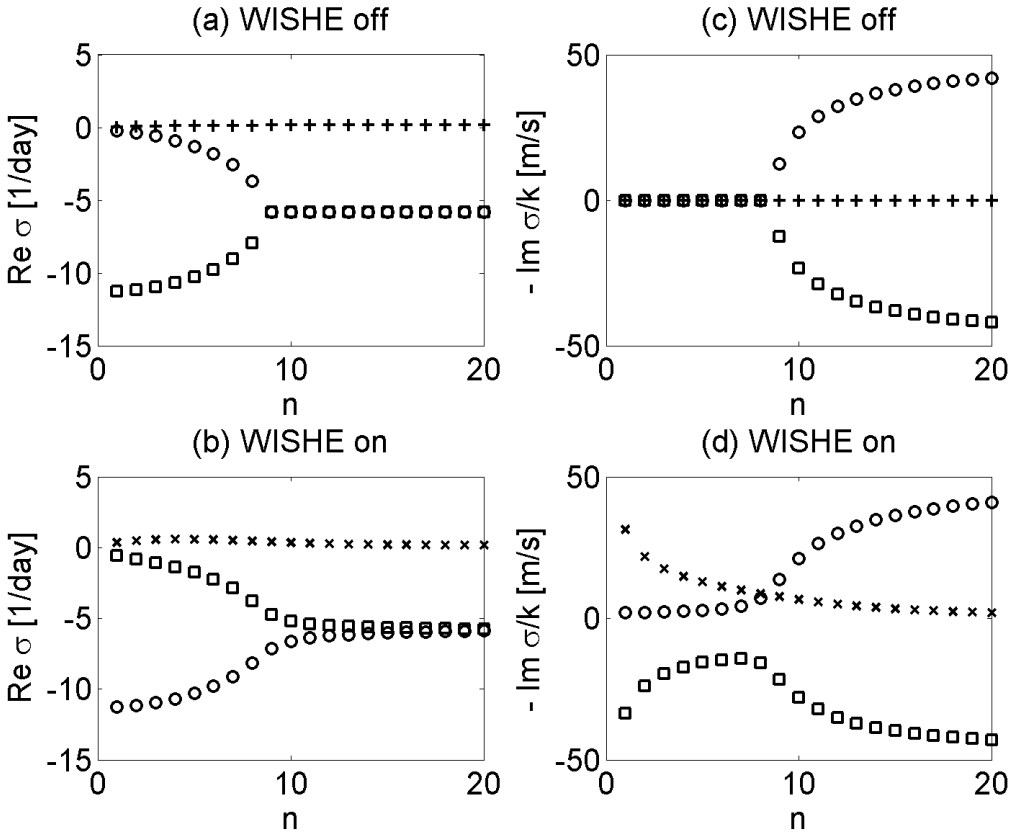

Figure 2-4: (a) growth rates and (b) phase speeds for the case without WISHE. (c) growth rates and (d) phase speeds for the case with WISHE. The horizontal axes represent planetary wavenumber whereas the vertical axes show growth rates ((a) and (c)) in [1/s] and phase speeds ((b) and (d)) in [m/s]. The results here assume no eddy diffusion: $K_q = 0$.

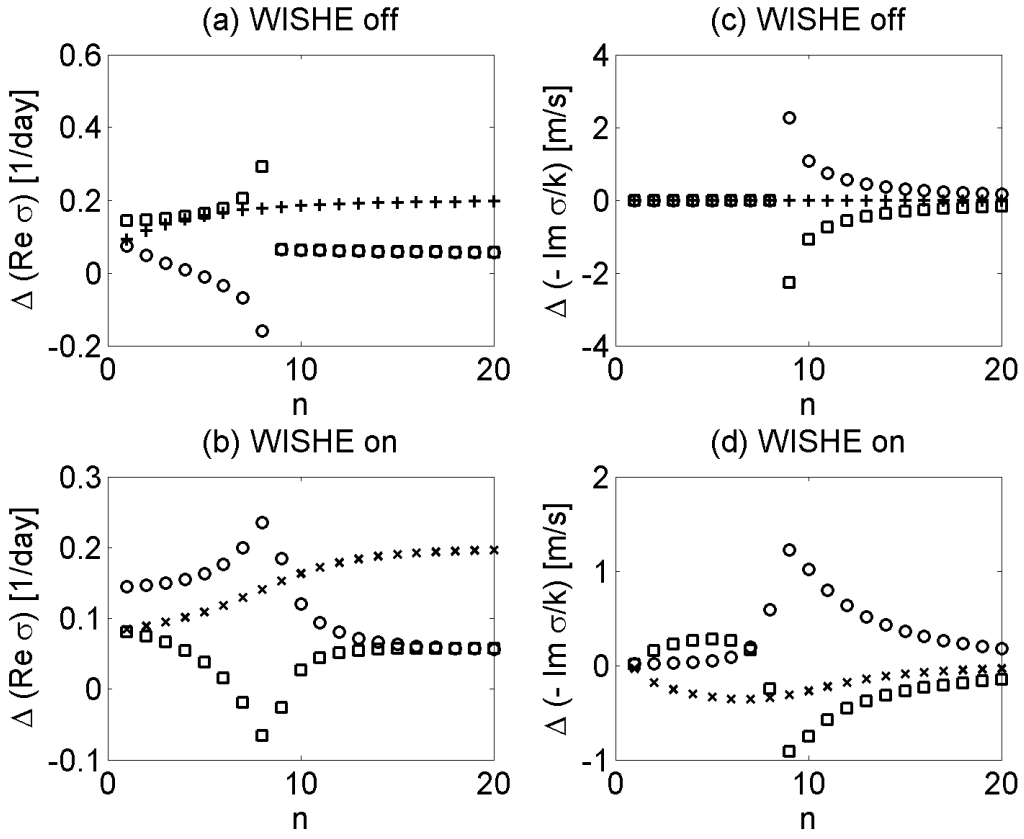

Figure 2-5: As in Figure 4 but for the difference between the reference case shown in Figure 4 and the limit of $\tau_m, \tau_R, \tau_E \to \infty$.

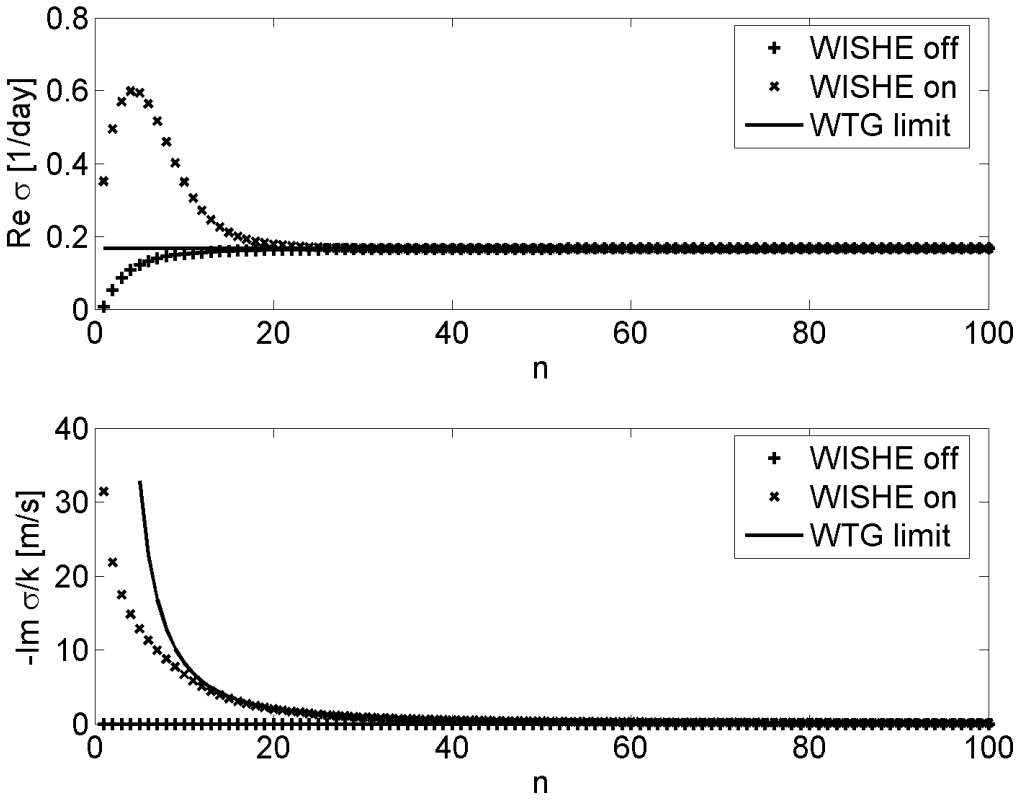

Figure 2-6: Growth rates (upper panel) and phase speeds (lower panel) for the moisture mode, with (crosses) and without WISHE (pluses). Also shown are the values from the WTG limit (solid line). The WTG phase speed for the no-WISHE case is not shown since it is zero for all n. Eddy diffusion is excluded: $K_q = 0$.

constant growth rate and vanishing phase speed at the small-scale limit. The asymptotic growth rate is about 0.16 day^{-1}, which converts to a timescale of about 6 days. This timescale roughly matches that of the initial growing stage of the MJO, as depicted in Figure 1-1 of Chapter 1.

A similar analysis is repeated with the eddy diffusion term, which is shown in Figure 2-7. As expected, high wavenumber modes are stabilized relative to diffusion-less cases. In this case, too, the WTG limit captures the small-scale behavior correctly.

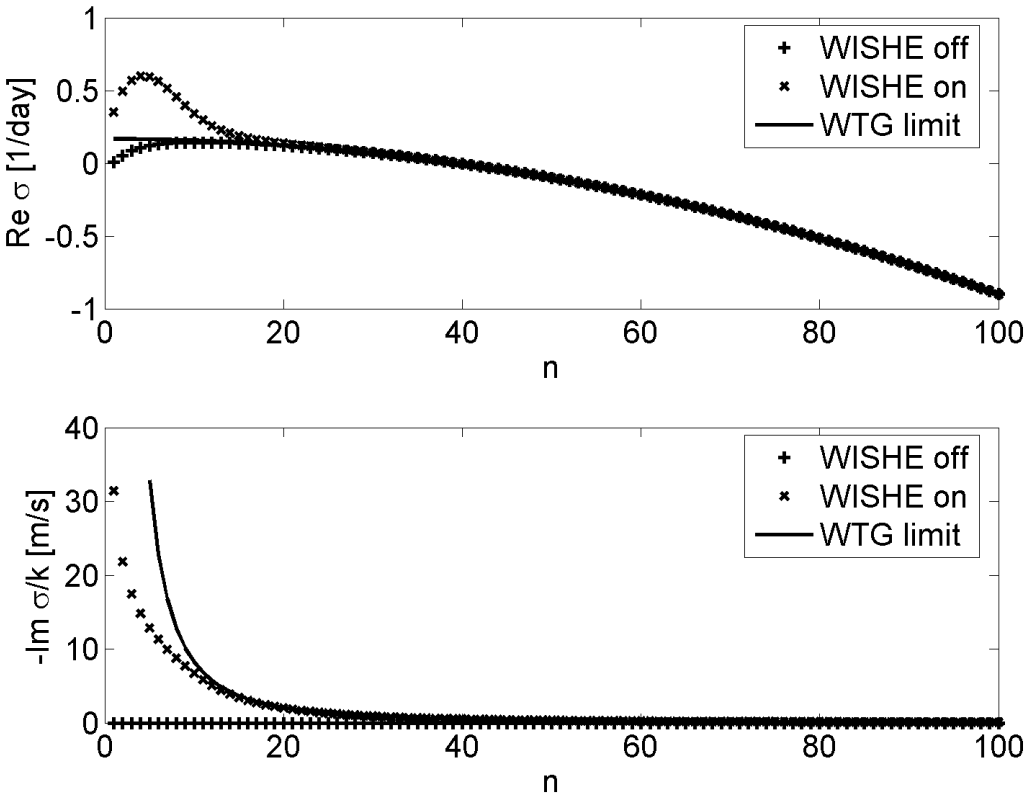

Figure 2-7: As in Figure 6 but with eddy diffusion included: $K_q = 10^4 \mathrm{m}^2/\mathrm{s}$.

2.4 WTG analysis

2.4.1 Mathematical analysis using WTG

Why is the WTG approximation successful in capturing the behavior of the moisture mode at the small scale ($n \to \infty$)? Physically speaking, the WTG approximation is valid when the tendency in the temperature equation is much smaller than the adiabatic cooling term. The condition may be expressed as

$$G \equiv \left| \left(\hat{a}_1 \frac{\partial T_1'}{\partial t} \right) \Big/ \left(\overline{M}_{s1} \frac{\partial u_1'}{\partial x} \right) \right| = \left| \left(\frac{\partial \tilde{T}}{\partial \tilde{t}} \right) \Big/ \left(\frac{\partial \tilde{u}}{\partial \tilde{x}} \right) \right| = \left| \frac{\tilde{\sigma}(\tilde{\sigma} + 1/\tilde{\tau}_m)}{\tilde{k}^2} \right| \ll 1, \quad (2.67)$$

where the momentum equation has been substituted. If momentum damping is negligible or at most on the order of $\tilde{\sigma}$, (2.67) is equivalent to

$$G \sim \left| \frac{1}{\tilde{k}^2} \right| \ll 1, \quad (2.68)$$

where I have used $\tilde{\sigma} \sim 1$. Recall that I have chosen the characteristic timescale μ so that $\tilde{\sigma} \sim 1$. To appreciate the physics behind this, let us define the zonal scale as $L \equiv 2\pi/k$, the characteristic timescale as $\tau_\sigma \equiv 1/|\sigma|$. Then, using the definition of the inviscid dry gravity wave phase speed, (2.67) reduces to, in dimensional terms,

$$L^2 \ll (2\pi c_{dry} |\tau_\sigma|)^2. \quad (2.69)$$

As described in Chapter 1, this is the scaling derived by Sobel and Gildor (2003). Since $2\pi c_{dry}|\tau_\sigma| \sim 10^5$km, the condition holds for all wavenumber realizable on the earth. In other words, the moisture mode satisfies the WTG scaling always. But it is also true that the WTG approximation represents the asymptotic limit of $G \to 0$ or $L \to 0$.

That the WTG scaling is satisfied does not automatically signify that the WTG approximation is numerically accurate. Figures 2-6 and 2-7 demonstrate that the growth rate of the moisture mode significantly exceeds the WTG value in the presence of WISHE. Higher-order effects can be important at the large scale.

Now that the physical understanding of WTG is illustrated, is it possible to obtain the WTG equation in a more formal way? Perturbation expansion analysis provides a more rigorous approach to the WTG approximation. Since the WTG condition is phrased in terms of wavelength, the expansion parameter should be $1/\tilde{k}$. Let us expand each variable as

$$(\tilde{\sigma}, \tilde{u}, \tilde{T}, \tilde{q}) = \sum_{n=0}^{\infty} \frac{1}{\tilde{k}^n} (\tilde{\sigma}_n, \tilde{u}_n, \tilde{T}_n, \tilde{q}_n). \tag{2.70}$$

The condition for perturbation expansion to be valid is $1/\tilde{k}^2 \ll 1$ or $L^2 \ll (2\pi c_{dry}\mu)^2$, the same condition derived above. I also utilize the standard Fourier expansion $\sim \exp(i\tilde{k}\tilde{x} + \tilde{\sigma}\tilde{t})$.

The present form of the perturbation expansion assumes that the growth rate tends to constant as the wavenumber approaches infinity. Such a presumption precludes inclusion of eddy diffusion since diffusion selectively damps small-scale modes and prohibits the growth rate from approaching a constant. Therefore I take $\tilde{K}_q = 0$.

From the balance of $O(\tilde{k})$ and $O(1)$ terms, the momentum equation yields

$$O(\tilde{k}): \quad \tilde{T}_0 = 0, \tag{2.71}$$

$$O(1): \quad \left(\tilde{\sigma}_0 + \frac{1}{\tilde{\tau}_m}\right) \tilde{u}_0 = -i\tilde{T}_1. \tag{2.72}$$

The temperature equation leads to

$$O(\tilde{k}): \quad \tilde{u}_0 = 0, \tag{2.73}$$

$$O(1): \quad i\tilde{u}_1 = \frac{\tilde{q}_0}{\tilde{\tau}_{c1}}. \tag{2.74}$$

The first relation means $\tilde{u}_0 = 0$, which also implies $\tilde{T}_1 = 0$ because of (2.72). The humidity equation then yields

$$O(1): \quad \tilde{\sigma}_0 \tilde{q}_0 - \tilde{M}_q i\tilde{u}_1 = -\frac{\tilde{q}_0}{\tilde{\tau}_{c2}} - \frac{\tilde{q}_0}{\tilde{\tau}_{E2}}. \tag{2.75}$$

Lastly combining (2.74) and (2.75) yields the WTG dispersion relation.

$$\tilde{\sigma}_0 = \frac{\tilde{M}_q}{\tilde{\tau}_{c1}} - \frac{1}{\tilde{\tau}_{c2}} - \frac{1}{\tilde{\tau}_{E2}} \quad \text{or,} \tag{2.76}$$

$$\frac{\partial \tilde{q}_0}{\partial \tilde{t}_0} = \left(\frac{\tilde{M}_q}{\tilde{\tau}_{c1}} - \frac{1}{\tilde{\tau}_{c2}} - \frac{1}{\tilde{\tau}_{E2}} \right) \tilde{q}_0, \tag{2.77}$$

where $\partial / \partial \tilde{t}_0 \equiv \tilde{\sigma}_0$.

It is noteworthy that the only zeroth order variable is humidity, and that temperature is second order.

$$\begin{pmatrix} \tilde{u} \\ \tilde{T} \\ \tilde{q} \end{pmatrix} = \begin{pmatrix} 0 \\ 0 \\ \tilde{q}_0 \end{pmatrix} + \frac{1}{\tilde{k}} \begin{pmatrix} \tilde{u}_1 \\ 0 \\ \tilde{q}_1 \end{pmatrix} + \frac{1}{\tilde{k}^2} \begin{pmatrix} \tilde{u}_2 \\ \tilde{T}_2 \\ \tilde{q}_2 \end{pmatrix} + O(\tilde{k}^{-3}). \tag{2.78}$$

Such a relation justifies the name of moisture mode and the dynamical balance of WTG approximation.

If the purpose is to obtain higher-order terms for the growth rate, it is easier to perform the perturbation expansion with the dispersion relationship. Defining $\tilde{B}_i \equiv \tilde{A}_i / \tilde{k}^2$ rewrites the dispersion relationship as

$$\tilde{B}_3 \tilde{\sigma}^3 + \tilde{B}_2 \tilde{\sigma}^2 + \tilde{B}_1 \tilde{\sigma} + \tilde{B}_0 = 0. \tag{2.79}$$

Now each term becomes

$$\tilde{B}_3 = O(\tilde{k}^{-2}), \tag{2.80}$$

$$\tilde{B}_2 = O(\tilde{k}^{-2}), \tag{2.81}$$

$$\tilde{B}_1 = 1 + i\frac{\tilde{c}_{hu}}{\tilde{k}} + O(\tilde{k}^{-2}), \tag{2.82}$$

$$\tilde{B}_0 = \frac{1}{\tilde{\tau}_{c2}} + \frac{1}{\tilde{\tau}_{E2}} - \frac{\tilde{M}_q}{\tilde{\tau}_{c1}} + \frac{1}{\tilde{k}} \left[i\tilde{c}_{hu} \left(\frac{1}{\tilde{\tau}_{c2}} + \frac{1}{\tilde{\tau}_{E2}} \right) + i\frac{\tilde{c}_u}{\tau_{c1}} \right] + O(\tilde{k}^{-2}). \tag{2.83}$$

Expanding the growth rate as $\tilde{\sigma} = \sum_{n=0}^{\infty} \tilde{\sigma}_n \tilde{k}^{-n}$, I immediately arrive at the WTG dispersion

relation up to the first order.

$$\tilde{\sigma}_0 = \frac{\tilde{M}_q}{\tilde{\tau}_{c1}} - \frac{1}{\tilde{\tau}_{c2}} - \frac{1}{\tilde{\tau}_{E2}}, \tag{2.84}$$

$$\tilde{\sigma}_1 = -\frac{i}{\tau_{c1}}(\tilde{c}_{hu}\tilde{M}_q + \tilde{c}_u). \tag{2.85}$$

The second order equation is fairly lengthy and omitted here.

Note that this can be obtained by omitting temperature variable from the system and retaining up to $O(\tilde{k}^{-1})$. That is, the WTG system is composed of

$$\frac{\partial \tilde{u}}{\partial \tilde{x}} = \frac{\tilde{q}}{\tilde{\tau}_{c1}} + \tilde{c}_{hu}\tilde{u}, \tag{2.86}$$

$$\frac{\partial \tilde{q}}{\partial \tilde{t}} - \tilde{M}_q \frac{\partial \tilde{u}}{\partial \tilde{x}} = -\frac{\tilde{q}}{\tilde{\tau}_{c2}} - \frac{\tilde{q}}{\tilde{\tau}_{E2}} + \tilde{c}_u\tilde{u}. \tag{2.87}$$

Note the similarity between these two equations and (2.74) and (2.75). Also notice that in the absence of linear WISHE, this mode has no scale dependence, which is seen in Figures 2-4 and 2-5.

2.4.2 Physical interpretation of linear WTG growth rates

By construction, the analysis above has excluded eddy diffusion. On physical grounds, even when diffusion is present, one would expect the temperature anomaly to be small for this mode, and the WTG balance to be valid. In general, therefore, the dimensional WTG system may be written as

$$\sigma_{WTG} = \Big(-\overbrace{\frac{\overline{M}_{s1} - \overline{M}_{q1}}{\overline{M}_{s1}}}^{\text{MSE export}} + \overbrace{\frac{\overline{M}_{q1}}{\overline{M}_{s1}}(r + c_{hs})}^{\substack{\text{cloud forcing and} \\ \text{sensible heat flux}}} + \overbrace{c_s\Big)\frac{1}{\hat{b}_1\tau_c} - \frac{b_{1s}}{\hat{b}_1\tau_E}}^{\text{Evaporation}} - \overbrace{K_q k^2}^{\text{Diffusion}} - \frac{i}{k}\frac{1 + r + c_h}{\hat{b}_1\overline{M}_{s1}\tau_c}c_u\left(1 + \frac{\overline{M}_{q1}}{\overline{M}_{s1}}\frac{c_{hu}}{c_u}\right), \tag{2.88}$$

$$\frac{\partial W'}{\partial t} = \sigma_{WTG}W' \qquad \text{or} \qquad \frac{\partial \langle h' \rangle}{\partial t} = \sigma_{WTG}\langle h' \rangle, \tag{2.89}$$

where the definition of precipitable water anomaly $W' \equiv (\Delta p/g)\hat{b}_1 q_1'$ has been used. Here h' represents moist static energy anomaly, which is proportional to specific humidity anomaly under WTG: $h' = T' + \varphi' + q' = q'$, with all variables in energy units. One can rewrite (2.88) using the effective gross moist stability $\overline{M}_{\text{eff}} \equiv \overline{M}_{s1} - \overline{M}_{q1}(1 + r + c_{hs})$ (Su and Neelin 2002; Bretherton and Sobel 2002) (the definition of Bretherton and Sobel is slightly different):

$$\sigma_{WTG} = \left(-\frac{\overline{M}_{\text{eff}}}{\overline{M}_{s1}} + c_s \right) \frac{1}{\hat{b}_1 \tau_c} - \frac{b_{1s}}{\hat{b}_1 \tau_E} - K_q k^2 - \frac{i}{k} \frac{1 + r + c_h}{\hat{b}_1 \overline{M}_{s1} \tau_c} c_u \left(1 + \frac{\overline{M}_{q1}}{\overline{M}_{s1}} \frac{c_{hu}}{c_u} \right). \quad (2.90)$$

(2.88) /(2.90) is the formula used for Figures 2-6 and 2-7. For all the cases considered, the growth rate and phase speed asymptote to the WTG values as $n \to \infty$. On a casual look, the WTG approximation and the full dispersion relation are indistinguishable for $n >\sim 20$.

Equations (2.88) and (2.89) concisely describe the physical mechanism behind the moisture mode instability. Perturbation precipitable water, which is identical to vertically integrated MSE under the WTG approximation, decreases with MSE export through effective gross moist stability (which includes the effect of cloud-radiation interaction and sensible heat flux) and increases with gustiness (c_s), and decreases with decreasing evaporation (the second-to-last term of the real part of (2.88)). One would expect an instability if cloud radiation interaction and gustiness overcompensate for the MSE export. Note that the physical picture is essentially the same as the mechanism of self-aggregation of moist convection found by Bretherton et al. (2005).

In the present formulation of QTCM, all the MSE sources are functions of precipitation. Under WTG, humidity is the only leading order variable. Moisture-convection feedback ($P' \propto W'$) is thus essential for exponential growth.

Curiously WISHE does not affect the growth rate at the zeroth order. On the other hand, its causes the moisture mode in the WTG limit to propagate at the first order. Nonetheless, the second-order effect does not have to be small. Figures 2-6 and 2-7 demonstrate that the growth rate of the moisture mode diverges significantly from the WTG limit at the large scale in the presence of WISHE. In other words, the second-order (or higher-order) effects may not be small *numerically* relative to the zeroth-order effect at the large scale.

Previous authors have already derived a simpler version of (2.88)/ (2.90). For example, in the absence of cloud-radiation interaction, gustiness, and perturbation evaporation, this simplifies to

$$\sigma = -\frac{\overline{M}}{\hat{b}_1 \tau_c \overline{M}_{s1}}, \tag{2.91}$$

where $\overline{M} \equiv \overline{M}_{s1} - \overline{M}_{q1}$. This is the same as $-B$ defined by Sobel et al. (2001, p. 3658, the unnumbered equation after (30)). Fuchs and Raymond (2002, 2005, 2007) worked on similar models, and found moisture mode instability. Note that although their diabatic parameterizations are simpler, the dynamical treatment of Fuchs and Raymond (2007) is much more sophisticated in that they used a model of the continuously stratified atmosphere rather than a modal model. Sobel and Gildor's (2003) model is very much like the system described here, except that their model additionally includes a mixed-layer ocean. [In the limit of an infinity heat capacity of the ocean, Sobel and Gildor's model yields a similar dispersion relation. See their Eq. (14).]

The difference between Fuchs and Raymond and the result here is worth elaborating. Simply stated, the current model has gustiness-enhanced surface heat flux while theirs does not. In other words, for instability to occur, Fuchs and Raymond required a negative effective gross moist stability. In the present case, that is not the case owing to gustiness.

In light of clarity of the dispersion relationship (2.88)/ (2.90), I can explore the sensitivity of growth rates to various parameters. From (2.88), one can immediately identify three key non-dimensional parameters: r, c_s, and $\overline{M}_{q1}/\overline{M}_{s1}$. In the absence of diffusion, it is evident that aside from the relaxation term in evaporation ($-b_{1s}/(\hat{b}_1 \tau_E)$), the growth rate is inversely proportional to the convective timescale τ_c, which explains why Fuchs and Raymond (2002) noted that the convective timescale is the most important parameter.

Figure 2-8 shows how the growth rate in the WTG limit changes when r, c_s, $\overline{M}_{q1}/\overline{M}_{s1}$, and τ_c are varied. In this graph, c_{hs} is taken to linearly scale with c_s; c_{hs}/c_s remains constant when c_s is varied from the reference value. As expected from (2.88), the growth rate increases with r, c_s, $\overline{M}_{q1}/\overline{M}_{s1}$, and $1/\tau_c$. The plus sign in each panel corresponds to the reference values in Table 1, for which the model is marginally unstable.

A key finding is that the model is quite sensitive to the normalized gross moisture strat-

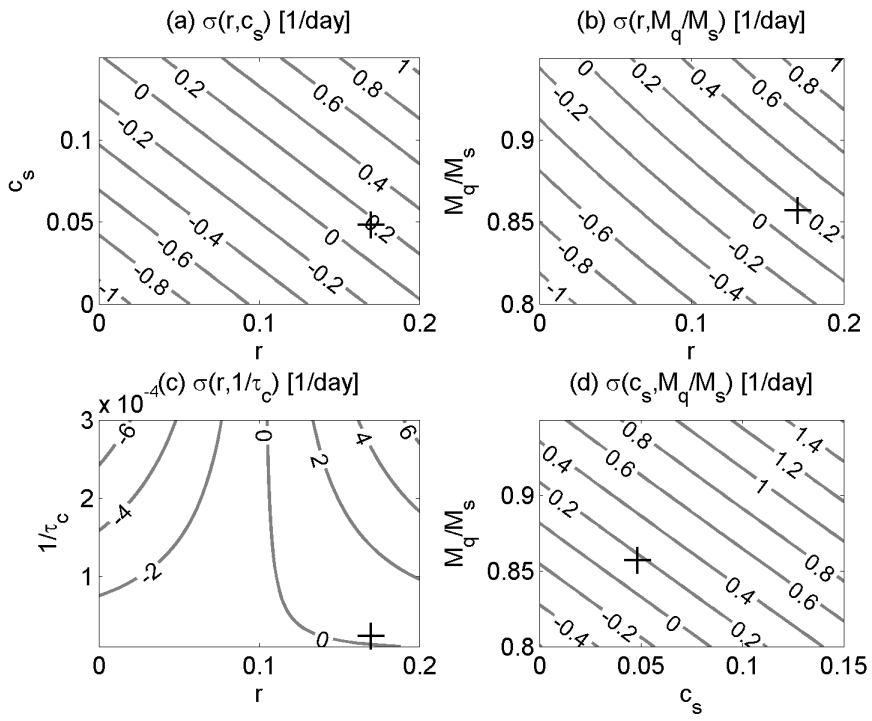

Figure 2-8: Growth rates for the moisture mode in the WTG limit as functions of various moist parameters. The parameters varied are (a) cloud forcing parameter r and gustiness parameter c_s; (b) r and gross moisture stratification normalized by static stability $\overline{M}_{q1}/\overline{M}_{s1}$; (c) r and the inverse of convective timescale τ_c; and (d) c_s and $\overline{M}_{q1}/\overline{M}_{s1}$. The crosses in each panel represent the reference values for each varied parameter.

ification, $\overline{M}_{q1}/\overline{M}_{s1}$. Note that normalized gross moist stability is just $1-\overline{M}_{q1}/\overline{M}_{s1}$. The reference value used here is ~ 0.86. For comparison, Peters and Bretherton (2005) reported an RCE value of ~ 0.85; Sobel and Gildor (2003) gave 0.863; Sobel and Neelin's (2006) reference value is ~ 0.83; Fuchs and Raymond (2002, 2005) used 0.9. In reality, gross moist stability is not an externally given number. The vertical profile of convective mass flux significantly affects gross moist stability (Back and Bretherton 2006). It is therefore desirable to analyze the instability without a predetermined gross moist stability.

The analysis so far has focused on the Kelvin-like mode, but what would happen to other modes, such as Rossby, mixed Rossby-gravity, and inertio-gravity waves? A unique feature of the WTG approximation is that in the absence of diffusion and linear WISHE, there is no scale dependence. I would thus expect that all modes would have the same growth rate at the small-scale limit, regardless of their wave structure and meridional scale.

A casual observation of Fuchs and Raymond (2005) suggests that this is indeed the case.

Also, it is interesting to note that in the WTG limit, the WTG humidity equation is equivalent to a column MSE budget of a large-scale disturbance that has weak temperature gradient. In that case, c_s could represent "nonlinear WISHE" (as opposed to traditional linear, wave WISHE) which has a local relationship between precipitation and large-scale wind. To put this another way, if one takes a single-column model and runs it under the WTG approximation, the model would be unstable if MSE sources overcompensate for MSE export, and increased precipitable water further enhances MSE sources through moisture-convection feedback. In Chapter 5, I turn to this question.

2.4.3 Nonlinear WTG without WISHE

The simplicity of the WTG analysis allows me to go beyond linear WTG analysis to a nonlinear analysis, as was done by Sobel and Gildor (2003), who examined an atmosphere under WTG coupled with a mixed layer ocean and found a nonlinear oscillation. Can a nonlinear WTG analysis provide a deeper insight into the problem at hand?

Although WISHE is clearly important, the preceding calculation demonstrated that it does not affect the WTG growth rate but rather enters the phase speed. As my focus is now on the growth rate, the following neglects WISHE.

I obtain the nonlinear WTG equation by setting the temperature anomaly to zero but otherwise retaining the nonlinearity for surface flux calculations and convective switch. The resulting system is

$$\overline{M}_{s1}\frac{\partial u_1'}{\partial x} = (1+r)\frac{q_1'}{\tau_c} + \frac{H'}{\Delta p/g}, \tag{2.92}$$

$$\hat{b}_1\frac{\partial q_1'}{\partial t} - \overline{M}_{q1}\frac{\partial u_1'}{\partial x} = \frac{E'}{\Delta p/g} - \frac{q_1'}{\tau_c}, \tag{2.93}$$

and evaporation and sensible heat flux anomalies are calculated using (2.31) and (2.32).

Drawn in Figure 2-9 is the phase diagram of the nonlinear WTG system. As the linear stability analysis has indicated, the RCE, a fixed point, is unstable to moisture mode instability. Interestingly there are two additional fixed points: one that corresponds to sat-

urated moisture mode and another to a no-precipitation regime. The nonlinearly saturated moisture mode has a precipitation of about 20 mm/day.

For the saturated moisture mode, the nonlinear saturation occurs as the gustiness curve flattens with increasing precipitation (Fig. 2-2). In a more realistic model, nonlinear saturation can result from changes in any of the following: gross moist stability, cloud-radiative forcing, and gustiness. Bretherton et al. (2005) noted that changing gross moist stability (through changing vertical motion profile) leads to saturation of the instability in their CRM. In the fixed vertical structure model like QTCM, such a mechanism is hard to incorporate, but in reality, the change in gross moist stability may be the key growth limiting process because the height of clouds can significantly change gross moist stability (Back and Bretherton 2006).

As with the linear analysis, the nonlinear behavior is sensitive to the choice of parameters. For instance, a slight change in parameters could drastically alter the phase diagram. Figure 2-10 shows the precipitation for the nonlinearly saturated moisture mode as a function of normalized gross moisture stratification $\overline{M}_{q1}/\overline{M}_{s1}$. Because stability parameters do not affect the RCE, the diagram isolates the nonlinear effect. Altering $\overline{M}_{q1}/\overline{M}_{s1}$ by 5% leads to a precipitation change of 50 mm/day. Such an extreme sensitivity to a moist parameter leaves an impression that although QTCM might be able to explain qualitative behavior, quantitative answers must await a more detailed numerical model.

2.5 Summary and discussions

This chapter has explored moisture mode instability in QTCM. The moisture mode is dominated by the humidity perturbation and its temperature gradient is weak (second-order in $1/\tilde{k}$ expansion). The moisture mode is unstable if MSE sources are directly related with the MSE anomaly. Since MSE sources are usually functions of deep convection, the condition involves two parts: (1) moisture-convection feedback exists and (2) sufficient MSE sources like cloud forcing and enhanced evaporation overcompensate for MSE export.

The simplicity of QTCM and WTG has enabled a thorough analysis of moisture mode.

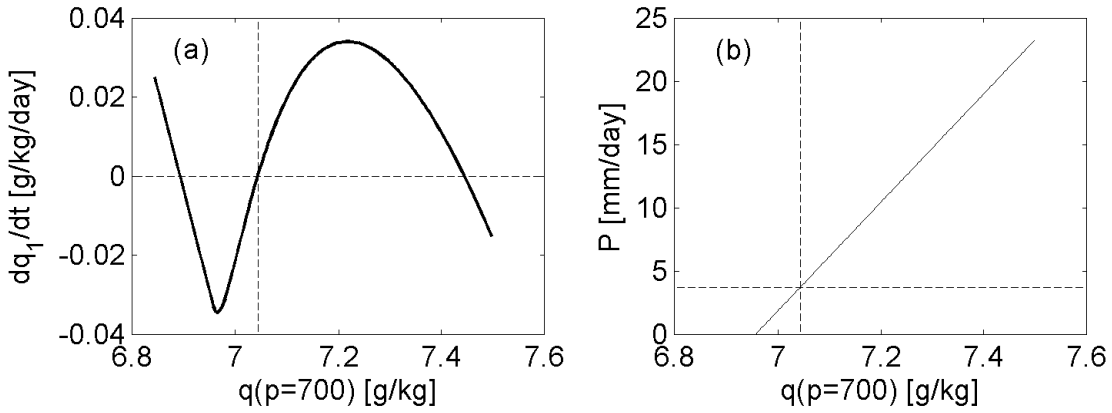

Figure 2-9: (a) Humidity tendency as a function of humidity for QTCM. (b) Precipitation corresponding to (a). The dotted lines denote the location of the RCE.

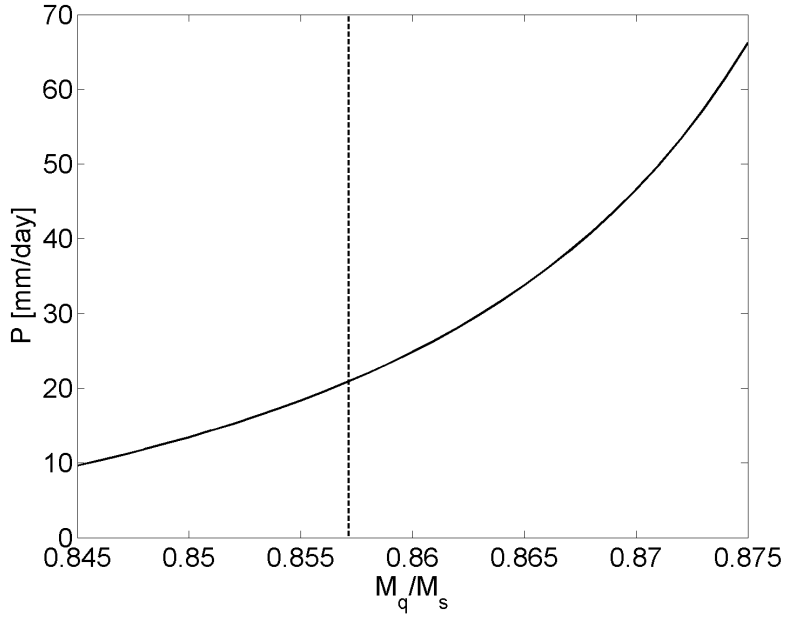

Figure 2-10: Precipitation at the fixed point of moisture mode instability for various values of normalized gross moisture stratification $\overline{M}_{q1}/\overline{M}_{s1}$. The dotted vertical line represents the reference value.

Nevertheless, more questions have been raised in this chapter than answered. Examples include:

1. *How universal is the moisture mode?* I have argued that moisture-convection feedback is essential for existence of the moisture mode, and that QTCM incorporates it in a crude way. However, as emphasized above, the linear Betts-Miller framework lacks a physical basis for humidity relaxation. The natural question is then, is the moisture mode a robust feature found in other theoretical models? Another issue concerns the gross moist stability. Moisture mode instability is sensitive to gross moist stability, but in nature, gross moist stability is heavily affected by the vertical profile of the large-scale circulation. Is the moisture mode still retained when gross moist stability is not prescribed?

2. *Is moisture-convection feedback really the essential component of the moisture mode?* Since moisture-convection feedback is implicit in QTCM, I could not suppress it and test its effect in this chapter. In particular, QTCM does not distinguish between boundary layer moist static energy and free-tropospheric humidity, and the finding of this chapter may be due to the effect of the boundary layer. Is it possible to isolate the effect of free-tropospheric water vapor, using a more elaborate model?

3. *The moisture mode is stationary and small scales are preferred. How is it related to the MJO?* The discussions presented above showed that in the absence of linear WISHE, the moisture mode is stationary and its growth rate asymptotes to the WTG limit in the small-scale limit. At best, the growth rate is nearly constant for a wide range of wavenumbers; the large scale is not preferred. How is it related with a moving, large-scale disturbance like the MJO? What would happen if a moisture mode nonlinearly saturates on an equatorial β-plane?

The subsequent chapters address each of these questions. The next chapter will examine the first half of question (1): Does a different theoretical model have moisture mode instability?

Chapter 3

Moisture modes in subcloud-layer quasi-equilibrium model

3.1 Introduction

Chapter 2 has shown that the quasi-equilibrium tropical circulation model (QTCM; Neelin and Zeng 2000) has a moisture mode, which is unstable in the presence of sufficient moist static energy sources. However, the existence of such a mode is rather tenuous because it depends on the convective scheme used. QTCM relies on a linear variant of the Betts-Miller scheme, which relaxes temperature and humidity to prescribed profiles over a finite convective timescale. Unfortunately, there is no physical basis for prescribing a humidity reference profile. This accentuates the problem since the target of analysis is a moisture mode, for which moist processes are paramount. Analyzing moisture modes would require a solid physical basis in representation of moist processes.

This chapter inquires whether the moisture mode is retained with a parameterization based on carefully considered physics. In particular, I examine whether or not the subcloud-layer quasi-equilibrium model (referred hereafter as SLQEM for shorthand) of Bony and Emanuel (2005) has a moisture mode. The analysis demonstrates that in spite of quite different parameterizations, SLQEM also has a moisture mode, and that its physics is analogous to that found in QTCM. There are certainly many differences, but the finding here

makes the case for a moisture mode stronger.

3.2 Model equations

The SLQEM of Bony and Emanuel (2005) has a long history of research. Since the seminal paper by Emanuel (1987), it has gone through subsequent improvements (Yano and Emanuel 1991; Emanuel 1993; Bony and Emanuel 2005). Below I sketch out a rough derivation of the model. In the strict quasi-equilibrium case, no modification is made except for a minor change in the length scale for nondimensionalization and slight differences in notation. In particular, I take a as the distance the gravest gravity wave travels for a characteristic timescale, rather than the radius of the earth. In the soft quasi-equilibrium case, I use an alternative formulation, which is described in the following. For details, the readers are referred to their papers.

The SLQEM is a simple two-layer model of the tropical atmosphere, consisting of the free troposphere and boundary layer. I focus on the Kelvin-like mode that has vanishing meridional wind.

Previous papers have demonstrated that combining moist convective neutrality and hydrostaticity constrains large-scale flow so that the first baroclinic mode dominates its dynamics (Emanuel 1987; Yano and Emanuel 1991). The following traces the argument presented by Emanuel (1987).

Consider a boundary layer momentum equation:

$$\left(\frac{\partial}{\partial t}+u_b\frac{\partial}{\partial x}\right)u_b=-\frac{\partial\varphi_b}{\partial x}-\frac{C_d}{h}|\mathbf{V}_b|u_b, \tag{3.1}$$

where x is the horizontal coordinate, t is time, u_b is the zonal velocity at the top of the subcloud layer, φ_b is the geopotential at the top of the subcloud layer, C_d is the drag coefficient, h is the depth of the subcloud layer, $|\mathbf{V}_b|$ is the surface wind speed. Here momentum damping takes a bulk formula. All variables represent the total fields; for example, $u_b=\overline{u}_b+u_b'$, where the overbar denotes the mean basic state and the prime implies the perturbation from it. For the readers' convenience, Table 3.1 lists definitions of all variables.

Table 3.1: Definition of symbols. Adapted from Table 1 of Bony and Emanuel (2005). Note that a has a meaning different from that of their paper.

u_b	Zonal wind at the top of the subcloud layer
U	Mean zonal wind
w_c	Vertical velocity in the deep convective area
w_d	Vertical velocity in the environment
σ	Fractional areal coverage of cumulus convection
$w = \sigma w_c + (1-\sigma) w_d$	Total vertical velocity
φ	Geopotential
θ	Average tropospheric potential temperature
θ_{eb}	Equivalent potential temperature of the subcloud layer
θ_{em}	Average equivalent potential temperature of the troposphere
ε_p	Precipitation efficiency
$\dot{R}_0$	Radiative cooling rate ($-\dot{R}_0$ is the radiative heating rate)
α	Intensity factor of cloud-radiation interactions, which Bony and Emanuel (2005) called moisture-radiation interactions.
γ	Intensity factor of moisture-convection feedback, which Bony and Emanuel (2005) termed moisture-precipitation efficiency interactions
a = 80000 km	Distance the gravest gravity wave travels for a characteristic timescale
g	Gravitational acceleration
$N^2 = 10^{-4}$ s^{-2}	N: buoyancy frequency of dry air
H_f = 8 km	Thickness of the troposphere
H_m = 5 km	Level of minimum θ_e in the troposphere
h = 0.5 km	Thickness of the subcloud layer
$C_k = 1.2 \cdot 10^{-3}$	Bulk coefficient of entropy exchange
$C_d = 1.0 \cdot 10^{-3}$	Bulk coefficient of momentum exchange rate
$\overline{\varepsilon} = (T_b - \langle T \rangle)/T_b = 0.1$	Thermodynamic efficiency
$\langle T \rangle$	Mass-weighted tropospheric averaged temperature
T_b	Mean temperature at the top of the subcloud layer
$\ln(\overline{\theta}_{es}/\overline{\theta}_{eb}) = 0.035$	Thermodynamic disequilibrium
$\lvert U \rvert = 5$ms^{-1}	Magnitude of the mean zonal wind
$C_p = 1000$J kg^{-1}K^{-1}	Specific heat at constant pressure
$\Gamma = \Gamma_d/\Gamma_m$ = 1.7	Ratio of dry and moist adiabatic temperature lapse rates
b	Subscript denoting boundary layer
α_v	Specific volume
s_{ms}	Saturation moist entropy
$\langle \quad \rangle$	Mass-weighted vertical average operator
(overbar)	Time-mean operator
(prime)	Denotes Perturbation

According to Emanuel (1987), it is possible to associate the geopotential gradient with moist entropy. Assuming a spatially homogeneous radiative-convective equilibrium as the background state, the hydrostatic equation for the perturbation from the basic state is

$$\frac{\partial \varphi'}{\partial p} = -\alpha_v' \tag{3.2}$$

where φ is geopotential, p is pressure, α_v signifies specific volume. The specific volume anomaly may be rewritten as $\alpha_v' = (\partial \alpha_v / \partial s_{ms})_p$, where s_{ms} is the saturation moist entropy, and the derivative is evaluated at the basic state radiative-convective equilibrium. Invoking the moist Maxwell relation $(\partial \alpha_v / \partial s_{ms})_p = (\partial T / \partial p)_{s_{ms}}$ (see Emanuel 1986, for derivation) leads to

$$\frac{\partial \varphi'}{\partial p} = -\left(\frac{\partial T}{\partial p}\right)_{s_{ms}} s_{ms}', \tag{3.3}$$

where T is temperature. This integrates to

$$\varphi' - \varphi_b' = (T_b - T) s_{ms}' = (T_b - T) s_b', \tag{3.4}$$

where s_b is moist entropy of the subcloud layer. Here moist convective neutrality $s_{ms}' = s_b'$ has been invoked. Taking the vertical average leads to

$$\left\langle \varphi' \right\rangle - \varphi_b' = \left(T_b - \left\langle T \right\rangle\right) s_b', \tag{3.5}$$

where the operator $\langle \quad \rangle$ denotes mass-weighted vertical average. Since the background state is barotropically stable, I would assume $\langle \varphi' \rangle = 0$. Finally I arrive at a simple relationship between geopotential and temperature:

$$\varphi_b' = -\left(T_b - \left\langle T \right\rangle\right) s_b' = -C_p \left(T_b - \left\langle T \right\rangle\right) \ln \theta_{eb}' \quad \text{or} \quad \nabla \varphi_b = -C_p \left(T_b - \left\langle T \right\rangle\right) \nabla \ln \theta_{eb}, \tag{3.6}$$

where θ_{eb} is the equivalent potential temperature of the subcloud layer. In the last step, I have invoked the definition of moist entropy and the fact that the basic state is spatially

homogeneous. With this relation, the momentum equation becomes

$$\left(\frac{\partial}{\partial t}+u_b\frac{\partial}{\partial x}\right)u_b = C_p\left(T_b-\langle T\rangle\right)\frac{\partial \ln\theta_{eb}}{\partial x}-\frac{C_d}{h}|\mathbf{V}_b|u_b. \tag{3.7}$$

The continuity equation for the present two-layer model is

$$\frac{\partial u_b}{\partial x}+\frac{w}{H_m}=0, \tag{3.8}$$

where w is vertical velocity and H_m is the level of minimum θ_e in the troposphere, the middle level of the model atmosphere.

Before describing the temperature equation, it is instructive to examine mass fluxes in the model. Figure 3-1 is a schematic representation of the model structure and convective mass fluxes. Deep, precipitating convection occupies a fractional area of σ, and its upward velocity is w_c. In the environment of clouds, gentle subsidence covers a fractional area of $1-\sigma$ with a descent velocity of w_d. The large-scale vertical velocity is thus a sum of the two: $w=\sigma w_c+(1-\sigma)w_d$. In addition to deep convention, the model incorporates a couplet of shallow updraft and downdraft, which may represent either shallow nonprecipitating clouds or in the case of downdraft, unsaturated downdraft driven by evaporation of precipitation. Yano and Emanuel (1991) assumed the equal mass fluxes for the updraft and downdraft of the couplet; its mass flux is denoted by w_s and its fractional area is σ_s.

Now the temperature equation can be written as

$$g\left(\frac{\partial}{\partial t}+u_b\frac{\partial}{\partial x}\right)\ln\theta = N^2(-w+\sigma w_c)-g\dot{R}. \tag{3.9}$$

Here g is acceleration due to gravity, θ is the (dry) potential temperature, N is the buoyancy frequency, $\dot{R}$ is the radiative cooling, to be specified below. Note that $N^2\sigma w_c$, heating due to compensating subsidence, is proportional to precipitation.

For small perturbations, I can rewrite potential temperature anomaly in terms of satu-

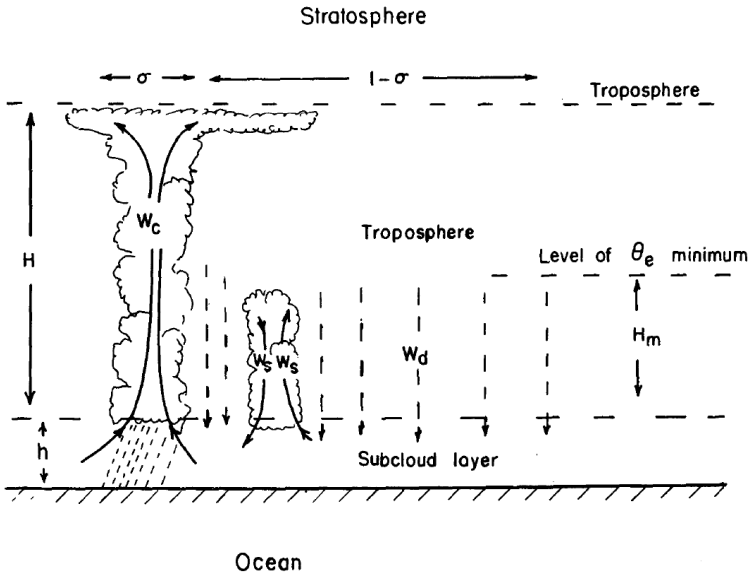

Figure 3-1: Schematic representation of the model structure and mass fluxes. Taken from the upper panel of Figure 1 of Yano and Emanuel (1991).

rated moist entropy anomaly (Emanuel 1987):

$$\ln\theta' \simeq \frac{\Gamma_m}{\Gamma_d}\ln\theta_e^{*\prime} \simeq \frac{\Gamma_m}{\Gamma_d}\ln\theta'_{eb}, \tag{3.10}$$

where Γ_m is moist adiabatic lapse rate, Γ_d is dry adiabatic lapse rate, θ_e^* is the saturation equivalent potential temperature. This relation leads to

$$g\frac{\Gamma_m}{\Gamma_d}\left(\frac{\partial}{\partial t}+u_b\frac{\partial}{\partial x}\right)\ln\theta_{eb} = N^2(-w+\sigma w_c) - g\dot{R}. \tag{3.11}$$

The model has two humidity-related variables: boundary layer moist entropy and free-tropospheric moist entropy. They are actually combinations of humidity and temperature. Nevertheless, vacillations in humidity are more important if the free troposphere is under WTG and the boundary layer's temperature is controlled by sea surface temperature.

The boundary layer moist entropy increases with surface heat flux and decreases through downdraft and shallow convective circulations, whereas the free tropospheric moist entropy changes with radiation and convective mass exchange. One can formulate

this as

$$h\left(\frac{\partial}{\partial t}+u_b\frac{\partial}{\partial x}\right)\ln\theta_{eb} = C_k|\mathbf{V}_b|(\ln\theta_{es}-\ln\theta_{eb})-X, \tag{3.12}$$

$$H_f\left(\frac{\partial}{\partial t}+u_b\frac{\partial}{\partial x}\right)\ln\theta_{em} = -H_f\dot{R}+X, \tag{3.13}$$

where C_k is the bulk coefficient of entropy exchange, θ_{es} is the saturation moist entropy at the sea surface, θ_{em} is the moist entropy of the free troposphere, and H_f is the thickness of the troposphere. X represents entropy exchange between the boundary layer and the free troposphere. It takes the form of bulk parameterization:

$$X=[-(1-\sigma)w_d+\sigma_s w_s](\ln\theta_{eb}-\ln\theta_{em}), \tag{3.14}$$

To simplify, Yano and Emanuel (1991) introduced the concept of bulk precipitation efficiency and set it to constant:

$$\varepsilon_p \equiv \frac{\sigma w_c}{\sigma_s w_s+\sigma w_c}=\text{const.} \tag{3.15}$$

ε_p is a measure of the bulk precipitation efficiency since the total upward mass flux is $\sigma_s w_s+\sigma w_c$ and mass flux associated with precipitation is σw_c. Noting that $w=\sigma w_c+(1-\sigma)w_d$ and using the definition of precipitation efficiency, I rewrite the entropy exchange term as

$$X=-\left(w-\frac{\sigma w_c}{\varepsilon_p}\right)(\ln\theta_{eb}-\ln\theta_{em}). \tag{3.16}$$

The equations thus far merely represent various conservation principles. Determining the convective mass flux or precipitation needs a closure assumption, the key assumption in the model. As the model's name suggests, the mass flux is calculated assuming quasi-equilibrium for the subcloud layer entropy. Raymond (1995) argued that convective mass fluxes are rapidly adjusting to production of instability so that the tendency of the boundary layer entropy is small. Introducing such an assumption in Eq. (3.12) yields

$$\sigma w_c \simeq \varepsilon_p \left(w + C_k |\mathbf{V}_b| \frac{\ln \theta_{es} - \ln \theta_{eb}}{\ln \theta_{eb} - \ln \theta_{em}} \right). \tag{3.17}$$

Applying this equation instantaneously is called strict quasi-equilibrium (SQE). Emanuel (1993) developed a method to include a small but finite time lag τ_c in determining convective mass flux, which one may call "soft" quasi-equilibrium (as opposed to strict) in the language of Emanuel et al. (1994). Bony and Emanuel (2005) utilized the same procedure, but here I use an alternative formulation for soft quasi-equilibrium by introducing a prognostic convective mass flux:

$$\left(\frac{\partial}{\partial t} + u_b \frac{\partial}{\partial x} \right) \sigma w_c = \frac{1}{\tau_c} \left[\varepsilon_p \left(w + C_k |\mathbf{V}_b| \frac{\ln \theta_{es} - \ln \theta_{eb}}{\ln \theta_{eb} - \ln \theta_{em}} \right) - \sigma w_c \right]. \tag{3.18}$$

Bony and Emanuel (2005) observed that changes in radiation in the tropics are dominated by clouds and moisture, not temperature, and showed that TOGA-COARE (Tropical Ocean Global Atmosphere-Coupled Ocean Atmosphere Response Experiment) data exhibit correlations between moist entropy and outgoing longwave radiation, albeit with some scatter. This observation is an indication that enhanced cloud radiative forcing is correlated with a humid troposphere. They proposed that radiative cooling be parameterized in terms of moist entropy as

$$\dot{R} = \overline{\dot{R}} + \dot{R}' = \dot{R}_0 \left(1 + \alpha \frac{\ln \theta'_{eb} - \ln \theta'_{em}}{\ln \overline{\theta}_{eb} - \ln \overline{\theta}_{em}} \right), \tag{3.19}$$

where $\dot{R}_0$ is the background radiative cooling rate, and α is a positive proportionality constant for cloud-radiation interaction.

Moisture-convection feedback is parameterized by making precipitation efficiency dependent on the difference between boundary layer moist entropy and mid-tropospheric moist entropy.

$$\varepsilon_p = \frac{\overline{\varepsilon}_p}{1 + \gamma \dfrac{\ln \theta'_{eb} - \ln \theta'_{em}}{\ln \overline{\theta}_{eb} - \ln \overline{\theta}_{em}}} \approx \overline{\varepsilon}_p \left(1 - \gamma \frac{\ln \theta'_{eb} - \ln \theta'_{em}}{\ln \overline{\theta}_{eb} - \ln \overline{\theta}_{em}} \right), \tag{3.20}$$

where γ is a measure of dependence of precipitation efficiency on tropospheric humidity. In the following, I call γ moisture-convection feedback parameter. Eq. (3.20) should be contrasted with the implicit moisture-convection feedback used in QTCM or Fuchs and Raymond (2002, 2005, 2007).

3.3 Linear analysis

3.3.1 Radiative-convective equilibrium

The radiative-convective equilibrium is forced by the barotropic mean wind U, the sea-surface equivalent potential temperature θ_{es}, and the background radiative cooling rate $\dot{R}_0$. Setting the time tendency to zero in Eqs. (3.11), (3.12), and (3.13) yields the equations for radiative-convective equilibrium with $\overline{u}_b = U$ and $\overline{w} = 0$:

$$0 = N^2 \sigma \overline{w}_c - g\dot{R}_0, \tag{3.21}$$

$$0 = -H_f \dot{R}_0 + \frac{\sigma \overline{w}_c}{\overline{\varepsilon}_p}(\ln \overline{\theta}_{eb} - \ln \overline{\theta}_{em}), \tag{3.22}$$

$$\sigma \overline{w}_c = \overline{\varepsilon}_p C_k |U| \frac{\ln \theta_{es} - \ln \overline{\theta}_{eb}}{\ln \overline{\theta}_{eb} - \ln \overline{\theta}_{em}}. \tag{3.23}$$

The solution is

$$\frac{C_k |U| (\ln \theta_{es} - \ln \overline{\theta}_{eb})}{H_f} = \dot{R}_0, \tag{3.24}$$

$$\sigma \overline{w}_c = g \frac{C_k |U| (\ln \theta_{es} - \ln \overline{\theta}_{eb})}{N^2 H_f}, \tag{3.25}$$

$$\ln \overline{\theta}_{eb} - \ln \overline{\theta}_{em} = \overline{\varepsilon}_p \frac{N^2 H_f}{g}. \tag{3.26}$$

These serve as a basis for nondimensionalization.

3.3.2 Linearization and nondimensionalization

The above set linearizes to the following.

$$\left(\frac{\partial}{\partial t}+U\frac{\partial}{\partial x}\right)u_b' = C_p\left(T_b-\langle T\rangle\right)\frac{\partial \ln\theta_{eb}'}{\partial x}-2\frac{C_d}{h}|U|u_b', \tag{3.27}$$

$$\frac{\partial u_b'}{\partial x}+\frac{w'}{H_m} = 0, \tag{3.28}$$

$$g\frac{\Gamma_m}{\Gamma_d}\left(\frac{\partial}{\partial t}+U\frac{\partial}{\partial x}\right)\ln\theta_{eb}' = N^2(-w'+\sigma w_c')-g\dot{R}_0\alpha\frac{\ln\theta_{eb}'-\ln\theta_{em}'}{\ln\overline{\theta}_{eb}-\ln\overline{\theta}_{em}}, \tag{3.29}$$

$$\begin{aligned} H_f\left(\frac{\partial}{\partial t}+U\frac{\partial}{\partial x}\right)\ln\theta_{em}' = {} & \left(\frac{\sigma w_c'}{\overline{\varepsilon}_p}-w'\right)\left(\ln\overline{\theta}_{eb}-\ln\overline{\theta}_{em}\right) \\ & +(1+\gamma)\frac{\sigma\overline{w}_c}{\overline{\varepsilon}_p}\left(\ln\theta_{eb}'-\ln\theta_{em}'\right) \\ & -H_f\dot{R}_0\alpha\frac{\ln\theta_{eb}'-\ln\theta_{em}'}{\ln\overline{\theta}_{eb}-\ln\overline{\theta}_{em}}. \end{aligned} \tag{3.30}$$

The convective mass flux is calculated as

$$\begin{aligned} \left(\frac{\partial}{\partial t}+U\frac{\partial}{\partial x}\right)\sigma w_c' = {} & \frac{1}{\tau_c}\Bigg[\overline{\varepsilon}_p w'+\overline{\varepsilon}_p C_k\,\mathrm{sgn}(U)u'\frac{\ln\theta_{es}-\ln\overline{\theta}_{eb}}{\ln\overline{\theta}_{eb}-\ln\overline{\theta}_{em}} \\ & -\overline{\varepsilon}_p C_k|U|\frac{\ln\theta_{eb}'}{\ln\overline{\theta}_{eb}-\ln\overline{\theta}_{em}} \\ & -(1+\gamma)\overline{\varepsilon}_p C_k|U|\frac{\ln\theta_{es}-\ln\overline{\theta}_{eb}}{(\ln\overline{\theta}_{eb}-\ln\overline{\theta}_{em})^2}\left(\ln\theta_{eb}'-\ln\theta_{em}'\right) \\ & -\sigma w_c'\Bigg]. \end{aligned} \tag{3.31}$$

In the limit of no convective lag $\tau_c \to 0$, Eq. (3.31) becomes a diagnostic equation:

$$\begin{aligned} \sigma w_c' = {} & \overline{\varepsilon}_p w'+\overline{\varepsilon}_p C_k\,\mathrm{sgn}(U)u'\frac{\ln\theta_{es}-\ln\overline{\theta}_{eb}}{\ln\overline{\theta}_{eb}-\ln\overline{\theta}_{em}} \quad -\overline{\varepsilon}_p C_k|U|\frac{\ln\theta_{eb}'}{\ln\overline{\theta}_{eb}-\ln\overline{\theta}_{em}} \\ & -(1+\gamma)\overline{\varepsilon}_p C_k|U|\frac{\ln\theta_{es}-\ln\overline{\theta}_{eb}}{(\ln\overline{\theta}_{eb}-\ln\overline{\theta}_{em})^2}\left(\ln\theta_{eb}'-\ln\theta_{em}'\right). \end{aligned} \tag{3.32}$$

Assuming a usual exponential solution $\sim \exp(ikx+\sigma t)$ and defining the Doppler-shifted complex frequency $D \equiv ikU+\sigma$, the nondimensionalization shown in Tables 2

Table 3.2: Definitions of nondimensionalization. Tildes denote nondimensional variables. Adapted from Table 2 from Bony and Emanuel (2005).

$x = a\tilde{x}$
$t = a^{1/2}A^{-1/2}\tilde{t}$
$u' = a^{1/2}A^{1/2}\tilde{u}$
$w' = H_m a^{-1/2}A^{1/2}\tilde{w}$
$\Phi' = -aA\tilde{T}_{eb}$
$\ln\theta' = \Delta\tilde{T}_{eb}/\Gamma$
$\ln\theta'_{eb} = \Delta\tilde{T}_{eb}$
$\ln\theta'_{em} = \Delta\tilde{T}_{em}$

Table 3.3: Definitions of nondimensional parameters. Table 3 from Bony and Emanuel (2005).

$A = \overline{\varepsilon}C_p T_b C_k H_f^{-1}\ln(\theta_{es}/\overline{\theta}_{eb})$
$\Delta = aH_f^{-1}C_k\ln(\theta_{es}/\overline{\theta}_{eb})$
$\lambda = (N^2 H_m)/(g\Delta)$
$\alpha_E = C_k\lvert U\rvert a^{1/2}A^{-1/2}/H_f$
$\alpha_D = \dfrac{a^{1/2}A^{-1/2}C_k\lvert U\rvert}{\overline{\varepsilon}_p H_f^2 N^2} g\ln\left(\dfrac{\theta_{es}}{\overline{\theta}_{eb}}\right)$
$F = C_d\lvert U\rvert a^{1/2}A^{-1/2}/h$

and 3 simplifies the present linear system to

$$
\begin{aligned}
(D+2F)u &= ikT_{eb}, && (3.33)\\
iku + w &= 0, && (3.34)\\
D\frac{T_{eb}}{\Gamma} &= \lambda(-w+\sigma w_c) - \alpha\alpha_D(T_{eb}-T_{em}), && (3.35)\\
DT_{em} &= \lambda(-\varepsilon_p w+\sigma w_c) + (1+\gamma)\alpha_D(T_{eb}-T_{em}) - \alpha\alpha_D(T_{eb}-T_{em}), && (3.36)\\
D\sigma w_c &= \frac{1}{\tau_c}\left[\varepsilon_p w + \frac{\mathrm{sgn}(U)u - \alpha_E T_{eb}}{\lambda} - \frac{1+\gamma}{\lambda}\alpha_D(T_{eb}-T_{em}) - \sigma w_c\right], && (3.37)
\end{aligned}
$$

where tildes have been dropped. The growth rate is $\mathrm{Re}\,D$ and the Doppler-shifted phase speed is $-\mathrm{Im}\,D/k$. Note that Eq. (24) of Bony and Emanuel (2005) contains a typographic error and (3.37) here reflects the necessary correction.

The dispersion relationship can be phrased as an eigenproblem:

$$\mathsf{A}\mathbf{x} = D\mathbf{x} \tag{3.38}$$

where $\mathbf{x} \equiv (u, T_{eb}, T_{em}, \sigma w_c)^T$ and the coefficient matrix is defined as

$$\begin{aligned}
A_{11} &= -2F, && (3.39)\\
A_{12} &= ik, && (3.40)\\
A_{13} &= 0, && (3.41)\\
A_{14} &= 0, && (3.42)\\
A_{21} &= \Gamma\lambda ik, && (3.43)\\
A_{22} &= -\Gamma\alpha\alpha_D, && (3.44)\\
A_{23} &= \Gamma\alpha\alpha_D, && (3.45)\\
A_{24} &= \Gamma\lambda, && (3.46)\\
A_{31} &= \lambda\varepsilon_p ik, && (3.47)\\
A_{32} &= (1+\gamma-\alpha)\alpha_D, && (3.48)\\
A_{33} &= -(1+\gamma-\alpha)\alpha_D, && (3.49)\\
A_{34} &= \lambda, && (3.50)\\
A_{41} &= \left(-\varepsilon_p ik + \frac{\mathrm{sgn}(U)}{\lambda}\right)\frac{1}{\tau_c}, && (3.51)\\
A_{42} &= \left(-\frac{\alpha_E}{\lambda} - \frac{1+\gamma}{\lambda}\alpha_D\right)\frac{1}{\tau_c}, && (3.52)\\
A_{43} &= \frac{1+\gamma}{\lambda}\alpha_D\frac{1}{\tau_c}, && (3.53)\\
A_{44} &= -\frac{1}{\tau_c}. && (3.54)
\end{aligned}$$

Note that this formulation can encompass the limit of $\tau_c \to 0$, if one multiplies the fourth row of both sides of Eq. (3.38) with τ_c before taking this limit. It is also important to notice that taking the limit of $\tau_c \to 0$ does reduce the order of the dispersion relation from fourth order to third order as the prognostic convective mass flux equation becomes a

diagnostic one.

3.3.3 Solutions

Now that the dispersion relationship has been obtained, the remaining task is to specify the parameter values. They are listed in Table 3.1, which is taken from Bony and Emanuel (2005). Actually Bony and Emanuel do not give the value for T_b. Since Yano and Emanuel (1991) give $A = \overline{\varepsilon} C_p T_b C_k H_f^{-1} \ln(\theta_{es}/\overline{\theta}_{eb}) \simeq 1.26 \times 10^{-4}$ ms^{-2}, it is possible to recover T_b:

$$T_b = \frac{A}{\overline{\varepsilon} C_p C_k H_f^{-1} \ln(\theta_{es}/\overline{\theta}_{eb})} = \frac{1.26 \times 10^{-4}}{0.1 \times 1000 \times 1.2 \cdot 10^{-3}/8000 \times 0.035} = 240\text{K}. \quad (3.55)$$

(3.55) gives a very small value. However, visual comparison shows that this parameter choice gives results similar to those of Bony and Emanuel (2005), and I proceed with this value. Fortunately, sensitivity tests demonstrate that the results are quite insensitive to T_b; changing T_b from 240 to 300 K does not affect the results in any significant way. With these parameter values, the dispersion relation is solved numerically.

Figure 3-2 shows the growth rates and phase speeds of three modes in the SQE case along with the WTG limit values (solid lines). In creating this figure, I have not applied the condition of boundedness at infinity. Had it been applied, the westward propagating mode (denoted by crosses) would be rejected. The WTG limit is discussed in later sections.

The model has three modes. The growth rate of moisture modes (circles) tends to constant as the planetary wavenumber increases. At high wavenumbers, the growth rate is about 0.65 day^{-1} and the timescale is $\sim$ 1.5 day. The phase speed is quite small and converges to zero relative to the mean flow, showing that it is an advective mode. Bony and Emanuel called this moisture mode at high wavenumbers "small-scale advective disturbances." The WTG limit explains the small-scale behavior of the moisture mode accurately. For most of the parameter regime presented here, the moisture mode is the most unstable mode, although Fig. 3-4 shows that at the largest scale, the gravity wave has a larger growth rate than the moisture mode. The other two modes represent eastward and westward propagating waves, whose phase speeds are about $\sim$ 20 m/s and reduced from

dry ones through effective stability under the influence of moist convection (Neelin et al. 1987; Yano and Emanuel 1991; Emanuel et al. 1994).

Figures 3-3, 3-4, and 3-5 present the same results as in Figure 3-2, but for different parameter values. Note that Figs. 3-3, and 3-5 show four solutions rather than three, since taking $\tau_c \neq 0$ changes the order of the dispersion relationship. Comparing Fig. 3-2 with Fig. 3-3 and Fig. 3-4 with Fig. 3-5 reveals effects of a small but finite convective lag. In addition to providing the fourth mode, a finite convective time lag increases the phase speed of dry gravity wave at the small-scale limit. It also decreases the growth rate of gravity waves, especially at the small scale. This might be reflection of what Emanuel et al. (1994) termed moist convective damping; they noted that a small convective lag selectively damps small-scale waves. However, Figs. 3-3 and 3-5 do not show selective damping, and the growth rates of gravity waves are generally reduced.

There are some subtleties in each graph, but the main point in the four figures is very clear: moisture modes also exist in the SLQEM, and the WTG approximation (represented by solid and dashed lines) captures its characteristics well.

3.4 WTG analysis

3.4.1 Physical motivation for WTG: case of SQE

Having seen the power of the WTG approximation, this section derives the WTG equation for the present model. Before systematically deriving the WTG system, it is instructive to explore the equation for column-integrated moist entropy. Consider the case of SQE. Adding (3.12) and (3.13) gives

$$\left(\frac{\partial}{\partial t}+u_b\frac{\partial}{\partial x}\right)(H_f\ln\theta_{em}+h\ln\theta_{eb})=C_k|\mathbf{V}_b|(\ln\theta_{es}-\ln\theta_{eb})-H_f\dot{R}. \tag{3.56}$$

The nondimensional, linear version of (3.56) is

$$D\left(T_{em}+\frac{h}{H_f}T_{eb}\right)=\mathrm{sgn}(U)u-\alpha_E T_{eb}-\alpha\alpha_D(T_{eb}-T_{em}). \tag{3.57}$$

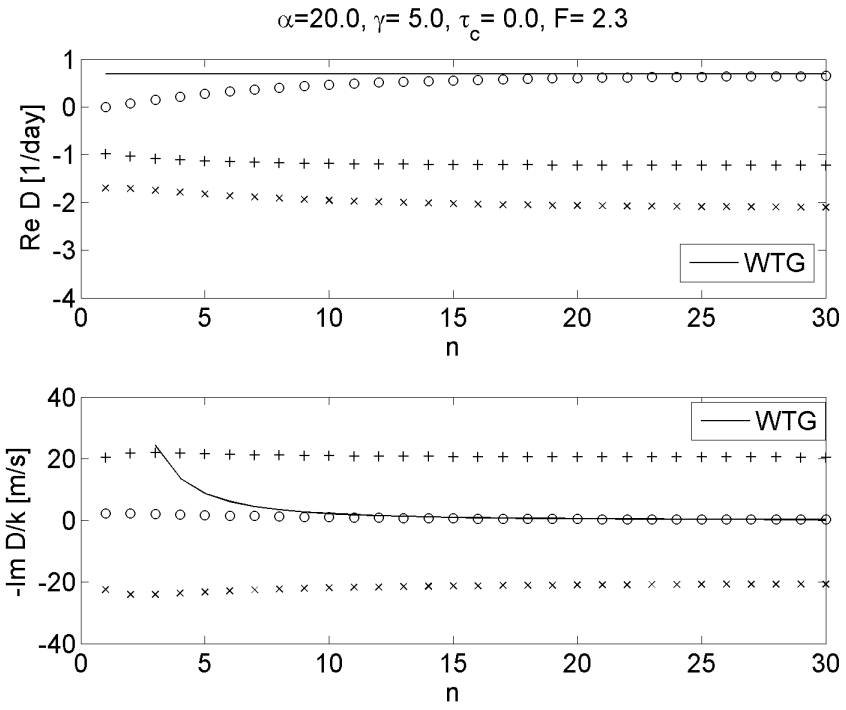

Figure 3-2: (Upper panel) growth rates and (lower panel) Doppler-shifted phase speeds of three modes as functions of planetary wavenumber n. The circle corresponds to the moisture mode, and the solid line represents the WTG limit. Parameters used are: cloud-radiation interaction parameter $\alpha = 20$, moisture-convection feedback parameter $\gamma = 5$, convective timescale $\tau_c = 0$, and friction $F = 2.3$. This figure does not reflect the boundedness-at-infinity condition on an equatorial β-plane. Had it been applied, the westward propagating mode (cross) would have been rejected. The phase speed for the WTG solutions is shown only for $n \geq 3$.

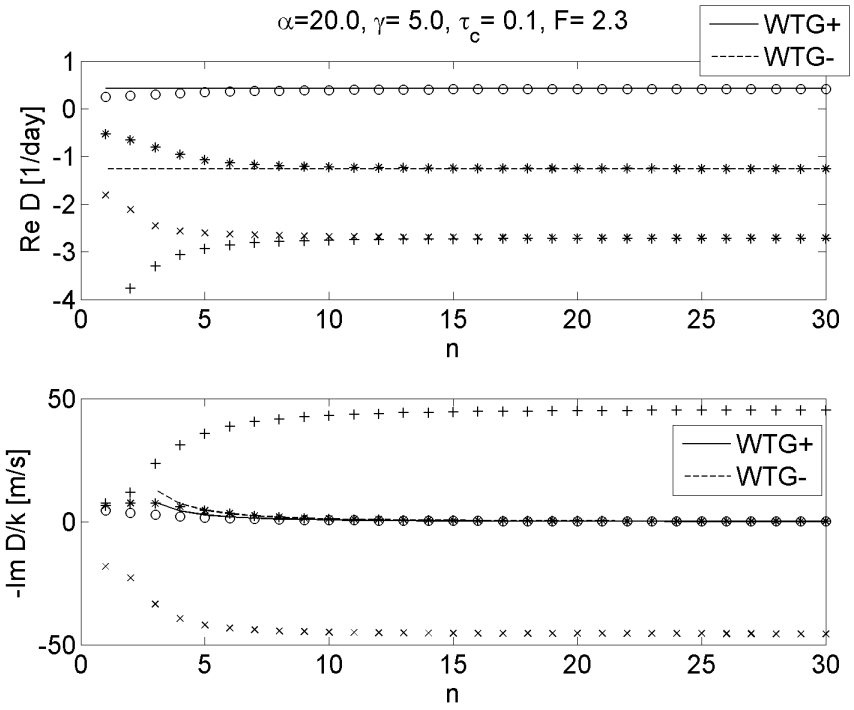

Figure 3-3: Same for Figure 3-2 but for $\alpha = 20$, $\gamma = 5$, $\tau_c = 0.1$, and $F = 2.3$. Note that because of the choice of the vertical axis of the upper panel, some solutions represented by pluses are not shown here. Since a finite convective time lag leads to two WTG solutions, both branches are shown (WTG+ and WTG-).

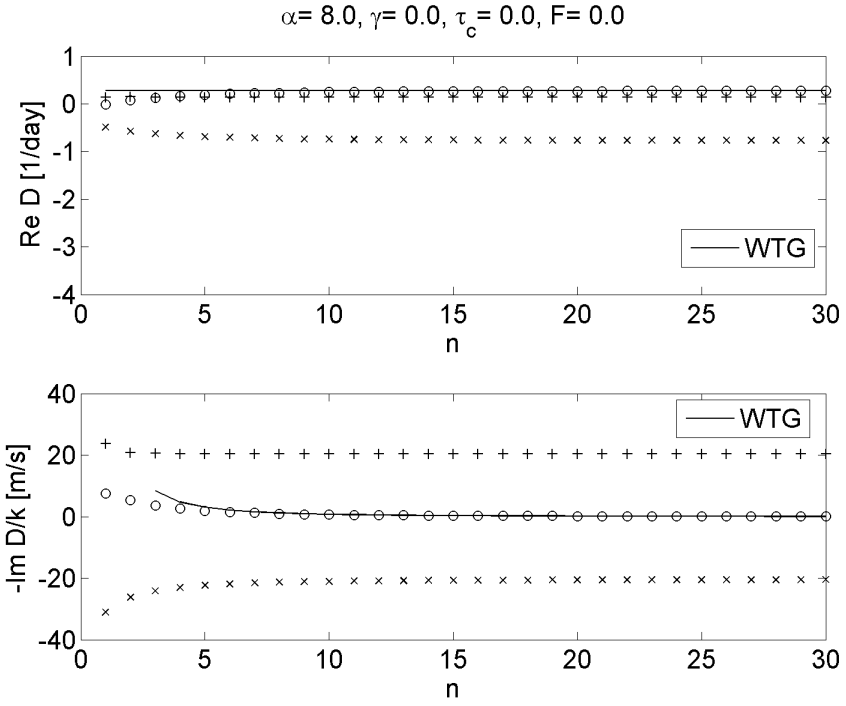

Figure 3-4: As in Figure 3-2 but for $\alpha = 8$, $\gamma = 0$, $\tau_c = 0$, and $F = 0$.

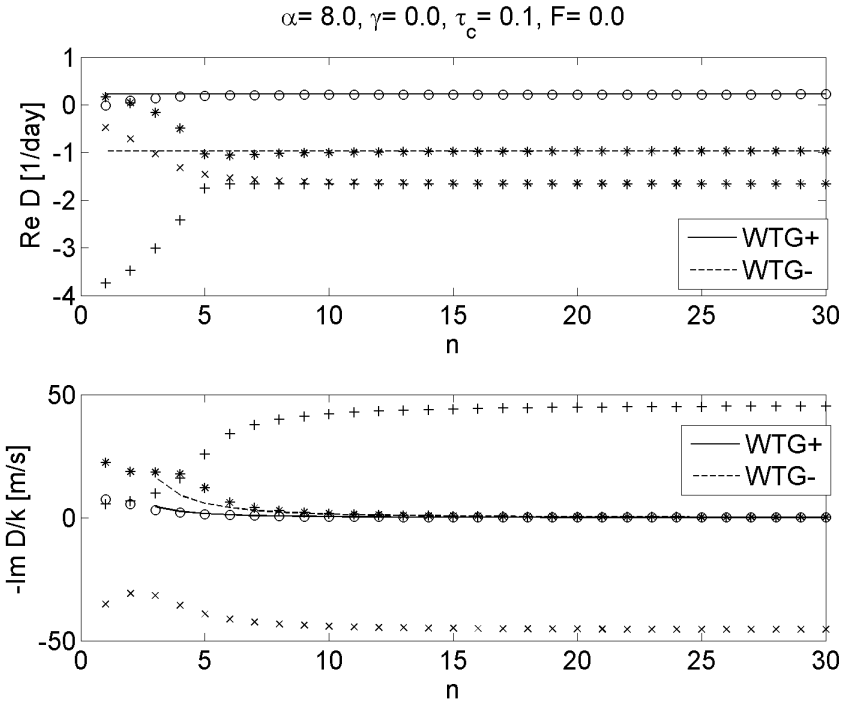

Figure 3-5: As in Figure 3-3 but for $\alpha = 8$, $\gamma = 0$, $\tau_c = 0.1$ and $F = 0$.

The WTG approximation amounts to neglecting T_{eb}. Also for the zeroth-order WTG, u must be neglected except for the convergence term. Then (3.57) simplifies to

$$DT_{em} = \alpha\alpha_D T_{em} \qquad \text{or} \qquad D = \alpha\alpha_D, \tag{3.58}$$

which indicates that the growth rate only depends on two parameters: the cloud-radiation interaction parameter α and a parameter α_D, which is proportional to mass flux (or precipitation) in the radiative-convective equilibrium. A simple physical picture is readily available. Cloud radiative forcing increases moist entropy in the troposphere, which in turn increases cloud radiative forcing. As shown below, if the convective timescale is finite, the argument is no longer as straightforward as this, but the physical mechanism is basically unchanged.

Why is this solution even simpler than the QTCM counterpart? Usually the approach taken here requires an expression for moist static energy (or moist entropy) transport, and one has to solve for w. But the present model of Bony and Emanuel (2005) has no w-dependent term in (3.57), rendering the solution for w unnecessary.

The condition for the WTG approximation is that the tendency term in the temperature equation be much smaller than the ascent term so that the dominant balance is between diabatic heating and adiabatic cooling. Formally the WTG approximation is valid in the present model if

$$G \equiv \left|\left(\frac{DT_{eb}}{\Gamma}\right)\right| \Big/ (\lambda w) = \left|\frac{D}{\Gamma\lambda}\frac{D+2F}{k^2}\right| \ll 1, \tag{3.59}$$

which is our familiar scaling (see Chapters 1 and 2). If F is negligible or at most on the order of D, this reduces to

$$G \approx \left|\frac{D^2}{\Gamma\lambda k^2}\right| \ll 1 \qquad \text{or} \qquad \frac{1}{k^2} \ll \left|\frac{\Gamma\lambda}{D^2}\right|. \tag{3.60}$$

Since the nondimensional dry gravity wave speed is $\sqrt{\Gamma\lambda}$, $\sqrt{\Gamma\lambda}/|D|$ represents the distance a dry gravity wave can travel for the characteristic timescale of the disturbance. The dimensional dry gravity wave speed is $c_{dry} = (\Gamma_d/\Gamma_m \cdot N^2 H_m C_p T_b \overline{\varepsilon}/g)^{1/2} \approx 45.6$ m/s and

it can travel $c_{dry} \times 2\text{day} \sim 79000\text{km}$ for a characteristic timescale of 2 days. WTG should therefore be applicable to virtually all the moisture modes in the present model regardless of wavenumber, as was so in QTCM.

The scaling here naturally suggests taking 80,000 km as the zonal scale, rather than the earth's radius, the choice of Bony and Emanuel (2005). In terms of algebra, adopting a different zonal scale does not lead to any change. For the purpose of a more formal WTG analysis below, I use the zonal scale of 80,000 km.

3.4.2 Mathematical derivation of WTG

Having seen the physics behind WTG, I now develop a mathematical derivation of WTG. Applying continuity simplifies the nondimensional system shown above.

$$
\begin{aligned}
(D+2F)u &= ikT_{eb}, && (3.61)\\
D\frac{T_{eb}}{\Gamma} &= \lambda(iku+\sigma w_c) - \alpha\alpha_D(T_{eb}-T_{em}), && (3.62)\\
DT_{em} &= \lambda(\varepsilon_p iku+\sigma w_c) + (1+\gamma)\alpha_D(T_{eb}-T_{em}) - \alpha\alpha_D(T_{eb}-T_{em}), && (3.63)\\
D\sigma w_c &= \frac{1}{\tau_c}\left[-\varepsilon_p iku + \frac{\mathrm{sgn}(U)-\alpha_E T_{eb}}{\lambda} - \frac{1+\gamma}{\lambda}\alpha_D(T_{eb}-T_{em}) - \sigma w_c\right]. && (3.64)
\end{aligned}
$$

Following the procedure described in Chapter 2, I expand each term in the series of $1/k$.

$$
(D,u,T_{eb},T_{em},w_c) = \sum_{n=0}^{\infty} \frac{1}{k^n}(D_n,u_n,T_{ebn},T_{emn},w_{cn}). \tag{3.65}
$$

As discussed above, the condition for this perturbation expansion to be valid is equivalent to the previously derived WTG condition. This series expansion filters out gravity waves, for which D scales as $\sim k$ at the small-scale limit.

The balance of the leading and next leading order terms in the momentum equation yields

$$
\begin{aligned}
O(k): &\quad 0 = T_{eb0}, && (3.66)\\
O(1): &\quad (D_0+2F)u_0 = iT_{eb1}. && (3.67)
\end{aligned}
$$

The temperature equation gives

$$O(k): \quad 0 = u_0, \tag{3.68}$$

$$O(1): \quad 0 = \lambda i u_1 + \lambda \sigma w_{c0} + \alpha \alpha_D T_{em0}. \tag{3.69}$$

Combining (3.67) and (3.68) indicates that $T_{eb1} = 0$.

The moist entropy equation and mass flux equation result in

$$O(1): \quad D_0 T_{em0} = \lambda \varepsilon_p i u_1 + \lambda \sigma w_{c0} - (1+\gamma-\alpha)\alpha_D T_{em0}, \tag{3.70}$$

$$O(1): \quad D_0 w_{c0} = \frac{1}{\tau_c}\left(-\varepsilon_p i u_1 + \frac{(1+\gamma)\alpha_D}{\lambda} T_{em0} - \sigma w_{c0}\right), \tag{3.71}$$

respectively. In sum, the $O(1)$ equations are

$$0 = \lambda i u_1 + \lambda \sigma w_{c0} + \alpha \alpha_D T_{em0}, \tag{3.72}$$

$$D_0 T_{em0} = \lambda \varepsilon_p i u_1 + \lambda \sigma w_{c0} - (1+\gamma-\alpha)\alpha_D T_{em0}, \tag{3.73}$$

$$D_0 w_{c0} = \frac{1}{\tau_c}\left(-\varepsilon_p i u_1 + \frac{(1+\gamma)\alpha_D}{\lambda} T_{em0} - \sigma w_{c0}\right). \tag{3.74}$$

The same forms of the equations can be obtained from Eqs. (3.33), (3.34), (3.35), (3.36), and (3.37), if temperature is set to zero and the horizontal wind is neglected except for the convergence term. Linear WISHE (wind-induced surface heat exchange) is not the zeroth order effect here. Eqs. (3.72), (3.73), and (3.74) combine to yield the zeroth-order dispersion relation:

$$0 = \tau_c D_0^2 + [\tau_c \alpha_D (1+\gamma-\alpha+\varepsilon_p\alpha) + 1 - \varepsilon_p] D_0 + -(1-\varepsilon_p)\alpha\alpha_D. \tag{3.75}$$

Interestingly the relative magnitude of each term is identical to that found in QTCM, as

(3.76) shows.

$$\begin{pmatrix} u \\ T_{eb} \\ T_{em} \\ \sigma w_c \end{pmatrix} = \begin{pmatrix} 0 \\ 0 \\ T_{em0} \\ \sigma w_{c0} \end{pmatrix} + \frac{1}{k} \begin{pmatrix} u_1 \\ 0 \\ T_{em1} \\ \sigma w_{c1} \end{pmatrix} + \frac{1}{k^2} \begin{pmatrix} u_1 \\ T_{eb2} \\ T_{em2} \\ \sigma w_{c2} \end{pmatrix} + O(k^{-3}). \tag{3.76}$$

It is thus natural to call this mode a moisture mode under the WTG balance because the temperature anomaly is second-order and the mode is dominated by moist entropy.

In the limit of $\tau_c \to 0$, the moist entropy and mass flux equations simplify to

$$\begin{aligned} D_0 T_{em0} &= \lambda \varepsilon_p i u_1 + \lambda \sigma w_{c0} - (1+\gamma-\alpha)\alpha_D T_{em0}, & (3.77) \\ \sigma w_{c0} &= -\varepsilon_p i u_1 + \frac{(1+\gamma)\alpha_D}{\lambda} T_{em0}. & (3.78) \end{aligned}$$

These two equations lead to $D_0 T_{em0} = \alpha \alpha_D T_{em0}$, confirming the result already obtained.

3.4.3 Perturbation expansion of the dispersion relationship

Although the zeroth-order dispersion relationship has been obtained, one can go further by examining the dispersion relationship directly, which is

$$0 = \det(\mathsf{A} - \mathsf{E}D) = \begin{vmatrix} A_{11}-D & A_{12} & 0 & 0 \\ A_{21} & A_{22}-D & A_{23} & A_{24} \\ A_{31} & A_{32} & A_{33}-D & A_{34} \\ A_{41} & A_{42} & A_{43} & A_{44}-D \end{vmatrix} \tag{3.79}$$

where E is an identity matrix. This form is not amenable to perturbation expansion since there are $O(k)$ terms in the elements of the coefficient matrix, which are A_{12}, A_{21}, A_{31}, and A_{41}. If we expand the determinant, we find $O(k^2)$ terms because of these coefficients. For the purpose of the perturbation expansion, it is useful to have only $O(1)$ terms or higher order terms in $1/k$. By dividing through by k^2, it is possible to convert this into such a

convenient form:

$$
\begin{aligned}
0 = \frac{1}{k^2}\det(\mathsf{A}-\mathsf{E}D) &= \begin{vmatrix} \frac{A_{11}}{k}-\frac{D}{k} & i & 0 & 0 \\ \Gamma\lambda i & \frac{A_{22}}{k}-\frac{D}{k} & A_{23} & A_{24} \\ \lambda\varepsilon_p i & \frac{A_{32}}{k} & A_{33}-D & A_{34} \\ -\frac{\varepsilon_p i}{\tau_c}+\frac{\mathrm{sgn}(U)}{\lambda\tau_c k} & \frac{A_{42}}{k} & A_{43} & A_{44}-D \end{vmatrix} \\
&= \begin{vmatrix} \Gamma\lambda i & A_{23} & A_{24} \\ \lambda\varepsilon_p i & A_{33}-D & A_{34} \\ -\frac{\varepsilon_p i}{\tau_c}+\frac{\mathrm{sgn}(U)}{\lambda\tau_c k} & A_{43} & A_{44}-D \end{vmatrix} + O(k^{-2}). \quad (3.80)
\end{aligned}
$$

Equating the terms on the same order in k gives

$$O(1): \quad 0 = \tau_c D_0^2 + [\tau_c\alpha_D(1+\gamma-\alpha+\varepsilon_p\alpha)+1-\varepsilon_p]D_0 - (1-\varepsilon_p)\alpha\alpha_D, \quad (3.81)$$

$$O(k^{-1}): \quad D_1 = i\frac{\mathrm{sgn}(U)}{\lambda}\frac{\alpha\alpha_D+(1+\gamma-\alpha)\alpha_D+D_0}{2\tau_c D_0+(1+\gamma-\alpha+\varepsilon_p\alpha)\tau_c\alpha_D+1-\varepsilon_p}. \quad (3.82)$$

Since the convective mass flux is a prognostic variable in the soft quasi-equilibrium case, (3.81) is a quadratic equation. In the limit of $\tau_c \to 0$, the convective mass flux becomes a diagnostic variable, and I find that the equation for D_0 becomes linear:

$$D_0 = \alpha\alpha_D, \quad (3.83)$$

$$D_1 = \frac{i\mathrm{sgn}(U)\alpha_D(\alpha+1+\gamma)}{\lambda(1-\varepsilon_p)}. \quad (3.84)$$

It it curious that Eqs. (3.81), (3.82), (3.83), and (3.84) illustrate that linear WISHE does not enter at the leading order. Moreover, as Eq. (3.85) shows below, D_0 is always real, representing the growth rate while D_1 is always imaginary and describes the phase speed.

3.4.4 WTG growth rates

The advantage of the WTG analysis lies in its simplicity, and the growth rate is easy to calculate. Since the growth rate for the SQE case is trivial, this subsection focuses on the

case of finite convective timescale.

Figure 3-6 depicts the sensitivity of the growth rate to various parameters for the unstable branch of moisture mode. The *e*-folding timescale is a few to about ten days. Increasing the cloud-radiation interaction parameter α and shortening the convective timescale τ_c leads to a larger growth rate, which is intuitive. However, the growth rate increases with a lower moisture-convection feedback parameter γ and a lower precipitation efficiency ε_p, although the growth rate is not particularly sensitive to changes in these parameters.

The most striking finding here is that in all cases explored here, the moisture mode instability exists for non-zero α. Chapter 2 showed that changing a parameter can easily suppress moisture mode instability in QTCM. The result here is vastly different. Indeed, this result can be confirmed from the growth rate equation directly. It is obvious for the SQE case ($D_0 = \alpha\alpha_D$). In the finite convective lag case, it is helpful to rewrite the WTG growth rate as

$$\begin{aligned} D_0 &= \frac{\tau_c\alpha_D(1+\gamma-\alpha+\varepsilon_p\alpha)+1-\varepsilon_p}{2\tau_c} \\ &\quad\times\left(\pm\sqrt{1+\frac{4\tau_c(1-\varepsilon_p)\alpha_D}{[\tau_c\alpha_D(1+\gamma-\alpha+\varepsilon_p\alpha)+1-\varepsilon_p]^2}\alpha}-1\right). \end{aligned} \tag{3.85}$$

Since all the coefficients are positive and the bulk precipitation efficiency is less than or equal to unity ($1-\varepsilon_p \geq 0$), there is a positive D_0 so long as α is positive and $\varepsilon_p \neq 1$, regardless of the sign of $\tau_c\alpha_D(1+\gamma-\alpha+\varepsilon_p\alpha)+1-\varepsilon_p$. On the other hand, setting $\alpha = 0$ proscribes instability:

$$D_0 = 0 \qquad \text{or} \qquad -\frac{\tau_c\alpha_D(1+\gamma)+1-\varepsilon_p}{\tau_c}. \tag{3.86}$$

Since the moisture mode is almost always unstable, it should be conspicuous. Figure 3-7 describes the growth rate and phase speed of the *most unstable mode*s as a function of planetary wavenumber and cloud-radiation interaction parameter α. There is a branch transition around $\alpha \sim 10$ and the graph exhibits some kink there. The signature of the moisture mode is evident in the phase speed diagram: small phase speed has a wide area

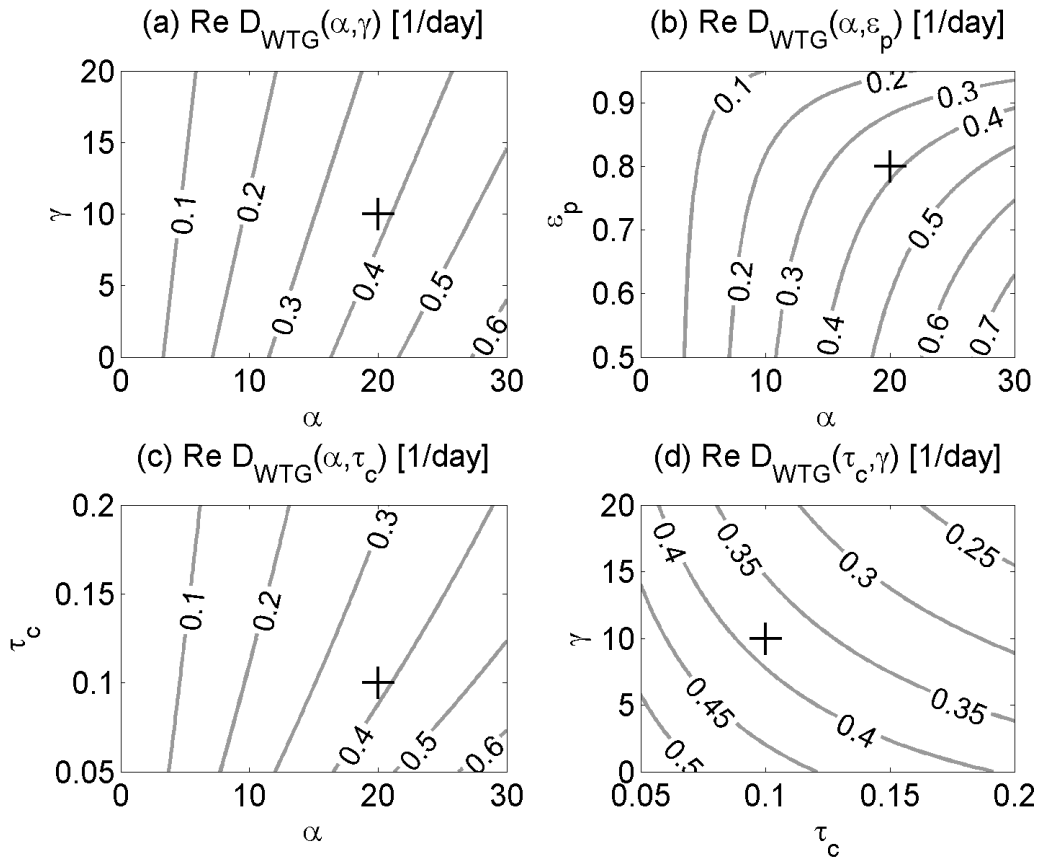

Figure 3-6: Growth rates for the moisture mode in the WTG limit as functions of various moist parameters. Varied parameters are (a) cloud- radiation interaction parameter α and moisture-convection feedback parameter γ; (b) α and background precipitation efficiency ε_p; (c) α and convective timescale τ_c; and (d) τ_c and γ. The crosses in each panel represent the reference values for each varied parameter.

covering the diagram. Such a feature is also identifiable in other parameter regimes, as shown by Bony and Emanuel (2005).

3.5 Summary and discussions

This chapter examined the SLQEM with cloud-radiation interaction and moisture-convection feedback developed by Bony and Emanuel (2005). In the SQE case, the model contains three modes (when the effect of rotation is excluded). They are two gravity waves and a quasi-stationary moisture mode. In the soft quasi-equilibrium case, the model has

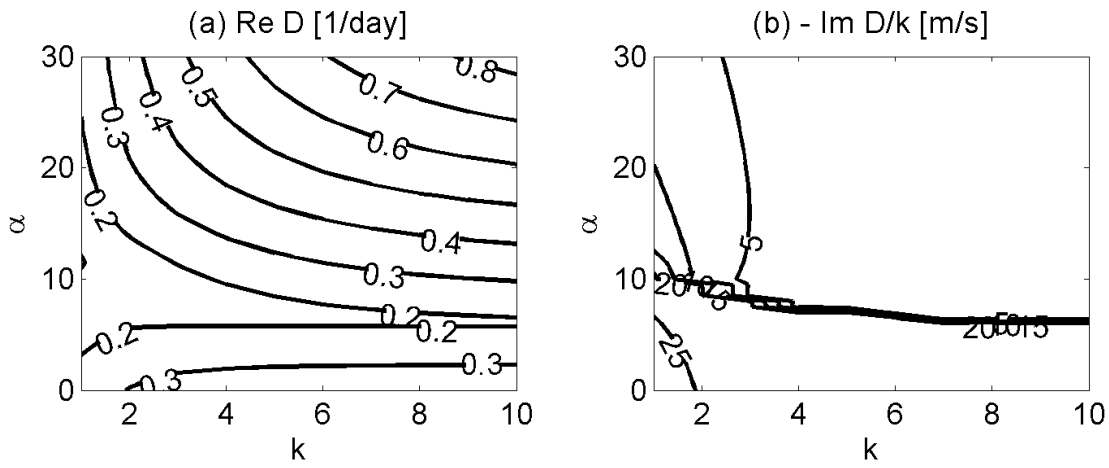

Figure 3-7: (a) Growth rate and (b) phase speed as a function of wavenumber k and cloud-radiation interaction parameter α. These are reproduction of parts of Figure 2 of Bony and Emanuel (2005). The following parameters have been used: $F = 0$, $\tau_c = 0$, and $\gamma = 0$.

four modes, with two moisture modes and two gravity waves.

Moisture mode is a quasi-stationary mode with a dominant humidity signal. As is the case with QTCM, SLQEM has unstable moisture modes. This makes a stronger case for moisture mode instability since quite different parameterizations allow for moisture mode. The WTG scaling applies to the moisture mode for any wavenumber, but the accuracy of approximation improves at the small scale as WTG is an asymptotic limit for $k \to \infty$. The humidity variable, moist entropy in the free troposphere, dominates the evolution of moisture mode.

There are many differences between the two models, however. First of all, the nature of stability vastly differs. In QTCM, the stability of moisture mode is sensitive to all the moist parameters. On the other hand, the present model is unstable to moisture mode instability as long as cloud-radiation interaction is present ($\alpha > 0$).

The lack of moist entropy export in the present model might account for the disparity. QTCM has a small but positive gross moist stability, which gives rise to an export term in the WTG growth rate equation. Such a term is absent in the present model since the moist entropy equation does not have an export term by construction; see Eq. (3.13). Also, this chapter skipped the nonlinear WTG analysis. In fact, had I performed the nonlinear

WTG analysis, I would not have been able to find nonlinear saturation of moisture mode instability because of the absence of the export term. A fairly elementary procedure should be able to add an export term, but this is left to future research.

Another difference concerns the representation of cloud-radiation interaction. Whereas QTCM parameterizes it as a function of precipitation, which in turn depends on humidity, Bony and Emanuel (2005) parameterized cloud forcing as a function of moist entropy difference. The difference in representation has a consequence on the WTG growth rates. QTCM's WTG growth rate is sensitive to convective timescale, the parameter related with moisture-convection feedback, but SLQEM is insensitive to γ, the moisture-convection feedback parameter. In fact, the WTG growth rate under SQE is not dependent on γ at all (Eq. (3.58)).

How is the difference in parameterization of cloud-radiation interaction related with the differing WTG results? As clear from Eqs. (3.56), (3.57), (3.58) and Chapter 2, one can regard the WTG equation as the equation of column-integrated moist entropy (or moist static energy). Convection simply mixes entropy vertically, and does not appear in the vertically integrated equation, unless it is related with diabatic forcing like cloud-radiation interaction or export of moist static energy. In QTCM, convection directly enters the WTG equation since the model has moist static energy export and its cloud forcing is based on precipitation. In contrast, SLQEM lacks the export term and its cloud forcing depends directly on the free-tropospheric humidity. Of course it is possible to examine an alternative formulation in SLQEM, but this is a topic of future analysis.

In combination, Chapters 2 and 3 demonstrated that moisture mode instability exists in at least two models with quite different parameterizations. Of course, finding a mode in different theoretical models does not guarantee that such a mode exists in nature. Moreover, one might discredit the result from QTCM since the use of a linear Betts-Miller scheme for humidity lacks a physical basis. Nevertheless, the case for moisture mode instability is stronger.

Chapter 4

Moistures modes in the quasi-equilibrium tropical circulation model with boundary layer

4.1 Introduction

Preceding chapters identified moisture mode instability and its nonlinear saturation in the quasi-equilibrium tropical circulation model (QTCM) of Neelin and Zeng (2000) and the subcloud-layer quasi-equilibrium model (SLQEM) of Bony and Emanuel (2005). The moisture mode is a mode with predominance of humidity anomaly, and is unstable if moist static energy sources like cloud radiative forcing and evaporation exceed its export. The weak temperature gradient (WTG) approximation of Sobel and Bretherton (2000) and Sobel et al. (2001) describes the behavior of the mode well, which has been confirmed by perturbation expansions.

One issue with the finding of Chapter 2 is that QTCM has only one humidity variable and fails to distinguish between the free troposphere and boundary layer. Chapter 3 explored moisture mode instability in the SLQEM, which separates the free-tropospheric moist entropy from the one in the boundary layer. The physical characteristics of moisture mode are similar to those found in SLQEM.

This chapter analyzes yet another model, QTCM with the boundary layer developed by Sobel and Neelin (2006). Almost physically identical results are obtained for the QTCM with and without boundary layer. Because of the similarities of the convective parameterization between QTCMs with and without the boundary layer, the finding here may not be surprising. Nonetheless, the conclusion of this chapter makes the case for moisture mode instability even stronger.

4.2 QTCM with boundary layer

As described in Chapter 2, the original QTCM is an intermediate complexity model of the tropical atmosphere, and is capable of reproducing a realistic tropical climate. With the quasi-equilibrium assumption, it applies a Galerkin expansion and retains the barotropic and baroclinic modes. Sobel and Neelin (2006) added the boundary layer to the QTCM model, and a simplified version of their model serves as a primary tool of this chapter. The derivation of the model is omitted here. Chapter 2 sketches out the derivation for QTCM to illustrate the concept behind QTCM.

Though the purpose of Sobel and Neelin (2006) was to understand the role of boundary-layer dynamics (e.g., low-level convergence), the present chapter neglects such dynamical effects. This is because the present chapter assumes a uniform sea-surface temperature (SST), eliminating the background pressure gradient in the boundary layer, whereas Sobel and Neelin assumed a meridionally varying SST. Nevertheless, the dynamical influence might be important in actuality (see Wang and Rui 1990, for instance) and this is left to future research. The neglect of the boundary-layer dynamics results in a system similar to that of Neggers et al. (2007), who augmented QTCM with a boundary-layer humidity variable without introducing a dynamically active boundary layer.

Since the boundary-layer dry static energy s_b does not drive dynamics here, there is no need to retain a separate equation for s_b; only the equation for boundary-layer moist static energy (MSE) h_b, which is a sum of s_b and boundary-layer specific humidity q_b, is needed. For simplicity, I neglect perturbation radiative cooling in the boundary layer, following

previous works (e.g., Yano and Emanuel 1991). Also fluctuations in the sensible heat flux are ignored because they are generally small.

To streamline the argument, I also set the perturbation of s_b to zero, which makes it easier to obtain one of the key relations emphasized repeatedly: precipitation anomaly P' is proportional to precipitable water anomaly W' (e.g., Bretherton et al. 2004). It is important to notice, however, that setting $s_b' = 0$ does not affect the quantitative results of the linear analysis and the qualitative nonlinear behavior.

Under the presumptions stated above, the model variables are expanded as a sum of the reference states that represent the radiative-convective equilibrium (RCE), and perturbations around it. The RCE solution is described in the appendix. For the troposphere, $p_T \leq p < p_B$, I have,

$$\mathbf{v}(x,y,p,t) = V_1(p)\mathbf{v}_1(x,y,t), \tag{4.1}$$

$$T(x,y,p,t) = T_r(p) + a_1(p)T_1(x,y,t), \tag{4.2}$$

$$q(x,y,p,t) = q_r(p) + b_1(p)q_1(x,y,t), \tag{4.3}$$

and for the boundary layer $p > p_B$,

$$s(x,y,p,t) = s_{rb}, \tag{4.4}$$

$$q(x,y,p,t) = q_{rb} + q_b(x,y,t), \tag{4.5}$$

where $\mathbf{v}$ is horizontal wind, T is temperature, s is dry static energy, and q is specific humidity. a_1, b_1, and V_1 represent basis functions for temperature, humidity, and baroclinic horizontal wind, respectively. The subscript r denotes the reference RCE state, and b the boundary layer. Note that all the thermodynamic variables are in energy units; T here actually denotes c_pT and q implies L_vq, where c_p is the specific heat at constant pressure and L_v is the latent heat of vaporization. Table 4.1 lists the parameters utilized in this chapter.

I consider a zonal channel without meridional variation or rotation, which yields a system of equations analogous to that for a Kelvin-like mode, except that the present formu-

Table 4.1: List of parameters. The stability parameters are different from those from Sobel and Neelin (2006). The convective timescale is expressed in terms of the QTCM equivalent number.

Parameter	Symbol	Reference value
Rayleigh damping timescale	τ_m	30 d
Newtonian cooling timescale	τ_R	30 d
Convective timescale (QTCM equivalent)	τ_c	12 h
Ratio of gas constant to specific heat at constant pressure	$\kappa = R_d/c_p$	287/1004
Acceleration due to gravity	g	9.8 m/s^2
Tropospheric average of temperature basis function	$\hat{a}_1 = \langle a_1 \rangle^F$	0.4243
Tropospheric average of humidity basis function	$\hat{b}_1 = \langle b_1 \rangle^F$	0.2406
Static stability	$\overline{M}_{s1}$	3500 J/kg
Gross moist stratification	$\overline{M}_{q1}$	3010 J/kg
Cloud-radiation interaction parameter	r	0.17
Gustiness parameter	c_s	0.048
WISHE parameter	c_u	0.0049
Depth of free troposphere in pressure	Δp_F	700 hPa
Depth of boundary layer in pressure	Δp_B	100 hPa
Pressure level of the tropopause	p_T	200 hPa
Pressure level of the top of the boundary layer	p_B	900 hPa
Air density at surface	ρ_a	1.2 kg/m^3
Enthalpy transfer coefficient	C_E	$1.2 \cdot 10^{-3}$
Specific heat of dry air at constant pressure	c_p	1004 J/kg/K
Latent heat of vaporization of water	L_v	$2.43 \cdot 10^6$ J/kg

lation lacks the meridional structure equation. By denoting perturbations by primes, one may write the linear equations for the QTCM with boundary layer in the reference frame with the mean flow as follows.

$$\frac{\partial u_1'}{\partial t} = -\kappa\frac{\partial T_1'}{\partial x} - \frac{u_1'}{\tau_m}, \tag{4.6}$$

$$\hat{a}_1\frac{\partial T_1'}{\partial t} + \overline{M}_{s1}\frac{\partial u_1'}{\partial x} = \left\langle Q_c' \right\rangle^F - \hat{a}_1\frac{T_1'}{\tau_R} + \left\langle Q_{R,cld}' \right\rangle^F, \tag{4.7}$$

$$\hat{b}_1\frac{\partial q_1'}{\partial t} - \overline{M}_{q1}\frac{\partial u_1'}{\partial x} = \left\langle Q_q' \right\rangle^F, \tag{4.8}$$

$$\frac{\partial q_b'}{\partial t} = \frac{E'}{\Delta p_B/g} + \left\langle Q_q' \right\rangle^B. \tag{4.9}$$

Here κ is the ratio of gas constant of dry air to its specific heat at constant pressure ($\kappa = R_d/c_p$), $\overline{M}_{s1}$ is the static stability, $\overline{M}_{q1}$ is gross moisture stratification, τ_m and τ_R are Rayleigh damping and Newtonian cooling timescales, Q_c is convecting heating, Q_q is convective drying, Q_R,cloud is cloud radiative forcing, E is evaporation, Δp_B is the depth of the boundary layer, g is the acceleration due to gravity, $\langle \quad \rangle^F$ and $\langle \quad \rangle^B$ represent the vertical averages for the troposphere and boundary layer, respectively, and $\hat{a}_1 \equiv \langle a_1 \rangle^F$, $\hat{b}_1 \equiv \langle b_1 \rangle^F$.

For an equatorial β-plane, the above set should be augmented by a meridional structure equation (y-momentum equation), but this is neglected here.

As in Chapter 2, the QTCM with boundary layer utilizes a linear variant of the Betts-Miller parameterization. Taking $h_b' = q_b'$, I can write the convective source terms as

$$\left\langle Q_c' \right\rangle^F = \frac{\varepsilon_c \hat{a}_1}{F}\left[\frac{\Delta p_B}{\Delta p_F}q_b' - \left(\frac{\Delta p_B}{\Delta p_F} + \hat{b}_1\right)T_1' + \hat{b}_1 q_1'\right], \tag{4.10}$$

$$\left\langle Q_q' \right\rangle^F = \frac{\varepsilon_c \hat{b}_1}{F}\left[\frac{\Delta p_B}{\Delta p_F}q_b' + \hat{a}_1 T_1' - \left(\frac{\Delta p_B}{\Delta p_F} + \hat{a}_1\right)q_1'\right], \tag{4.11}$$

$$\left\langle Q_q' \right\rangle^B = \frac{\varepsilon_c}{F}\left[-(\hat{a}_1 + \hat{b}_1)q_b' + \hat{a}_1 T_1' + \hat{b}_1 q_1'\right], \tag{4.12}$$

where $F \equiv \Delta p_B/\Delta p_F + \hat{a}_1 + \hat{b}_1$ and I have set $\langle Q_c' \rangle^B = 0$ to be consistent with the assumption of $s_b' = 0$. (By the same token, σ, the partitioning coefficient of the downdraft between dry static energy and humidity, is set to unity, which allows me to neglect σ below.) The

convective switch parameter is defined as

$$\varepsilon_c = \frac{1}{\tau_c} H(P), \tag{4.13}$$

where τ_c is the convective timescale and H is the Heaviside step function. Here P is total precipitation, a sum of the mean and perturbation precipitation:

$$P = \overline{P} + P' = \frac{\Delta p_F}{g} \left\langle \overline{Q}_c \right\rangle^F + \frac{\Delta p_B}{g} \left\langle \overline{Q}_q \right\rangle^B + \frac{\Delta p_F}{g} \left\langle Q_c' \right\rangle^F, \tag{4.14}$$

where the overbar denotes the mean. While the original formulation by Sobel and Neelin (2006) includes the effect of shallow convection, such effects are ignored here since the primary focus of this chapter is the situation where deep convection is taking place.

Just like the QTCM counterpart, this scheme is prone to the criticism that there is no universal reference profile for humidity. However, another interpretation of this convective closure is possible, at least for perturbation precipitation. Let us write the perturbation precipitation as

$$P' = \frac{\Delta p_F}{g} \left\langle Q_c' \right\rangle^F = \frac{\varepsilon_c \hat{a}_1}{F} \left(W' - \frac{\Delta p_B + \Delta p_F \hat{b}_1}{g} T_1' \right), \tag{4.15}$$

where $W' \equiv (\Delta p_F \hat{b}_1 q_1' + \Delta p_B q_b')/g$ is a perturbation precipitable water. As Chapter 2 argued, such a form can be thought of as a crude fit to the observed relationship between column relative humidity and precipitation. Strictly speaking, one has to carefully choose the coefficient for temperature, but this issue becomes minor for a disturbance under WTG, the primary subject in the present chapter.

Following Chapter 2, I would like to take the convective timescale to be 12 h, which is longer than the standard value of 7.2 h in Sobel and Neelin (2006). The long value is supported by the observational analyses by Bretherton et al. (2004), Biasutti et al. (2006), and Peters and Neelin (2006). However, choosing an appropriate number for τ_c demands careful thinking. It is imperative to recall that the convective timescale in QTCM has been rescaled by some constant. One therefore has to obtain a proper rescaling for the present

model as well. For the QTCM with boundary layer, precipitation becomes, under the WTG approximation,

$$P' = \frac{\hat{a}_1}{F}\frac{W'}{\tau_c}. \tag{4.16}$$

On the other hand, rainfall in QTCM is

$$P' = \frac{W'}{\hat{b}_1^{(\mathrm{QTCM})}\tau_c^{(\mathrm{QTCM})}}, \tag{4.17}$$

where the superscript (QTCM) denotes parameter values for QTCM. Naturally it is necessary to rescale the convective timescale as

$$\tau_c = \frac{\hat{a}_1\hat{b}_1^{(\mathrm{QTCM})}}{F}\tau_c^{(\mathrm{QTCM})}. \tag{4.18}$$

Here I take $\tau_c^{(\mathrm{QTCM})} = 12\mathrm{h}$.

As in Chapter 2, cloud-radiation interaction is parameterized as

$$\left\langle Q'_{R,cld}\right\rangle^F = r\left\langle Q'_c\right\rangle^F, \tag{4.19}$$

with a reference value of $r = 0.17$. Likewise, evaporation is expressed using a bulk formula:

$$E = \rho_a C_E V_s(q_s^* - q_{rb} - q_b) = \rho_a C_E\sqrt{(U + V_1(p_b)u'_1)^2 + v_g^2}(q_s^* - q_{rb} - q_b), \tag{4.20}$$

where ρ_a is the density of air at the surface, C_E is the enthalpy exchange coefficient, V_s is the surface wind speed, q_s^* is the saturation specific humidity at the surface, q_{rb} is the reference surface specific humidity, U is the mean surface wind and v_g is the gustiness that is driven by deep convection. As in Chapter 2, I explicitly include downdraft-enhanced gustiness. The gustiness parameterization follows that of Redelsperger et al.'s (2000); see Eq. (2.34) in Chapter 2.

Notice that including the WISHE (wind-induced surface heat exchange) effect ($V_1(p_b)u'_1$ term in the square root of Eq. (4.20)) gives rise to inconsistency in the model since the present QTCM should have a separate velocity for the boundary layer. That is,

the wind at the top of the boundary layer should be different from the surface wind. The effect is nevertheless included for the purpose of exploring potential effect of WISHE.

Evaporation therefore linearizes to

$$\frac{E'}{\Delta p_B/g} = -\frac{q_b'}{\tau_E} + c_s \frac{P'}{\Delta p_B/g} + c_u u_1' \tag{4.21}$$

where

$$\frac{1}{\tau_E} \equiv \frac{\rho_a C_E \overline{V}_s}{\Delta p_B/g}, \tag{4.22}$$

$$c_s = \overline{E}\frac{\overline{v}_g}{\overline{V}_s^2}\frac{0.669 - 0.00952\overline{\tilde{P}}}{1 + 0.669\overline{\tilde{P}} - 0.00476\overline{\tilde{P}}^2}\frac{86400}{L_v}, \tag{4.23}$$

$$c_h = \frac{\overline{E}}{\Delta p_B/g}\frac{U}{\overline{V}_s^2}V_1(p_b), \tag{4.24}$$

where $\tilde{P}$ is precipitation in mm/day; compare this with P, which is in W/m^2. Note the plus sign of c_u since the sign of u_1 represents the direction of winds in the upper troposphere.

4.3 Nondimensionalization

Following Chapter 2, I nondimensionalize the system by scaling variables as follows.

$$(t, \tau_c, \tau_m, \tau_R, \tau_E) = \mu(\tilde{t}, 1/\tilde{\varepsilon}_c, \tilde{\tau}_m, \tilde{\tau}_R, \tilde{\tau}_E), \tag{4.25}$$

$$x = \mu c_{dry}\tilde{x}, \tag{4.26}$$

$$u_1' = c_{dry}\tilde{u}, \tag{4.27}$$

$$(T_1', q_1', q_b', \overline{M}_{s1}, \overline{M}_{q1}) = \frac{c_{dry}^2}{\kappa}(\tilde{T}, \tilde{q}_1, \tilde{q}_b, \hat{a}_1, \hat{b}_1\tilde{M}_q), \tag{4.28}$$

$$c_u = \frac{c_{dry}}{\mu\kappa}\tilde{c}_u. \tag{4.29}$$

Here c_{dry} is the dry gravity wave phase speed $c_{dry} = \sqrt{\kappa\overline{M}_{s1}/\hat{a}_1}$, and μ is a characteristic timescale, which is taken such that the nondimensional growth rate is on the order of unity:

$\tilde{\sigma} \sim 1$. Also the parameters below facilitate algebraic manipulation.

$$\tilde{c}_s \equiv c_s \frac{\Delta p_B}{\Delta p_F} \hat{a}_1, \tag{4.30}$$

$$(\tilde{\varepsilon}_{c1}, \tilde{\varepsilon}_{c2}, \tilde{\varepsilon}_{c3}) \equiv \frac{\tilde{\varepsilon}_c}{F} \left(\frac{\Delta p_B}{\Delta p_F}, \hat{b}_1, \hat{a}_1 \right). \tag{4.31}$$

Upon substitution of diagnostic equations and with nondimensionalization above, Eqs. (4.6), (4.7), (4.8), and (4.9) simplify to

$$\frac{\partial \tilde{u}}{\partial \tilde{t}} = -\frac{\partial \tilde{T}}{\partial \tilde{x}} - \frac{\tilde{u}}{\tilde{\tau}_m},, \tag{4.32}$$

$$\frac{\partial \tilde{T}}{\partial \tilde{t}} + \frac{\partial \tilde{u}}{\partial \tilde{x}} = (1+r)\left[\tilde{\varepsilon}_{c1}\tilde{q}_b + \tilde{\varepsilon}_{c2}\tilde{q}_1 - (\tilde{\varepsilon}_{c1} + \tilde{\varepsilon}_{c2})\tilde{T}\right] - \frac{\tilde{T}}{\tilde{\tau}_R},, \tag{4.33}$$

$$\frac{\partial \tilde{q}_1}{\partial \tilde{t}} - \tilde{M}_q \frac{\partial \tilde{u}}{\partial \tilde{x}} = \tilde{\varepsilon}_{c1}\tilde{q}_b + \tilde{\varepsilon}_{c3}\tilde{T} - (\tilde{\varepsilon}_{c1} + \tilde{\varepsilon}_{c3})\tilde{q}_1,, \tag{4.34}$$

$$\begin{aligned} \frac{\partial \tilde{q}_b}{\partial \tilde{t}} = & -\frac{\tilde{q}_b}{\tilde{\tau}_E} + \tilde{c}_s\left[\tilde{\varepsilon}_{c1}\tilde{q}_b + \tilde{\varepsilon}_{c2}\tilde{q}_1 - (\tilde{\varepsilon}_{c1} + \tilde{\varepsilon}_{c2})\tilde{T}\right] + \tilde{c}_u\tilde{u} \\ & -(\tilde{\varepsilon}_{c2} + \tilde{\varepsilon}_{c3})\tilde{q}_b + \tilde{\varepsilon}_{c3}\tilde{T} + \tilde{\varepsilon}_{c2}\tilde{q}_1. \end{aligned} \tag{4.35}$$

4.4 Linear analysis

Assuming an exponential form of solution $\sim \exp(\tilde{\sigma}\tilde{t} + i\tilde{k}\tilde{x})$ allows me to write the linearized wave equation concisely as

$$\mathsf{A}\mathbf{x} = \tilde{\sigma}\mathbf{x}, \tag{4.36}$$

where $\mathbf{x} = (\tilde{u}, \tilde{T}, \tilde{q}_1, \tilde{q}_b)^T$. The coefficient matrix A is

$$A_{11} = -1/\tilde{\tau}_m, \tag{4.37}$$

$$A_{12} = -i\tilde{k}, \tag{4.38}$$

$$A_{13} = 0, \tag{4.39}$$

$$A_{14} = 0, \tag{4.40}$$

$$A_{21} = -i\tilde{k}, \tag{4.41}$$

$$A_{22} = -(1+r)(\tilde{\varepsilon}_{c1} + \tilde{\varepsilon}_{c2}) - 1/\tilde{\tau}_R, \tag{4.42}$$

$$A_{23} = (1+r)\tilde{\varepsilon}_{c2}, \tag{4.43}$$

$$A_{24} = (1+r)\tilde{\varepsilon}_{c1}, \tag{4.44}$$

$$A_{31} = \tilde{M}_q i\tilde{k}, \tag{4.45}$$

$$A_{32} = \tilde{\varepsilon}_{c3}, \tag{4.46}$$

$$A_{33} = -\tilde{\varepsilon}_{c1} - \tilde{\varepsilon}_{c3}, \tag{4.47}$$

$$A_{34} = \tilde{\varepsilon}_{c1}, \tag{4.48}$$

$$A_{41} = \tilde{c}_u, \tag{4.49}$$

$$A_{42} = \tilde{\varepsilon}_{c3} - \tilde{c}_s(\tilde{\varepsilon}_{c1} + \tilde{\varepsilon}_{c2}), \tag{4.50}$$

$$A_{43} = (1+\tilde{c}_s)\tilde{\varepsilon}_{c2}, \tag{4.51}$$

$$A_{44} = -1/\tilde{\tau}_E + \tilde{c}_s\tilde{\varepsilon}_{c1} - (\tilde{\varepsilon}_{c2} + \tilde{\varepsilon}_{c3}). \tag{4.52}$$

The growth rate is Re $\tilde{\sigma}$, and the phase speed is $-$Im $\tilde{\sigma}/\tilde{k}$. Were I dealing with the equatorial β-plane, the boundedness at infinity implied a non-negative phase speed, Im$\tilde{\sigma} < 0$; this is not applied here, however.

Figure 4-1 describes growth rates and phase speeds of linear modes as a function of planetary wavenumber n in the absence of WISHE, whereas Figure 4-2 shows the same plot with WISHE. The circumference of the equator is taken to be 40000 km. There are two gravity waves, which asymptote to dry gravity waves at the small-scale limit, and two moisture modes, whose dynamics can be described by the WTG approximation, as discussed below. Compared with Chapter 2, the model in this chapter shows similar characteristics, except that there are two moisture modes because of the two prognostic humidity variables.

For the case without WISHE, the only unstable wave is stationary relative to the mean flow and its growth rate is rather insensitive to wavenumber. Cloud-radiation interaction and gustiness fail to destabilize gravity waves, as was found by Fuchs and Raymond (2002, 2005). Including linear WISHE increases the growth rate of the slow moisture wave for large waves, and allows it to propagate eastward. But WISHE fails to destabilize gravity waves as well. These findings are in line with those of Fuchs and Raymond.

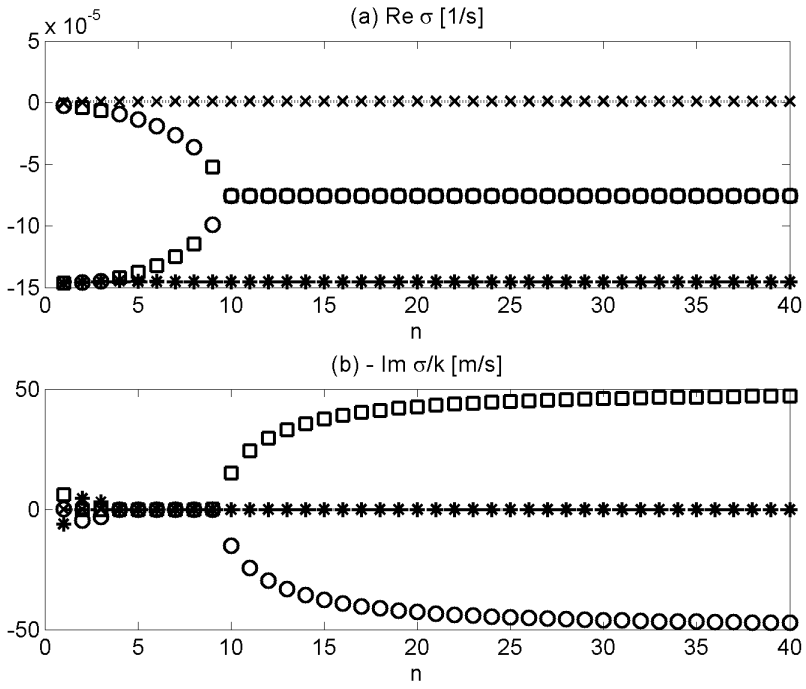

Figure 4-1: (a) growth rates [1/day] and (b) phase speeds [m/s] of linear modes in the absence of WISHE. The condition of boundedness at infinity is not applied, and therefore this figure shows all of the four eigenvalues in the linear problem. The horizontal axis is the planetary wavenumber, n, where $k = 2\pi n/L_x$ and $L_x = 40,000$km. Crosses and asterisks denote growing and decaying moisture modes, respectively. Dotted and solid lines represent the WTG solutions

In addition to the full solutions from the linear problem, I have plotted the WTG solutions in Figures 4-1 and 4-2. Consistent with Chapters 2 and 3, the WTG solutions accurately capture both the growth rate and phase speed of the moisture mode, especially at the small scale. Figure 4-3 focuses on the unstable moisture mode. The WTG solutions and the full growth rates and phase speeds are indistinguishable for $n >\sim 20$. But it is also true that the WTG solutions are not *quantitatively* accurate at the large scale. Since the WTG scaling applies to virtually any wavelength possible (see below), the difference between the full solution and the WTG solution indicates that higher order effects do influence the growth rates and phase speeds at the large scale.

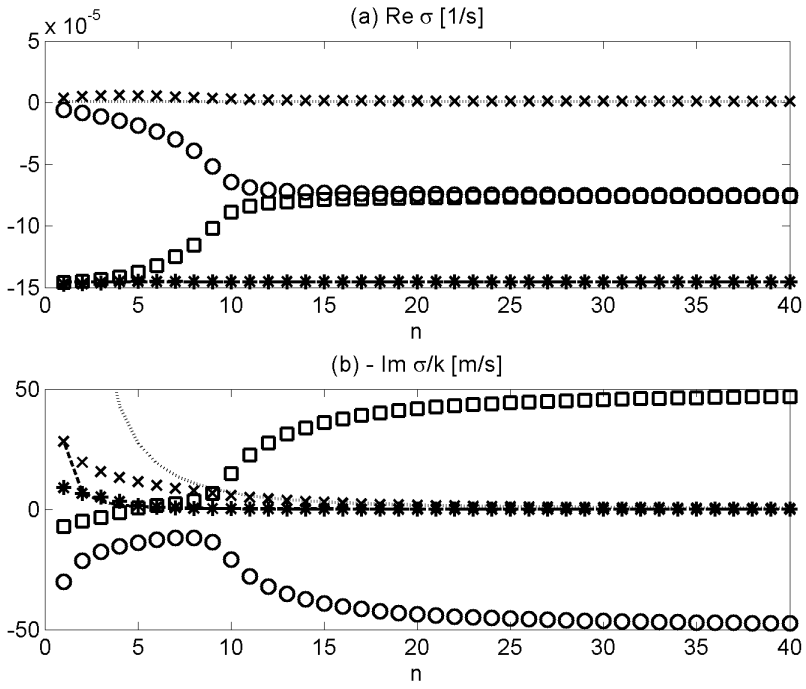

Figure 4-2: As in Figure 1 but with WISHE.

4.5 WTG analysis

4.5.1 Mathematical derivation of WTG

As in Chapters 2 and 3, Figures 4-1, 4-2, and 4-3 indicate that the WTG approximation describes the behavior of moisture modes in the present case. Below I develop a systematic method to derive the WTG solution for QTCM with boundary layer, extending the analyses of Chapters 2 and 3.

The WTG approximation is valid if the primary balance in the temperature equation is between adiabatic cooling and diabatic heating. Mathematically one can express the condition as

$$G \equiv \left| \left(\hat{a}_1 \frac{\partial T_1'}{\partial t} \right) \Big/ \left(\overline{M}_{s1} \frac{\partial u_1'}{\partial x} \right) \right| = \left| \frac{\tilde{\sigma}(\tilde{\sigma} + 1/\tilde{\tau}_m)}{\tilde{k}^2} \right| \ll 1. \tag{4.53}$$

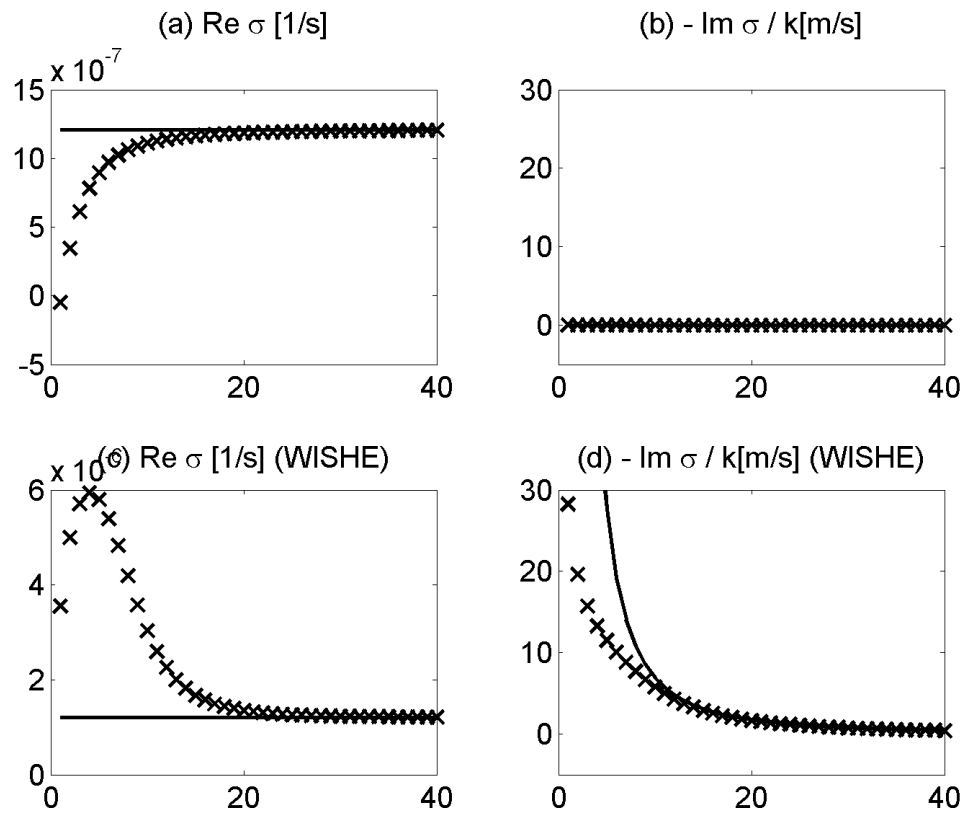

Figure 4-3: (a) Growth rates [1/day] and (b) phase speeds [m/s] for the unstable moisture mode without WISHE. (c) and (d) are the same as (a) and (b), respectively, but with WISHE included. The modes presented here correspond to crosses in Figures 1 and 2. Solid lines represent the WTG solutions.

Noting that $\tilde{\sigma} \sim 1$, the above condition may be rewritten as

$$\frac{1}{\tilde{k}^2} \ll 1, \tag{4.54}$$

which is the same scaling for QTCM (Eq. (2.68) of Chapter 2). (4.54) is satisfied if the characteristic zonal scale is smaller than the distance the gravity wave can travel for a characteristic timescale. Note that my repeated analyses show that the WTG scaling is determined by the momentum and temperature equations only and does not appear to be directly affected by convective parameterization.

I now expand the growth rate and each prognostic variable as

$$(\tilde{\sigma}, \tilde{u}, \tilde{T}, \tilde{q}_1, \tilde{q}_b) = \sum_{n=0}^{\infty} \frac{1}{\tilde{k}^n} (\tilde{\sigma}^{(n)}, \tilde{u}^{(n)}, \tilde{T}^{(n)}, \tilde{q}_1^{(n)}, \tilde{q}_b^{(n)}). \tag{4.55}$$

Equating the same powers on each side of Eqs. (4.32), (4.33), (4.34), and (4.35), a straightforward algebra gives

$$\begin{pmatrix} \tilde{u} \\ \tilde{T} \\ \tilde{q}_1 \\ \tilde{q}_b \end{pmatrix} = \begin{pmatrix} 0 \\ 0 \\ \tilde{q}_1^{(0)} \\ \tilde{q}_b^{(0)} \end{pmatrix} + \frac{1}{\tilde{k}} \begin{pmatrix} \tilde{u}^{(1)} \\ 0 \\ \tilde{q}_1^{(1)} \\ \tilde{q}_b^{(1)} \end{pmatrix} + \frac{1}{\tilde{k}^2} \begin{pmatrix} \tilde{u}^{(2)} \\ \tilde{T}^{(2)} \\ \tilde{q}_1^{(2)} \\ \tilde{q}_b^{(2)} \end{pmatrix} + O(\tilde{k}^{-3}). \tag{4.56}$$

The tropospheric and boundary-layer humidity variables are zeroth-order whereas temperature is second-order, which again justifies calling this mode a moisture mode under WTG.

Expanding $\tilde{\sigma}$ in the dispersion relationship leads to an approximate solution to the complex growth rate. However, it requires some manipulation. In matrix form, one may write the dispersion relation as

$$\begin{vmatrix} A_{11} - \tilde{\sigma} & A_{12} & 0 & 0 \\ A_{21} & A_{22} - \tilde{\sigma} & A_{23} & A_{24} \\ A_{31} & A_{32} & A_{33} - \tilde{\sigma} & A_{34} \\ A_{41} & A_{42} & A_{43} & A_{44} - \tilde{\sigma} \end{vmatrix} = 0. \tag{4.57}$$

Note that the only $O(\tilde{k})$ terms are $A_{12} = -i\tilde{k}, A_{21} = -i\tilde{k}, A_{31} = \tilde{M}_q i\tilde{k}$, which arises from the horizontal derivative. If we expand the determinant, we find $O(\tilde{k}^2)$ terms because of these three coefficients. For the purpose of the perturbation expansion, it is useful to have only $O(1)$ terms or higher order terms in $1/\tilde{k}$. Dividing through by $\tilde{k}^2$, I obtain

$$\begin{vmatrix} \frac{A_{11}}{\tilde{k}} - \frac{\tilde{\sigma}}{\tilde{k}} & -i & 0 & 0 \\ -i & \frac{A_{22}}{\tilde{k}} - \frac{\tilde{\sigma}}{\tilde{k}} & A_{23} & A_{24} \\ \tilde{M}_q i & \frac{A_{32}}{\tilde{k}} & A_{33} - \tilde{\sigma} & A_{34} \\ \frac{A_{41}}{\tilde{k}} & \frac{A_{42}}{\tilde{k}} & A_{43} & A_{44} - \tilde{\sigma} \end{vmatrix} = 0. \tag{4.58}$$

Now all the coefficients are $O(1)$, and this form is more amenable to perturbation expansion. Eq. (4.58) further simplifies to

$$0 = i \cdot \begin{vmatrix} -i & A_{23} & A_{24} \\ \tilde{M}_q & A_{33} - \tilde{\sigma} & A_{34} \\ \frac{A_{41}}{\tilde{k}} & A_{43} & A_{44} - \tilde{\sigma} \end{vmatrix} + O(\tilde{k}^{-2}). \tag{4.59}$$

Equating terms at the same order gives, for $O(1)$,

$$0 = [\tilde{\sigma}^{(0)}]^2 - (A_{33} + A_{44} + \tilde{M}_q A_{23})\tilde{\sigma}^{(0)} + A_{34}A_{43} - \tilde{M}_q(A_{24}A_{43} - A_{23}A_{44}), \tag{4.60}$$

and for $O(\tilde{k}^{-1})$,

$$\tilde{\sigma}^{(1)} = i\frac{\tilde{c}_u\left[A_{23}A_{34} - A_{24}(A_{33} - \tilde{\sigma}^{(0)})\right]}{A_{33} + A_{44} - 2\tilde{\sigma}^{(0)} + \tilde{M}_q A_{23}}. \tag{4.61}$$

Here I have used $A_{41} = \tilde{c}_u$. By examining the coefficients, I find that $\tilde{\sigma}^{(0)}$ is always real and represents the growth rate, whereas $\tilde{\sigma}^{(1)}$ is always imaginary and describes the phase speed. Moreover, the phase propagation is entirely due to WISHE for $\tilde{\sigma}^{(1)}$ is proportional to $\tilde{c}_u$. These are also confirmed below.

4.5.2 Physical interpretation of WTG

Now that the mathematical derivation of WTG is given, the next topic is the physical interpretation of WTG. Retaining terms up to $O(1)$ in the perturbation expansion is equivalent to dropping temperature and neglecting horizontal winds except for the convergence terms. Generally the WTG system may be written as, in dimensional form,

$$\overline{M}_{s1}\frac{\partial u_1'}{\partial x} = (1+r)\left\langle Q_c'\right\rangle^F, \tag{4.62}$$

$$\hat{b}_1\frac{\partial q_1'}{\partial t} = \overline{M}_{q1}\frac{\partial u_1'}{\partial x} + \left\langle Q_q'\right\rangle^F, \tag{4.63}$$

$$\frac{\partial q_b'}{\partial t} = \frac{E'}{\Delta p_B/g} + \left\langle Q_q'\right\rangle^B. \tag{4.64}$$

Here I have used the parameterization for cloud radiative forcing, but not for deep convection; Eqs. (4.62), (4.63), and (4.64) do not depend on the Betts-Miller closure. The number of prognostic variables is now two, but an even simpler expression can be obtained for precipitable water $W' \equiv (\Delta p_F \hat{b}_1 q_1' + \Delta p_B q_b')/g$, by substituting (4.62) into (4.63) and invoking the conservation of moist enthalpy $0 = \Delta p_F \left\langle Q_c'\right\rangle^F + \Delta p_F \left\langle Q_q'\right\rangle^F + \Delta p_B \left\langle Q_q'\right\rangle^F$:

$$\begin{aligned}\frac{\partial W'}{\partial t} &= \left(-\frac{\overline{M}_{s1}-\overline{M}_{q1}}{\overline{M}_{s1}} + \frac{\overline{M}_{q1}}{\overline{M}_{s1}}r + c_s\right)P' - \frac{\Delta p_B}{g}\frac{q_b'}{\tau_E} \\ &= \left(-\frac{\overline{M}_{s1}-\overline{M}_{q1}}{\overline{M}_{s1}} + \frac{\overline{M}_{q1}}{\overline{M}_{s1}}r + c_s\right)\frac{\varepsilon_c \hat{a}_1}{F}W' - \frac{\Delta p_B}{g}\frac{q_b'}{\tau_E}.\end{aligned} \tag{4.65}$$

The last step involves substituting the WTG version of (4.15), $P' = (\varepsilon_c \hat{a}_1/F)W'$. Also the WTG version of (4.21), $E' = -(\Delta p_B/g)q_b'/\tau_E + c_s P'$, has been used. Note that the relaxation term in evaporation is usually small. For example,

$$\left(\frac{F\tau_c}{\hat{a}_1\tau_E}\right) \Big/ \left(-\frac{\overline{M}_{s1}-\overline{M}_{q1}}{\overline{M}_{s1}} + \frac{\overline{M}_{q1}}{\overline{M}_{s1}}r + c_s\right) \sim 0.004 \tag{4.66}$$

for the parameters listed in Table 4.1. The growth rate is approximately

$$\sigma_{WTG} \approx \frac{\hat{a}_1}{F}\left(-\frac{M_{\text{eff}}}{\overline{M}_{s1}} + c_s\right)\frac{1}{\tau_c}, \tag{4.67}$$

where the subscript WTG is added to emphasize the approximation utilized. Here $M_{\text{eff}} \equiv M - r\overline{M}_{q1}$ is the effective gross moist stability that includes cloud radiative forcing (Su and Neelin 2002; Bretherton and Sobel 2002), and $M \equiv \overline{M}_{s1} - \overline{M}_{q1}$ is gross moist stability (Neelin and Held 1987). As shown below, neglecting the damping term in the simplified growth rate equation leads to an overestimate; nevertheless, the expression is helpful for physical understanding.

Eq. (4.65) concisely describes the physical mechanism, which is almost identical to Eqs. (2.88) and (2.89) of Chapter 2, although the results in Chapter 2 reflect more physical processes. The perturbation precipitable water, which is identical to vertically integrated MSE under the WTG approximation, decreases with MSE export through effective gross moist stability (which includes the effect of cloud-radiation interaction) and increases with gustiness (c_s), and decreases with decreasing evaporation (the last term in (4.65)). One would expect that instability would arise if cloud radiation interaction and gustiness overcompensate for the MSE export. Interestingly, the derivation here did not have to utilize a particular choice of convective parameterization until the second half of (4.65). This illustrates the importance of the relationship $P' \propto W'$ for moisture mode instability.

The dimensional WTG system heuristically derived here is equivalent to the nondimensional one, Eq. (4.60). Utilizing (4.62), I can rewrite ((4.63) and ((4.64) to obtain the eigenproblem:

$$\frac{\partial}{\partial t}\begin{pmatrix} q_1' \\ q_b' \end{pmatrix} = \sigma \begin{pmatrix} q_1' \\ q_b' \end{pmatrix} = \begin{pmatrix} C_{11} & C_{12} \\ C_{21} & C_{22} \end{pmatrix} \begin{pmatrix} q_1' \\ q_b' \end{pmatrix}, \tag{4.68}$$

where

$$C_{11} = \left(\frac{\overline{M}_{q1}}{\overline{M}_{s1}}(1+r)\hat{a}_1 - \frac{\Delta p_B}{\Delta p_F} - \hat{a}_1 \right) \frac{\varepsilon_c}{F}, \tag{4.69}$$

$$C_{12} = \left(\frac{\overline{M}_{q1}}{\overline{M}_{s1}}(1+r)\frac{\hat{a}_1}{\hat{b}_1} + 1 \right) \frac{\Delta p_B}{\Delta p_F}\frac{\varepsilon_c}{F}, \tag{4.70}$$

$$C_{21} = \left(c_s \frac{\Delta p_F}{\Delta p_B}\hat{a}_1 + 1 \right) \varepsilon_c \frac{\hat{b}_1}{F}, \tag{4.71}$$

$$C_{22} = -\frac{1}{\tau_E} + (c_s\hat{a}_1 - \hat{a}_1 - \hat{b}_1)\frac{\varepsilon_c}{F}. \tag{4.72}$$

The WTG dispersion is

$$\sigma_{WTG}^2 - (C_{11} + C_{22})\sigma_{WTG} + C_{11}C_{22} - C_{12}C_{21} = 0. \tag{4.73}$$

It is possible to show that this quadratic equation is equivalent to the equation for $\tilde{\sigma}^{(0)}$, Eq. (4.60).

The dimensional solution is

$$\sigma_{WTG} = \frac{C_{11} + C_{22} \pm \sqrt{(C_{11} + C_{22})^2 - 4(C_{11}C_{22} - C_{12}C_{21})}}{2} \tag{4.74}$$

$$\frac{C_{11} + C_{22} \pm \sqrt{(C_{11} - C_{22})^2 + C_{12}C_{21}}}{2} \tag{4.75}$$

It is clear that the WTG growth rate is always real in the absence of WISHE since C_{12} and C_{21} are positive constants.

As in Chapter 2, Eq. (4.60) indicates three important nondimensional parameters: r, c_s, and $\overline{M}_{q1}/\overline{M}_{s1}$. Also evident is that to the extent the evaporation relaxation term is negligible, the growth rate is inversely proportional to the convective timescale.

Figure 4-4 shows how the growth rate in the WTG limit changes when r, c_s, $\overline{M}_{q1}/\overline{M}_{s1}$, and τ_c are varied. As expected from (4.65) and (4.67), the growth rate increases with r, c_s, $\overline{M}_{q1}/\overline{M}_{s1}$, and $1/\tau_c$. The plus sign in each panel corresponds to the reference values in Table 4.1, for which the model is marginally unstable. Comparing Figure 4-4 in this chapter and Figure 2-8 in Chapter 2 shows that these are almost identical, which is not surprising given that Eq. (4.65) resembles Eqs. (2.88) and (2.89) of Chapter 2. Figure 4-5 exhibits the growth rate calculated from the simplified equation (4.67). Although the values are overestimated compared with those in Figure 4-4 because of the absence of the damping term, the simplified formula gives a rough approximation to the quadratic equation.

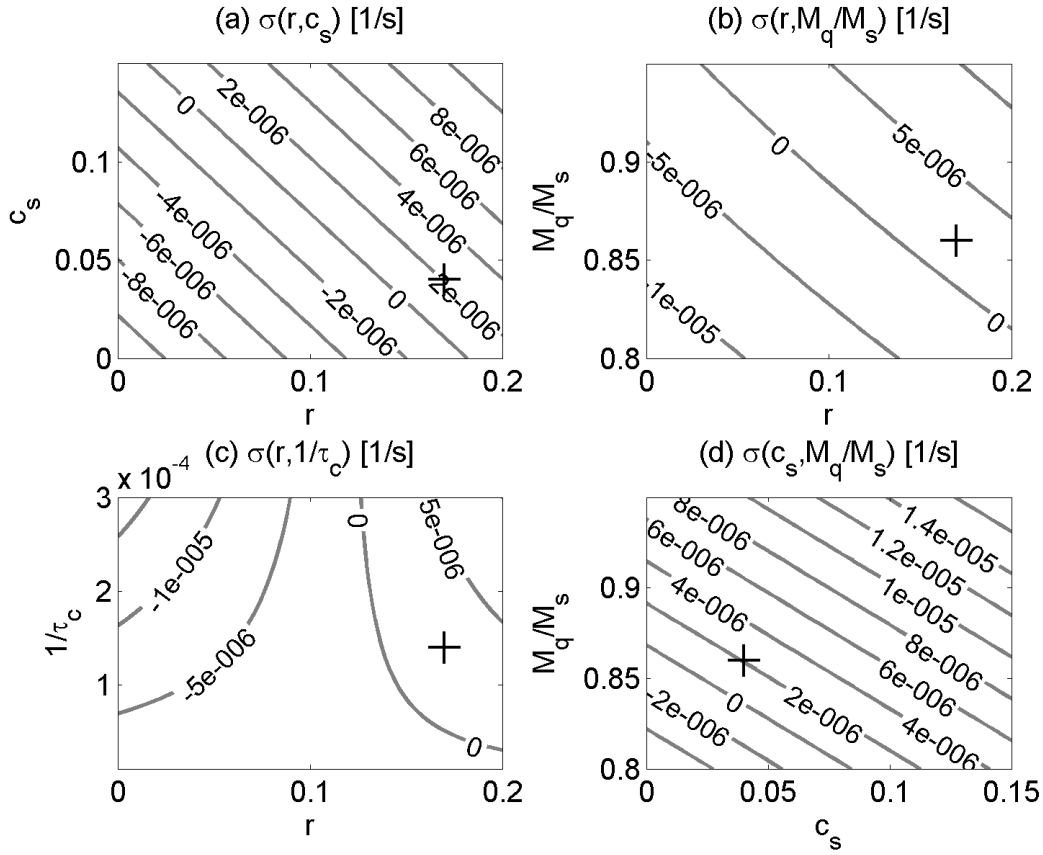

Figure 4-4: Growth rate as a function of (a) cloud-radiation interaction parameter r and gustiness parameter c_s; (b) r and a nondimensional gross moisture stratification, $\overline{M}_{q1}/\overline{M}_{s1}$; (c) r and the inverse convective timescale $1/\tau_c$; and (d) c_s and $\overline{M}_{q1}/\overline{M}_{s1}$. Other parameters are taken from Table 4.1. The convective timescale signifies the values after rescaling of Eq. (4.18). c_s here represents the parameter without tilde.

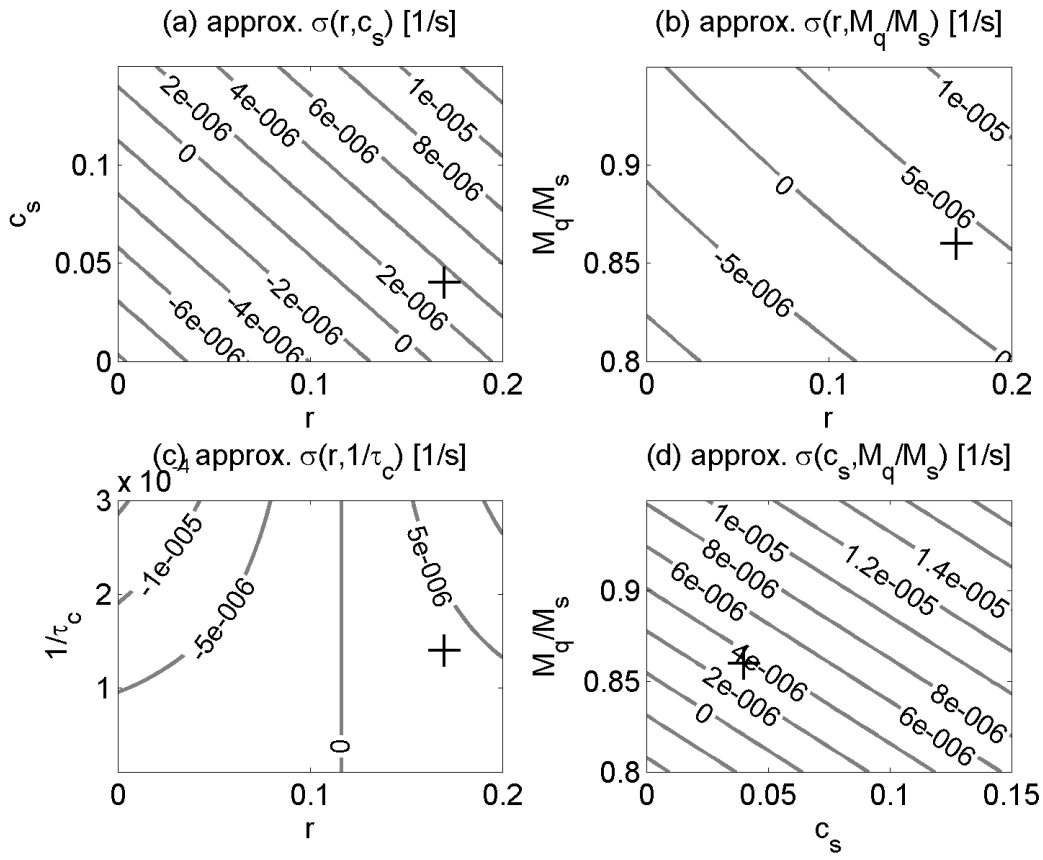

Figure 4-5: As in Figure 4-4 but for the approximate WTG growth rate, Eq. (4.67).

4.5.3 Nonlinear WTG

The simplicity of the WTG approximation motivates a more elaborate analysis, such as a nonlinear analysis. Nonlinearity in the governing equations here reside only in the convective switch and gustiness. To avoid complications, the following only considers the case with positive precipitation perturbation. The nonlinear WTG system thus consists of (4.62), (4.63), and (4.64), with nonlinearity retained in gustiness.

Figure 4-6 depicts the phase diagram of the WTG system. Figs. 4-6a and 4-6b describe the time tendencies of q_1' and q_b' as functions of q_1' and q_b'. Fig. 4-6c shows the two lines, $\partial_t q_1' = 0$ and $\partial_t q_b' = 0$, while Fig. 4-6d exhibits the difference between the two lines; more precisely, the difference of implicit functions of $q_b' = q_b'(q_1')$ for $\partial_t q_1' = 0$ and $\partial_t q_b' = 0$. As the difference between the two lines $\partial_t q_1' = 0$ and $\partial_t q_b' = 0$ shows, there are two fixed points: one corresponding to RCE and another to a nonlinearly saturated moisture mode. The moisture mode fixed point corresponds to $P = \sim 79$ mm/day.

Drawn in Fig. 4-7 is a schematic of the phase diagram, which describes the stability of the two fixed points (e.g., Strogatz 1994, chapter 6). For illustration purposes, the lines are distorted so that each fixed point can be readily examined. As indicated by the linear analysis, the RCE fixed point is unstable. On the other hand, the moisture mode fixed point is stable.

Since the RCE is unstable, what would happen if the initial perturbations were negative? If Fig. 4-6 is further extended in the directions of negative q_1' and q_b', one discovers a somewhat complicated structure in the phase diagram with multiple fixed points because of the nonlinear operator in the precipitation.

Since the only nonlinearity considered here is in the gustiness, the nonlinear saturation occurs as the gustiness curve flattens with increasing precipitation (Fig. 2-2 of Chapter 2). As I argued in Chapter 2, in a more realistic model, nonlinear saturation can result from changes in any of the following: gross moist stability, cloud-radiative forcing, and gustiness.

As with the linear analysis, the results here are sensitive to the choice of parameters. For instance, a slight change in parameters could drastically alter the phase diagram since

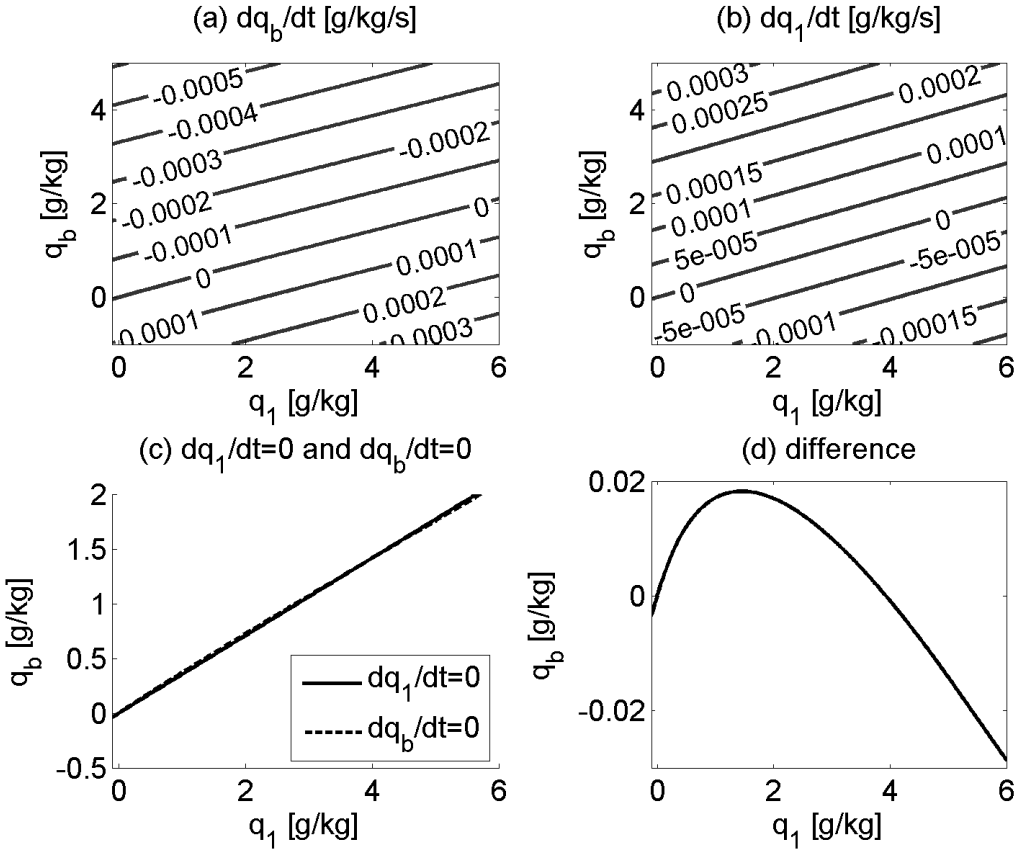

Figure 4-6: (a) $\partial_t q_b'(q_1', q_b')$. (b) $\partial_t q_1'(q_1', q_b')$. (c) Implicit functions of $q_b' = q_b'(q_1')$ for $\partial_t q_1' = 0$ and $\partial_t q_b' = 0$. (d) The difference between the two lines shown in (c).

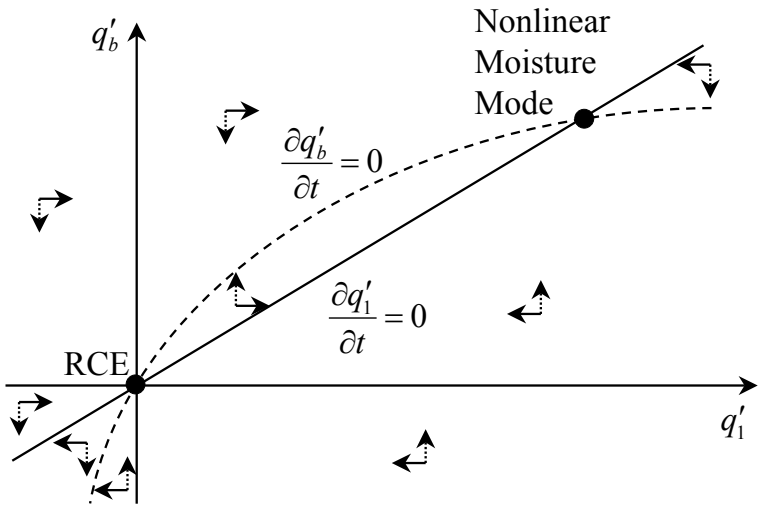

Figure 4-7: Schematic explaining the phase diagram depicted in Fig. 4-6c. This diagram is not to scale and the lines are distorted for illustration purposes. The solid line represents $\partial_t q'_b = 0$ and the dotted line $\partial_t q'_1 = 0$ Two filled circles correspond to the two fixed points: RCE (denoted by "RCE") and a nonlinearly saturated moisture mode (denoted by "Nonlinear Moisture Mode"). The RCE is unstable whereas the "Nonlinear Moisture Mode" fixed point is stable. The horizontal arrows denote whether $\partial_t q'_1$ is positive or negative (a rightward arrow indicates positive), and the vertical arrows indicate the sign of $\partial_t q'_b$ (an upward arrow indicates positive).

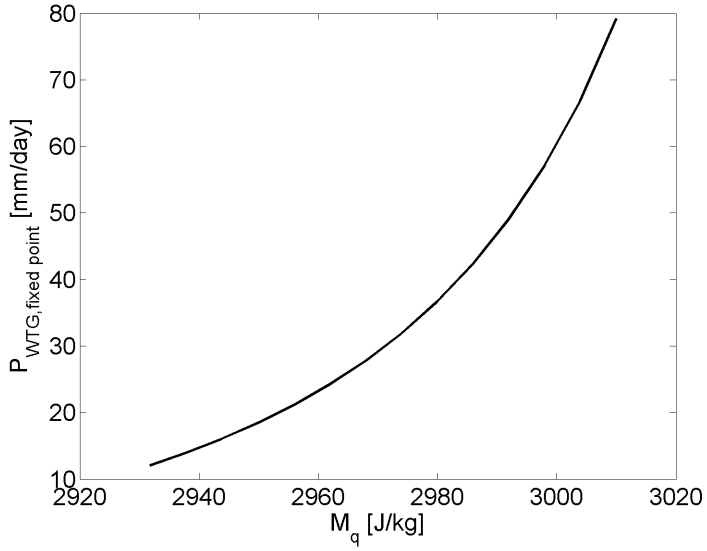

Figure 4-8: Precipitation (vertical axis in mm/day) at the fixed point of the nonlinearly saturated moisture mode as a function of gross moisture stratification (horizontal axis in J/kg).

the two lines representing $\partial_t q_1' = 0$ and $\partial_t q_b' = 0$ in Fig. 4-6 almost coincide with each other. (The fact that the two lines are close to each other does not negate the existence of fixed points, but it does indicate that the locations and even existence of fixed points are sensitive to variations in parameters.) Figure 4-8 shows how the precipitation rate for the nonlinearly saturated moisture mode changes when gross moisture stratification is varied. A slight variation in gross moisture stratification yields a large change in the precipitation rate.

4.6 Summary

Having examined QTCM with boundary layer, the present chapter gives further credence to moisture mode instability. Adding a separate boundary layer humidity variable to QTCM does not change the physical characteristics of the moisture mode significantly. In fact, QTCM with boundary layer yields an almost identical equation for perturbation precipitable water, and anomalous MSE increases because of enhanced MSE sources overcompensate for MSE export.

It is curious that moisture mode instability is found in all three models examined in this thesis. As noted above, in all three cases, the WTG scaling came from the momentum and temperature equations. It is then natural to ask what the more general conditions are for the existence of moisture mode instability. Chapter 7 discusses this point.

Thus far I have demonstrated that simple models have moisture modes whose dynamics can be described by the WTG approximation. But is it found in a more detailed model? The next chapter addresses this question.

Appendix: Radiative-convective equilibrium

Neglecting shallow convection, the RCE equations for QTCM with boundary layer are

$$\begin{aligned}
0 &= \hat{a}_1 \frac{\partial T_1}{\partial t} = \langle Q_c \rangle^F + \langle Q_R \rangle^F , && (4.76)\\
0 &= \hat{b}_1 \frac{\partial q_1}{\partial t} = \langle Q_q \rangle^F , && (4.77)\\
0 &= \frac{\partial s_b}{\partial t} = \frac{H}{\Delta p_B / g} + \langle Q_c \rangle^B + \langle Q_R \rangle^B , && (4.78)\\
0 &= \frac{\partial q_b}{\partial t} = \frac{E}{\Delta p_B / g} + \langle Q_q \rangle^B . && (4.79)\\
& && (4.80)
\end{aligned}$$

The convective scheme is similar to what is described in the body of the text, but here it includes the boundary-layer dry static energy:

$$\begin{aligned}
\delta h_b &= \frac{-(\hat{a}_1 + \hat{b}_1) h_b + \hat{a}_1 T_1 + \hat{b}_1 q_1}{\Delta p_B / \Delta p_F + \hat{a}_1 + \hat{b}_1}, && (4.81)\\
\langle Q_c \rangle^F &= \varepsilon_c \hat{a}_1 (h_b + \delta h_b - T_1), && (4.82)\\
\langle Q_q \rangle^F &= \varepsilon_c \hat{b}_1 (h_b + \delta h_b - q_1), && (4.83)\\
\langle Q_c \rangle^B &= \varepsilon_c \sigma \delta h_b, && (4.84)\\
\langle Q_q \rangle^B &= \varepsilon_c (1 - \sigma) \delta h_b . && (4.85)
\end{aligned}$$

Table 4.2: Inputs and outputs of the RCE calculation. Note that σ is different from 0.2, the value used by Sobel and Neelin (2006).

Parameter			
	Partitioning parameter for downdraft	σ	0.1
Forcing			
	Sea surface temperature	T_s	29.5°C
	Clear-sky radiative cooling	$\langle Q_{R,clear} \rangle^F$	130 W/m^2
		$\langle Q_{R,clear} \rangle^B$	10 W/m2
	Mean wind or background gustiness	$-U$ or v_{bg}	4 m/s
Outputs			
	Surface air temperature	$(s_{rb} + \overline{s}_b)/c_p$	26.3 ° C
	Surface specific humidity	$(q_{rb} + \overline{q}_b)/L_v$	18.6 g/kg
	Surface relative humidity	$(q_{rb} + \overline{q}_b)/q_s^*$	72.5 %
	Precipitation/evaporation	$\overline{P} = \overline{E}$	3.67 mm/day = 103.1 W/m^2
	Sensible heat flux	$\overline{H}$	19.3 W/m^2
	Surface wind speed	$\overline{V}_s$	4.18 m/s
	Downdraft-driven gust	$v_g(\overline{P})$	1.22 m/s

Here σ is taken to be 0.1, rather 0.2, the value used by Sobel and Neelin (2006). The radiative terms are written as

$$\langle Q_R \rangle^i = \langle Q_{R,clear} \rangle^i + + \langle Q_{R,cld} \rangle^i, \tag{4.86}$$

$$\langle Q_{R,cld} \rangle^i = r \frac{\Delta p_F \langle Q_c \rangle^F + \Delta p_B \langle Q_c \rangle^B}{\Delta p_F + \Delta p_B}, \tag{4.87}$$

for $i = F, B$, so that

$$\Delta p_F \langle Q_{R,cld} \rangle^F + \Delta p_B \langle Q_{R,cld} \rangle^B = r \left(\Delta p_F \langle Q_c \rangle^F + \Delta p_B \langle Q_c \rangle^B \right). \tag{4.88}$$

The clear-sky components $\langle Q_{R,clear} \rangle^i$ are prescribed. Other diagnostic variables follow the definitions given in the main text.

Table 4.2 shows the input parameters and output values of the radiative-convective equilibrium calculation. The results here are comparable to what is shown in Chapter 2.

Chapter 5

Moisture modes in a single-column model

5.1 Introduction

Previous chapters have shown that radiative-convective equilibrium (RCE) may be unstable to moisture mode instability, and that the weak temperature gradient (WTG) approximation describes the asymptotic behavior of the moisture mode at the small scale. However, these analyses relied on theoretical models and assumed a fixed gross moist stability, to which the moisture mode instability is sensitive. It remains to be seen whether relaxing these assumptions would suppress moisture mode instability.

In order to address this issue, this chapter performs numerical runs of the single-column model (SCM) developed by Rennó et al. (1994), Emanuel and Živković-Rothman (1999), and Bony and Emanuel (2001). It exploits the equivalence in formulation between the WTG equation of theoretical models and the SCM under the WTG configuration. If the prediction from theoretical models were correct, we would expect to see moisture mode instability in an SCM and its nonlinear saturation.

In addition to confirming the prediction of previous chapters, there is another motivation for this chapter. There are already some modeling studies on moisture mode instability, but the results are mixed. For instance, a two-column model study of Raymond and Zeng

(2000) and a cloud-resolving model (CRM) study of Bretherton et al. (2005) found instabilities analogous to moisture mode instability. On the other hand, Sobel and Bretherton (2000) showed that in their simulations, the SCM they used was stable under the WTG configuration, indicating that moisture mode is damped in their model, if ever present. In this chapter, I attempt to provide a reason for this discrepancy, showing that moisture mode instability requires moisture-convection feedback and moist static energy (MSE) sources that overcompensate for MSE export, and that the model of Sobel and Bretherton lacked both.

5.1.1 Relating QTCM and SCM

So far this thesis has been examining Kelvin-like modes that have a horizontal dimension. But the subject of this chapter is an SCM, which does not possess any horizontal coordinate by design. Naturally a question arises as to how an SCM is related to Kelvin-like modes.

Chapters 2 and 3 showed that the WTG approximation characterizes the small-scale limit of moisture mode accurately. Recall that in QTCM, the WTG system may be written as

$$\left\langle -\Omega_1 \frac{\partial \overline{s}}{\partial p} \right\rangle \frac{\omega_1'}{\Delta p} = (1+r)\frac{P'}{\Delta p/g} + \frac{H'}{\Delta p/g}, \tag{5.1}$$

$$\hat{b}_1 \frac{\partial q_1'}{\partial t} - \left\langle \Omega_1 \frac{\partial \overline{q}}{\partial p} \right\rangle \frac{\omega_1'}{\Delta p} = \frac{E'-P'}{\Delta p/g}. \tag{5.2}$$

Here p is pressure, t is time, Ω_1 is the basis function for pressure velocity, s is dry static energy, ω_1 is the amplitude of vertical motion associated with the first-baroclinic mode and defined as $\omega_1/\Delta p \equiv \partial u_1/\partial x$, Δp is the thickness of the troposphere, r is the cloud-radiation interaction parameter, P is precipitation, H is sensible heat flux, g is acceleration due to gravity, $\hat{b}_1$ is mass-weighted vertical average of the humidity basis function b_1, q_1 is the amplitude of the first humidity mode, q is specific humidity, and E is evaporation. An overbar denotes the time mean and a prime implies a perturbation. All thermodynamic variables are in energy units. Eqs. (5.1) and (5.2) are identical to Eqs. (2.93) and (2.93); the only difference is in notation.

On the other hand, the prognostic equations of a single-column model under a standard RCE configuration are

$$\frac{\partial T}{\partial t} = Q_c + Q_R, \tag{5.3}$$

$$\frac{\partial q}{\partial t} = Q_q, \tag{5.4}$$

where T is temperature, Q_c is convective heating, Q_R represents radiative heating, and Q_q is convective moistening/drying. As before, all the variables are in energy units. In the RCE configuration, the SCM is meant to represent an average of a wide area such as the entire tropics. Sobel and Bretherton (2000) proposed an alternative formulation, which is now termed the WTG approximation:

$$\omega \frac{\partial \overline{s}}{\partial p} = Q_c + Q_R, \tag{5.5}$$

$$\frac{\partial q}{\partial t} + \omega \frac{\partial q}{\partial p} = Q_q. \tag{5.6}$$

Here $\overline{s}$ (or $\overline{T}$) must be either specified or calculated using the domain-averaged equation for $\overline{T}$. In contrast with the RCE configuration, the model now represents a local area in the tropics where temperature gradient is efficiently removed by gravity waves.

As noted by Sobel and Gildor (2003), the analogy between the WTG equations of SCM (5.5) and (5.6) and the QTCM WTG equations (5.1) and (5.2) is easy to grasp. Vertical motion is diagnosed from the balance between diabatic heating and adiabatic cooling in the temperature equation, and the prognostic humidity equation is calculated based on this diagnosed pressure velocity. We would anticipate that the result on moisture mode instability from QTCM would carry over to an SCM, provided that key physical processes are also present in the SCM.

5.2 Single-column model and experimental design

5.2.1 Model description

The primary tool of this chapter is the SCM of Bony and Emanuel (2001). The model was developed by Rennó et al. (1994), and subsequently refined by Emanuel and Živković-Rothman (1999) and Bony and Emanuel (2001). It has the convective scheme of Emanuel (1991) and Emanuel and Živković-Rothman (1999), which the authors optimized against the TOGA-COARE data. It also includes the statistical cloud scheme of Bony and Emanuel (2001), which has also been tested against TOGA-COARE observations. The radiative schemes are based on Fouquart and Bonnel (1980) for shortwave and Morcrette (1991) for longwave.

The version of the convection scheme used is 4.3b but with minor modifications as described in Bony and Emanuel (2001). It relies on three key hypotheses:

1. *Buoyancy-sorting hypothesis of Raymond and Blyth (1986).* The conventional entraining plume models assume that parcels from the boundary layer entrain environmental air continuously until it detrains at the level of neutral buoyancy (e.g., Arakawa and Schubert 1974). In contrast, Raymond and Blyth (1986) noted that mixing in a cloud is highly sporadic, and that mixing creates air parcels with different buoyancy, each reaching its level of neutral buoyancy.

2. *Mixing hypothesis partially based on Bretherton and Smolarkiewicz (1989).* Their work suggests that entrainment and detrainment rates are functions of the vertical gradients of buoyancy in clouds. One could express this as

$$\frac{\delta M}{M_b} = \frac{|\delta B| + \Lambda \delta p}{\sum_{i=1}^{N} [|\delta B| + \Lambda \delta p]}, \tag{5.7}$$

where δM is the rate of mixing of undiluted cloud air, M_b represents the net upward mass flux through cloud base, Λ is a mixing coefficient, B is the buoyancy of undiluted cloud air, δB is the change in undiluted buoyancy over a pressure interval δp,

and N is the number of model levels.

3. *Subcloud-layer quasi-equilibrium.* The quasi-equilibrium hypothesis contends that moist convection is a rapid process relative to large-scale motion, and that it is constantly consuming instability created by large-scale flows. This implies that some cloud-related variables are quasi-invariant. The original paper by Arakawa and Schubert (1974) assumed that the time tendency of the cloud work function, a CAPE (convective available potential energy)-like quantity, is small because by their fast response, clouds never allow for accumulation of the cloud work function. Raymond (1995) argued that convective mass fluxes are constantly adjusting to production of instability so that the buoyancy of boundary layer air with respect to the environment air just above the boundary layer remains near zero. This idea is implemented in the present SCM as

$$\frac{\partial M_b}{\partial t} = \frac{\alpha}{\Delta t}(T_{\rho p} - T_\rho + \Delta T_k) - \frac{D}{\Delta t} M_b, \tag{5.8}$$

where α is a parameter that measures how fast the subcloud layer reaches statistical equilibrium, $T_{\rho p}$ is the density temperature of a parcel lifted adiabatically from the subcloud layer, T_ρ is the environmental density temperature, D is the damping parameter, ΔT_k represents the effect of subgrid-scale temperature variability that could overcome negative buoyancy, and Δt is the time step, which is used to normalize α and D. Density temperature is an extension of the virtual temperature and equivalent to the temperature that dry air would have to obtain the same density as moist, cloudy air. In addition to the virtual effect, it also incorporates the density of cloud droplets.

These hypotheses combine to determine the vertical profile of mass flux. In particular, hypothesis (1), buoyancy-sorting, and hypothesis (2) represented by Eq. (5.7) dictate mass flux *vertical distribution* whereas hypothesis (3), the subcloud-layer quasi-equilibrium, determines the total mass flux *at the cloud base*.

The advantage of the Emanuel scheme is that it incorporates various microphysics that affect how moist convection distributes humidity in the vertical. The key microphysical parameters include:

1. Precipitation efficiency $\varepsilon_p(p)$, the fraction of condensates that fall out as precipitation rather than staying as cloud water;

2. Fractional area covered by the unsaturated downdraft driven by re-evaporation of precipitation σ_d; and

3. Fraction of rain shaft falling through unsaturated environment σ_s.

The focus of this chapter is the third one, σ_s, which controls the strength of moisture-convection feedback.

One of the conditions for moisture mode instability is that there exist an MSE source that overcompensates for MSE export, implying that cloud-radiation interaction plays a key role here. The cloud scheme of Bony and Emanuel (2001) takes the large-scale variables and the subgrid-scale condensate content from the convective scheme, and calculates the distribution of the condensate in a gridbox:

$$f = f(\overline{q}_t, \overline{q}^*, q_c^{\text{in,SUB}}), \tag{5.9}$$

$$q_c^{\text{in}} = q_c^{\text{in}}(\overline{q}_t, \overline{q}^*, q_c^{\text{in,SUB}}), \tag{5.10}$$

where $\overline{q}_t$ is the grid-average total water content (a sum of all phases), $\overline{q}^*$ is the grid-average saturation specific humidity, and $q_c^{\text{in,SUB}}$ is the subgrid-scale in-cloud condensate (a sum of liquid and ice) predicted by the convective scheme, f denotes cloud fraction, and q_c^{in} is the in-cloud condensate water content, including both ice and liquid phases. The functional forms of f and q_c^{in} arise from statistical assumptions of the generalized log-normal distribution of total water content within a grid box. Some additional assumptions on the partitioning of condensate into liquid and ice phases enables one to estimate cloud optical depth.

The model also incorporates interactive gustiness, which was developed by Emanuel and Živković-Rothman (1999). Their formula is

$$w_d = \frac{\beta M_d}{\rho \sigma_d}, \tag{5.11}$$

where w_d is gustiness, β is a proportionality constant, M_d denotes the unsaturated downdraft mass flux at the base of a cloud, and ρ is the air density. Note the difference in notation between Chapter 2 and the present chapter; Chapter 2 used v_g instead of w_d.

In general, one may write evaporation including subgrid-scale variance as

$$E = \rho C_k \left[|\mathbf{V}|(q_s^* - q_a)\right] = \rho C_k \left[|\mathbf{V}|\right](q_s^* - [q_a]) - \rho C_k \left[|\hat{\mathbf{V}}|\hat{q}_a\right], \tag{5.12}$$

where E is evaporation, C_k is the drag coefficient, $|\mathbf{V}|$ is the surface wind speed, q_s^* is the surface saturation specific humidity, q_a is the surface air specific humidity, a bracket denotes the horizontal mean, and a hat implies deviation from the spatial mean. The actual formula used in the SCM is

$$E = \rho C_k \left\{ \sqrt{U^2 + w_d^2}(q_s^* - q_a) - \left(\sqrt{U^2 + w_d^2} - U \right) q'' \right\}, \tag{5.13}$$

where U is the imposed mean wind speed, and q'' is a specific humidity anomaly due to downdraft.

5.2.2 Experimental setup

The vertical resolution of the model is 25 hPa for $p \geq 100$ hPa, and additional levels are placed at p = 80, 60, 40, 30, 25, 20, 15, 10, 5 hPa. The time step is 4 minutes and the radiation calculation is conducted once an hour. The surface flux is forced by the large-scale surface wind, which is set to 5 m/s. The CO_2 concentration is taken to be 360ppm. An annual-mean radiative forcing at 10 degrees latitude is applied with a fixed zenith angle but without a diurnal cycle, although the effect of solar forcing is secondary since the sea-surface temperature is fixed.

Of particular interest is whether a physical mechanism implied by the analysis of QTCM translates into a more realistic model. The growth rate equation suggests three important physical mechanisms: moisture-convection feedback, cloud radiation interaction, and gustiness. Which of these is the most important? To address this, I examine the effect of each physical process one by one.

Turning on and off cloud-radiation interaction and gustiness is straightforward. To turn off cloud-radiation interaction, radiative heating and cooling are replaced with their clear-sky values. Suppressing gustiness requires simply removing it from the bulk formula for surface heat fluxes.

Treatment of moisture-convection feedback deserves some elaboration. Following Grabowski and Moncrieff (2004) and Zurovac-Jevtić et al. (2006), I change the micro-physical parameter σ_s, the fraction of precipitation falling outside the cloud. Grabowski and Moncrieff (2004) found that increasing σ_s from the standard value, 0.12, to 0.30 substantially improved an MJO-like disturbance in their model. Zurovac-Jevtić et al. (2006) discovered that enhancing moisture-convection feedback by modifying σ_s has weakened small-scale advective disturbances in favor of planetary-scale modes.

Altering σ_s is, however, not the correct way of representing moisture-convection feedback, as noted by Grabowski and Moncrieff (2004). A more accurate path is to modify how entrainment is parameterized. For the Arakawa and Schubert (1974) scheme, Tokioka et al. (1988) proposed a simple correction to impose a lower limit to the entraining rate, essentially eliminating non-entraining penetrative plume. The authors themselves and others (e.g., Lee et al. 2001) have shown that this modification improves the MJO simulation in GCMs. In the case of the Emanuel scheme, Grandpeix et al. (2004) tried to modify the probability density function for mixing fraction in the parameterization, obtaining a limited success. Therefore, one should think of the approach of changing σ_s as a "quick fix"; it amounts to implementing a correct physics in a crude way.

The model is run under two configurations: the RCE configuration as described in Eqs. (5.3) and (5.4), and the WTG configuration which is implemented using Eqs. (5.5) and (5.6). In the RCE configuration, the model represents a horizontal average of the tropics. In the WTG configuration, the model is interpreted as a localized column in the tropics, where temperature gradient remains weak because of weak rotation and fast gravity wave dynamics, and diabatic heating is nearly balanced by adiabatic cooling of vertical motion.

The detailed procedure of the WTG configuration calculation closely follows Sobel and Bretherton (2000). The temperature tendency for $p < 850$ hPa is set to zero, and the

vertical motion is diagnosed from the temperature equation (5.5). The pressure velocity ω is linearly extrapolated downward from the value at the lowest level where temperature is fixed, with a rigid lid at the bottom level. The humidity advection is calculated from the diagnosed vertical motion with upstream differencing.

The model is run for 1000 days to ensure that it reaches an RCE. A slight perturbation is added to the temperature at 1000hPa to create a 100-member ensemble for each parameter set. After additional 70 days of the RCE configuration, the integration is switched to the WTG configuration.

The reason for creating an ensemble is that cloud-radiation interaction enhances an internal oscillation of the RCE with a period of $< \sim$10 days. Table 5.1 indicates that implementing cloud-radiation interaction yields a higher standard deviation of precipitation. A power spectral analysis demonstrates that there is no clear preferred periodicity. As discussed below, this internal oscillation has impact on the behavior of the model under WTG; the phase of the oscillation and the timing of turning on the WTG configuration combine to determine the time evolution of the model.

There is an issue of which temperature profile should be used for the WTG configuration integration. Initially I used the snapshot temperature profile at the time of starting the WTG integration. The alternative is to use a time-averaged profile. As it turned out, the model quantitative results are sensitive to the choice of temperature profile. The sensitivity of the model to the temperature profile is likely due to the interaction between convective and cloud parameterizations, which essentially yield the internal oscillation, the key to moisture mode instability. I discuss this point later in the chapter.

The sensitivity test considers six parameter combinations. Table 5.1 summarizes them along with precipitation rates in RCE.

Table 5.1: Summary of sensitivity studies. Moisture-convection feedback is strengthened when $\sigma_s = 0.30$. The standard deviation of P is from the 6-hourly instantaneous output of the last 500 days of the RCE calculations.

Case number	Description (CRI: cloud-radiation interaction, GUST: gustiness)	P [mm/day] for RCE	Standard deviation of P [mm/day]	Clear-sky radiative flux [W/m^2]
Case 1	(σ_s, CRI, GUST) = (0.12, on, on)	3.8	0.42	218
Case 2	(σ_s, CRI, GUST) = (0.12, off, on)	4.3	0.022	213
Case 3	(σ_s, CRI, GUST) = (0.12, on, off)	3.9	0.47	217
Case 4	(σ_s, CRI, GUST) = (0.30, on, on)	3.8	0.82	220
Case 5	(σ_s, CRI, GUST) = (0.30, off, on)	4.3	0.023	215
Case 6	(σ_s, CRI, GUST) = (0.30, on, off)	3.8	0.79	218

5.3 Model results

5.3.1 Radiative-convective equilibrium

Figs. 5-1 and 5-2 plot the vertical profiles of temperature and specific humidity averaged over the last 20 days of the 1000-day RCE runs for Case 4 and differences between Case 4 and others. Most of the results are straightforward to interpret. Fig. 5-1 shows that suppressing cloud-radiation interaction naturally cools the troposphere. Another salient feature is warming of the stratosphere when cloud-radiation interaction is excluded. Clouds are efficient emitters of longwave radiation and induce local cooling. Fig. 5-2 illustrates that weakening moisture-convection feedback results in a dryer troposphere since a smaller amount of rainfall is subject to re-evaporation.

Table 5.1 shows the corresponding precipitation (or evaporation) rates and vertically integrated clear-sky radiative cooling, indicating that cloud-radiation interaction decreases precipitation. One can comprehend this with the help of the column-integrated heating balance:

$$0 = P + \left\langle Q_{R,cld} \right\rangle + \left\langle Q_{R,clear} \right\rangle + H, \tag{5.14}$$

where P is precipitation, $\left\langle Q_{R,cld} \right\rangle$ is vertically-averaged cloud radiative forcing, $\left\langle Q_{R,clear} \right\rangle$ is vertically-averaged clear-sky radiative cooling, and H is sensible heat flux. H is generally small and neglected here. Table 5.1 implies that the difference in clear-sky radiative cool-

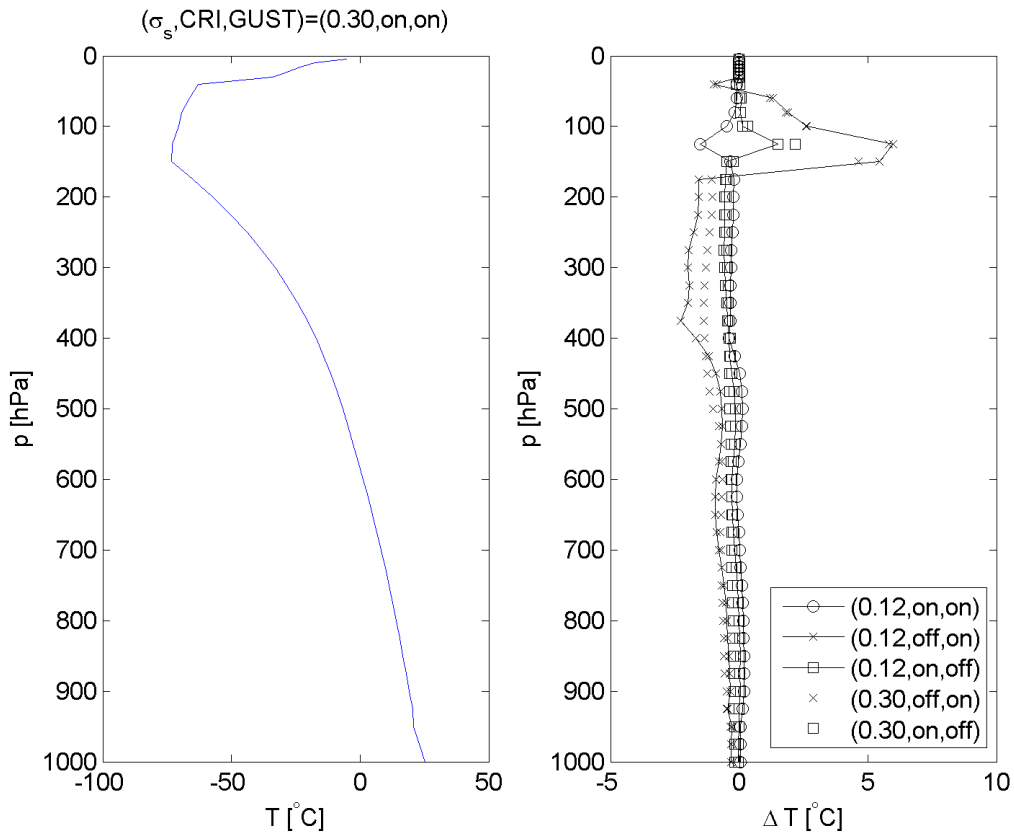

Figure 5-1: (Left) Temperature profile from the last 20 days of the RCE calculation for Case 4, with $\sigma_s = 0.30$ and both cloud-radiation and gustiness included. (Right) Differences in temperature: T(each case) - T(Case 4). Markers with lines denote σ_s = 0.12 whereas markers without imply σ_s = 0.30. Note relative cooling of the troposphere and warming of the lower stratosphere when cloud-radiation interaction is excluded.

ing between Cases 4 and 5 is about $(220-215)/220 \approx 2\%$ whereas precipitation differs by about $(4.3-3.8)/3.8 \approx 12\%$. Since the clear-sky radiative cooling does not change appreciably, the balance implies that the inclusion of cloud forcing is balanced by decreased precipitation.

The effect of interactive gustiness is not clear but fortunately its effect is weak.

5.3.2 WTG results

Fig. 5-3 presents the times series of precipitation for 6 cases. The WTG configuration calculation starts on day 1070. For Case 2 (Fig. 5-3b), which is closest to the configuration of

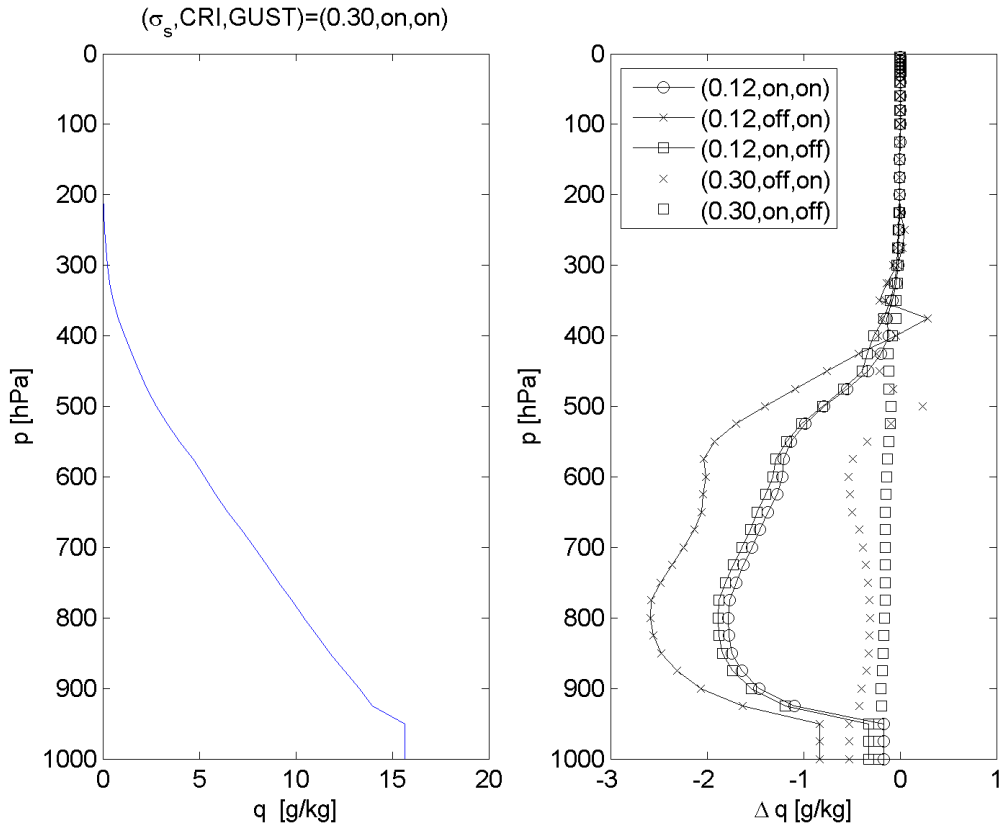

Figure 5-2: (Left) Specific humidity vertical profile from the last 20 days of the RCE calculation for $\sigma_s = 0.30$ with both cloud-radiation and gustiness included. (Right) Differences in specific humidity between the one shown in the left and each case. Markers with lines denote $\sigma_s = 0.12$ whereas markers without imply $\sigma_s = 0.30$. Weaker moisture-convection feedback ($\sigma_s = 0.12$) leads to relative drying of the free troposphere since a smaller amount of rainfall is subject to re-evaporation.

Sobel and Bretherton (2000), the WTG configuration simulation leads to slight oscillations in some runs, but in general, the model does not diverge from the RCE. For Cases 1 and 3 (Figs. 5-3a and 5-3c), including cloud-radiation interaction causes multiple equilibria, which I discuss in detail below. Precipitation collapses to a near-zero rate for numerous runs while other runs stay close to the RCE.

Once moisture-convection feedback is enhanced and cloud-radiation interaction is included, markedly different results emerge (Cases 4 and 6, Figs. 5-3d and 5-3f). As before, precipitation drops to virtually zero for some runs, but in others, precipitation achieves a rate much higher than in the RCE. Some runs even crash after sustained growth in precipitation or show oscillations with large amplitudes. In most cases, the model reaches another state within 10–20 days, a timescale relevant for the initial stage of the MJO; our focus here is the initial, stationary stage of the MJO that corresponds to the stages of F and G in Fig. 1-1 of Chapter 1 and the pertinent timescale is weeks, not 30–60 days. Also recall that the linear WTG analysis of QTCM predicted an *e*-folding timescale of $\sim$5.8 days for the reference values (see Fig. 2-8 of Chapter 2). If nonlinear saturation occurs over a couple of the *e*-folding period, these two are roughly consistent.

The arguments repeatedly presented in the preceding chapters provide a framework for making sense of the physics behind the WTG behavior: moisture mode instability occurs after the model is turned into the WTG configuration, and the model in some cases reaches nonlinear saturation. However, there are multiple equilibria and how different runs achieve differing ending states is obscure. Turning off cloud-radiation interaction hinders such instability (Case 5, Fig. 5-3e) but suppressing the effect of gustiness on evaporation does not (Case 6, Fig. 5-3f). In the present configuration with a mean surface wind speed of 5 m/s, cloud-radiation interaction seems to dominate the MSE forcing in this SCM. While both Cases 2 (Fig. 5-3b) and 5 (Fig. 5-3e) exhibit oscillations in the WTG configuration, the frequencies are much higher in Case 5; the reason for this difference is not understood.

Regardless of all the caveats, one finding stands out: strong moisture-convection feedback yields qualitatively different results. The analysis of QTCM in Chapters 2 and 4 implicitly assumes moisture-convection feedback, and I could not weaken such an effect.

Changing the convective timescale affects the growth rate in QTCM, but its role is different from that of σ_s. The SCM calculations allow for a test of differing strengths of moisture-convection feedback.

Furthermore, the finding here implies that the reason Sobel and Bretherton (2000) found no instability under the WTG configuration is likely to be the lack of both moisture-convection feedback and cloud-radiation interaction. Not surprisingly, in contrast with Sobel and Bretherton, the models with both physical effects, such as those of Raymond and Zeng (2000) and Bretherton et al. (2005), saw moisture mode instability-like behavior.

What is the reason for apparent multiple equilibria when cloud-radiation interaction is included? It might have to do with complex structures of vertical motion. Clouds cause strong radiative cooling above and heating below, which in turn lead to vertical motion profile peaking at the levels bounding clouds. Such effects can be seen in the middle panels of Fig. 5-5, which show the vertical profiles of Case 4. In nature, such localized heating would probably lead to turbulence, which is not included in the SCM outside the planetary boundary layer.

Another notable characteristic about multiple equilibria is that the final state is determined by the phase of the internal oscillation. To confirm this, Fig. 5-4 shows the time series of precipitation for Case 4 as in Fig. 5-3d. In creating an ensemble, instead of perturbing temperature at day 1000, I randomly chose 100 numbers from day 1069.5 to 1070.5 and turned the SCM into the WTG configuration on these randomly chosen times. Although Figs. 5-3 and 5-4 differ in that a vast majority of solutions with P greater than the RCE rate are vacillating, changing the starting times of WTG does reproduce multiple equilibria-like behavior. The finding suggests that the phase of internal oscillation is a key factor in affecting the model behavior under WTG. Yet how exactly multiple equilibria arise is not clear.

To better understand the physical mechanism of the WTG results, I focus on Case 4. The 100 runs are classified into 3 categories, according to precipitation averaged over the last 20 days of simulation: $P < 1$ mm/day, $1 \leq P < 6$mm/day, and $6 \leq P < 10$mm/day. The upper limit of the last category is to exclude one outlier with a precipitation of about

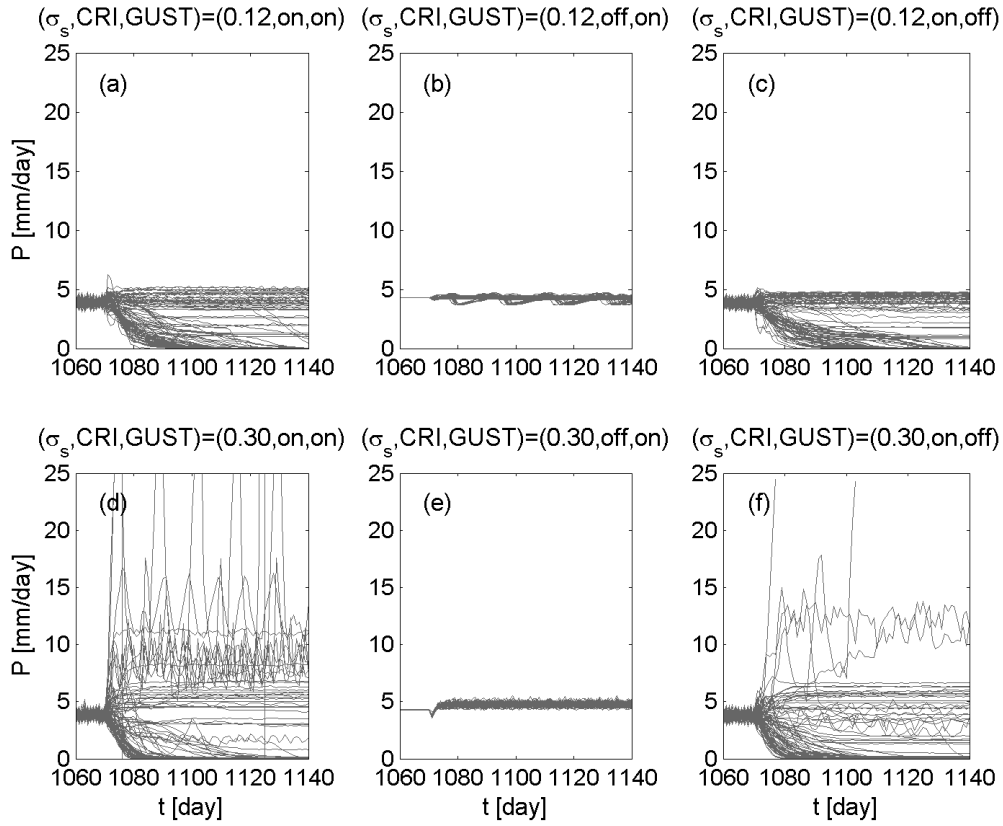

Figure 5-3: Time series of precipitation for (a) case 1, (b) case 2, (c) case 3, (d) case 4, (e) case 5, and (f) case 6. The cases are summarized in Table 5.1.

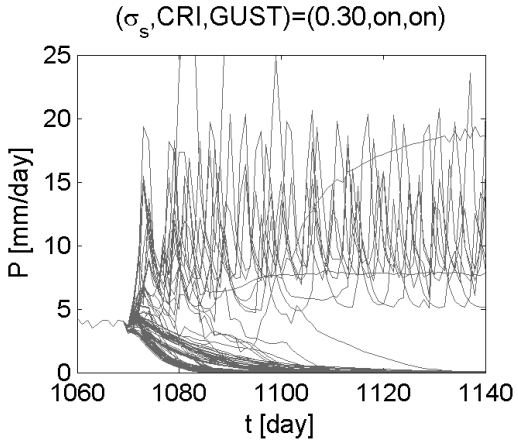

Figure 5-4: As in Fig 5-3d but here the time of starting the WTG configuration is perturbed, rather than the initial condition. The horizontal axis represents time in days while the vertical axis indicates *P* in mm/day.

12mm/day, which can be found in Fig. 5-3. This particular run deviates from other runs in many ways. Unfortunately the reason for the existence of this run is not understood. Oscillatory solutions are excluded by removing runs whose standard deviation of P for the last 20 days of simulation exceeds 0.2 mm/day. The categorization is subjective and arbitrary, and there is actually even a spectrum of solutions. Nevertheless, it helps visualize the differences among numerous runs.

Fig. 5-5 shows precipitation time series and vertical profiles of selected variables for Case 4, classified in the way described above. The left column shows runs where precipitation drops to near zero. Cooling in the troposphere leads to subsidence, which dries the troposphere. The perturbation MSE is negative. There are several outliers with a different vertical motion profile and extremely dry troposphere. Fig. 5-6 describes such runs. The left panel shows the MSE profile and the right panel depicts specific humidity. Specific humidity is close to zero above 800 hPa for many runs. Temperature even exhibits trade-inversion-like profiles in some cases (the middle panel).

The right column of Fig. 5-5 exhibits the runs where $6 \leq P < 10$ mm/day. ω is negative aside from the region under influence of strong cloud radiative forcing. The MSE anomaly tends to be positive, especially in the middle and lower troposphere, reflecting moistening at this level. Note the asymmetry of the MSE perturbations between Figs. 5-5g and 5-5i. The former shows much larger dry anomalies than the latter's moist anomalies. Because precipitation is an exponential function of precipitable water (see below), small moist anomalies result in a huge variation in precipitation.

The behavior of the model for $1\text{mm/day} \leq P < 6\text{mm/day}$ is quite complicated but seems to be in between cases of $P < 1$ mm/day and $P \geq 6$mm/day.

In the present implementation of the WTG approximation, tropospheric temperature is fixed at RCE values (or to be more precise, the value on the day when the SCM is switched to the WTG configuration, which is very close to the RCE). Therefore changes in convection primarily reflect variations in free-tropospheric humidity and boundary-layer MSE, suggesting that the design of numerical calculations is analogous to that of Derbyshire et al. (2004). Motivated by the similarity, I depict in Fig. 5-7 the upward mass flux for

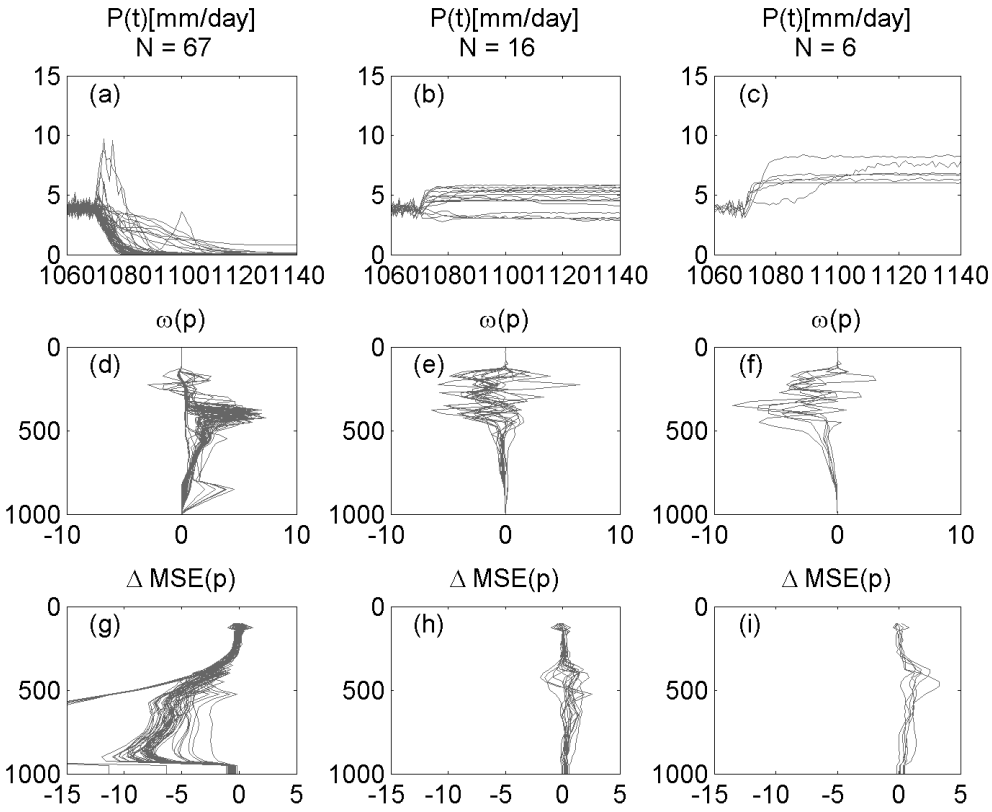

Figure 5-5: Results of 100 runs in Case 4, classified according to the precipitation in the last 20 days of the simulation. The 3 panels in the left column ((a), (d), and (g)) correspond to $P < 1$ mm/day; the middle column ((b), (e), and (h)) $1\text{mm}/\text{day} \leq P < 6\text{mm}/\text{day}$; the right column ((c), (f), and (i)) $6\text{mm}/\text{day} \leq P < 10\text{mm}/\text{day}$. 11 runs are excluded that either have a standard deviation of precipitation exceeding 0.2 mm/day for the last 20 days, or blow up before completing the numerical calculation. The top row ((a), (b), and (c)) describes precipitation time series, and the middle row ((d), (e), and (f)) pressure velocity, and the bottom row ((g), (h), and (i)) the MSE difference between RCE and each WTG run. The N's at the top panels show the numbers of runs in each category. The units are: P in mm/day, ω in hPa/hour, and MSE in Kelvin (converted from J/K/kg to K by dividing c_p).

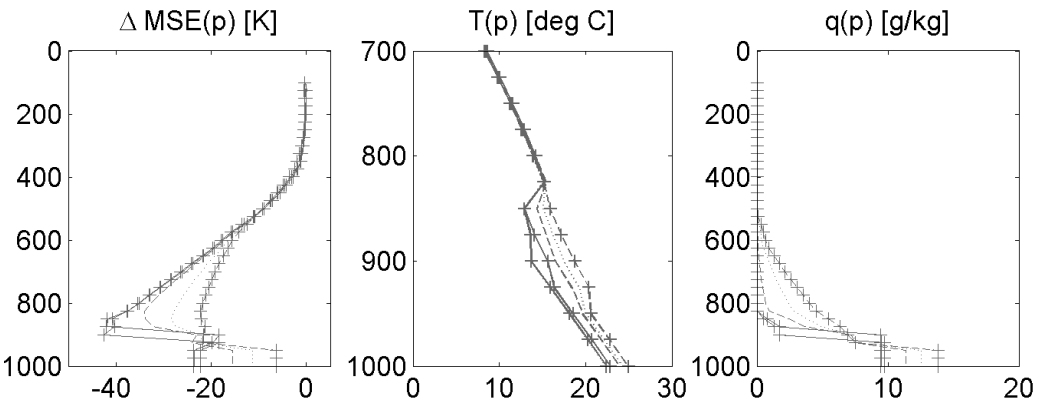

Figure 5-6: Runs with an extremely dry troposphere. (Left) MSE difference for each run from the RCE. (Middle) Temperature profile for each run. (Right) Specific humidity structure. Slight differences in temperature arise because there is a small fluctuation in temperature even in the RCE configuration.

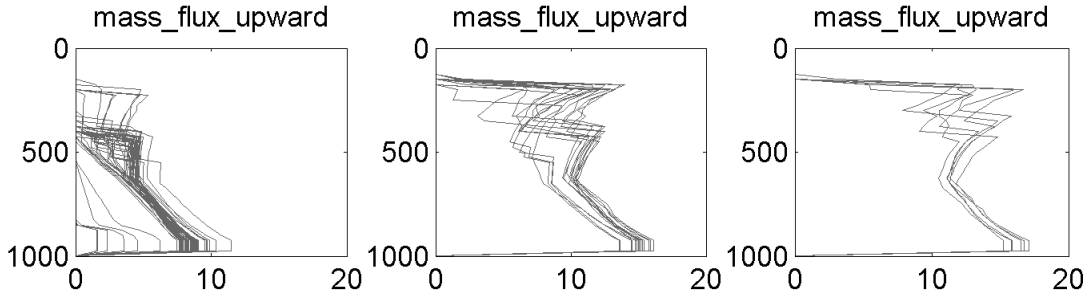

Figure 5-7: Upward mass flux for (left) $P < 1$ mm/day, (middle) $1\text{mm/day} \leq P < 6\text{mm/day}$, and (right) $6\text{mm/day} \leq P < 10\text{mm/day}$. Units are in 10^{-3} kg /(m^2 s).

the 3 categories of precipitation. Comparison of Figs. 5-5 and 5-7 reveals that a dry troposphere lowers the cloud height and reduces cloud mass flux. This behavior is consistent with CRM simulations but quite different from that of many parameterizations, as detailed in Derbyshire et al. (2004).

Fig. 5-8 plots cloud radiative forcing (CRF), gustiness, and evaporation against precipitation. Gustiness increases with precipitation roughly monotonically, but evaporation is not affected by enhanced gustiness; this might be due to too weak downdrafts in the parameterization. The weak effect of gustiness suggests that moisture mode instability is due to an increased MSE source by cloud radiative forcing. Although with some scatter, cloud radiative forcing increases with precipitation. A linear regression restricted to runs with P

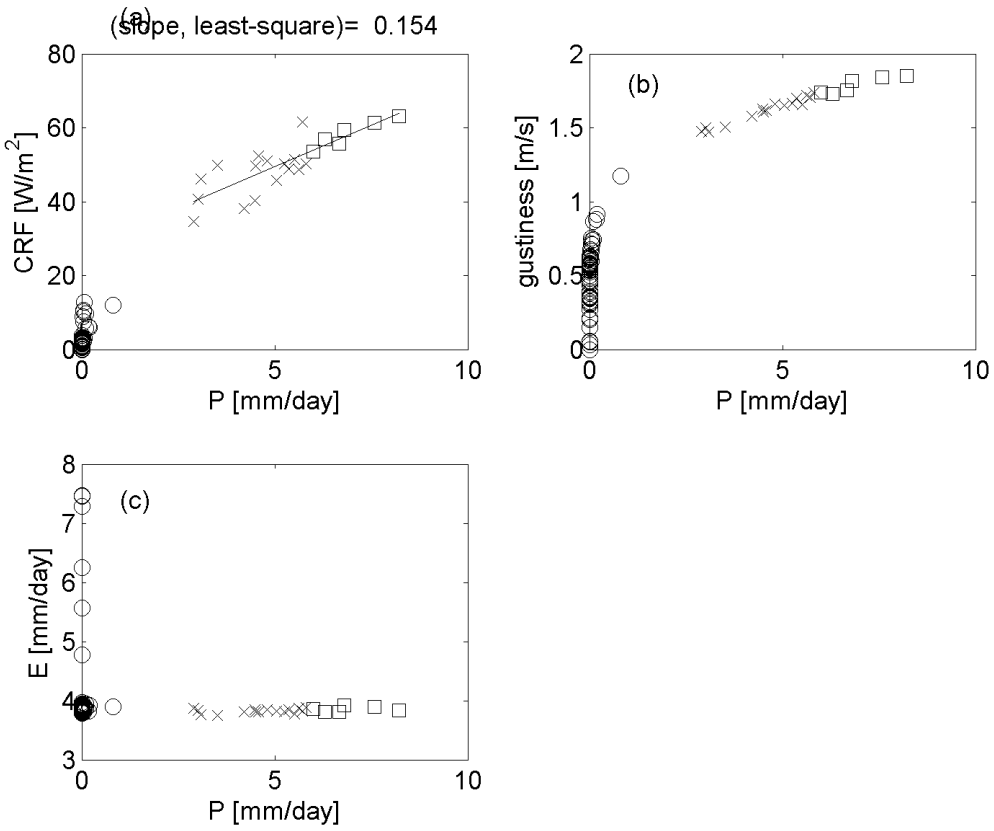

Figure 5-8: Precipitation P and (a) cloud radiative forcing CRF, (b) gustiness, and (c) evaporation E for the last 20 days of the runs in Case 4. Circles imply $P < 1$mm/day, crosses 1mm/day $\leq P < 6$mm/day, and squares 6mm/day $\leq P < 10$mm/day, each corresponding to the left, middle, and right columns in Figs. 5-5 and 5-7. The line in panel (a) shows a least-square fit to the points with $P > 1$, with a slope of 0.154.

> 1mm/day gives $dCRF/dP$ (both in W/m^2) of 0.154, which is statistically significant at 1% level for a two-sided t test with a correlation coefficient of 0.83. The strength of cloud forcing in the SCM is slightly weaker than the observed $dCRF/dP$ value of 0.16-0.17.

As illustrated in Fig. 5-3, moisture-convection feedback significantly influences model runs. To quantify it, Fig. 5-9 plots precipitation against precipitable water, denoted by W. Fig. 5-10 describes the same relation but with column relative humidity as the abscissa. The column relative humidity is defined as precipitable water divided by its value at saturation of the entire atmospheric column.

In discussing moisture-convection feedback, Bretherton et al. (2004, 2005) noted a tight

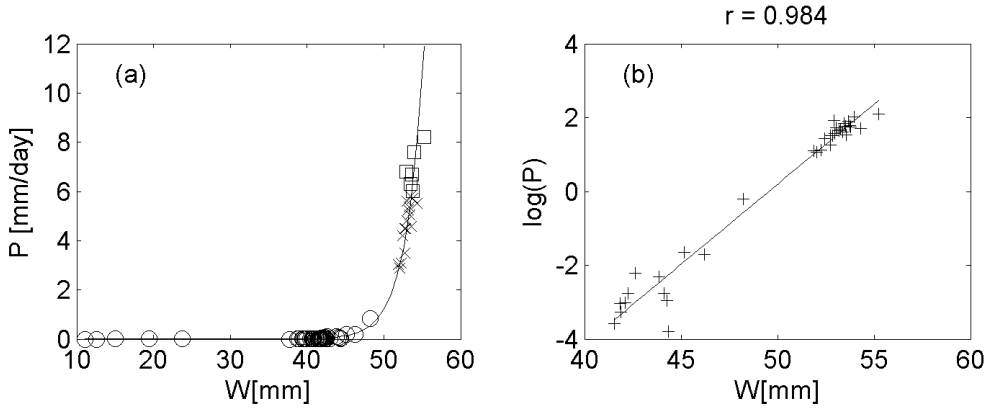

Figure 5-9: (a) Precipitation P as a function of precipitable water W. (b) As in (a) but with a logarithmic scale. Runs with $P < 0.01$ mm/day are excluded from regression.

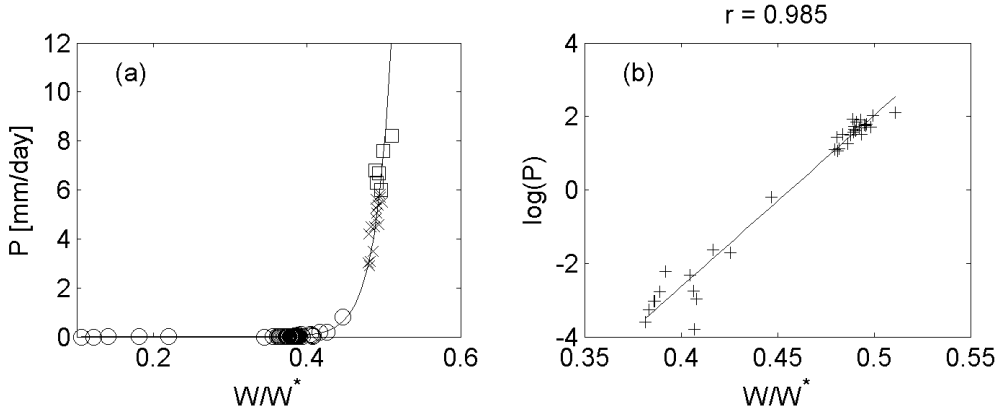

Figure 5-10: As in Fig. 5-9 but with W replaced with column relative humidity W/W^*.

association between column relative humidity and precipitation. In the WTG configuration, the tropospheric temperature is fixed and the boundary-layer temperature does not appreciably change in general, and the saturation precipitable water does not change much. Therefore we would expect the same relation to hold for P and W, which is found in Figs. 5-9 and 5-10. The correlation between logarithm of $\log(P)$ and W is 0.984 while the correlation coefficient between $\log(P)$ and W/W^* is 0.985; they are indistinguishable. (Since the two figures are equivalent, they look redundant, but they are helpful for comparison with the analysis of Bretherton et al. (2004).) The fact that points in Figs. 5-9b and 5-10b are concentrated in the upper right and lower left corners might have led to artificially high correlations. Nevertheless, Figs. 5-9 and 5-10 give another line of evidence for the essential role of moisture-convection feedback.

However, a careful look at Figs. 5-9 and 5-10 speaks to the discrepancy between the SCM and observations. Compared with the graphs of Bretherton et al. (2004), the SCM gives too much precipitation with too little precipitable water. As pointed out by Zurovac-Jevtić et al. (2006), moisture-convection feedback in the present SCM seems to be weaker than in CRMs and observations.

5.4 Sensitivity to temperature profile for the WTG integration

To produce results presented so far, I stored the snapshot of the temperature profile at the last time step under the RCE configuration and used it for the WTG integration. As mentioned above, the alternative is to employ time-averaged temperature. The key question here is whether the model is sensitive to the temperature profile during the WTG integration.

I have conducted additional experiments to explore the sensitivity. By perturbing initial temperature at the lowest level, I created a 100-member ensemble of the RCE integrations which were run for 600 days. After the RCE integration, the model is switched to the WTG configuration. Here instead of using the instantaneous temperature profile for the

WTG integration, I use temperature averaged for a certain period.

As before, 6 ensembles are produced to test different parameter combinations. The perturbed parameters are σ_s and the averaging duration for temperature used under the WTG configuration, $\tau_{\rm ave}$ (in days). Three averaging periods are considered: $\tau_{\rm ave}$ = 0, 0.5, and 2 days. Note that 0-day averaging is identical to using the snapshot temperature profile.

Figure 5-11 shows precipitation time series for six cases. The upper panels indicates that averaging temperature for the WTG integration eliminates oscillatory solutions for $\sigma_s = 0.12$, but the effect of applying time-averaged temperature is not drastic.

In contrast, there is an appreciable influence of time averaging for $\sigma_s = 0.30$ (lower panels). Again averaging temperature for 0.5 days greatly suppresses oscillatory solutions. If temperature is averaged for 2 days, however, there remains only one ensemble member with a rainfall rate higher than 5 mm/day (Figure 5-11f).

Why is the model sensitive to the choice of temperature profile? Figure 5-12 focuses on the two cases, (σ_s, $\tau_{\rm ave}$) = (0.30, 0) and (σ_s,$\tau_{\rm ave}$) = (0.30, 2). The upper left panel shows the difference in temperature between ensemble members with $P > 5$mm/day and those with $P < 2$mm/day for (σ_s,$\tau_{\rm ave}$) = (0.30, 0). P is from the last 10 days of Figure 5-11. As before, the oscillating solutions are excluded. There are clear signatures of cloud radiative forcing. Comparing the upper left and lower panels, one finds that the lower troposphere is generally warmer and the levels right above clouds are significantly colder just before the beginning of the WTG integration .

The right panel shows the difference in temperature between ensemble members with $P > 5$mm/day for (σ_s,$\tau_{\rm ave}$) = (0.30, 0) and each ensemble member for (σ_s,$\tau_{\rm ave}$) = (0.30, 2). The black line is the same but for the ensemble average. Comparison of the upper left and right panels illustrates that time averaging yields an equivalent temperature profile that is associated with the lower P for the WTG integration.

How do the WTG results depend on the temperature profile? Given a fairly large perturbation near the levels of clouds (up to $\sim$0.5K in magnitude), such changes could significantly affect entrainment and detrainment dynamics, not to mention CAPE (although the effect of CAPE is not immediately obvious since the lower troposphere is *warmer* in

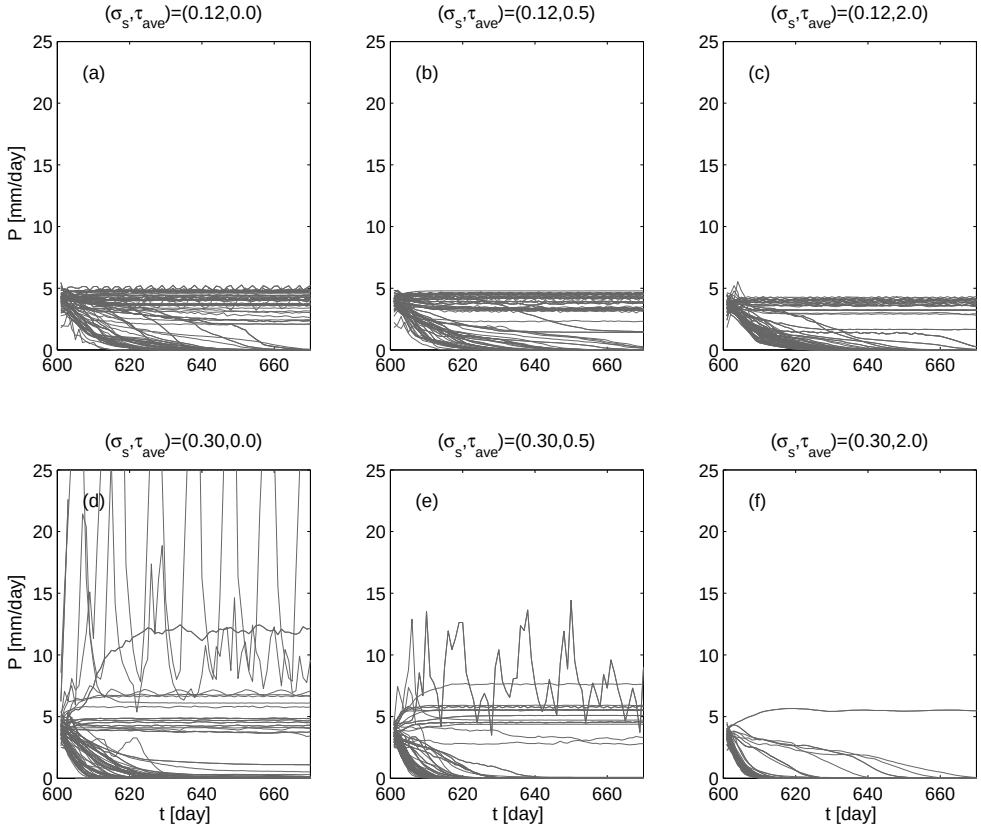

Figure 5-11: As in Figure 5-3 but for different combinations of σ_s and the duration that temperature is averaged for the WTG integration. The horizontal axis is time in days and the vertical axis denotes precipitation in mm/day. The parameter combinations are shown above each panel.

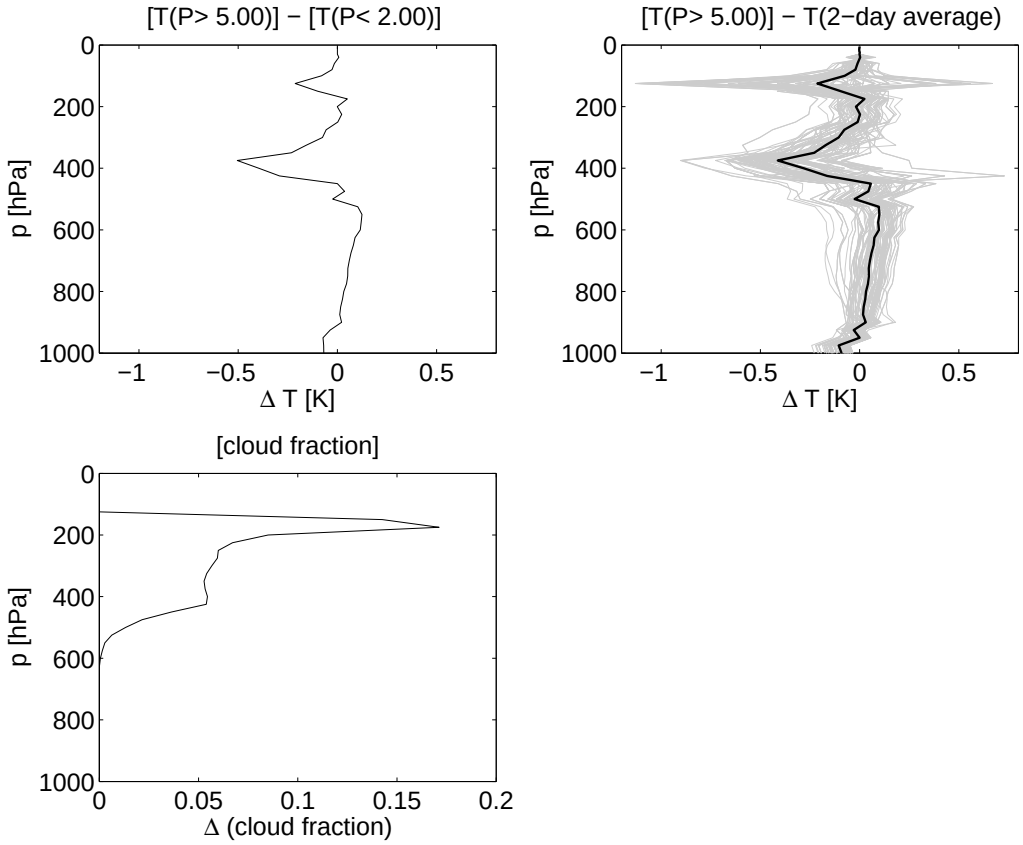

Figure 5-12: (Upper left) Difference between the ensemble-averaged temperature profile for $P > 5\text{mm/day}$ and that for $P < 2\text{mm/day}$, both profiles from the case $(\sigma_s, \tau_{\text{ave}})$ = (0.30,0 days). (Upper right) Difference between the ensemble-averaged temperature profile for $P > 5\text{mm/day}$, $(\sigma_s, \tau_{\text{ave}})$ = (0.30,0 days) and temperature for each ensemble member (gray) and ensemble average (black) for the case $(\sigma_s, \tau_{\text{ave}})$ = (0.30,2 days). (Lower left) Ensemble-averaged profile of cloud fraction for the case $(\sigma_s, \tau_{\text{ave}})$ = (0.30,0 days) right before the start of the WTG integration.

runs where the moisture mode instability develops.) Presumably a particular temperature profile favors detrainment at levels where clouds already exist. Investigation of detailed mechanisms of detrainment and cloud-radiation interaction is beyond scope of this chapter.

In spite of sensitivity of the model to the choice of temperature profile for the WTG integration, the qualitative finding of this chapter still holds; the model does not exhibit solutions with a rainfall rate higher than the RCE value unless moisture-convection feedback is enhanced and cloud-radiation interaction is included.

5.5 Summary and discussions

The findings of this chapter are encouraging in that they basically support the results of the simple model analysis. When cloud-radiation interaction and enhanced moisture-convection feedback are included, the SCM develops moisture mode instability and the instability nonlinearly saturates, as predicted from theoretical models. Examining each of the three physical mechanisms, the numerical experiments have shown that both cloud-radiation interaction and strong moisture-convection feedback are essential ingredients for moisture mode instability in the SCM under the WTG configuration. Since MSE sources are functions of precipitation in this SCM, the MSE anomaly results in increased precipitation, which in turn enhances the MSE sources.

Some of the points made in this chapter are particularly illuminating because of their connection with the published literature. As already discussed, Grabowski and Moncrieff (2004) attained a better simulation of the MJO-like disturbance by changing σ_s. The physics identified in this chapter could partially explain the impact of σ_s. Grabowski and Moncrieff discovered that increasing σ_s ameliorates the simulation of the MJO-like disturbance in their GCM. If their disturbance is under the WTG balance, just like Raymond's (2001) model, the core of convection is equivalent to the SCM under the WTG configuration discussed in this chapter. However, there is a significant difference between their simulation and mine: their run had prescribed radiative cooling. Presumably the MSE source in their case was nonlinear WISHE (wind-induced surface heat exchange). Also I

have demonstrated that the configuration of Sobel and Bretherton (2000) corresponds to a stable regime, providing a possible explanation for the gap between Sobel and Bretherton and other studies such as Bretherton et al. (2005) and Raymond and Zeng (2000).

But the findings in this chapter are much more complicated than those from simple models like QTCM and that of Bony and Emanuel (2005). The SCM has yielded multiple equilibria and oscillatory solutions, probably as a result of cloud-radiation interaction and its strong effect on vertical motion. One way to ameliorate this is to filter the heating using a prescribed vertical profile to suppress the concentrated vertical motion in the upper troposphere. Another problem is that a different σ_s results in a different mean state. How much of the differing behavior can be attributed to the direct effect of moisture-convection feedback as opposed to the varied mean state, the indirect consequence of the change in σ_s?

Subtleties aside, a more fundamental question remains as to whether the results are robust with regard to the implementation of moisture-convection feedback. As mentioned above, changing the value of σ_s is not the best way to include moisture-convection feedback. Ideally one should be changing the representation of entrainment in the scheme. Besides, moisture-convection feedback seems to be weaker than observed (Figs. 5-9 and 5-10). Addressing these questions requires a successful development of the modified Emanuel scheme, which is a formidable task on its own right. Such an endeavor is left for future research.

Chapter 6

Nonlinear moisture modes on the equatorial β-plane

6.1 Introduction

In Chapter 1, I began with a hypothesis that the MJO can be characterized as a nonlinear moisture mode. In the initial stage, the MJO grows as a linear, quasi-stationary moisture mode and nonlinearly saturates through thermodynamic limiting processes. Once it reaches a nonlinear regime, the β-plane dynamics come into play.

Previous chapters have shown that at least one subcloud-layer quasi-equilibrium model (Bony and Emanuel 2005) and two versions of a quasi-equilibrium tropical circulation model (QTCM; Neelin and Zeng 2000; Sobel and Neelin 2006) have moisture mode instability. The findings from the theoretical models have been confirmed by numerical experiments using the single-column model of Bony and Emanuel (2001).

This chapter investigates the second stage of the moisture mode. I perform numerical runs of a simplified version of QTCM and examine impacts of various moist processes such as wind-induced surface heat exchange (WISHE) and nonlinear advection. The novel finding of this chapter is the role of nonlinear advection. Benedict and Randall (2007) discussed the demise of deep convection in the MJO, and found that drying occurs because of horizontal advection rather than subsidence. However, such an idea has never been

explored in the context of simple modeling. In particular, I find that nonlinear advection due to Rossby gyres can move a nonlinearly saturated moisture mode to the east because of its asymmetry.

6.2 Model description

6.2.1 Equations

The model used here is the quasi-linear version of QTCM that has linear momentum and temperature equations coupled with a nonlinear humidity equation. Chapter 2 outlined a casual derivation of QTCM to illustrate the physical concepts behind the model. Although equations are given in Chapter 2, I describe them here briefly for readability. Omitting the barotropic mode and focusing on the equatorial β-plane, the prognostic equations are written as

$$\frac{\partial \mathbf{v}_1'}{\partial t} + \beta y \mathbf{k} \times \mathbf{v}_1' = -\kappa \nabla T_1' - \frac{\mathbf{v}_1'}{\tau_m}, \tag{6.1}$$

$$\hat{a}_1 \frac{\partial T_1'}{\partial t} + \overline{M}_{s1} \nabla \cdot \mathbf{v}_1' = \frac{P'}{\Delta p/g} + \left\langle Q_{R,cld}' \right\rangle - \hat{a}_1 \frac{T_1'}{\tau_R} + \frac{H'}{\Delta p/g}, \tag{6.2}$$

$$\hat{b}_1 \frac{\partial q_1'}{\partial t} - \overline{M}_{q1} \nabla \cdot \mathbf{v}_1' - M_{qp} \nabla \cdot (q_1' \mathbf{v}_1') = -\frac{P'}{\Delta p/g} + \frac{E'}{\Delta p/g} + K_q \hat{b}_1 \nabla^2 q_1'. \tag{6.3}$$

Here primes imply perturbations, and overbars denote the mean state. $\mathbf{v}_1 = (u_1, v_1)$ is the first baroclinic component of the horizontal wind vector, $\beta = df/dy$ and f is the Coriolis parameter, $\kappa = R_d/c_p$, R_d is the gas constant for dry air, and c_p is the specific heat of dry air at constant pressure, T_1 is the first baroclinic component of temperature, and τ_m is the Rayleigh damping timescale. a_1 represents temperature basis function for the first baroclinic mode and $\hat{a}_1$ is its mass-weighted vertical average, $\overline{M}_{s1}$ is the dry static stability, P is precipitation, Δp is pressure thickness of the troposphere, g is acceleration due to gravity, $\left\langle Q_{R,cld}' \right\rangle$ is cloud radiative forcing, τ_R is Newtonian cooling timescale, and H is sensible heat flux. b_1 is the humidity basis function and $\hat{b}_1$ is its mass-weighted vertical average, $\overline{M}_{q1}$ is gross moisture stratification, and M_{qp} is a coefficient that comes from

the variation in gross moisture stratification due to q_1. E is evaporation, and K_q is eddy diffusion coefficient. Note that temperature and humidity are expressed in energy units; T and q here actually represent c_pT and L_vq in usual notation, respectively.

The convective scheme takes a linear Betts-Miller form,

$$P' = \frac{\Delta p}{g} \cdot \max\left(\frac{q_1' - T_1'}{\tau_c}, -\frac{\overline{q}_1 - \overline{T}_1}{\tau_c}\right), \tag{6.4}$$

which, as I discussed in Chapter 2, may be thought of as a crude empirical fit to the observed exponential relationship between precipitable water and precipitation.

Sensible heat flux and evaporation follow bulk formulae (6.5) and (6.5).

$$H' = \rho_a C_E \sqrt{V_{1s}^2({u_1'}^2 + {v_1'}^2) + v_g^2 + v_{bg}^2}(T_s - T_{rs} - a_{1s}\overline{T}_1 - a_{1s}T_1') - \overline{H}, \tag{6.5}$$

$$E' = \rho_a C_E \sqrt{V_{1s}^2({u_1'}^2 + {v_1'}^2) + v_g^2 + v_{bg}^2}(q_s^* - q_{rs} - b_{1s}\overline{q}_1 - b_{1s}q_1') - \overline{E} \tag{6.6}$$

The gustiness comes from Redelsperger et al.'s (2000) parameterization:

$$v_g(\tilde{P}) = \begin{cases} \ln(1 + 0.669\tilde{P} - 0.00476\tilde{P}^2) & \tilde{P} < 70.3 \\ 3.20 & \tilde{P} \geq 70.3 \end{cases}, \tag{6.7}$$

where $\tilde{P}$ is precipitation in mm/day and P is in W/m^2.

Cloud radiative forcing follows a formula similar to that used in Chapters 2 and 4. Here instead of growing indefinitely, cloud forcing saturates to a prescribed value. I choose

$$\left\langle Q_{R,cld}' \right\rangle = \begin{cases} \lambda\left[1 - \exp\left(-\frac{r_0}{\lambda}\frac{P'}{\Delta p/g}\right)\right] & P' \geq 0 \\ r_0 \frac{P'}{\Delta p/g} & P' < 0 \end{cases} \tag{6.8}$$

Here λ is the maximum strength of cloud forcing, and r_0 is the derivative of cloud forcing at $P' = 0$:

$$\left\langle Q_{R,cld}' \right\rangle\Big|_{P' \to \infty} = \lambda, \tag{6.9}$$

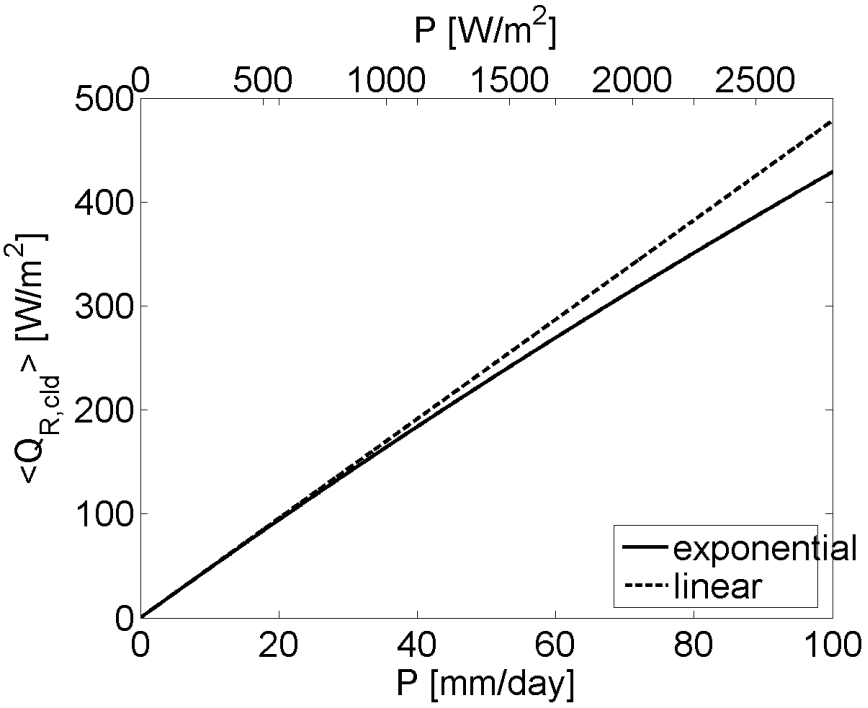

Figure 6-1: Linear and exponential formulations of cloud radiative forcing. The dashed line implies $(\Delta p/g)\left\langle Q_{R,cld}\right\rangle = r_0 P$ while the solid line represents Eq. (6.10) plus the cloud forcing in RCE. The figure assumes $(\Delta p/g)\lambda = 2000\mathrm{W/m}^2$.

$$\left.\frac{d\left\langle Q'_{R,cld}\right\rangle}{d(P'/(\Delta p/g))}\right|_{P'=0} = r_0. \tag{6.10}$$

Fig. 6-1 shows the total cloud radiative forcing $\left\langle \overline{Q}_{R,cld}\right\rangle + \left\langle Q'_{R,cld}\right\rangle$, which is a sum of the radiative-convective equilibrium (RCE) value and the perturbation. For a moderate precipitation rate, the linear and exponential formulations do not deviate significantly from each other.

6.2.2 Numerics and model description

The domain is an equatorial β-plane with a zonal cyclic condition and meridional rigid walls. The sea surface temperature (SST) is uniform and there is no background mean wind, which suppresses linear wind-induced surface heat exchange (WISHE). Parameter values are given in Table 6.1 and Chapter 2, Table 2.1. Note that this chapter utilizes different values for certain parameters, and the values in Table 6.1 here override those in Chapter 2.

The discretization is based on Arakawa C grid for space and second-order Adams-Bashforth for time-stepping. For advection, the model relies on the Lax-Wendroff scheme with the Euler forward time-stepping. For details of these standard schemes, readers are referred to Durran (1999). Note that large numerical diffusion is applied to the humidity variable. The linear analysis in Chapter 2 demonstrated that the growth rate is largest at the smallest scale, and without large diffusion, one just sees grid-scale instabilities. The necessity of unphysical diffusion is a significant drawback of the present model, which I discuss toward the end of this chapter. The resolution is Δx = 40000km/128 = 312.5 km, Δy = 12000km/80 = 150km, and Δt = 300 s.

The integration starts with random initial perturbations for temperature applied to the basic state, which is a spatially homogeneous RCE. Table 6.2 describes the forcing and output of RCE calculation. It is slightly different from that used in Chapter 2.

Model outputs are archived every model day. Although each variable has not been daily-averaged, such a treatment should not affect the interpretation here since most of the fields vary smoothly and there is no reason for expecting disturbances on the hourly timescale.

6.3 Main numerical calculations

This section describes the main numerical simulations. I isolate the effects of various nonlinear effects by turning on and off each physical process. The physical processes examined here are: (i) the strength of cloud forcing in the nonlinear regime, (ii) nonlinear

Table 6.1: Parameters applied to numerical simulations.

Parameter	Symbol	Reference value
Static stability	$\overline{M}_{s1}$	3500 J/kg
Gross moisture stratification	$\overline{M}_{q1}$	3130 J/kg
Rayleigh damping timescale	τ_m	5 d
Newtonian cooling timescale	τ_R	$20 \cdot 10^5$ s $\approx$ 23 d
Convective timescale	τ_c	12 h
Cloud-radiation interaction parameter	r_0	0.17
Eddy diffusion coefficient for humidity	K_q	$1.5 \cdot 10^5$ m^2/s

Table 6.2: Forcing parameters and output values for RCE. Clear-sky radiative forcing was taken from Peters and Bretherton (2005).

Forcing			
	Sea surface temperature	T_s	30.00°C
	Clear-sky radiative cooling	$(\Delta p/g)\langle Q_{R,clear}\rangle$	140 W/m^2
	Mean wind or background gustiness	$-U$ or v_{bg}	4.5 m/s
Output			
	Surface air temperature	$T_{rs} + a_{1s}\overline{T}_1$	27.0°C
	Surface specific humidity	$q_{rs} + b_{1s}\overline{q}_1$	20.7 g/kg
	Surface relative humidity	$(q_{rs} + b_{1s}\overline{q}_1)/q_s^*$	78.4 %
	Precipitation/evaporation	$\overline{P} = \overline{E}$	3.59 mm/day = 101 W/m^2
	Sensible heat flux	$\overline{H}$	22.0 W/m^2
	Cloud radiative forcing	$r\overline{P}$	17.2 W/m^2
	Surface wind speed	$\overline{V}_s$	4.66 m/s
	Downdraft-driven gust	$v_g(\overline{P})$	1.21 m/s

Table 6.3: List of main runs. Nonlinear advection is turned off by setting $M_{qp} = 0$ in Eq. (6.3) whereas nonlinear WISHE is suppressed by taking $V_{1s} = 0$ in Eqs. (6.5) and (6.6).

Case #	Case Name	Nonlinear advection	WISHE	$(\Delta p/g)\lambda$ [W/m^2]
1	Reference	Off	Off	2000
2	Weak cloud forcing	Off	Off	10
3	Nonlinear advection	On	Off	2000
4	Nonlinear WISHE	Off	On	2000

advection of humidity, and (iii) nonlinear WISHE. By changing λ, it is possible to modify the strength of cloud forcing in the nonlinear regime without changing linear instability. Nonlinear advection is removed if $M_{qp} = 0$ in Eq. (6.3) whereas setting $V_{1s} = 0$ in Eqs. (6.5) and (6.6) amounts to suppressing nonlinear WISHE. Table 6.3 lists the main runs on which I focus.

Some clarification on nonlinear WISHE is in order. The model here assumes no background mean wind, and that all the background surface wind speed is specified as gustiness. Because of this specification, all the WISHE effects are nonlinear in the model. In the context of the MJO, starting with Emanuel (1987) and Neelin et al. (1987), many papers have been devoted to linear WISHE. In contrast, there are a limited number of studies on nonlinear WISHE (Xie et al. 1993; Maloney and Sobel 2004), and its effect is not obvious *a priori*.

Figs. 6-2 and 6-3 show the Hovmöller diagram of total precipitation (sum of RCE mean value and anomaly) for the four main cases. Fig. 6-2 focuses on the initial linear stage whereas Fig. 6-3 describes the total simulation period. Fig. 6-4 depicts final snapshots of the four cases. I have chosen parameters such that linear moisture mode instability results, with an e-folding time of 2.97 days in the inviscid, weak temperature gradient limit.

Fig. 6-2 demonstrates that all cases have moisture mode instability, creating disturbances with a wavenumber of $\sim$ 12-16; it is not straightforward to count crests of the waves because they are not uniformly spaced and some of them are almost merged. The scale selection is due to a particular choice of numerical diffusion, as implied by Chapter 2. From the viewpoint of linear analysis, all simulations are exactly the same because the changes across different calculations manifest only as nonlinear effects. The model behav-

ior is, however, different from case to case; notice the differing gray scales for each panel. Since the duration in Fig. 6-2 corresponds to many *e*-folding timescales, such difference is not surprising.

Fig. 6-3a shows that after linear growth, quasi-stationary moisture modes nonlinearly saturate at $\sim$ day 40-50. The preferred wavenumber at the final time is 7, almost halved from the linear regime. Upon nonlinear saturation, moisture modes begin to move eastward at about 0.08 m/s. As shown in Fig. 6-4a, the disturbances are concentrated at the equator and exhibit a "$<$"-like shape. The reason for eastward movement and a rather peculiar meridional structure is not clear, but they are surely affected by numerical diffusion.

Contrasting Figs. 6-3a/6-4a and 6-3b/6-4b reveals the influence of the nonlinear limiting process, as linear stability is identical in the two cases. Figs. 6-3b and 6-4b resemble Figs. 6-3a and 6-4a respectively, except that the dominant wavenumber is higher and the final precipitation rate is smaller. The only parameter that differs between the two cases is λ, the strength of cloud forcing for an infinite precipitation rate. Because of weak nonlinear cloud forcing, the moisture modes saturate at a weaker precipitation rate in Case 2. While Fig. 6-3a shows wavenumber 7 as a preferred mode, there are 11 disturbances at the final time in Fig. 6-3b. From this discussion, it is clear that linear stability analysis is *not* the only factor that selects wavenumber, and that the preferred wavenumber in the nonlinear analysis is affected by the nonlinear limiting process.[1]

Figs. 6-3c and 6-4c describe the effects of nonlinear advection. Initially moisture mode disturbances grow and nonlinearly saturate (Fig. 6-3c), but after the nonlinear saturation, modes begin to translate eastward. The speed of movement is not constant for all the disturbances, and the fastest speed is about 0.6 m/s. This speed is appreciably faster than the ones implied in Fig. 6-3a and 6-3b.

The subject of Figs. 6-3d and 6-4d is the effect of nonlinear WISHE. Now the model exhibits somewhat complicated behavior. The maximum precipitation rate is much higher than in other cases and reaches $\sim$ 40 mm/day; note the different gray scale for Figs. 6-3d

[1]It may not be suitable to use the word "wavenumber" since in the nonlinear regime, ascent regions are much more concentrated than descent regions. Nonetheless, for the lack of a better word, I have chosen this term.

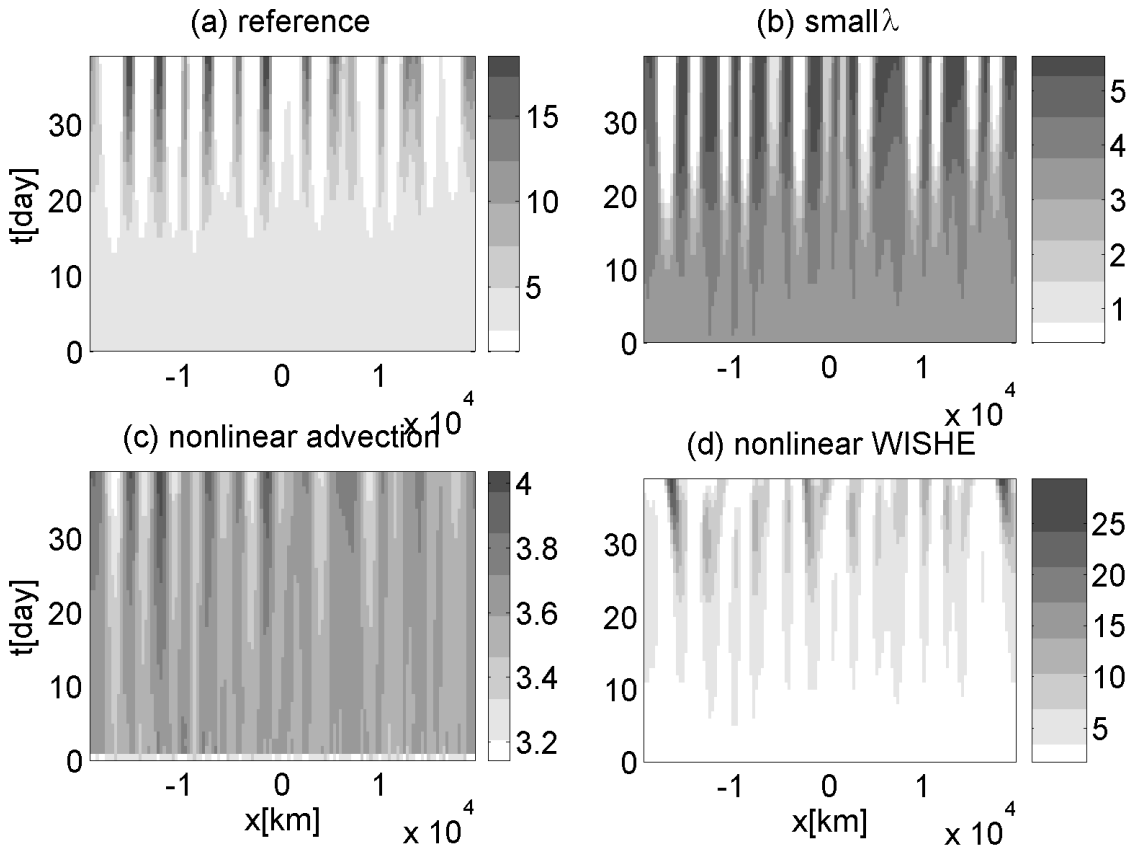

Figure 6-2: Hovmöller (longitude-time) diagram of precipitation in mm/day averaged from $y = -400$km to $y = 400$km for the main runs listed in Table 6.3 for the quasi-linear regime. The horizontal axis is the zonal coordinate x in km and the vertical axis time t in days up to day 39. (a) Case 1, reference; (b) Case 2, weak cloud forcing; (c) Case 3, nonlinear advection; and (d) Case 4, nonlinear WISHE.

and 6-4d. In addition, large-scale disturbances irregularly develop and move toward the west at ~ 3.8 m/s. The duration for which each disturbance remains coherent seems to be somewhat random. Also seen are small-scale eastward propagating modes. An animation of precipitation suggests that they are probably Kelvin-like waves.

Why do nonlinear advection and nonlinear WISHE yield results qualitatively different from the reference case? I first analyze the nonlinear advection case, in which moisture disturbances move to the east. Fig. 6-5 analyzes each term in the humidity equation. It decomposes the humidity budget at the final time step for the domain -20000km $\leq$ x $\leq$ 6000km. Since the evolution of the field is smooth, a snapshot should offer a fairly good

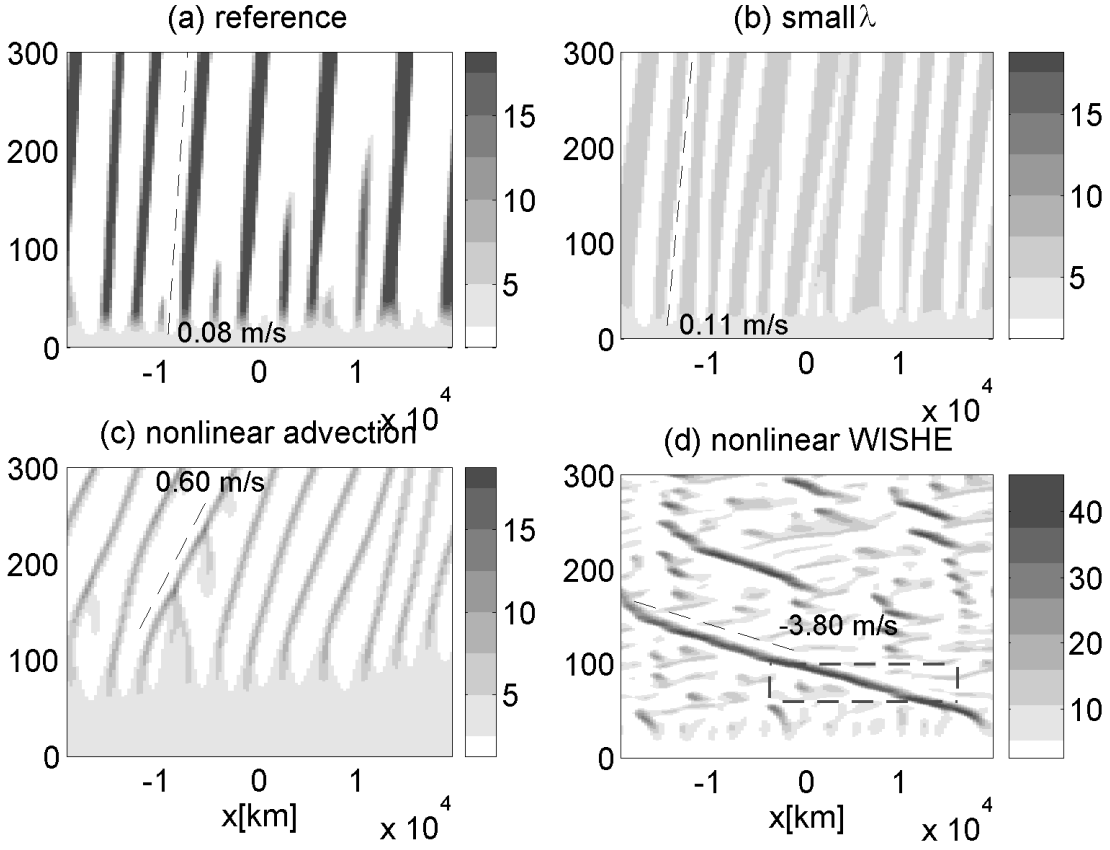

Figure 6-3: As in Fig. 6-2 but out to $t = 300$d. Dashed lines in (a), (b), (c), and (d) represent phase speeds of 0.08 m/s, 0.11m/s, 0.6m/s, and -3.8m/s, respectively. The phase speeds were subjectively chosen only for illustration purposes. The box in (d) indicates the target disturbance for the composite in Figs. 6-6, 6-7, 6-8, and 6-9.

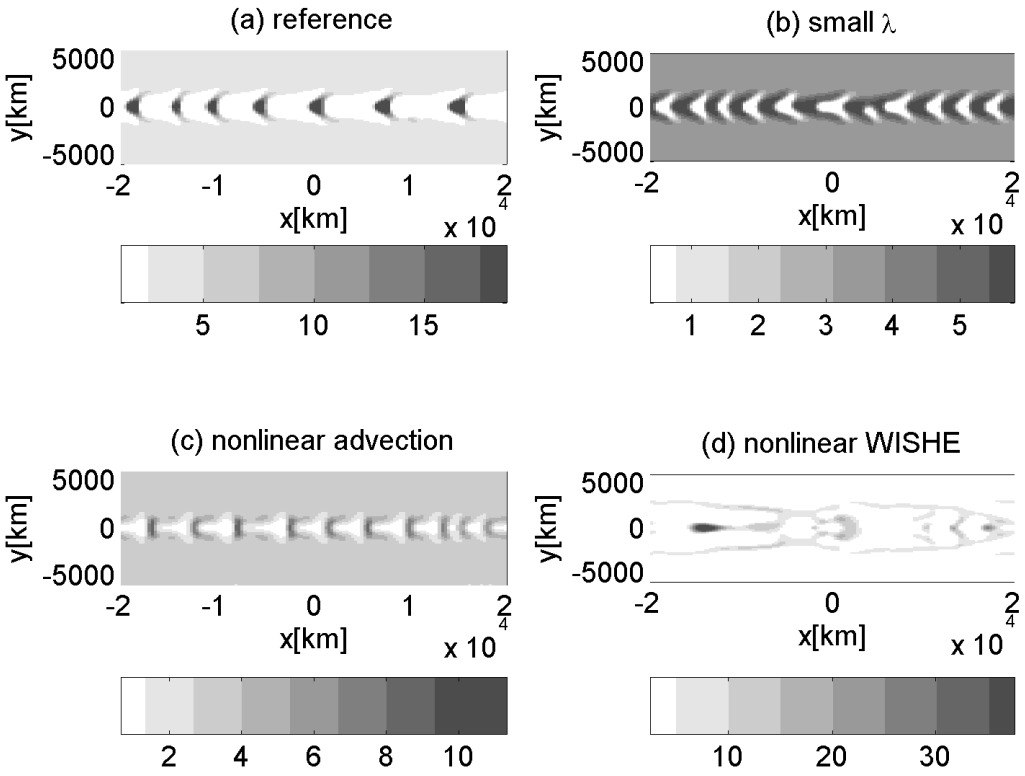

Figure 6-4: Snapshots of total precipitation $P = \overline{P} + P'$ in mm/day for the main runs listed in Table 6.3 at day 300. (a) Case 1, reference; (b) Case 2, weak cloud forcing; (c) Case 3, nonlinear advection; and (d) Case 4, nonlinear WISHE.

idea about progression of the modes. The upper panel shows P, E, $(\overline{q}_1 + q'_1)/\tau_c$, and $(\overline{T}_1 + T'_1)/\tau_c$, all in units of mm/day. Recall that the total precipitation is $(\overline{q}_1 + q'_1 - \overline{T}_1 - T'_1)/\tau_c$. The graph shows that E and T_1 change little and most of the variation in P is attributable to q_1. Eastward movement of precipitation is roughly equivalent to that of humidity anomaly.

Turning to the moisture budget, the middle panel describes the two dominant terms: moisture convergence/divergence $\overline{M}_{q1}\nabla \cdot \mathbf{v}'_1$, and net precipitation $P - E$. There is a strong cancellation between the moisture convergence term and the net precipitation. Also shown in the figure is the surface zonal wind. To the west of a peak of precipitation lies a westerly anomaly, and a very weak easterly anomaly is found to the east. This implies that the wind pattern is reminiscent of the Gill (1980) pattern. Gill's solution has a Kelvin response to the east of convection and a Rossby response to the west, and the Rossby gyres induce stronger low-level westerlies than easterlies in the Kelvin response in general (see below).

Westerlies that are stronger than easterlies yield asymmetric advection, resulting in eastward movement. The lower panel of Fig. 6-5 compares the sum of moisture convergence/divergence and net evaporation $\overline{M}_{q1}\nabla \cdot \mathbf{v}'_1 - P + E$ and the term that represents nonlinear advection $M_{qp}\nabla \cdot (q'_1\mathbf{v}'_1)$. The solid line in this panel ($M_{qp}\nabla \cdot (q'_1\mathbf{v}'_1)$) indicates that there is clearly a negative advective tendency on the western side of each disturbance, which favors eastward translation. In addition, it shows that diffusion actually plays an active role on the eastern side of disturbances. (The diffusive tendency is larger on the western flack of disturbances, but the advective tendency is still bigger. The opposite is true for the eastern side.)

Next I turn to the case of nonlinear WISHE, Case 4. Because the nonlinear WISHE case lacks a smooth evolution as found in the nonlinear advection case, I have created a composite of daily outputs to enhance the signal-to-noise ratio. As an index for making a composite, I employ the maximum precipitation for day 60-100, essentially isolating the disturbance in the box in Fig. 6-3d. Figs. 6-6, 6-7, 6-8, and 6-9 describe the composites created in this manner. The zonal coordinate is shifted so that the peak of precipitation is at x = 0km.

Depicted in Fig. 6-6 is the zonal section of the composite precipitation, evaporation,

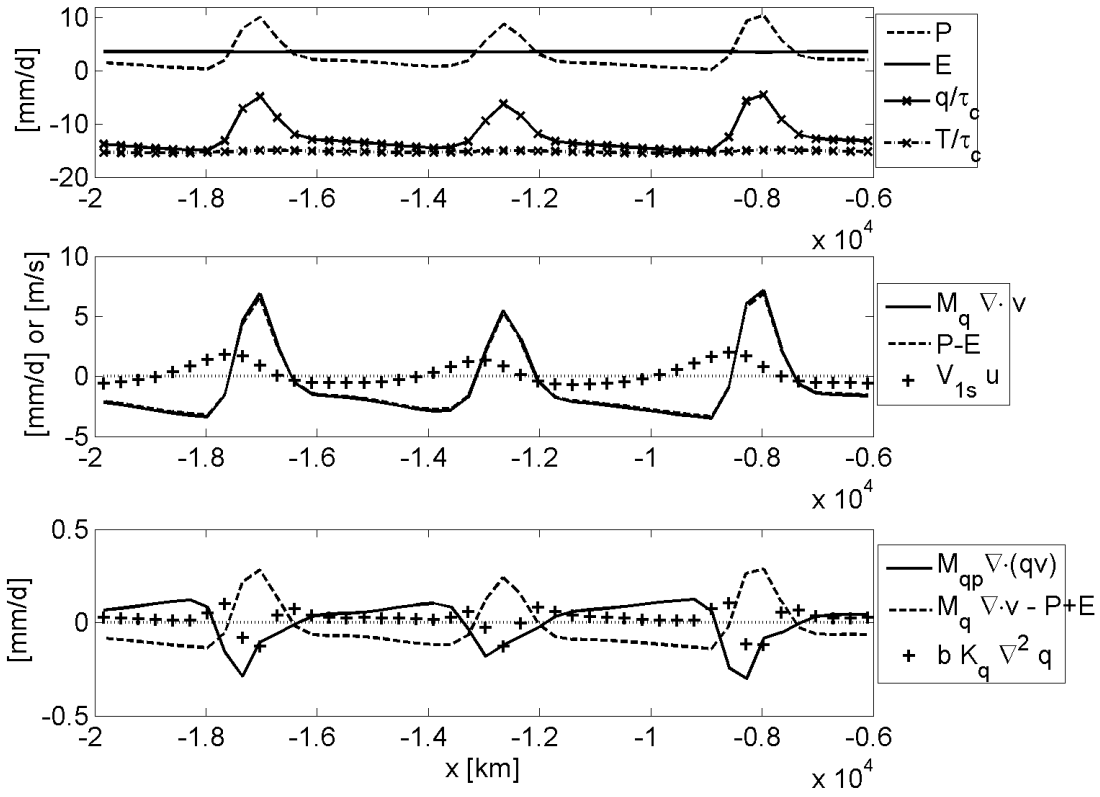

Figure 6-5: Snapshots of terms in the humidity budget for Case 3, nonlinear advection at day 300. The horizontal axis represents the zonal coordinate x from -20000km to -6000km. (Upper panel) total precipitation P, total evaporation E, $(\overline{q}_1 + q'_1)/\tau_c$, and $(\overline{T}_1 + T'_1)/\tau_c$, all in units of mm/day. (Middle panel) $\overline{M}_{q1}\nabla\cdot\mathbf{v}'_1$, $P-E$, both in units of mm/day, and surface zonal wind speed $V_{1s}u'_1$ in m/s. (Lower panel) $\overline{M}_{q1}\nabla\cdot\mathbf{v}'_1 - P + E$, $M_{qp}\nabla\cdot(q'_1\mathbf{v}'_1)$, and $\hat{b}_1 K_q \nabla^2 q'_1$.

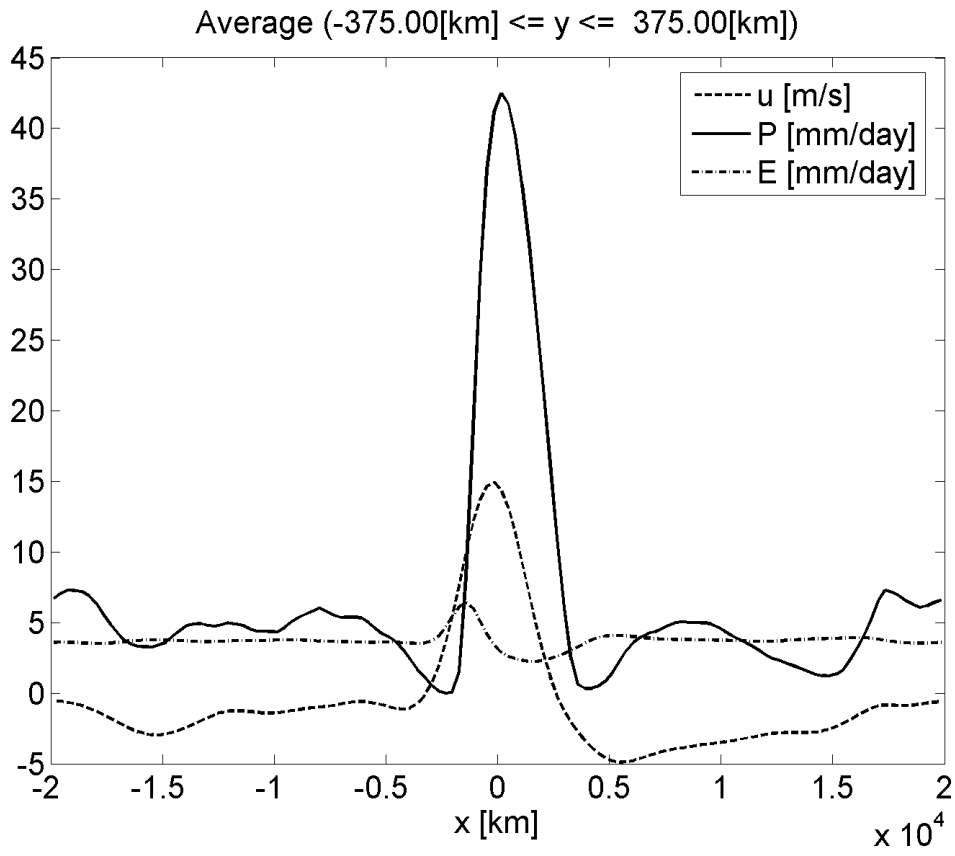

Figure 6-6: Zonal section of the composite of the precipitation, evaporation, and zonal mean wind for Case 4, nonlinear WISHE. All variables are averaged over $-375\text{km} \leq y \leq 375\text{km}$. The zonal coordinate has been shifted so that the peak of precipitation is at $x = 0\text{km}$.

and surface zonal wind. There is a significant peak of precipitation at the center of the domain with a zonal width of about 5000km. Accompanying this core of anomalous precipitation is the zonal wind field that again looks like a Gill pattern. Evaporation depends on humidity anomaly, surface winds, and gustiness. Because of the nonlinear WISHE effect, the maximum evaporation appears slightly to the west of anomalous convection.

Fig. 6-7 shows the horizontal structure of winds and precipitation, confirming that the spatial structure indeed resembles that of the Gill pattern. In contrast with the zonal scale, the meridional scale is very narrow and still seems to be controlled by eddy diffusion of humidity.

Figs. 6-8 and 6-9 examine the humidity budget of the moisture mode. The upper panel

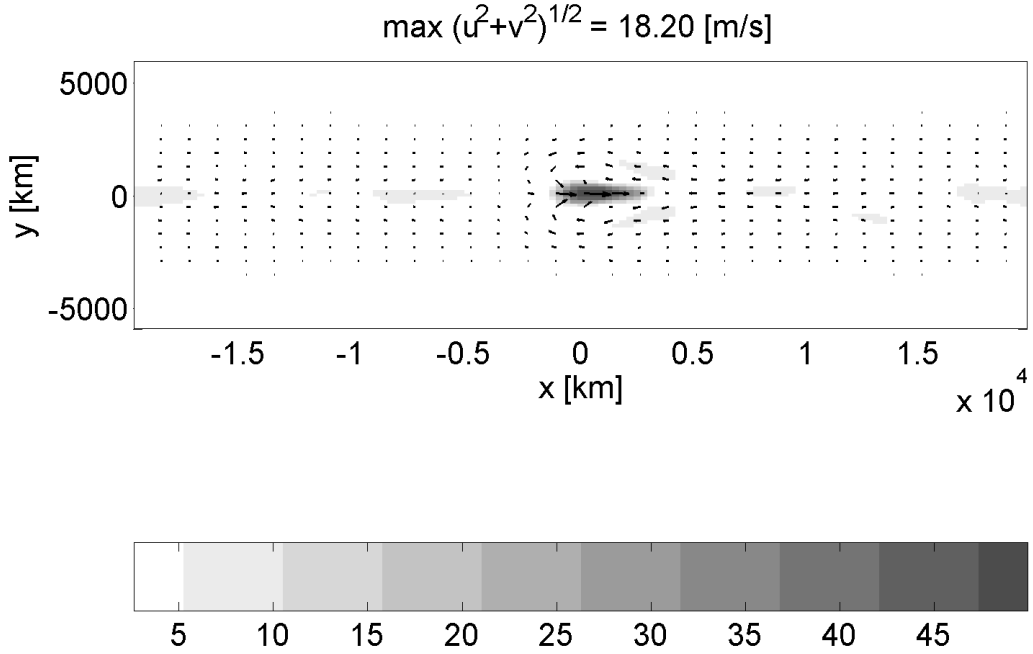

Figure 6-7: Horizontal structures of the composite of the precipitation and horizontal winds for Case 4, nonlinear WISHE. The shading represents precipitation, whose scale is shown in the gray bar in mm/day. Arrows indicate surface winds and the maximum wind speed is about 18.2 m/s.

of Fig. 6-8 plots the total precipitation P, $(\overline{q}_1 + q'_1)/\tau_c$, and $(\overline{T}_1 + T'_1)/\tau_c$ for the composite, all in units of mm/day. Unlike the case of nonlinear advection, temperature contributes to the structure of P, although humidity still dominates the variation. The reason for temperature being important in this case could be that the precipitation anomaly in Case 4 is much larger than in Case 3. The larger heating causes temperature perturbations to be discernible, which in turn affects the precipitation anomaly. The lower panel compares moisture divergence $\overline{M}_{q1}\nabla\cdot\mathbf{v}'_1$, net precipitation $P-E$, evaporation E, and numerical diffusion. Moisture convergence and net precipitation closely follow each other, but the residual is shifted to the western side of the disturbance presumably because of nonlinear WISHE; evaporation has a clear peak west of active convection. The reason for westward movement thus appears like nonlinear WISHE. Unlike Case 3 with nonlinear advection, diffusion is not significant in this case.

Though the disturbance proceeds to the west, Fig. 6-8 demonstrates that the atmosphere is drier to the immediate west of the core of convection. One might invoke the idea put forth by Rodwell and Hoskins (1996, 2001) to explain the drying. They noted that the Gill pattern has a strong subsidence west of the heating, and that in the case of the subtropics the subsidence due to monsoon heating can account for a significant fraction of strong descent regions to its west. (They also pointed out that a diabatic feedback further reinforces the subsidence in the descent region.) As expected, the lower panel of Fig. 6-8 shows that the subsidence is contributing to drying on the western flank of convection.

Fig. 6-9 shows the zonal average of the composites of $\overline{M}_{q1}\nabla\cdot\mathbf{v}'_1$, P, and E. The figure vividly indicates non-wavelike nature of the disturbance, exhibiting a mean meridional circulation. Also notice the increase in the domain-integrated evaporation; evaporation near the meridional boundaries represents the values of RCE, and evaporation exceeds this value near the equator. One possible reason for this is that enhanced precipitation has led to enhanced gustiness, which in turn has increased evaporation. Another mechanism is the lack of the mean wind in the basic state. Recall that the surface wind speed for surface heat flux is $\sqrt{V_{1s}^2({u'_1}^2 + {v'_1}^2) + v_g^2 + v_{bg}^2}$. In this formulation, any large-scale wind anomalies always lead to larger heat fluxes because large-scale winds enter as quadratic quantities.

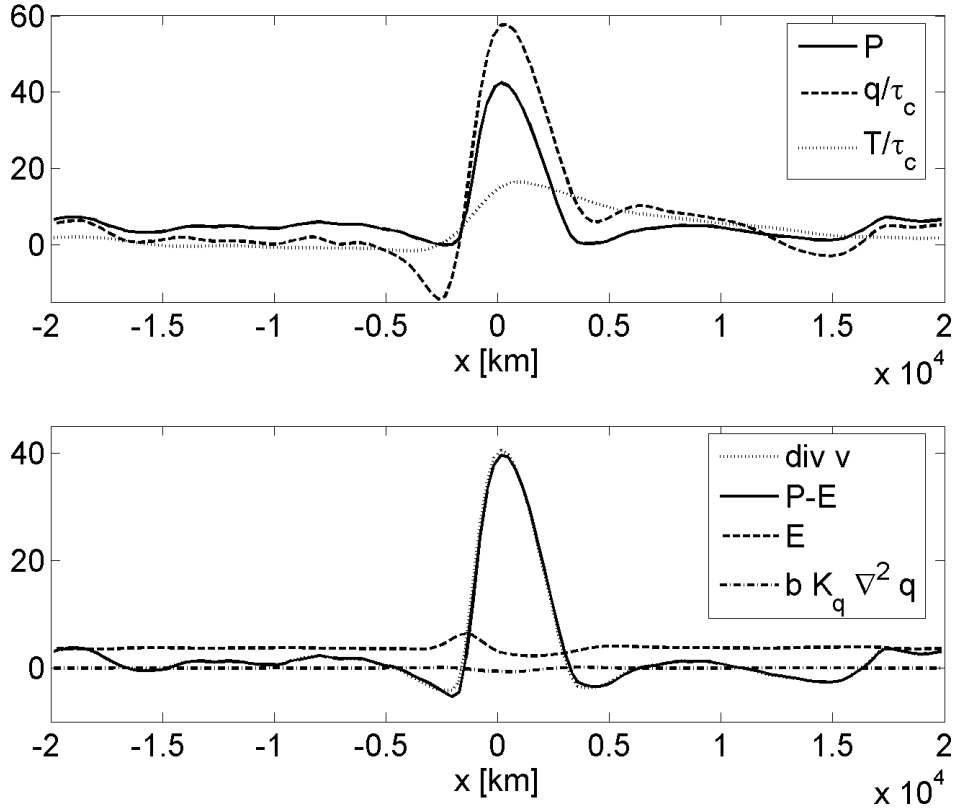

Figure 6-8: Zonal section of moisture budget of the composited nonlinear moisture mode, averaged over $-375\text{km} \leq y \leq 375\text{km}$. (Upper panel) total precipitation P, $(\overline{q}_1 + q_1')/\tau_c$, and $(\overline{T}_1 + T_1')/\tau_c$, all in units of mm/day. (Lower panel) $\overline{M}_{q1}\nabla\cdot\mathbf{v}_1'$, $P-E$, and E, all in mm/day.

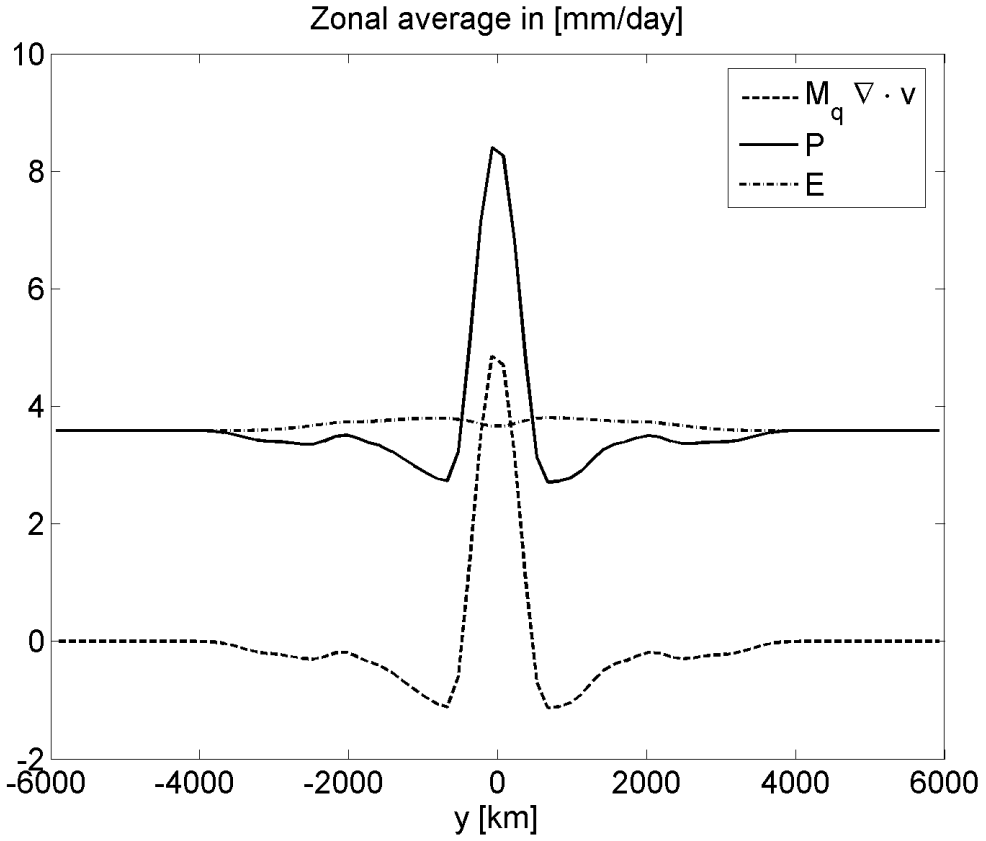

Figure 6-9: Zonal averages of composited $\overline{M}_{q1}\nabla\cdot\mathbf{v}_1'$, P, and E, all in units of mm/day.

Compare the present equation with

$$\sqrt{(U+V_{1s}u_1')^2+V_{1s}^2{v_1'}^2+v_g^2+v_{bg}^2}, \tag{6.11}$$

where U indicates a barotropic zonal mean flow. The alternative formula could decrease surface fluxes if the variations in meridional wind and gustiness are small and if U and $V_{1s}u_1'$ are of different sign. Such a mechanism is impossible in the present run.

So far I have resorted to the concept of the Gill (1980) pattern many times, but is it really relevant? The Gill pattern is a damped, stationary response of the tropical atmosphere to a localized heating. Here disturbances are moving either eastward or westward. How is a stationary solution related to a moving one?

The key to resolve the apparent conundrum is to recognize that in addition to momentum and temperature, the model has another prognostic variable, namely humidity. Now consider a system composed of Eqs. (6.12), (6.13), and (6.14):

$$\frac{\mathbf{v}_1'}{\tau_m}+\beta y\mathbf{k}\times\mathbf{v}_1' = -\kappa\nabla T_1', \tag{6.12}$$

$$\hat{a}_1\frac{T_1'}{\tau_R}+\overline{M}_{s1}\nabla\cdot\mathbf{v}_1' = \frac{P'}{\Delta p/g}+\left\langle Q_{R,cld}'\right\rangle+\frac{H'}{\Delta p/g}, \tag{6.13}$$

$$\hat{b}_1\frac{\partial q_1'}{\partial t}-\overline{M}_{q1}\nabla\cdot\mathbf{v}_1'-M_{qp}\nabla\cdot(q_1'\mathbf{v}_1') = -\frac{P'}{\Delta p/g}+\frac{E'}{\Delta p/g}+K_q\hat{b}_1\nabla^2q_1'. \tag{6.14}$$

In these equations, the time tendencies of momentum and temperature are set to zero, and Eqs. (6.12) and (6.13) are similar to Gill's equations. Nonetheless, the system still has a capacity to evolve with time owing to the prognostic humidity equation (6.14). Since the analyses so far have indicated a similarity between the Gill's solution and the full model, one would anticipate that the equations (6.12), (6.13), and (6.14) should reproduce results akin to those of the full model.

To explore whether my interpretation is correct, I solve Eqs. (6.12), (6.13), and (6.14) numerically. A possible solution method is to solve an elliptic problem. To simplify alge-

bra, let us define the following:

$$\varepsilon \equiv \frac{1}{\tau_m}, \tag{6.15}$$

$$\varphi' \equiv \kappa T_1', \tag{6.16}$$

$$c^2 \equiv \frac{\tau_R}{\tau_m}\frac{\kappa \overline{M}_{s1}}{\hat{a}_1}, \tag{6.17}$$

$$-Q' \equiv \frac{\tau_R}{\tau_m}\frac{\kappa}{\hat{a}_1}\left(\frac{P'}{\Delta p/g} + \left\langle Q'_{R,cld}\right\rangle + \frac{H'}{\Delta p/g}\right). \tag{6.18}$$

By indicating nondimensional variables with tildes, I next introduce Gill's (1980) nondimensionalization, a modification of Matsuno's (1966):

$$\mathbf{v}_1' = c\tilde{v}, \tag{6.19}$$

$$\varphi' = c^2\tilde{\varphi}, \tag{6.20}$$

$$(x,y) = \sqrt{\frac{c}{2\beta}}(\tilde{x},\tilde{y}), \tag{6.21}$$

$$\left(t,\frac{1}{\varepsilon}\right) = \sqrt{\frac{1}{2c\beta}}\left(\tilde{t},\frac{1}{\tilde{\varepsilon}}\right), \tag{6.22}$$

$$Q' = c^2\sqrt{2c\beta}\tilde{Q}. \tag{6.23}$$

This leads to the nondimensional momentum and temperature equations, (6.24) and (6.25).

$$\tilde{\varepsilon}\tilde{\mathbf{v}} + \frac{1}{2}\tilde{y}\mathbf{k}\times\tilde{\mathbf{v}} = -\tilde{\nabla}\tilde{\varphi}, \tag{6.24}$$

$$\tilde{\varepsilon} + \tilde{\nabla}\cdot\tilde{\mathbf{v}} = -\tilde{Q}. \tag{6.25}$$

One can then reduce Eqs. (6.24) and (6.25) to an elliptic problem (6.26).

$$\left(\frac{\partial^2}{\partial\tilde{x}^2} + \frac{\partial^2}{\partial\tilde{y}^2}\right)\tilde{\varphi} - \frac{1}{2\tilde{\varepsilon}}\frac{\tilde{\varepsilon}^2 - \tilde{y}^2/4}{\tilde{\varepsilon}^2 + \tilde{y}^2/4}\frac{\partial\tilde{\varphi}}{\partial\tilde{x}} - \frac{\tilde{y}/2}{\tilde{\varepsilon}^2 + \tilde{y}^2/4} - \left(\tilde{\varepsilon}^2 + \frac{\tilde{y}^2}{4}\right)\tilde{\varphi} = -\frac{\tilde{\varepsilon}^2 + \tilde{y}^2/4}{\tilde{\varepsilon}}\tilde{Q}. \tag{6.26}$$

As it turns out, solving (6.26) is not straightforward because of nonlinearities in surface fluxes and precipitation that affect Q. In other words, solving (6.26) alters temperature, which in turns directly changes precipitation and indirectly affects surface fluxes. This

reduces the merit of using (6.26) for numerical solutions.

An easier approach is to iterate Eqs. (6.1) and (6.2) many times for each time step of Eq. (6.3). If the number of iterations is sufficient, such a system should look like Eqs. (6.12), (6.13), and (6.14). I choose the number of iterations as 20. Alternatively, one can suppose that the time step for momentum and temperature is smaller by a factor of 20 than that for humidity.

Sensitivity runs demonstrate that increasing iteration from 20 to 100 does not alter the outcomes significantly. (Since the initial perturbation is given for temperature, in the first time step, the momentum and temperature equations are calculated only once.)

Figs. 6-10 and 6-11 show the Hovmöller diagrams and snapshots of precipitation for the system (6.12), (6.13), and (6.14), which are counterparts of Figs. 6-3 and 6-4. As expected, these calculations reproduce the main features that are found in Figs. 6-3 and 6-4. In Fig. 6-10d, the simulation filters out almost all the waves and the nonlinear moisture mode becomes even more coherent, although there are still some remnants of waves. Another significant difference is that the disturbance in Fig. 6-10d is much more rapid than in Fig. 6-3d.

In any event, the results from the simplified system give a strong support for the Gill-model interpretation of dynamics of nonlinear moisture modes. It also points out that the time evolution of such a mode resides solely in the humidity variable, vindicating the centrality of moisture.

6.4 Sensitivity tests

The preceding section has discovered that once a moisture mode reaches a nonlinear regime, its dynamics can be understood in terms of Gill's (1980) model, and that it can move owing to moist processes. However, relying on the Gill model might be problematic since away from the boundary layer, it is difficult to justify short damping timescales employed in the Gill model (Lindzen and Nigam 1987; Neelin 1989). Lin et al. (2005) recently reported a strong damping in the MJO, finding that linear advection of momentum

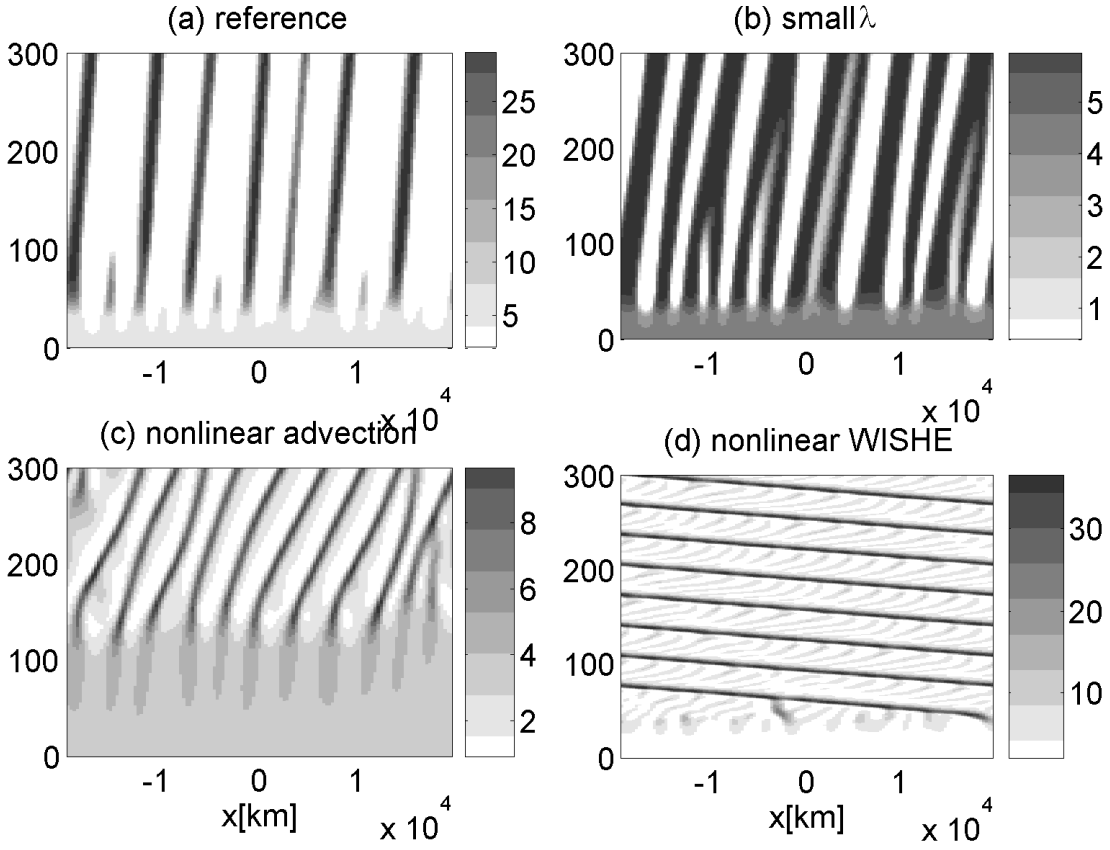

Figure 6-10: As in Fig. 6-3 but for the system composed of Eqs. (6.12), (6.13), and (6.14).

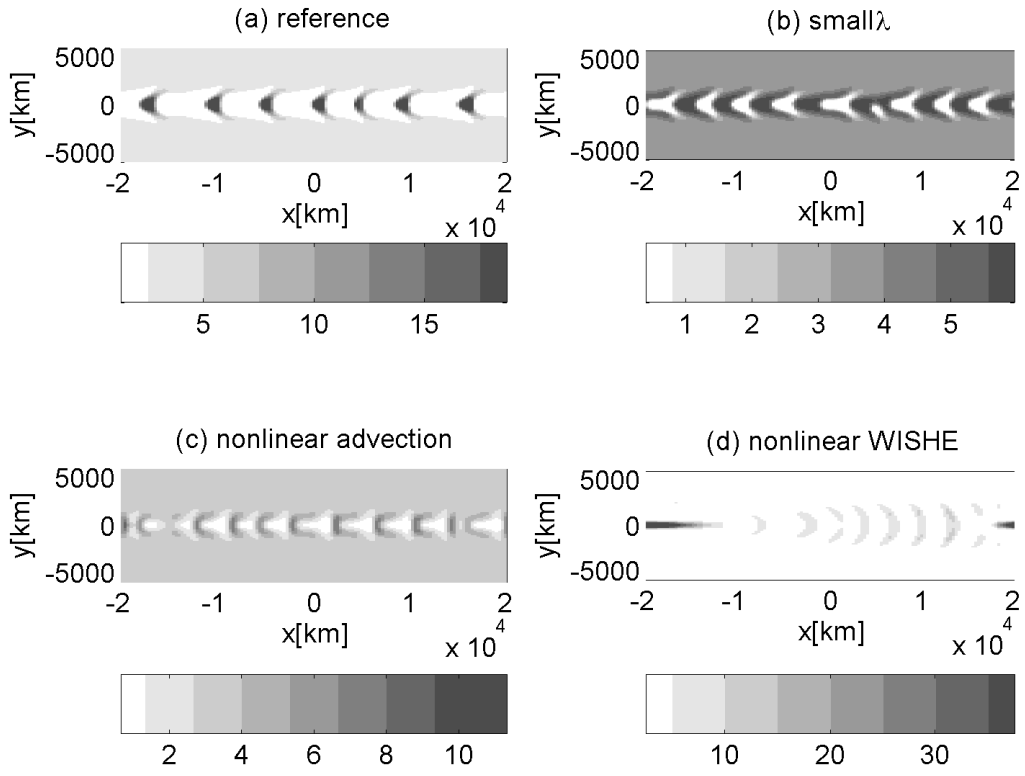

Figure 6-11: As in Fig. 6-4 but for the system composed of Eqs. (6.12), (6.13), and (6.14).

Table 6.4: List of sensitivity tests.

Group name	Notes	Parameters changed
A	Increased resolution	Δx=156.25, Δy=75km, Δt = 150s
B	Weakened Rayleigh damping	$\tau_m = 50 \cdot 10^5 \text{s} \approx 57.9\text{d}$
C	Nonlinear momentum damping	See Eq. (6.27)

and cumulus friction causes an equivalent damping timescale of about 5 days, but whether their finding is robust remains to be seen. Also using Rayleigh damping and Newtonian cooling automatically guarantees that dynamics is linear, and that nonlinear limiting processes must be of thermodynamic origin. And yet dynamics could be an essential nonlinear limiting process as well. Yano et al. (1995) argued that quadratic momentum damping through boundary layer friction is important.

In order to address these issues, the following examines sensitivity tests, which are listed in Table 6.4. As is necessary for any numerical calculations, the first test concerns resolution. The second sensitivity test explores the impact of elongating the Rayleigh damping timescale. The third set explores whether quadratic damping leads to a substantial change in the simulations.

In the case of nonlinear damping, the momentum equation (6.1) is replaced with

$$\frac{\partial \mathbf{v}_1'}{\partial t} + \beta y \mathbf{k} \times \mathbf{v}_1' = -\kappa \nabla T_1' - \frac{V_{1s}^2}{\left\langle V_1^2 \right\rangle} \frac{\rho_a C_D}{\Delta p / g} \sqrt{V_{1s}^2 |\mathbf{v}_1'|^2 + v_g^2 + v_{bg}^2} \cdot \mathbf{v}_1'. \tag{6.27}$$

The coefficient $V_{1s}^2 / \left\langle V_1^2 \right\rangle$ arises from the systematic derivation of the first-baroclinic mode equation; see Neelin and Zeng (2000).

Fig. 6-12 represents the Hovmöller diagrams for the sensitivity test with resolution. The results are very similar to those in Fig. 6-3. Fig. 6-12c describes the effect of nonlinear advection, which concurs with Fig. 6-3c. The agreement between the two resolutions confirms that the effect of nonlinear advection is well captured, in spite of the coarse resolution and crude advection scheme employed in the simulation. In the nonlinear WISHE case, the most of the characteristics are reproduced here as well.

However, there is a slight difference. Although the agreement on the speed of movement between the standard and high resolution cases is assuring for the nonlinear advection

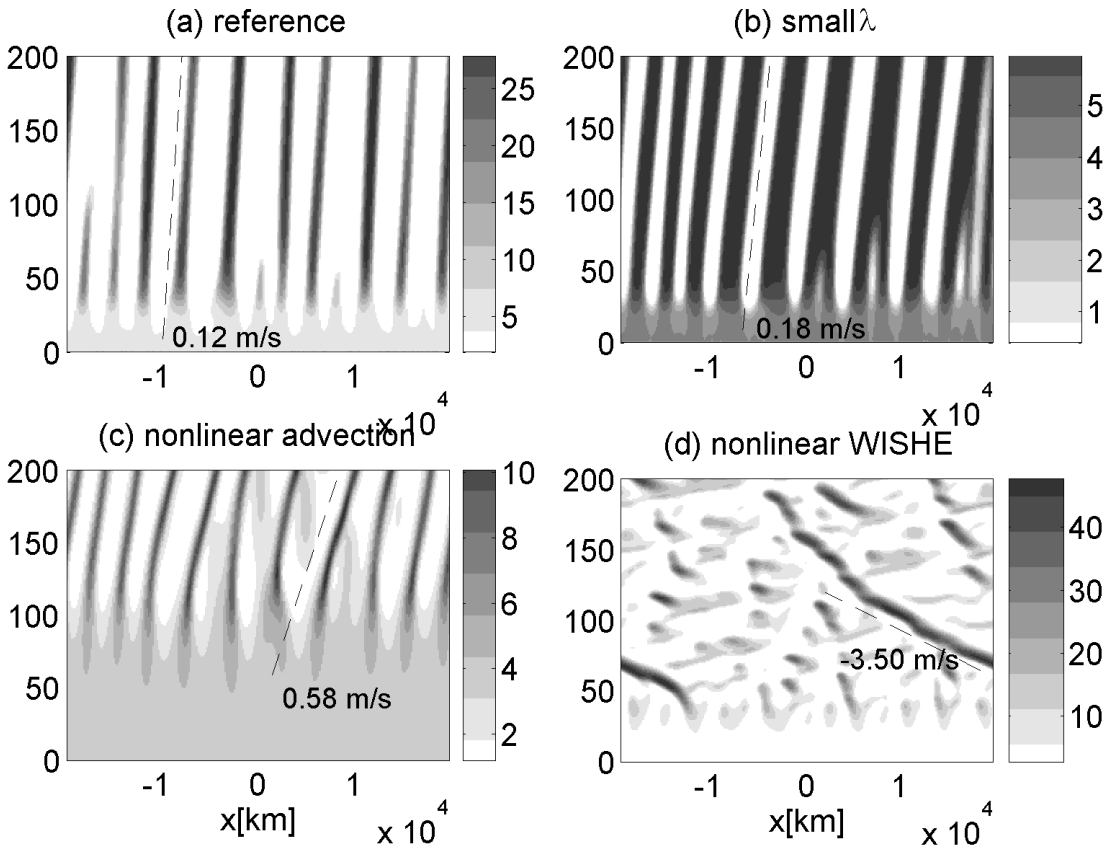

Figure 6-12: As in Fig. 6-3 but for the sensitivity test group A, with increased resolution. Note that the last time for the plot is 200 days rather than 300 days used in Fig. 6-3. Dashed lines in (a), (b), (c), and (d) represent phase speeds of 0.12 m/s, 0.18m/s, 0.58m/s, and -3.5m/s, respectively. The phase speeds were subjectively chosen only for the illustration purposes.

and nonlinear WISHE cases, it is substantially (about 50%) higher in the high resolution case for the diffusion only cases. Unfortunately the reason is not clear.

Fig. 6-13 shows the time evolution of precipitation for the sensitivity test on the strength of Rayleigh damping. In the reference case (Fig. 6-13a), now the preferred wavenumber at the final time is 6, rather than 7 found in Fig. 6-3a. The weak damping has increased the saturation precipitation rate, and led to a lower wavenumber. The nonlinear evolution is also evident in Fig. 6-13a. Until about day $\sim$ 30, the predominant wavenumber is 13 but the nonlinear saturation reduces the number of disturbances to 6.

In the nonlinear advection case (Fig. 6-13c), the weak damping also contributes to

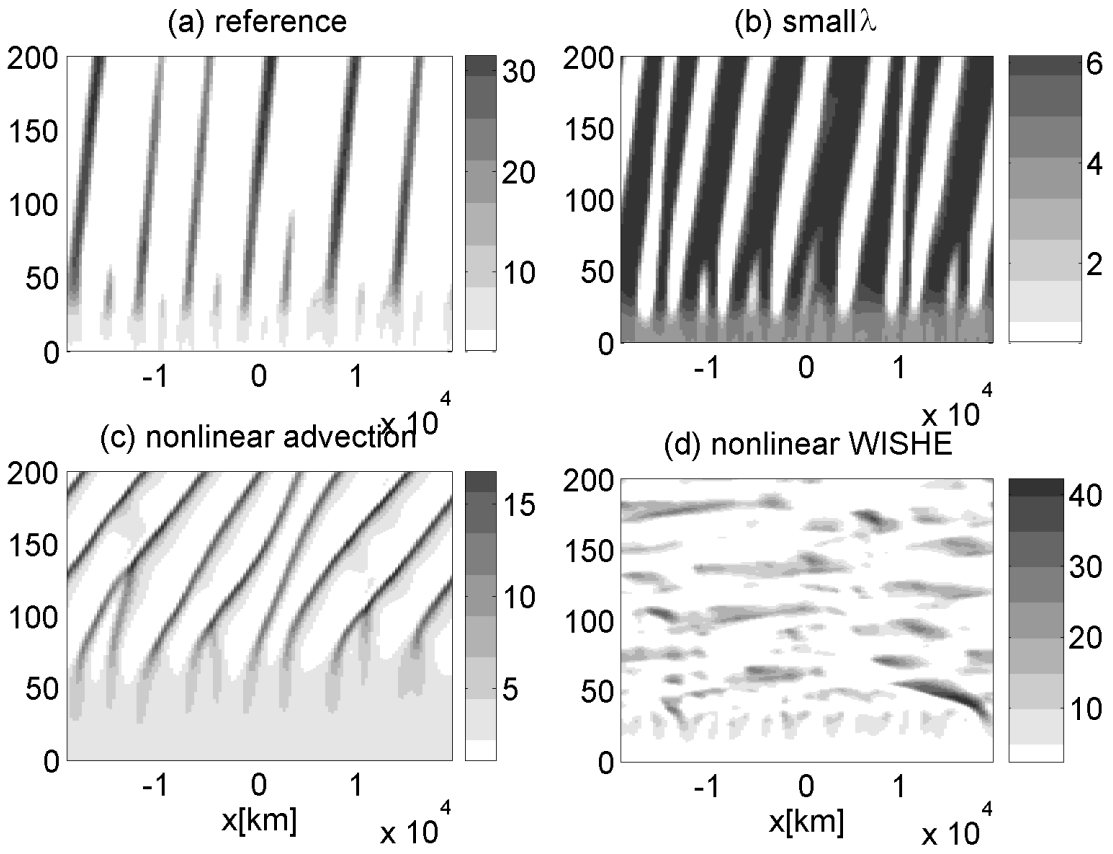

Figure 6-13: As in Fig. 6-12 but for the sensitivity test group B, with weakened Rayleigh damping.

a faster movement of disturbances since for a given precipitation rate, a weaker damping gives a stronger wind response. As the nonlinear advection is a magnitude-dependent mechanism, a stronger zonal wind implies a faster movement.

The nonlinear WISHE case interestingly shows less coherent disturbances (Fig. 6-13d). Although one can still trace westward disturbances, they are more intermittent and last for a much shorter duration.

Shown in Fig. 6-14 are the Hovmöller diagrams for the sensitivity test on nonlinear momentum damping. The results are qualitatively similar to what is shown in Fig. 6-3, showing that thermodynamics play more important roles as a nonlinear limiting process in the present simple formulation of QTCM.

In conclusion, the sensitivity tests performed in this section confirm robustness of basic

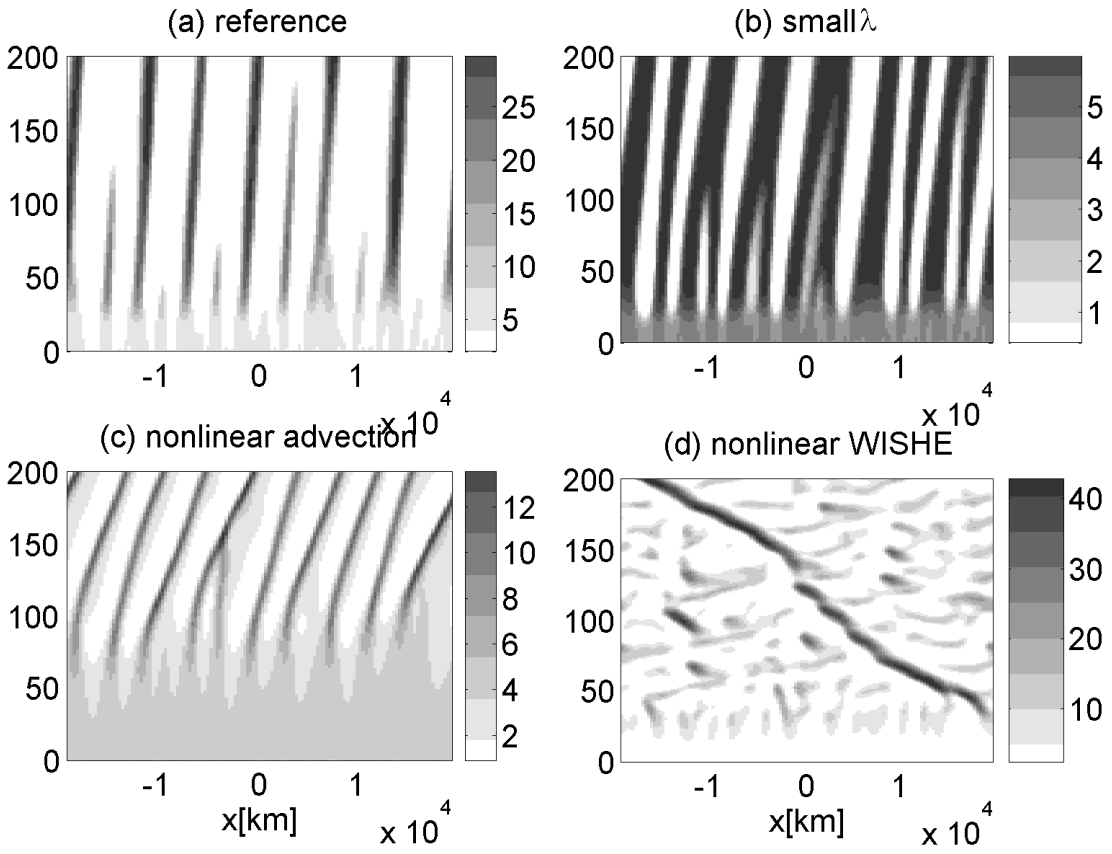

Figure 6-14: As in Fig. 6-12 but for the sensitivity test group C, with nonlinear momentum damping.

features of nonlinear moisture modes.

6.5 Including all nonlinear moist processes

Thus far I have been isolating each moist process to analyze, but in nature, different processes operate at the same. What would happen if one combines different mechanisms? Unfortunately, when both nonlinear WISHE and nonlinear advection are included, the model blows up because of negative gross moist stability. To understand this, add Eqs. (6.2) and (6.3) and one finds the moist enthalpy equation:

$$\frac{\partial}{\partial t}(\hat{a}_1 T_1' + \hat{b}_1 q_1') + M\nabla\cdot\mathbf{v}_1' - M_{qp}\mathbf{v}_1'\cdot\nabla q_1' = \left\langle Q_{R,cld}\right\rangle' - \hat{a}_1\frac{T_1'}{\tau_R} + \frac{H'+E'}{\Delta p/g} + K_q\hat{b}_1\nabla^2 q_1', \tag{6.28}$$

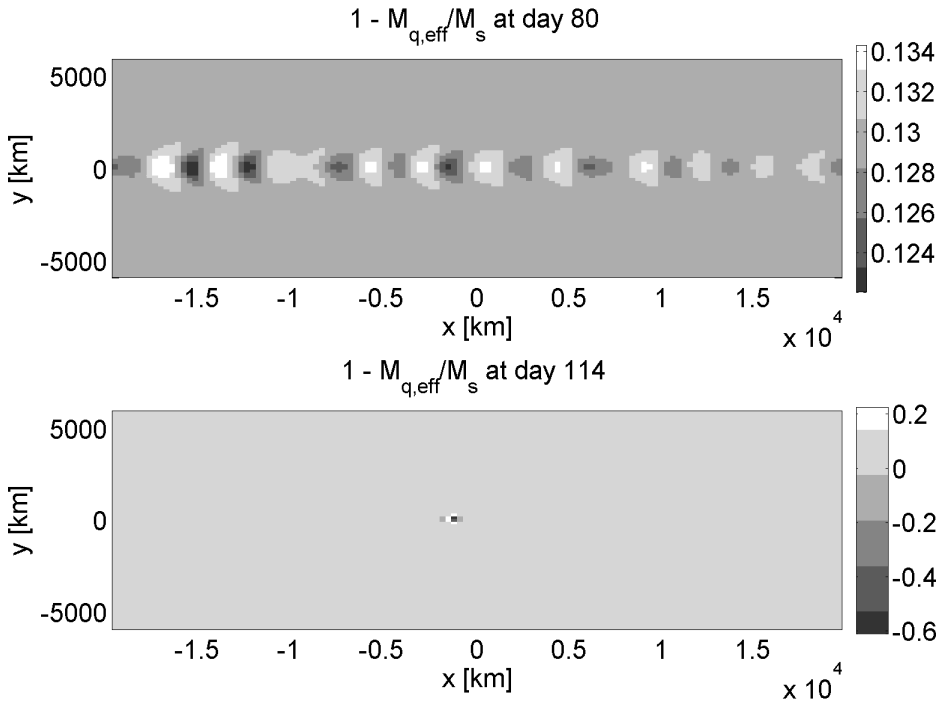

Figure 6-15: Normalized gross moist stability $M/\overline{M}_{s1} = 1-(\overline{M}_{q1}+M_{qp}q_1')/\overline{M}_{s1}$ for the simulation with both nonlinear WISHE and nonlinear advection included. The upper panel corresponds to day 80 whereas the lower panel represents day 114, just before the model blows up.

where the gross moist stability is defined as $M \equiv \overline{M}_{s1} - \overline{M}_{q1} - M_{qp}q_1'$. Notice that the gross moist stability is now a function of humidity because of the nonlinear advection term. For $q_1' > (\overline{M}_{s1} - \overline{M}_{q1})/M_{qp}$, the gross moist stability becomes negative, which yields a radiative-convective instability that cannot be regulated by nonlinear thermodynamic processes in the model. Such an instability does not necessarily have to occur. Indeed, the nonlinear advection case has this effect but does not exhibit this instability.

Fig. 6-15 shows the normalized gross moist stability $M/\overline{M}_{s1} = 1-(\overline{M}_{q1}+M_{qp}q_1')/\overline{M}_{s1}$ at day 80 and day 114 for a simulation with both nonlinear WISHE and nonlinear advection. In the linear regime at day 80, the gross moist stability remains close to the reference value. At day 114, just before the model blows up, one finds a negative gross moist stability near the center of the domain. The model's inability to incorporate nonlinear WISHE and nonlinear advection is a fatal issue that requires elaboration, to which I turn later.

6.6 Analysis using the classical Gill model

Section 6.3 has demonstrated usefulness of the classical Gill (1980) model in interpreting the behavior of nonlinear moisture modes in QTCM. Since an analytical solution is readily available, this section attempts to gain more insight into the problem at hand, focusing on the effect of nonlinear advection.

Gill made a long-wave approximation to Eqs. (6.24) and (6.25) by dropping the tendency and damping terms in the meridional momentum equation to allow for an analytic solution. This amounts to filtering inertio-gravity waves but retaining Kelvin, Rossby, and mixed Rossby-gravity waves. His equations are my Eqs. (6.24) and (6.25) with tildes dropped and the long-wave approximation:

$$\varepsilon u - \frac{1}{2} y v = -\frac{\partial \varphi}{\partial x}, \tag{6.29}$$

$$\frac{1}{2} y u = -\frac{\partial \varphi}{\partial y}, \tag{6.30}$$

$$\varepsilon \varphi + \frac{\partial u}{\partial x} + \frac{\partial v}{\partial y} = -Q. \tag{6.31}$$

The heating function used by Gill is

$$Q(x) = \begin{cases} \cos kx \, \exp(-y^2/4), & |x| < L \\ 0, & |x| > L \end{cases}, \tag{6.32}$$

where $k \equiv \pi/(2L)$. Gill expanded u,v, φ in terms of parabolic cylinder functions, which are eigenfunctions for the homogeneous problem, and solved for each component. Because of his choice of the heating, his solution can be fully represented with low-order parabolic cylinder functions only. His solution for u is

$$u(x,y) = \overbrace{\frac{1}{2} q_0(x) \exp\left(-\frac{y^2}{4}\right)}^{\text{Kelvin response}} + \overbrace{\frac{1}{2} q_2(x)(y^2-3) \exp\left(-\frac{y^2}{4}\right)}^{\text{Rossby response}}, \tag{6.33}$$

where

$$q_0(x) \equiv \frac{1}{\varepsilon^2+k^2}\begin{cases} 0, & x<-L \\ -\varepsilon\cos kx - k\sin kx - k\exp[-\varepsilon(L+x)], & |x|<L \\ -k(1+\exp[-2\varepsilon L])\exp[-\varepsilon(x-L)], & x>L \end{cases} \tag{6.34}$$

$$q_2(x) \equiv \frac{1}{9\varepsilon^2+k^2}\begin{cases} -k(1+\exp[-6\varepsilon L])\exp[3\varepsilon(x+L)], & x<-L \\ -3\varepsilon\cos kx + k\sin kx - k\exp[-3\varepsilon(L-x)], & |x|<L \\ 0. & x>L \end{cases} \tag{6.35}$$

Note that q_0 corresponds to the Kelvin response whereas q_2 implies the Rossby response; q_0 is zero west of heating since the Kelvin wave propagates eastward, and vice versa.

Now I make an analogy between QTCM and the Gill model. In the Gill model, heating is prescribed and stationary whereas in QTCM, it is interactive. However, one can regard the Gill model as a snapshot of the evolving QTCM in the idealized situation where heating takes a simple form of (6.32).

To the extent that the temperature anomaly is weak, heating is proportional to q_1' because it is usually dominated by convection and cloud radiative forcing. Examining nonlinear advection of moisture is therefore *mathematically* equivalent to nonlinear advection of heating:

$$-u_1'\frac{\partial q_1'}{\partial x} \sim -u\frac{\partial Q}{\partial x}. \tag{6.36}$$

Gill's analytic solution above allows for explicit calculation of Eq. (6.36), which is

$$-u\frac{\partial Q}{\partial x}\bigg|_{y=0} = \begin{cases} k\sin kx\left(\frac{1}{2}q_0 - \frac{3}{2}q_2\right), & |x|<L \\ 0, & |x|>L \end{cases} \tag{6.37}$$

Because of the cosine form of heating, $\partial Q/\partial x$ at $x=\pm L$ is not unique and arbitrarily set to zero for graphical purposes.

Fig. 6-16 shows the implied nonlinear advection Eq. (6.37) along with heating and zonal wind for $L=1$ and $\varepsilon=0.1$, with $\varepsilon L=0.1$. In the upper panel, one sees a Kelvin response to the east of heating and a Rossby response to the west, with anomalous wester-

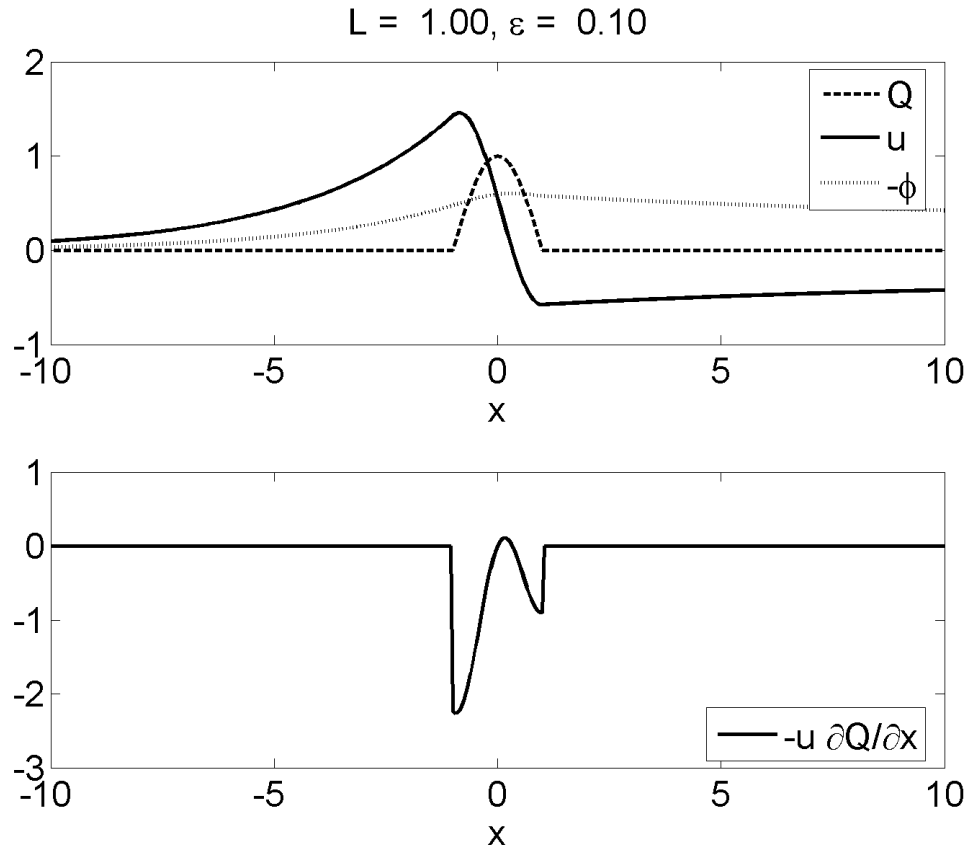

Figure 6-16: The analytical solution of Gill (1980) and implied humidity advection for the standard case $L = 1$ and $\varepsilon = 0.1$. (Upper panel) Heating Q and zonal wind u. (Lower panel) implied nonlinear advection, Eq. (6.37).

lies much larger than the easterly counterpart. This has a consequence on advection, which is depicted in the lower panel. The advective tendency on the western side is larger than the eastern side. The net effect is to slightly move the disturbance while squeezing it. The tendency of nonlinear advection to squeeze the humidity anomaly is also illustrated in Fig. 6-5.

Does the Gill pattern always have stronger westerlies than easterlies? Strictly speaking, the answer is no. It is instructive to compare the magnitudes of Kelvin and Rossby responses. In particular, I examine the ratio of the Kelvin and Rossby responses at the periphery of the heating:

$$\left|\frac{u_{\text{Kelvin}}}{u_{\text{Rossby}}}\right| \equiv \left|\frac{u(x=L,y=0)}{u(x=-L,y=0)}\right| = \frac{1}{3}\frac{9+[\pi/(2\varepsilon L)]^2}{1+[\pi/(2\varepsilon L)]^2}\frac{1+e^{-2\varepsilon L}}{1+e^{-6\varepsilon L}}. \tag{6.38}$$

Although this measure does not compare the maximum westerly and maximum easterly, it gives a reasonable comparison. In the two different limits, one finds contrasting behaviors:

$$\left|\frac{u_{\text{Kelvin}}}{u_{\text{Rossby}}}\right| \rightarrow \frac{1}{3} \qquad (\varepsilon L \rightarrow 0), \tag{6.39}$$

$$\left|\frac{u_{\text{Kelvin}}}{u_{\text{Rossby}}}\right| \rightarrow 3 \qquad (\varepsilon L \rightarrow \infty). \tag{6.40}$$

The nondimensional parameter εL measures how much a wave is damped while traveling across the heating region. The regime $\varepsilon L \rightarrow \infty$ corresponds to a limit of strong damping relative to the zonal scale of heating, whereas the other regime $\varepsilon L \rightarrow 0$ indicates a weak, relative damping. In the strong relative damping limit, either waves are strongly damped or the heating region is wide so that they are confined to the heating region. This regime is quite different from that envisaged by Gill and others, where a localized heating leads to a widespread dynamical response.

Fig. 6-17 performs sensitivity tests, showing (6.37) for various L. When the width of heating is expanded substantially, one sees the Kelvin response taking over the Rossby component. While this confirms suggestions from Eqs. (6.39) and (6.40), such a large change in the width is hard to realize on the earth.

As noted above, nonlinear advection has two effects; it moves the moisture mode eastward, and squeezes it. If nonlinear advection continues to squeeze, the disturbance keeps shrinking and would not travel a long distance. How, then, do the moisture modes move eastward with nonlinear advection? As Fig. 6-5 indicated, it is because of the effect of numerical diffusion. If the diffusion is made weaker, the squeezing effect might end up splitting a disturbance.

Although I have substantially altered the parameters here, such changes do not violate the assumptions utilized by Gill. To obtain the long wave approximation, he assumed $\varepsilon \ll 1$ and $2\varepsilon k \ll 1$. Increasing L does not affect the validity of these assumptions (it actually improves the relation $2\varepsilon k \ll 1$ since $k \equiv \pi/2L$).

Nevertheless, for the purpose of ensuring accuracy, I have numerically integrated Eqs. (6.24) and (6.25) in a time stepping manner for a sufficiently long period. The details of the

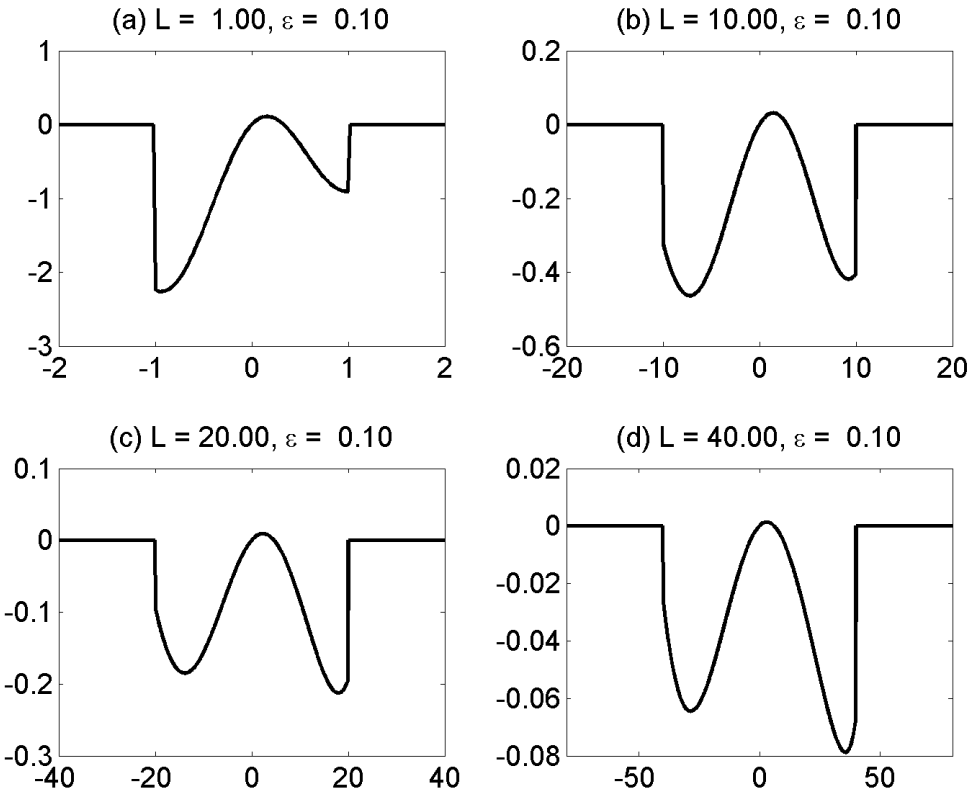

Figure 6-17: Sensitivity tests on Eq. (6.37). Note the different vertical scales for each panel.

simulation are as follows. The zonal domain width is 240, the meridional domain length is 15, $\Delta x = 240/399 \approx 0.60$, $\Delta y = 15/81 \approx 0.19$, and $\Delta t = 0.002$, with all variables in nondimensional units. The integration starts with an atmosphere at rest, and the model is run until $t = 100$

The output is shown in Fig. 6-18. The minimum wind speed (or maximum easterly) is -1.24 while the maximum wind speed (or maximum westerly) is 1.15; the Kelvin response is stronger, which corroborates the results in Fig. 6-17. However, the width of heating is expanded larger than the circumference of the earth (which is ~ 40 in nondimensional units), showing again that the limit of the Kelvin response exceeding the Rossby component is unlikely.

The analysis here also leads to a simple interpretation of nonlinear WISHE. To the extent evaporation fluctuations are controlled by large-scale winds, the Gill pattern would yield enhanced evaporation to its west. This spatial configuration is opposite to the classical linear WISHE (Emanuel 1987; Neelin et al. 1987), but Xie et al. (1993) and Maloney and Sobel (2004) found the same phase relationship as in this chapter.

6.7 Summary and discussion

By way of numerical calculations of QTCM, the present chapter has investigated the nonlinear behavior of an unstable moisture mode on the equatorial β-plane. In particular, it has examined different moist processes in isolation. Dynamics of nonlinear moisture modes can be interpreted as a linear damped response of momentum and temperature combined with a prognostic humidity equation. In other words, the model is a Gill's (1980) model augmented with a humidity equation. Nonlinear advection moves a disturbance eastward because of asymmetric advective effects due to Rossby gyres, whereas nonlinear WISHE selects the largest scale and contributes to the westward movement.

When I attempted to include both effects, however, the model blew up because of negative gross moist stability. The inability to include both nonlinear advection and nonlinear WISHE is a significant defect of the present model, and this is attributable to the choice

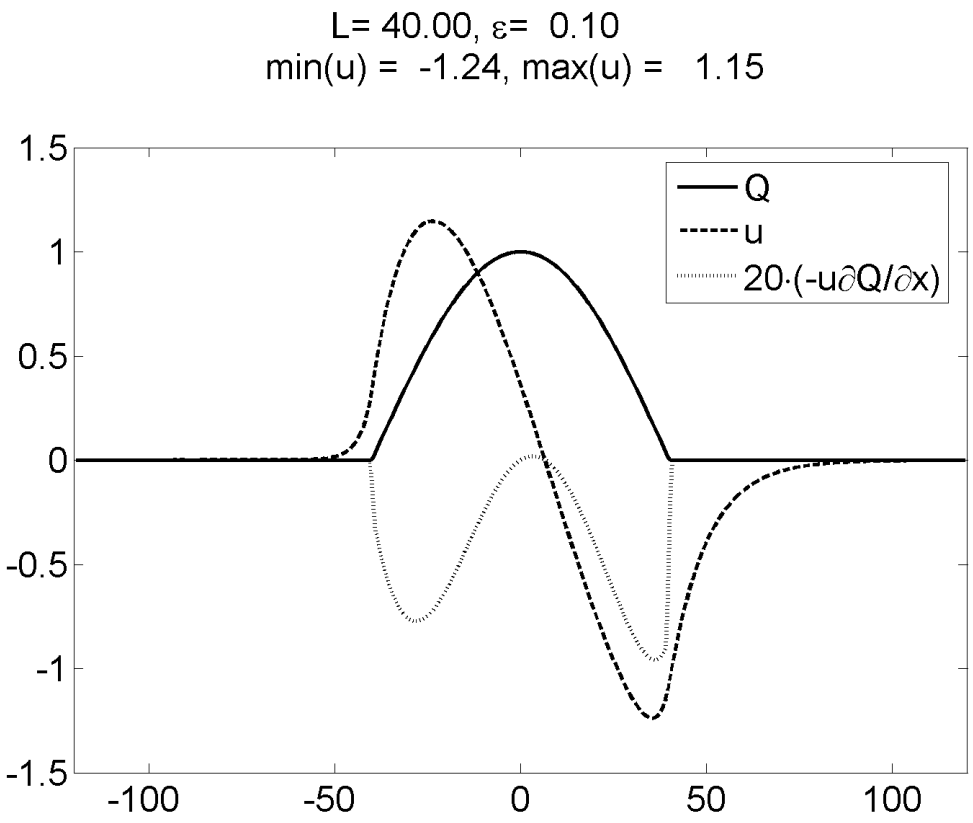

Figure 6-18: Numerical solutions to the Gill model, Eqs. (6.24) and (6.25), without the long wave approximation for $\varepsilon = 0.1$ and $L = 40$. The solid line represents heating Q, the dashed line the zonal velocity u, and the dotted line the advection of "heating" $-u\partial Q/\partial x$, all at the equator $y = 0$.

of a linear Betts-Miller scheme in QTCM. However, the issue is deeper than problems with the convective parameterization. For example, QTCM does not distinguish between the boundary layer and free troposphere, which is a serious drawback. This is because nonlinear WISHE is a surface process that affects the boundary layer whereas nonlinear advection is more likely to be important in the free troposphere. Separating humidity into two variables requires a model like that of Sobel and Neelin (2006). This is left to future research.

Both numerical simulations and a simple analysis have demonstrated that nonlinear advection moves the disturbance eastward (but much more slowly than observed) and squeezes it simultaneously, and that nonlinear advection cannot complete the task of eastward movement. What is then missing in the present model, compared with nature? Recent observational studies point to the importance of shallow convection that increases MSE in a column (Kikuchi and Takayabu 2004; Benedict and Randall 2007). QTCM is not equipped with the second baroclinic mode that is vital to implement the effect of shallow convection. Such a treatment would require a model like Khouider and Majda's (2006).

Another pertinent issue is the role of diffusion. Diffusion plays two roles; it suppresses grid-scale instabilities, and helps the disturbance move eastward in conjunction with nonlinear advection. The latter effect is unphysical but including shallow convective moistening might alleviate the problem. On the other hand, scale selection is a more severe issue. It is true that linear stability analysis is not the final word on scale selection, as is evident from my results, particularly from the nonlinear WISHE case. Even in that case, however, the meridional scale seemingly is determined by numerical diffusion.

In fact, the issue of scale selection seems to be a tough question. In a study on self-aggregation of moist convection in a cloud-resolving model, Bretherton et al. (2005) did not derive any equation for scale selection. Fuchs and Raymond (2002, 2005, 2007) found that in a theoretical model like the one used here, the smallest scales tend to be favored. Mapes (2000) noted that gust fronts are instrumental in organizing deep convection at the mesoscale. In essence, gust fronts are connecting different "columns" of the atmosphere. Although it is unknown to what extent this is effective at the large scale, interaction among

atmosphere columns is completely absent in the present formulation. A future analysis should at least give more consideration to scale selection of moisture modes, both in linear and nonlinear regimes.

Chapter 7

Some common properties of the tropical linear primitive equation models

7.1 Introduction

Sobel et al. (2001) identified a moisture mode in a simplified QTCM, which was confirmed by many recent studies. Although they attempted to physically justify the relevance of such modes to nature, they noted that any result dependent on a particular choice of convective scheme is subject to some doubt, and that moisture modes do not escape from this caution.

In this thesis, I have examined moisture modes in three different models: Neelin and Zeng's (2000) quasi-equilibrium tropical circulation model (QTCM), both with and without boundary layer, and Bony and Emanuel's (2005) subcloud layer quasi-equilibrium model (SLQEM) (see Chapters 2, 3, and 4). In all cases, the procedure of the inverse wavenumber expansion led to a systematic derivation of the weak temperature gradient (WTG) systems for moisture modes. In light of robust findings across differing models, it is tempting to claim that moisture modes universally exist. Physically speaking, one would intuitively expect the moisture mode to be present in the model, if convection and humidity interact with each other in some way. However, it is desirable to phrase this physical intuition in a more formal manner. One objective of this chapter is to show that moisture modes do exist in linear primitive equation models of the tropical atmosphere if the usual quasi-equilibrium

parameterizations are utilized.

Just like moisture modes, it turns out that linear primitive equation models have another common property: the existence of Kelvin-like modes. Chapters 2, 3, and 4 all sought Kelvin-like modes with vanishing meridional velocity. There is nothing contentious about the assumption of Kelvin-like modes, but it is instructive to see under what conditions one can obtain a $v = 0$ solution. For example, does adding a dynamic ocean change the model behavior? Would a multiple-mode model lead to different results? This analysis is important since one of the lingering questions about the MJO is why it appears like a coupled Kelvin-Rossby mode. To the extent an independent Kelvin-like mode exists, it would be hard to couple Kelvin and Rossby modes.

This chapter first illustrates the conditions for the existence of moisture modes. It then derives the conditions for the existence of self-consistent Kelvin-like modes, and illustrates why coupling of Kelvin and Rossby modes in a linear fashion is difficult.

7.2 Conditions for the existence of moisture modes under WTG

7.2.1 Moisture modes

This section derives conditions for the existence of moisture modes under WTG. Physically speaking, moisture modes would be expected if moisture-convection feedback is operating. But would such a mode always be under WTG? As in previous chapters, I expand the equations in terms of the inverse wavenumber and attempt to identify conditions, under which the solution is self-consistent.

One can write the mode-decomposed primitive equations linearized around the spatially homogeneous radiative-convective equilibrium for a Kelvin-like mode on the equatorial β-plane as

$$\frac{\partial u_i}{\partial t} = -\frac{\partial T_i}{\partial x} - \varepsilon_i u_i, \tag{7.1}$$

$$\frac{\partial T_i}{\partial t} + c_i^2 \frac{\partial u_i}{\partial x} = Q_i(u_1,...,u_I,T_1,...,T_I,q_1,...,q_J), \tag{7.2}$$

$$\frac{\partial q_j}{\partial t} = S_j(u_1,...,u_I,T_1,...,T_I,q_1,...,q_J), \tag{7.3}$$

where $i = 1,2,...,I$, and $j = 1,2,...,J$. Here u_i and T_i are the zonal wind and temperature for the ith baroclinic mode, ε_i is the Rayleigh damping coefficient for the ith mode, c_i is the phase speed of the dry gravity wave for the ith baroclinic mode, Q_i is a generic heating operator for the ith mode which may include effects like diffusion, q_j is a generic thermodynamic variable which could be humidity, boundary-layer moist static energy (MSE), or sea-surface temperature, and S_j is a generic source operator which could involve divergence/convergence. As with QTCM, the sign of the zonal wind corresponds to the direction of the upper level, and hence a negative sign in front of temperature gradient in Eq. (7.1). The barotropic mode is ignored.

From the outset, I have assumed that the model contains a Kelvin-like mode with $v = 0$. The next section addresses the validity of such an assumption.

A number of studies indicate that retaining up to the second baroclinic mode ($I = 2$) is sufficient for describing the basic features of tropical dynamics (e.g., Mapes 2000). On the other hand, there is no simple argument on the number of thermodynamic variables. Prognostic non-temperature thermodynamic variables may include free-tropospheric humidity, boundary-layer MSE, deep convective mass flux, sea-surface temperature, and stratiform precipitation. For example, according to the present definition, Khouider and Majda's (2006) model has four non-temperature thermodynamic variables ($J = 4$).

If one assumes an exponential form of the solution $\sim \exp(ikx + \sigma t)$, weak temperature gradient becomes equivalent to weak temperature perturbations. This allows me to write the condition for WTG as

$$\left| \left(\frac{\partial T_i}{\partial t} \right) \Big/ \left(c_i^2 \frac{\partial u_i}{\partial x} \right) \right| = \left| \frac{\sigma(\sigma + \varepsilon_i)}{c_i^2 k^2} \right| \ll 1 \quad \text{for} \quad 1 \le i \le I. \tag{7.4}$$

If the Rayleigh damping coefficient is smaller than, or on the order of, the complex growth rate, it can be ignored for the scaling purposes. Since c_i is smallest for $i = I$, if the condition

(7.4) holds for $i = I$, it must be true for all other i. Neglecting damping, it is possible to concisely write (7.4) as

$$L^2 \ll (2\pi c_I \tau_\sigma)^2, \tag{7.5}$$

where $L \equiv (2\pi)/k$ and $\tau_\sigma \equiv 1/|\sigma|$.

Figure 7-1 plots $2\pi c_I \tau_\sigma$ in units of km. For $I = 1$ (first baroclinic mode only) and $\tau_\sigma =$ 5days, $c_I \sim 50\mathrm{m/s}$ and $2\pi c_I \tau_\sigma \sim 100000\mathrm{km}$. (The linear analysis in Chapter 2 indicates a timescale of about 6 days.) The WTG thus easily applies to such disturbances for any wavelength realizable on the earth, as shown by Sobel and Gildor (2003) and discussed in Chapter 1. If the second baroclinic mode is also included, $2\pi c_I \tau_\sigma \sim 50000\mathrm{km}$ since $c_I \sim 20\mathrm{m/s}$. Naturally, the more modes one retains, the fewer the wavenumbers amenable to WTG. Although the WTG best applies to the model with the first baroclinic mode only, I present a general argument below without making an assumption about I.

I introduce the following nondimensionalization:

$$\begin{aligned} &\left(t, \frac{1}{\sigma}, \frac{1}{\varepsilon_i}\right) = \tau \left(\tilde{t}, \frac{1}{\tilde{\sigma}}, \frac{1}{\tilde{\varepsilon}_i}\right), \ \left(x, \frac{1}{k}\right) = c_I \tau \left(\tilde{x}, \frac{1}{\tilde{k}}\right), \\ &(u_i, c_i) = c_I(\tilde{u}_i, \tilde{c}_i), \ (T_i, Q_i) = c_I^2 \left(\tilde{T}_I, \frac{\tilde{Q}_i}{\tau}\right), \end{aligned} \tag{7.6}$$

where tildes denote nondimensional variables and τ is a characteristic timescale of the disturbance. τ is chosen such that $\tilde{\sigma} \sim O(1)$. (7.6) enables me to conveniently write the WTG condition as

$$\frac{\tilde{\sigma}^2}{\tilde{k}^2} \sim \frac{1}{\tilde{k}^2} \ll 1, \tag{7.7}$$

where $\tilde{k}$ is a dimensionless wavenumber and I have invoked $\tilde{\sigma} \sim O(1)$. Nondimensionalization of thermodynamic variables depends on the actual formulation of heating and source terms, and I assume that a suitable nondimensionalization is applied.

Applying (7.6) to Eqs. (7.1), (7.2), and (7.3) yields

$$\frac{\partial \tilde{u}_i}{\partial \tilde{t}} = -\frac{\partial \tilde{T}_i}{\partial \tilde{x}} - \tilde{\varepsilon}_i \tilde{u}_i, \tag{7.8}$$

$$\frac{\partial \tilde{T}_i}{\partial \tilde{t}} + \tilde{c}_i^2 \frac{\partial \tilde{u}_i}{\partial \tilde{x}} = \tilde{Q}_i(\tilde{u}_1, ..., \tilde{u}_I, \tilde{T}_1, ..., \tilde{T}_I, \tilde{q}_1, ..., \tilde{q}_J), \tag{7.9}$$

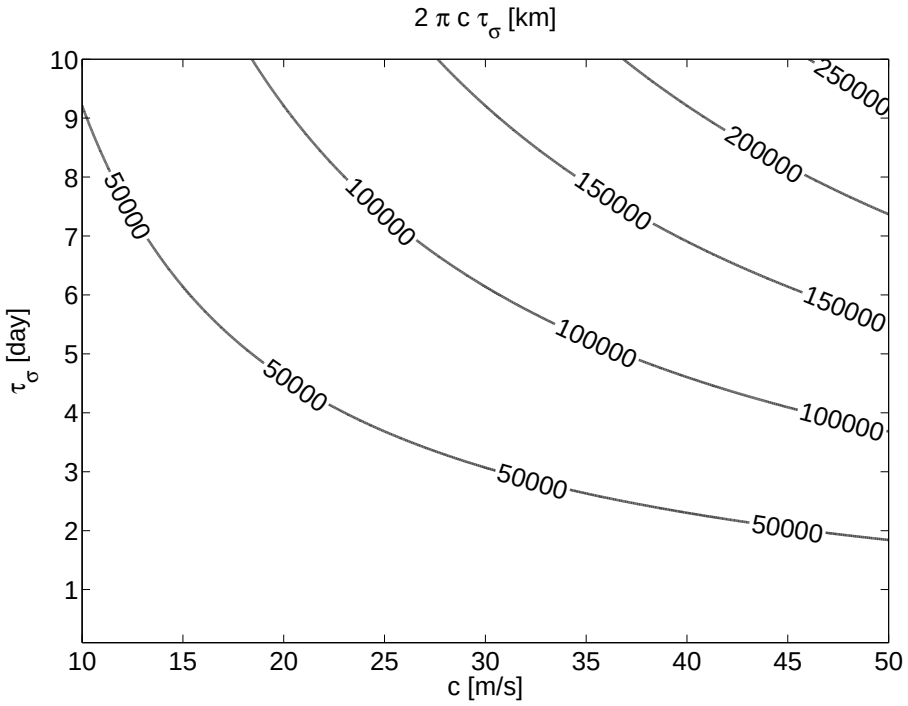

Figure 7-1: Plot of $2\pi c\tau_\sigma$. The vertical axis is τ_σ [day] whereas the horizontal axis represents c [m/s].

$$\frac{\partial \tilde{q}_j}{\partial \tilde{t}} = \tilde{S}_j(\tilde{u}_1,...,\tilde{u}_I,\tilde{T}_1,...,\tilde{T}_I,\tilde{q}_1,...,\tilde{q}_J), \tag{7.10}$$

Obviously $\tilde{c}_i$ only for $i = I$. As the nondimensional system is formally equivalent to the dimensional system, I interchangeably use the two systems.

Following previous chapters, I now expand as

$$(\sigma,u_1,...,u_I,T_1,...,T_I,q_1,...,q_J) = \sum_{n=0}^{\infty} \frac{1}{k^n}(\sigma^{(n)},u_1^{(n)},...,u_I^{(n)},T_1^{(n)},...,T_I^{(n)},q_1^{(n)},...,q_J^{(n)}). \tag{7.11}$$

Because heating and source terms are operators, they require more careful treatment. Anticipating possible singularities, one may write symbolically

$$(Q_1,...,Q_I,S_1,...,S_J) = \sum_{n=-N}^{\infty} \frac{1}{k^n}(Q_1^{(n)},...,Q_I^{(n)},S_1^{(n)},...,S_J^{(n)}). \tag{7.12}$$

Here heating and source terms are assumed to have poles of order N at $k \to \infty$. Singularities could arise for various reasons. For instance, diffusion scales as $\sim k^2$. The role of singularity is discussed in detail below.

Upon substitution of (7.11), the momentum equation (7.1) becomes, for all i,

$$\begin{aligned} &\left(\sigma^{(0)} + \frac{\sigma^{(1)}}{k} + \cdots\right)\left(u_i^{(0)} + \frac{u_i^{(1)}}{k} + \cdots\right) \\ &\qquad = -i\left(kT_i^{(0)} + T_i^{(1)} + \cdots\right) - \varepsilon_i\left(u_i^{(0)} + \frac{u_i^{(1)}}{k} + \cdots\right), \end{aligned} \tag{7.13}$$

which yields

$$O(k): \qquad T_i^{(0)} = 0, \tag{7.14}$$

$$O(1): \qquad (\sigma^{(0)} + \varepsilon_i)u_i^{(0)} = -iT_i^{(1)}. \tag{7.15}$$

The temperature equation (7.2) gives, for all i,

$$\left(\sigma^{(0)}+\frac{\sigma^{(1)}}{k}+\cdots\right)\left(T_i^{(0)}+\frac{T_i^{(1)}}{k}+\cdots\right)+c_i^2\left(iku_i^{(0)}+iu_i^{(1)}+\cdots\right)=\frac{Q_i^{(-N)}}{k^{-N}}+\cdots. \tag{7.16}$$

Recall that I am now seeking a moisture mode under the WTG balance; the desired result is $u_i^{(0)}=0$. For this to hold, either of the following must be satisfied: $Q_i=O(1)$, or that in case $Q_i=O(k)$ ($N=1$), the $O(k)$ term is proportional to u_i. If either condition holds, then,

$$O(k): \qquad u_i^{(0)}=0, \tag{7.17}$$

$$O(1): \qquad c_i^2 iu_i^{(1)}=Q_i^{(0)}. \tag{7.18}$$

Combining Eqs. (7.15) and (7.17) implies

$$T_i^{(1)}=0. \tag{7.19}$$

The thermodynamic equation yields

$$\left(\sigma^{(0)}+\frac{\sigma^{(1)}}{k}+\cdots\right)\left(q_j^{(0)}+\frac{q_j^{(1)}}{k}+\cdots\right)=\frac{S_j^{(-N)}}{k^{-N}}+\cdots. \tag{7.20}$$

The leading order term on the left-hand side is $\sigma^{(0)}q_j^{(0)}$. To balance this, the right-hand side must be $O(1)$. Note that one requires $S_j=O(1)$ under the condition $u_i^{(0)}=T_i^{(0)}=T_i^{(1)}=0$. With the assumption of $S_j=O(1)$, I find

$$\sigma^{(0)}q_j^{(0)}=S_j^{(0)}. \tag{7.21}$$

Noting that $w\sim iku$, I can summarize the above findings as follows.

$O(1)$ variables: w_i, q_j;

$O(1/k)$ variables: u_i; and

$O(1/k^2)$ variables: T_i.

These hold for all i, and the expansion (7.11) gives a nontrivial result, as long as the char-

acteristic equation of the matrix resulting from the thermodynamic equations has nonzero eigenvalues, which is usually the case.

The key to the present analysis is that the WTG balance is fundamentally a consequence of gravity wave dynamics (Sobel et al. 2001); gravity waves are effective at wiping out temperature gradient (Bretherton and Smolarkiewicz 1989). The dimensional WTG condition (7.4) originates from the momentum and temperature equations and is affected by the formulation of convective schemes only *indirectly*. This is the physical reason for the general existence of moisture modes. Furthermore, as found in previous chapters, the WTG approximation improves as $k \to \infty$ since the small parameter in the WTG condition (7.4) is inversely dependent on k.

To recap, the conditions for existence of moisture modes are:

1. $Q_i = O(1)$, or that in case $Q_i = O(k)$, the $O(k)$ term is proportional to u_i;

2. $S_i = O(1)$ under the WTG balance; and

3. The resulting dispersion relation has nonzero eigenvalues.

A more restrictive but useful condition is that each term in convective heating Q_i and the generic source S_j be linear in variables (u_i, w_i, T_i, q_j) with constant coefficients independent of k. This is indeed applicable to various types of quasi-equilibrium parameterizations. In such a situation, one might express the WTG system as

$$c_i^2 w_i^{(0)} = Q_i\left(w_1^{(0)}, ..., w_I^{(0)}, q_1^{(0)}, ..., q_J^{(0)}\right), \tag{7.22}$$

$$\frac{\partial q_j^{(0)}}{\partial t_m^{(0)}} = S_j\left(w_1^{(0)}, ..., w_I^{(0)}, q_1^{(0)}, ..., q_J^{(0)}\right), \tag{7.23}$$

where $w_i^{(0)} \equiv i u_i^{(1)}$ and $\partial / \partial t_m^{(0)} \equiv \sigma^{(0)}$. Here both heating and source terms are regarded as functions of $w_i^{(0)}$ and $q_j^{(0)}$. The system now resembles the simplest, irrotational moisture modes without background humidity gradient that were conceived by Sobel et al. (2001).

What if the condition is violated? For example, if Q_i includes diffusion, $Q_i = O(k^2)$ and the order of pole is $N = 2$. This would in fact give rise to inconsistency. As another

example, if $Q_i = 0$ (no heating) or $Q_i \sim iku_i$ (linear wave-CISK), we only obtain the trivial solution $u_i^{(n)} = T_i^{(n)} = 0$.

Also implicit in this analysis is the existence of prognostic thermodynamic variables. In other words, moisture modes require moisture variables (or more precisely, non-temperature thermodynamic variables), as its name suggests. Were it not for them, vertical motion could not be balanced by any variables in (7.16), and we would again find a trivial solution $u_i^{(n)} = T_i^{(n)} = 0$.

The discussion above means that although the models of the tropical atmosphere are sensitive to the choice of convective parameterizations, the existence of moisture modes under WTG is a very robust feature of models with quasi-equilibrium parameterizations. In fact, the finding here is congruent with a physical intuition that interaction between moisture and convection leads to a moisture mode. In contrast, a CISK-type parameterization would inhibit moisture modes since the parameterization is based on a quasisteady-state assumption of humidity. As Emanuel et al. (1994) critiqued the CISK, degrading the predictability of water vapor is a significant drawback of the CISK parameterizations.

Although one can be quite assured of the existence of moisture modes, whether they are unstable or not is a different question altogether. Examining detailed characteristics of the dispersion relationship would certainly require an analysis that depends on model details. Nonetheless, the present analysis clarifies some of the dispersion properties. First, at the leading order, the moisture mode is stationary (with respect to the mean flow) since the phase speed is $-\mathrm{Im}\sigma/k \to 0$ as $k \to \infty$. Second, linear WISHE (wind-induced surface heat exchange) does not enter the dispersion relation at the leading order. This is because u is not a leading order variable although convergence, which scales as $\sim ku$, is.

The results here also give some hint on whether such modes would be unstable. Since leading order terms are non-temperature thermodynamic variables and vertical motion, it should be straightforward to form an energy equation (such as that on MSE) by summing up the non-temperature thermodynamic equations. The resulting equation would then describe a column energy budget. As usual, vertical motion would export or import energy out of a column, depending on the gross moist stability, whereas diabatic sources would accumulate

energy. If the import surpasses the export, instability would occur. In fact, Chapters 2, 3, and 4 all confirmed this: the models are unstable to moisture mode instability when diabatic sources are strong enough.

One of the implicit assumptions used above is that the frame of reference is moving with the barotropic mean wind, or that if the model includes a prognostic SST, the basic state is a resting atmosphere. However, if the model has an interactive ocean plus a barotropic mean flow, a complication arises with the ocean variable. For instance, consider an equation for the SST that takes the form of (7.3) in the reference frame with the mean atmospheric flow:

$$\frac{\partial q_s}{\partial t} - U\frac{\partial q_s}{\partial x} = S_s(u_1, ..., u_I, T_1, ..., T_I, q_1, ..., q_J), \tag{7.24}$$

where U is the barotropic mean flow and the subscript s denotes SST. The left-hand side contains an operator $-U\partial/\partial x$ since SST is not advected by the *atmospheric* mean flow. In this case, one finds $q_s^{(0)} = 0$ if $S_s = O(1)$; the SST is not a zeroth order variable.

7.2.2 Gravity waves

The WTG limit gives moisture modes, but what about the rest of the solutions? Presumably other modes are gravity waves. Not surprisingly, the perturbation expansion described above ($\sigma \to$ const as $k \to \infty$) precludes gravity waves since $\sigma \sim O(k)$ as $k \to \infty$.

The following considers a case where the phase speed tends to constant for high wavenumber and seeks a solution of the form $\exp(ikx - ikct)$. Also I assume that the conditions for the existence of a moisture mode hold.

Whether these waves significantly interact with deep convection is an interesting question, but for the moment, assume that such waves are not affected by convective heating significantly. Mathematically this can be phrased as

$$\left| Q_i \Big/ \left(\frac{\partial T_i}{\partial t} \right) \right| \sim \left| \left(\frac{T_i}{\tau_{Q,i}} \right) \Big/ \left(\frac{\partial T_i}{\partial t} \right) \right| = \frac{1}{\tau_{Q,i} k |c|} \ll 1, \tag{7.25}$$

where $T_{Q,i}$ represents the characteristic timescale associated with the general heating oper-

ator Q_i. Alternatively I can express the condition as

$$L \ll 2\pi|c|\tau_{Q,i}. \tag{7.26}$$

For this condition to be satisfied, $L \ll 2\pi|c| \min \tau_{Q,i}$. Below I rescale all the variables using $\min \tau_{Q,i}$ instead of τ, which was used for the WTG scaling. As with the WTG scaling, the nondimensional system is formally equivalent to the dimensional one, and I interchangeably use them.

Now I expand each variable as follows:

$$(c, u_1, ..., u_I, T_1, ..., T_I, q_1, ..., q_J) = \sum_{n=0}^{\infty} \frac{1}{k^n} (c^{(n)}, u_1^{(n)}, ..., u_I^{(n)}, T_1^{(n)}, ..., T_I^{(n)}, q_1^{(n)}, ..., q_J^{(n)}). \tag{7.27}$$

The momentum equation (7.1) then becomes, for all i,

$$\begin{aligned} -i\left(kc^{(0)} + c^{(1)} + \cdots\right)\left(u_i^{(0)} + \frac{u_i^{(1)}}{k} + \cdots\right) & \\ = \quad -i\left(kT_i^{(0)} + T_i^{(1)} + \cdots\right) - \varepsilon_i\left(u_i^{(0)} + \frac{u_i^{(1)}}{k} + \cdots\right), & \end{aligned} \tag{7.28}$$

which yields

$$O(k): \qquad c^{(0)} u_i^{(0)} = T_i^{(0)}. \tag{7.29}$$

The temperature equation (7.2) gives, for all i,

$$-i\left(kc^{(0)} + c^{(1)} + \cdots\right)\left(T_i^{(0)} + \frac{T_i^{(1)}}{k} + \cdots\right) + c_i^2 i\left(ku_i^{(0)} + u_i^{(1)} + \cdots\right) = Q_i^{(-1)} k + \cdots. \tag{7.30}$$

Since Q_i could include a term proportional to vertical motion, one may write

$$d_i^2 \equiv Q_i^{(-1)} \,/\, \left(iu_i^{(0)}\right). \tag{7.31}$$

Note that d_i could be zero. Then, the above yields

$$O(k): \qquad c^{(0)} T_i^{(0)} = (c_i^2 - d_i^2) u_i^{(0)}. \tag{7.32}$$

The equation for thermodynamic variables (7.3) leads to

$$-i\left(kc^{(0)} + c^{(1)} + \cdots\right)\left(q_j^{(0)} + \frac{q_j^{(1)}}{k} + \cdots\right) = S_j^{(-1)} k + S_j^{(0)} + \cdots, \tag{7.33}$$

which yields

$$O(k): \qquad -ic^{(0)} q_j^{(0)} = S_j^{(-1)}. \tag{7.34}$$

Since I have assumed $S_j = O(1)$ under the WTG balance, S_j can be $O(k)$ in the gravity wave limit as u is $O(1)$ here and w is $O(k)$. If $S_j = O(1)$, however, $q_j^{(0)} = 0$.

Assuming $S_j = O(k)$, the prognostic equations at the leading order are

$$\frac{\partial u_i^{(0)}}{\partial t_g^{(0)}} = -\frac{\partial T_i^{(0)}}{\partial x}, \tag{7.35}$$

$$\frac{\partial T_i^{(0)}}{\partial t_g^{(0)}} + (c_i^2 - d^2)\frac{\partial u_i^{(0)}}{\partial x} = 0, \tag{7.36}$$

$$\frac{\partial q_j^{(0)}}{\partial t_g^{(0)}} = S_j^{(-1)}, \tag{7.37}$$

where $\partial / \partial t_g^{(0)} \equiv -ikc^{(0)}$. Clearly each vertical mode is decoupled from each other. Furthermore, thermodynamic variables are slaved to momentum and temperature and do not affect the dynamics of gravity waves. The only interaction is "reduced static stability"; the effective static stability is $c_i^2 - d_i^2$, not c_i^2. It is also noteworthy that linear damping such as Rayleigh damping or Newtonian cooling does not affect the leading-order behavior. These can be made even clearer by combining (7.29) and (7.32), which yields the dispersion re-

lationship for each vertical mode:

$$c^{(0)} = \pm\sqrt{c_i^2 - d_i^2}. \tag{7.38}$$

7.3 Conditions for Kelvin-Rossby coupling

The preceding section showed that moisture modes are nearly universal features of models with quasi-equilibrium parameterizations. This section turns to another common property of the linear primitive equation models, namely the difficulty of Kelvin-Rossby coupling.

As discussed in Chapter 1, numerous theories characterized the MJO as a Kelvin-like mode of low zonal wavenumber. However, observations show that the structure of the MJO is closer to Gill's (1980) solution than a Kelvin wave. For a disturbance like the MJO, one may write the momentum and temperature equations as

$$\varepsilon\mathbf{v} + \beta y\mathbf{k}\times\mathbf{v} = -\nabla T, \tag{7.39}$$

$$\varepsilon_T + c_0^2\nabla\cdot\mathbf{v} = Q(x,y,t), \tag{7.40}$$

where $\mathbf{v} = (u,v,0)^T$ is the horizontal wind vector (with the sign representing upper-tropospheric directions), T is the temperature or geopotential height for the first baroclinic mode, Q represents heating (precipitation), $\beta = df/dy$, f is the Coriolis parameter, $c_0^2 = gh$, and h is the equivalent depth, ε is the Rayleigh damping coefficient and ε_T is the Newtonian cooling coefficient. Of course, what moves Q eastward has been the mystery, and many theoreticians do not favor this formulation. The alternative is to assume that the MJO is a coupled Kelvin-Rossby wave. But coupling turned out to be fairly complicated. I attempt to offer a simple argument to describe why. To my knowledge, no previous paper explicitly described this argument although many authors invoked it.

Consider the model used in Chapter 1:

$$\frac{\partial\mathbf{v}}{\partial t} + \beta y\mathbf{k}\times\mathbf{v} = -\nabla T - \varepsilon\mathbf{v}, \tag{7.41}$$

$$\frac{\partial T}{\partial t} + c_0^2 \nabla \cdot \mathbf{v} = Q, \tag{7.42}$$

$$\frac{\partial q}{\partial t} - a^2 \nabla \cdot \mathbf{v} = -Q + E, \tag{7.43}$$

where q is humidity, a^2 represents gross moisture stratification, and E is evaporation. Here I consider a general formula for precipitation: $Q = Q(u, v, T)$, where $Q(u, v, T)$ is a linear operator. I seek conditions under which there is a separate solution with $v = 0$. In particular, I assume $v = 0$ and see if this results in contradiction. The approach here does not prove the absence of coupled Kelvin-Rossby waves. But since the Kelvin-like *moist* wave with $v = 0$ is a self-consistent linear solution, it does not interact with other *moist* waves without nonlinear effects.

By setting $v = 0$, I obtain

$$\frac{\partial u}{\partial t} = -\frac{\partial T}{\partial x} - \varepsilon u, \tag{7.44}$$

$$\beta y u = -\frac{\partial T}{\partial y}, \tag{7.45}$$

$$\frac{\partial T}{\partial t} + c_0^2 \frac{\partial u}{\partial x} = Q(u, 0, T), \tag{7.46}$$

$$\frac{\partial q}{\partial t} - a^2 \frac{\partial u}{\partial x} = -Q(u, 0, T) + E. \tag{7.47}$$

The meridional structure equation is obtained by combining the first two. The result is

$$\frac{\partial T}{\partial y} = \beta y \frac{ik}{\sigma + \varepsilon} T, \tag{7.48}$$

where a usual exponential solution $\sim \exp(ikx + \sigma t)$ has been assumed. The meridional structure is $u, T \sim \exp\left[ik\beta/(\sigma + \varepsilon) \cdot y^2/2\right] \equiv Y(y)$. Unlike the dry case, the moist equatorial deformation radius

$$\sqrt{-\frac{(\mathrm{Re}\sigma + \varepsilon)^2 + (\mathrm{Im}\sigma)^2}{\beta k \cdot \mathrm{Im}\sigma}}$$

cannot be specified *a priori*; it is necessary to solve the dispersion relationship to determine it.

Now I ask if there is a self-consistent solution with $v = 0$. In essence, I test if separation

of variables of the form $\sim \exp(ikx+\sigma t)Y(y)$ is possible or not. Were it not for precipitation Q, there must be such a solution, a trivial result. However, some forms of Q lead to contradiction, if the meridional structure for momentum and temperature is $Y(y)$. A necessary condition for the existence of the $v=0$ mode is

$$\frac{\partial}{\partial y}\left(\frac{Q(u,0,T)}{Y(y)}\right)=0. \tag{7.49}$$

If (7.49) does not hold, then the meridional structures of (7.46) would be different between the two sides. Unless (7.49) holds, separating variables in the form $\sim \exp(ikx+\sigma t)Y(y)$ is impossible.

A condition that is more stringent but more illuminating than (7.49) is that Q does not involve any y-related operation on u and T:

$$Q(u,0,T)=Q(\tilde{u}e^{ikx+\sigma t},0,\tilde{T}e^{ikx+\sigma t})Y(y), \tag{7.50}$$

where $(u,T)=(\tilde{u}e^{ikx+\sigma t},\tilde{T}e^{ikx+\sigma t})Y(y)$. As noted below, usual quasi-equilibrium parameterizations satisfy (7.50). On other hand, if Q involves $1/y\cdot\partial/\partial y$, for example, (7.49) is satisfied but not (7.50).

Assuming (7.49), let us define

$$\tilde{Q}(\tilde{u}e^{ikx+\sigma t},0,\tilde{T}e^{ikx+\sigma t})\equiv Q(u,0,T)/Y(y). \tag{7.51}$$

Combining (7.44) and (7.46) yields

$$\left(\sigma\tilde{T}+c_0^2 ik\frac{-ik}{\sigma+\varepsilon}\tilde{T}\right)e^{ikx+\sigma t}=\tilde{Q}\left(-\frac{ik}{\sigma+\varepsilon}\tilde{T}e^{ikx+\sigma t},0,\tilde{T}e^{ikx+\sigma t}\right). \tag{7.52}$$

As we are dealing with a linear problem, the heating operator is homogeneous of degree one and $(\sigma+\varepsilon)\tilde{Q}(\tilde{u}e^{ikx+\sigma t},0,\tilde{T}e^{ikx+\sigma t})=\tilde{Q}((\sigma+\varepsilon)\tilde{u}e^{ikx+\sigma t},0,(\sigma+\varepsilon)\tilde{T}e^{ikx+\sigma t})$. Note that $\tilde{T}$ is just a complex coefficient that represents phase and amplitude; the property of the homogeneity of degree one can be used for $\tilde{T}$ as well. Finally I obtain the dispersion

relationship:

$$\left(\sigma^2 + \varepsilon\sigma + c_0^2 k^2\right) e^{ikx+\sigma t} + \tilde{Q}\left(ike^{ikx+\sigma t}, 0, -(\sigma+\varepsilon)e^{ikx+\sigma t}\right) = 0 \tag{7.53}$$

If Eq. (7.53) has nonzero solutions, the moist Kelvin-like $v = 0$ mode is self-consistent. Because of linearity, such $v = 0$ mode does not interact with other *moist* modes, and coupling is difficult in a sense that there is no interaction between a *moist* Kelvin-like mode with $v = 0$ and *moist* Rossby waves without nonlinear effects.

Now I generalize this proposition. The result holds even if (i) multiple thermodynamic variables are added to the system (Yano and Emanuel 1991; Emanuel 1993; Fuchs and Raymond 2002, 2005; Bony and Emanuel 2005) or (ii) the model consists of multiple vertical modes (Khouider and Majda 2006). Note that adding a mixed layer ocean is equivalent to having an additional thermodynamic equation, and that including a dynamic ocean mathematically amounts to addition of another "vertical mode."

As an example of adding a thermodynamic variable, consider the previous set of equations with a QTCM-like precipitation parameterization: $Q = (q - T)/\tau$. This scheme is derived as a linear Betts-Miller parameterization (Betts 1986; Betts and Miller 1986), and it is well known that such a scheme is problematic and might be even unphysical since there is no universal relaxation target profile for humidity (e.g., Emanuel et al. 1994). However, this choice is useful for the illustration purposes because of its mathematical simplicity. Using (7.47) and $E = Au$, we can write out the formulation of Q as

$$Q(u,v,T) = \frac{A}{1+\sigma\tau}u + \frac{a^2}{1+\sigma\tau}\left(iku + \frac{\partial v}{\partial y}\right) - \frac{\sigma\tau}{1+\sigma\tau}\frac{T}{\tau}. \tag{7.54}$$

Since the operator (7.54) does not involve any y-operation aside from the convergence term, it satisfies (7.49) and (7.50) with $v = 0$. A more physically based example is the Q operator employed by Bony and Emanuel (2005), which takes the form of

$$Q(u,v,T) \quad = \quad +\Gamma\left[1 + \frac{1+\gamma}{\alpha_D}\sigma\right]\mathrm{sgn}(U)u - \Gamma\lambda\varepsilon_p\left(iku + \frac{\partial v}{\partial y}\right)$$

$$-\Gamma\left[\alpha_E+\frac{(1+\gamma)\alpha_D\alpha_E}{\sigma}+(1+\gamma)\alpha_D\right]T. \tag{7.55}$$

This again satisfies (7.49) and (7.50) with $v=0$. Note that T here corresponds to T_{eb} in Chapter 3. For notation, see Chapter 3. Although I have neglected moist radiative feedback, including it does not alter the outcome.

For models with multiple vertical modes, consider the next set of equations:

$$\frac{\partial \mathbf{v}_i}{\partial t}+\beta y\mathbf{k}\times\mathbf{v}_i = -\nabla T_i-\varepsilon_i u_i, \tag{7.56}$$

$$\frac{\partial T_i}{\partial t}+c_i^2\nabla\cdot\mathbf{v}_i = Q_i(u_1,v_1,T_1,...,u_I,v_I,T_I), \tag{7.57}$$

where the subscript $i=1,2,...,I$ denotes each vertical mode. If a dynamic ocean is included, it is also included as a "vertical mode"; T would actually denote the vertical displacement of an ocean layer multiplied by a reduced gravity.

I again seek a solution of the form $\sim\exp(ikx+\sigma t)Y(y)$. For the $v=0$ mode, combining $\partial u_i/\partial t=-\partial T_i/\partial x$ and $\beta y u_i=-\partial T_i/\partial y$ leads to

$$u_i,T_i,\sim\exp\left(\frac{ik\beta}{\sigma+\varepsilon_i}\frac{y^2}{2}\right), \tag{7.58}$$

which shows that the meridional structure is not directly constrained by c_i. It is simply because the meridional structure arises from the zonal and meridional momentum equations. On the other hand, Eq. (7.58) depends on ε_i; for the moment, I assume $\varepsilon_i=\varepsilon$ for all i. I will comment on this point later. Under the present assumptions, all the vertical modes thus take the same moist equatorial deformation radius. This holds true even when a dynamic ocean is included, as long as damping is the same for both the atmosphere and ocean. Next, invoking separability of variables, I write

$$\tilde{Q}_i(\tilde{u}_1e^{ikx+\sigma t},0,\tilde{T}_1e^{ikx+\sigma t},...,\tilde{u}_Ie^{ikx+\sigma t},0,\tilde{T}_Ie^{ikx+\sigma t})\equiv Q_i(u_1,0,T_1,...,u_I,0,T_I)/Y(y), \tag{7.59}$$

where $(u_i,T_i)=(\tilde{u}_ie^{ikx+\sigma t},\tilde{T}_ie^{ikx+\sigma t})Y(y)$. As before, the equation is homogeneous of de-

gree one. The temperature equation for each mode then becomes

$$(\sigma^2+\varepsilon\sigma+c_i^2k^2)\tilde{T}_ie^{ikx+\sigma t}-\tilde{Q}_i\Big(-ik\tilde{T}_1e^{ikx+\sigma t},0,(\sigma+\varepsilon)\tilde{T}_1e^{ikx+\sigma t},...,$$
$$-ik\tilde{T}_Ie^{ikx+\sigma t},0,(\sigma+\varepsilon)\tilde{T}_Ie^{ikx+\sigma t}\Big)=0. \quad (7.60)$$

Linearity of the problem allows me to write

$$\tilde{Q}_i\Big(-ik\tilde{T}_1e^{ikx+\sigma t},0,(\sigma+\varepsilon)\tilde{T}_1e^{ikx+\sigma t},...,-ik\tilde{T}_Ie^{ikx+\sigma t},0,(\sigma+\varepsilon)\tilde{T}_Ie^{ikx+\sigma t}\Big)$$
$$\equiv \quad e^{ikx+\sigma t}\sum_{j=1}^{I}\tilde{Q}_i^{(j)}(\sigma,k)\tilde{T}_j, \quad (7.61)$$

which yields a matrix equation:

$$\begin{pmatrix} \sigma^2+\varepsilon\sigma+c_1^2k^2-\tilde{Q}_1^{(1)} & -\tilde{Q}_1^{(2)}(\sigma,k) & \cdots & -\tilde{Q}_1^{(N)}(\sigma,k) \\ -\tilde{Q}_2^{(1)}(\sigma,k) & \sigma^2+\varepsilon\sigma+c_2^2k^2-\tilde{Q}_2^{(2)} & & \\ \vdots & & \ddots & \\ -\tilde{Q}_I^{(1)}(\sigma,k) & & & \sigma^2+\varepsilon\sigma+c_I^2k^2-\tilde{Q}_I^{(I)} \end{pmatrix}$$
$$\times(\tilde{T}_1,\tilde{T}_2,...,\tilde{T}_I)^T=0. \quad (7.62)$$

The dispersion relation can be obtained by taking the determinant of the coefficient matrix to be zero. All this shows that the two conditions for a self-consistent $v=0$ mode are (7.49) and the coefficient matrix in (7.62) having nonzero eigenvalues.

However, if Q is (rather obviously) nonlinear or involves some y-operator, the system no longer supports the $v=0$ solution. For example, boundary layer convergence could couple Kelvin and Rossby waves in a sense that there is no independent $v=0$ solution. Wang and Rui (1990) and Moskowitz and Bretherton (2000) considered the following heating operator:

$$Q(u,v,T)=-\alpha\frac{\partial}{\partial y}\left(\frac{1}{\varepsilon_b^2+y^2}\frac{\partial T}{\partial y}\right). \quad (7.63)$$

Note that both Wang and Rui and Moskowitz and Bretherton made a long-wave approximation by dropping the v tendency term, and that they also incorporated Newtonian cooling.

Here ε_b is the Rayleigh damping coefficient for the boundary layer, α is a measure of heating due to frictional moisture convergence. The linear operator here represents the equatorial analog of the Ekman pumping. Clearly setting $v = 0$ leads to contradiction since

$$\frac{\partial}{\partial y}\left(\frac{Q(u,0,T)}{Y(y)}\right) \neq 0 \tag{7.64}$$

The analysis has thus far assumed a uniform Rayleigh damping. As Eq. (7.58) has shown, the present finding does not hold true if Rayleigh damping coefficient is different for each mode. It may be reasonable to assume a constant coefficient for all the modes in the troposphere, but not for the boundary layer. Indeed, such an effect is the reason for the form of the heating function (7.63); the Ekman pumping results from the difference in the Rayleigh damping coefficients (and the steady-state assumption). Notice that a dynamic ocean leads to a effect similar to that of the boundary layer since it could have a different damping timescale.

To recap, the main condition for the existence of the $v = 0$ mode is (7.49). It is satisfied if the Q operator does not involve any y operation aside from convergence, and if Q is linear. It is interesting to note that quasi-equilibrium parameterizations ordinarily satisfy these two conditions, and hence (7.50), the stringent version of the constraint (Emanuel 1987; Neelin et al. 1987; Yano and Emanuel 1991; Emanuel 1993; Neelin and Zeng 2000; Fuchs and Raymond 2002, 2005; Bony and Emanuel 2005; Khouider and Majda 2006, among others). Moreover, a dynamic ocean does not alter the physical picture. The issue of coupling therefore remains elusive.

Even if one succeeds in coupling Kelvin and Rossby waves, there still exists another problem: east-west asymmetry. As Chapter 1 discussed, an exponential solution $\sim e^{ikx+\sigma t}$ cannot explain the profound east-west asymmetry in the MJO such as strong surface westerlies. Such an approach would require coupling of different wavenumbers, which is formidable because moist waves, including Kelvin-like waves, are generally dispersive.

7.4 Summary

This section clarified some common properties of linear primitive models of the tropical atmosphere. First I have derived the conditions for the existence of moisture modes under WTG. Since the WTG condition derives from momentum and temperature equations and is only affected by convective parameterizations indirectly, such conditions are found to be fairly broad. Indeed, models with quasi-equilibrium parameterizations are very likely to have moisture modes. Also simple considerations have shown that moisture mode instability would require diabatic heat sources such as cloud radiative forcing or enhanced surface heat fluxes (or negative gross moist stability).

Second, I explored conditions under which a self-consistent Kelvin-like $v = 0$ mode exists. I found that in the absence of the Ekman effect or nonlinearity, models with quasi-equilibrium parameterizations would have a $v = 0$ mode, regardless of whether they have multiple vertical modes, a dynamic ocean (with multiple layers), or multiple thermodynamic variables. The meridional scale, the moist equatorial Rossby radius, is common for all the vertical modes (including oceanic ones) because it is determined by the zonal and meridional momentum equations that do not contain gravity wave phase speeds.

It is often believed that the choice of convective parameterizations is the key determinant of the research outcomes. However, there should be some common properties of the tropical models as shown in this chapter. Understanding such characteristics would be helpful for further improving the representation of interaction between moist convection and large-scale dynamics.

Chapter 8

Concluding remarks

8.1 Conclusions and key findings

This thesis began with a rather bleak assessment of our understanding of the Madden-Julian Oscillation (MJO). In spite of the significance of this intraseasonal tropical variability and more sophisticated observational analyses, decades of research have not led to a solid physical understanding of its mechanism, and state-of-the-art general circulation models (GCMs) are not capable of simulating its amplitude, planetary scale, slow eastward propagation, and seasonality well. Moreover, we do not even understand why a majority of GCMs cannot achieve a reasonable MJO simulation. I speculate that GCMs share a certain defect that leads to a poor MJO simulation. Focusing on such physics may also lead us to a better understanding of the phenomenon itself.

Inspired by recent work, I have argued that moisture-convection feedback, the interplay between deep convection and environmental free-tropospheric humidity, is the key to the MJO problem. As detailed in Chapter 1, I hypothesized that the initial stage of the MJO can be characterized as a linear moisture mode, which owes its existence to moisture-convection feedback, and that once it nonlinearly saturates, the disturbance starts to move eastward by moist processes. This hypothesis would naturally suggest that the poor MJO simulations by GCMs could be attributed to their parameterizations' lack of sensitivity to free-tropospheric humidity. Previous authors, such as Bretherton et al. (2005) and Fuchs

and Raymond (2006), already suggested the relevance of moisture-convection feedback for the MJO, especially in the linear regime; the novelty of my thesis lies more with the second, nonlinear stage, particularly the role of nonlinear advection.

This last chapter of my thesis summarizes how well my hypothesis has fared, what my findings imply for modeling, limitations, and prospects for future research.

8.1.1 Initial, linear stage as linear moisture mode

Chapters 2, 3, and 4 inspected moisture modes in different models with various types of convective parameterizations. Chapter 2 looked into the quasi-equilibrium tropical circulation model (QTCM; Neelin and Zeng 2000), Chapter 3 examined the subcloud layer quasi-equilibrium model (Bony and Emanuel 2005), and Chapter 3 investigated the simplified form of QTCM with boundary layer developed by Sobel and Neelin (2006). Interestingly for all the models examined, I found moisture mode instability and obtained simple dispersion relationships using the weak temperature gradient (WTG) approximation of Sobel et al. (2001).

The WTG approximation is valid if the primary balance in the temperature equation is between adiabatic cooling and diabatic heating. In other words, the temperature tendency must be much smaller than the ascent term. Invoking the momentum equation, for a Kelvin-like wave on the equatorial β-plane, one can write this condition as

$$\left| \frac{\sigma^2}{c_d^2 k^2} \right| \ll 1 \qquad \text{or} \qquad \left| \frac{\tau_g}{\tau_\sigma} \right|^2 \ll 1 \tag{8.1}$$

where σ is a complex growth rate, c_d is the phase speed of the slowest of the gravity waves considered, k is wavenumber, $|\tau_\sigma| \equiv 1/|\sigma|$ is the e-folding timescale of the disturbance, $\tau_g \equiv 1/(c_d k)$ is the timescale a gravity wave travels across the wavelength. Physically speaking, the WTG balance holds if the timescale of the disturbance is much longer than the timescale associated with gravity wave dynamics. This is analogous to the geostrophic adjustment, in which gravity waves are much faster than the balanced component of the large-scale flow.

One can simplify the condition (8.1) by rescaling the complex growth by a characteristic timescale, the wavelength by the timescale times the dry gravity wave speed:

$$\frac{1}{\tilde{k}^2} \ll 1, \tag{8.2}$$

where $\tilde{k}$ is the nondimensional wavenumber and I have utilized the nondimensional complex growth rate is order 1, $|\tilde{\sigma}| \sim O(1)$. In what follows, I call the inverse of nondimensional wavenumber the WTG parameter. Sobel and Gildor (2003) have noted that the condition applies to all wavenumbers realizable on the earth. While this is true for the model with the first baroclinic mode only, the accuracy of the WTG approximation improves steadily as the WTG parameter approaches zero in the limit of $\tilde{k} \to \infty$.

Note that the discussion here is restricted to perturbations in a homogeneous background since it invokes a wave solution of the exponential form.

Chapters 2, 3, 4, and 7 demonstrated that a perturbation expansion in the WTG parameter greatly simplifies the system and dispersion relationship. The resulting equations showed that in all cases, moisture modes are under WTG balance and quasi-stationary (stationary without linear WISHE (wind-induced surface heat exchange)). In such a WTG system, the leading-order variables were humidity and vertical motion only. Symbolically, one may write the time evolution of a moisture mode under the WTG balance as

$$\frac{\partial q}{\partial t} = S, \tag{8.3}$$

$$S = (\text{cloud radiative forcing}) + (\text{surface heat flux}) - (\text{MSE export}), \tag{8.4}$$

where q denotes specific humidity, S is the sum of all the source/sink terms, and all variables represent perturbations around the basic state. Surface heat fluxes may be enhanced through gustiness. If S is expressed in terms of q, Eq. (8.3) yields a simple growth rate equation. The mode becomes unstable if $\partial S/\partial q > 0$ at the basic state, or if cloud radiative forcing and surface heat fluxes exceed the export of moist static energy (MSE). The key physical process here is moisture-convection feedback, an intimate relationship between tropospheric humidity and precipitation. In the WTG system in which $T \approx 0$, the

increase of MSE appears as a rise in humidity: $T+q+\varphi \approx q$, where T is temperature, φ is geopotential, and all variables are perturbations in energy units. Instability would naturally require deep convection to be responsive to tropospheric humidity.

For MSE sources, previous theoretical analyses relied on cloud radiative forcing alone (Fuchs and Raymond 2002, among others), but my analysis has shown that gustiness is a leading-order effect and can play a significant role especially with a weak mean wind. That is, a negative effective gross moist stability is not necessary for moisture mode instability. Curiously, linear WISHE is not the zeroth-order (in the WTG parameter) effect for the growth rate. The difference between gustiness and WISHE is that gusts are always in phase with precipitation, and hence humidity, while WISHE is usually nearly in quadrature with precipitation. However, numerical calculations of the growth rates demonstrated that second-order effects sometimes affect growth rates significantly.

In light of its simplicity, the WTG analysis has been extended to nonlinear cases as well. From Eq. (8.3), the necessary condition for nonlinear saturation is that $\partial^2 S/\partial q^2 < 0$ for some q so that there exists another fixed point where $\partial q/\partial t = 0$. Diminishing incremental gustiness or incremental cloud radiative forcing act as nonlinear thermodynamic limiting processes.

It is important to notice that nearly identical findings are obtained from three different models. In fact, Chapter 7 generalized the conditions for the existence of the moisture mode, and demonstrated that in a usual quasi-equilibrium model without Ekman convergence, the model should have a moisture mode under WTG balance.

The results from the simple models are reassuring, but does this translate into a more realistic model? The analysis of Chapter 5 using a single-column model (SCM) of Bony and Emanuel (2001) has shown that indeed this seems to be the case. I applied the method of the WTG approximation by Sobel and Bretherton (2000) to the SCM. In the WTG mode, the temperature tendency was set to zero above a certain level near the cloud base and vertical motion was diagnosed from the temperature equation. With this configuration, I explored sensitivity of the SCM to cloud-radiation interaction, inclusion of gustiness, and moisture-convection feedback. Of particular interest was the effect of the last process. Grabowski

and Moncrieff (2004) used a GCM with the Emanuel scheme (Emanuel 1991; Emanuel and Živković-Rothman 1999) and showed that moisture-convection feedback is essential for organization of MJO-like disturbances. As the SCM here has the same convective scheme, it is important to understand how their analysis is related to moisture mode instability.

In the case closest to Sobel and Bretherton's configuration, the SCM was stable to the WTG-mode run, supporting those authors' conclusion. When cloud radiative forcing was included and moisture-convection feedback was enhanced, however, the SCM exhibited behavior analogous to moisture mode instability. Diagnostic analyses revealed an exponential dependence of precipitation on precipitable water.

Unfortunately, the SCM outputs turned out to be much more complex than anticipated from the simple model results; multiple equilibria were found and some runs even crashed. The cause for such behaviors is likely to be cloud forcing. Clouds induce very strong cooling above and heating below, and a standard WTG approach leads to sharp vertical motion profiles that inevitably spawn complications. The difficulties notwithstanding, the findings generally confirm that moisture-convection feedback is essential for moisture mode instability in a realistic model as well.

8.1.2 Second stage as a nonlinear moisture mode

Having established the case for moisture mode instability, I then turned to the nonlinear dynamics of moisture modes. After all, moisture modes are quasi-stationary. How do they relate to a slowly moving disturbance like the MJO? Another pertinent questions is the role of β-plane dynamics. In the linear stability analysis, Kelvin-like modes are not affected by the β effect (except for the selection of eastward propagating modes). But does it matter to a nonlinear moisture mode?

In Chapter 6, a series of numerical calculations of a simplified QTCM showed that the following set of equations captures the essence of dynamics of nonlinear moisture modes:

$$0 = \frac{\partial \mathbf{v}}{\partial t} \quad = \quad \cdots - \varepsilon \mathbf{v}, \tag{8.5}$$

$$0 = \frac{\partial T}{\partial t} = \cdots - \varepsilon_T T, \tag{8.6}$$

$$\frac{\partial q}{\partial t} = \cdots, \tag{8.7}$$

where $\mathbf{v}$ is the horizontal wind vector, ε is the Rayleigh damping coefficient, T is temperature, and ε_T is the Newtonian cooling coefficient. In other words, its dynamics is a Gill's (1980) model plus a prognostic humidity equation. Therefore it is moist processes, not wave mechanisms, that determine the movement of the nonlinear moisture mode.

Given the centrality of moist processes, numerical runs examined two processes in isolation: nonlinear WISHE and nonlinear advection. I found that while nonlinear WISHE selects large scale and favors westward movement, nonlinear advection contributes to the eastward progression of the disturbances, albeit at a much slower speed than observed. For both of the effects, Gill's simple analytic model provides straightforward interpretations. Strong Rossby gyres give an asymmetric wind response, westerlies dominating easterlies at the surface. Since evaporation is primarily determined by nonlinear WISHE, it favors westward progression. Nonlinear advection tends to squeeze and move the moisture disturbance to the east. Unfortunately, including both nonlinear WISHE and nonlinear advection resulted in a blow-up of the model simulation because of a negative gross moist stability. To this point I will return later.

One of the novelties of my research lies in elucidating the role of nonlinear advection in a theoretical framework. A recent observational study by Benedict and Randall (2007) has discovered that after the passage of anomalous deep convection, horizontal advection dries the atmosphere, terminating the active phase of the MJO. However, this study is the first to show such an effect in a theoretical context.

Another important contribution is the connection between the MJO and the Gill (1980) model. In particular, this thesis seems to answer one of the long-standing questions about the MJO: why does the MJO look like a Gill pattern that couples Kelvin and Rossby components? Chapter 7 argued that it is difficult to couple them in a linear fashion, and that either Ekman convergence or nonlinearity is required to eliminate an independent moist Kelvin-like wave. On the other hand, if a system like Eqs. (8.5), (8.6), and (8.7 character-

izes the MJO, the difficulty of Kelvin-Rossby coupling is entirely circumvented.

Although the simplified QTCM has clarified the basic physical pictures associated with the MJO, there are many deficiencies with the QTCM simulations. The last section discusses them extensively.

8.1.3 Testable prediction of the thesis

The central theme of this thesis is the importance of moisture-convection feedback in the MJO. My hypothesis yields a testable prediction if one could enhance or suppress moisture-convection feedback in a model. Grabowski and Moncrieff (2004) performed such a numerical simulation, enhancing moisture-convection feedback in a GCM with the Emanuel scheme. They indeed found that an MJO-like disturbance became more coherent with enhanced moisture-convection feedback. It would be desirable to see whether improved moisture-convection feedback leads to a better simulation of the MJO in other GCMs.

8.1.4 Critique of CISK

Numerous papers have been written to dispute the validity of CISK (conditional instability of the second kind) (e.g., Emanuel et al. 1994). Despite the theoretical and observational problems associated with CISK, this theoretical concept still continues to be popular in the MJO literature. For instance, Lee et al. (2003) compare three different parameterizations, including the CISK-type Kuo (1974) scheme. Analyzing the data from the Atmospheric Infrared Sounder (AIRS)/Advanced Microwave Sounding Unit on the NASA *Aqua* satellite, Tian et al. (2006) noted that "[o]verall, the AIRS results are quite consistent with those predicted by the frictional Kelvin-Rossby wave/conditional instability of the second kind (CISK) theory for the MJO."

As pointed out by Emanuel et al. (1994), closing a convective scheme on the moisture budget fundamentally compromises the predictability of water vapor. If the evolution of water vapor is dynamically important, as is the case with the moisture mode, then the use of CISK-type parameterizations would be flawed. While recognizing the problem with CISK

parameterizations, Arakawa (2004) offered another viewpoint that in terms of numerical results, CISK-type schemes are similar to quasi-equilibrium parameterizations. Such an interpretation is possible, but it does not resolve the deeply embedded problem with the CISK approach.

8.2 Implications for modeling

In spite of incompleteness and some problems, this thesis gives some guidance on modeling of the MJO. If the MJO is indeed a nonlinear moisture mode, moist processes are paramount to its simulation. However, a study like this cannot quite delineate the direction of future model development, aside from a general statement on the centrality of moisture. Nevertheless, in what follows I discuss some implications of the thesis for various modeling exercises.

8.2.1 Moisture-convection feedback in GCMs

Ideally GCMs should be able to reproduce any physically-based observed relationship between different variables. Such relationships include the exponential dependence of precipitation on column relative humidity discovered by Bretherton et al. (2004). Biasutti et al. (2006) found that compared with observations, too much rainfall takes place with too dry a free troposphere in GCMs, indicating weak moisture-convection feedback in models. (Their analysis was restricted to the Atlantic, and it would be desirable to extend their analysis to other ocean basins.) The present thesis suggests that improving this relationship is a prerequisite to better MJO simulations by GCMs. However, regardless of the consideration on the MJO and my hypothesis, models should be capable of capturing the relationship between precipitable water and free-tropospheric humidity.

To test moisture-convection feedback, one actually does not have to await full GCM simulations; more idealized tests are readily available. Raymond (2007) applied Sobel and Bretherton's (2000) WTG methodology to an SCM. Derbyshire et al. (2004) proposed a test in which SCMs are run under relaxation of potential temperature and relative humid-

ity. They revealed inability of many convective parameterizations to represent moisture-convection feedback.

How can one improve moisture-convection feedback in a model? The literature points to some simple approaches. For example, for the Emanuel scheme, Grabowski and Moncrieff (2004) modified a cloud microphysical parameter, the fraction of precipitation falling outside clouds (σ_s), effectively altering the strength of the feedback. Chapter 5 applied the same methodology in examining moisture mode instability in an SCM. Tokioka et al. (1988) proposed limiting the entrainment used in the scheme of Arakawa and Schubert (1974) based on the boundary layer depth. In a GCM study, Suzuki et al. (2006) suppressed deep convection when the cloud-mean relative humidity did not reach 80%, obtaining improved simulations of the convectively coupled equatorial waves, but not the MJO. (Cloud-mean relative humidity is similar to column relative humidity but the average is taken from the cloud bottom to the cloud top.) Such "quick fixes" are not necessarily available for many parameterizations, nor are they practical to begin with; they might deteriorate the climatology of a GCM or simulations of other climate events. To refine a parameterization, one would need a study like Grandpeix et al. (2004), who carefully investigated the treatment of entrainment in the Emanuel scheme.

8.2.2 MJO in GCM

In addition to climatological relationship between precipitable water and precipitation, such correlation must be reproduced in the MJO as well. An increasing number of observational studies confirm such a relationship during the MJO events. Sperber (2003), Kiladis et al. (2005), Tian et al. (2006), and Benedict and Randall (2007) all show that humidity is correlated with precipitation on the intraseasonal timescale. However, such analyses are rarely repeated with model outputs.

Lin et al. (2006) discovered that the MJO continues to be a very tough test for the IPCC-class GCMs. It is true that the test on the MJO in GCM is getting more stringent as our understanding of the phenomenon itself is revised (Slingo et al. 2005). Old tests mainly concerned with upper-level winds (Swinbank et al. 1988; Slingo et al. 1996, among others);

recent studies examined dynamical structures (e.g., Sperber et al. 1997). For the purpose of physically faithful simulation of the MJO, my work suggests even more rigorous tests on the MJO that includes the humidity structure are desirable. For example, creating a composite similar to that of Kiladis et al. (2005) (see Figure 1-5).

Analyzing the humidity field (or MSE field) is beneficial not only from the MJO perspective but also from the viewpoint of other modes in the tropics. For instance, Peters and Bretherton (2006) calculated the MSE budget for the simulation of convectively coupled equatorial waves, illustrating the life cycle of waves and concomitant MSE changes. Such an analysis is useful for comparing observations and modeling results.

8.2.3 Global cloud-resolving models, superparameterizations, and DARE/hypohydrostatic approaches

Given ever-increasing computational resources, some models have begun to simulate MJO-like disturbances these days. Proposed methods include (i) global cloud-resolving models (CRMs); (ii) superparameterizations; and (iii) the DARE (Diabatic Acceleration and REscaling) approach or hypohydrostatic rescaling. Each of these implements a cloud-resolving model in one way or another, trying to calculate deep convective activity explicitly rather than relying on parameterized convection.

Since the DARE method is new, it requires some elaboration. Kuang et al. (2005) proposed this novel approach to climate modeling that deals with moist convection explicitly. They rescaled the equation for vertical motion as

$$\gamma^2 \frac{Dw}{Dt} = -\frac{1}{\rho}\frac{\partial p'}{\partial z} + B, \tag{8.8}$$

where w is vertical velocity, ρ is density, p' is pressure, B is buoyancy, and $\gamma(\geq 1)$ is the rescaling factor. This formulation is actually an equivalent formulation called Reduced Acceleration in the Vertical (RAVE); it is mentioned here because of its simplicity. As γ tends to unity, the model smoothly approaches a global CRM. The crux of DARE is to reduce the scale difference between convection and large-scale circulations, which saves compu-

tational time significantly. Pauluis et al. (2006) called the same approach hypohydrostatic rescaling.

Each of the methods has its own problems. For example, superparameterization simulates a 2-D CRM in each gridbox. Because of the difference in energy cascades in 2-D and 3-D turbulence, this might create a bias in simulations. Nevertheless, these new methods have been successful in simulating various tropical modes. For instance, Tomita et al. (2005) performed a global cloud-resolving model simulation of an aquaplanet with a 3.5-km resolution and identified an MJO-like disturbance. Grabowski and Moncrieff (2004) ran a GCM with superparameterization and also identified an MJO-like disturbance. Using the DARE method, Kuang et al. (2005) and Peters and Bretherton (2006) successfully simulated convectively coupled waves.

Moisture-convection feedback should be reproduced by CRMs as long as entrainment dynamics is well simulated, since the feedback arises primarily through entrainment of environmental air by ascending parcels in deep convective clouds. On the one hand, it is not immediately clear whether one can alter the strength of moisture-convection feedback by changing cloud microphysical parameters. On the other hand, moisture-convection feedback might be sensitive to resolution. To elucidate the resolution dependence, idealized CRM simulations similar to those of Derbyshire et al. (2004) would be useful.

Even for high-resolution modeling, MSE budget analyses are indispensable too. This is valuable not only for testing the nonlinear moisture mode hypothesis, but also for distinguishing different hypotheses. For example, how much of preconditioning before anomalous convection is due to frictional convergence versus shallow convection in models? Admittedly detailed analyses of large models are cumbersome because of the immense amount of data produced, but a careful analysis of the humidity/MSE budget would be helpful for our improved understanding of the MJO.

8.3 Limitations and remaining issues

In spite of progress made in this thesis, substantial issues remain unresolved, especially with my results from QTCM. The biggest deficiency lies in the inability of the simplified QTCM to include both nonlinear advection and nonlinear WISHE in tandem. Another significant issue is the role of humidity diffusion. This section discusses them in turn.

Chapter 6 showed that incorporating both effects led the model to blow up owing to a negative gross moist stability. How can this be alleviated? One may attribute the entire fault to the linear Betts-Miller convective scheme in QTCM, but this is not the whole story. For instance, QTCM does not distinguish between the boundary layer and the free troposphere although WISHE and advection operate at different levels. Nonlinear WISHE is a surface process, and thus modifies the boundary layer MSE while nonlinear advection mainly enters the free-tropospheric budget. Such a distinction is impossible in the original QTCM framework with a single basis function for humidity. In fact, Neggers et al. (2007) found that separating the boundary layer humidity from the free-tropospheric one in QTCM led to a substantial change in the inter-tropical convergence zone (ITCZ) dynamics.

Secondly, the numerical runs of QTCM required enormous numerical diffusion with a horizontal diffusion coefficient of $10^5 \mathrm{m}^2/\mathrm{s}$. Linear stability analysis in Chapter 2 showed that in the absence of linear WISHE, the growth rate is highest at the smallest scale, although unlike wave-CISK, the growth rate asymptotes to a constant. As one would expect, numerical calculations without diffusion exhibited grid-scale instabilities.

Scale selection would probably require more careful analysis. Mapes (2000) noted that gust fronts are instrumental in organizing deep convection at the mesoscale. Although gusts may not be effective at large scale, my analysis throughout this thesis lacks any mechanisms by which different atmospheric columns interact with each other. Numerical diffusion may be considered to be a rough surrogate for such effects.

Also problematic is the necessity of numerical diffusion for the QTCM simulation with nonlinear advection. Chapter 6 found that a Gill pattern tends to move a disturbance to the east and squeeze it at the same time, and does not provide a physical explanation why the MJO moves on the *eastern* side. Indeed, the numerical calculation showed diffusion

played an important role in the humidity budget on the eastern flank of disturbances. One might dismiss such a result as completely unphysical, but it may be worth asking, does the numerical diffusion represent something physical, at least crudely?

A series of recent papers have shown that transients are important in MSE budget of the ITCZ. Back and Bretherton (2006) estimated the MSE budget of the ITCZ and found that in the central-eastern Pacific, the gross moist stability for the mean circulation is negative. Peters et al. (submitted to the *Journal of Climate*) showed that transients balance the accumulation of MSE from the mean circulation in the central-eastern Pacific. Sobel and Neelin (2006) analyzed QTCM augmented with boundary layer dynamics and reached a similar conclusion, noting the importance of diffusion in their model. They needed a very large diffusion coefficient, comparable to that used in this thesis ($\sim 10^5 \mathrm{m}^2/\mathrm{s}$).

Does the MJO have some sort of transient effects analogous to those found in the ITCZ? Since the seminal paper by Nakazawa (1988), there is ample evidence of multi-scale organization of convection during MJO episodes, and the smaller-scale convective and wave activity might play a role similar to that of transients in the ITCZ dynamics. It might therefore be possible to interpret numerical diffusion as a crude representation of the effect of transients, however tenuous this argument may be.

There is a surge of interest in scale interaction recently, but much of the literature is devoted to the effects of scale interaction on momentum and temperature (Majda and Klein 2003; Majda 2007, for example). My work, along with other studies cited above, suggest that scale interaction deserves careful attention from the humidity (or MSE) budget perspective as well.

Given these suggestions, how can I improve the model? Incorporating column-column interaction or scale interaction might be a tough problem, and the initial focus should be on separating humidity into two variables, one for the free troposphere and the other for the boundary layer. Since observations imply that shallow convection preceding the core of deep convection moistens the atmosphere, one would need a shallow convection scheme as well as the second baroclinic mode. Such a model is already available; the model of Khouider and Majda (2006) and Kuang (accepted to *Journal of the Atmospheric Sciences*)

give the right configuration, for instance. Their parameterization may not be the most appropriate one, but their dynamical formulation would probably serve as a point of departure for future study.

Bibliography

Agudelo, P. A., J. A. Curry, C. D. Hoyos, and P. J. Webster, 2006: Transition between suppressed and active phases of intraseasonal oscillations in the Indo-Pacific warm pool. *Journal of Climate*, **19**, 5519–5530.

Arakawa, A., 2004: The Cumulus Parameterization Problem: Past, Present, and Future. *Journal of Climate*, **17**, 2493–2525.

Arakawa, A. and W. H. Schubert, 1974: Interaction of a cumulus cloud ensemble with the large-scale environment, Part I. *Journal of the Atmospheric Sciences*, **31**, 674–701.

Back, L. E. and C. S. Bretherton, 2006: Geographic variability in the export of moist static energy and vertical motion profiles in the tropical pacific. *Geophysical Research Letters*, **33**, L17810, doi:10.1029/2006GL026672.

Bantzer, C. and J. M. Wallace, 1996: Intraseasonal Variability in Tropical Mean Temperature and Precipitation and Their Relation to the Tropical 40–50 Day Oscillation. *Journal of the Atmospheric Sciences*, **53**, 3032–3045.

Benedict, J. J. and D. A. Randall, 2007: Observed characteristics of the MJO relative to maximum rainfall. *Journal of the Atmospheric Sciences*, **64**, 2332–2354.

Bergman, J. W., H. H. Hendon, and K. M. Weickmann, 2001: Intraseasonal air-sea interactions at the onset of El Ninõ. *Journal of Climate*, **14**, 1702–1719.

Betts, A. K., 1986: A new convective adjustment scheme. Part I: Observational and theoretical basis. *Quarterly Journal of the Royal Meteorological Society*, **112**, 677–691.

Betts, A. K. and M. J. Miller, 1986: A new convective adjustment scheme. Part II: Single column tests using GATE wave, BOMEX, ATEX and arctic air-mass data sets. *Quarterly Journal of the Royal Meteorological Society*, **112**, 693–709.

Biasutti, M., A. H. Sobel, and Y. Kushnir, 2006: AGCM Precipitation Biases in the Tropical Atlantic. *Journal of Climate*, **19**, 935–958.

Biello, J. A. and A. J. Majda, 2005: A New Multiscale Model for the Madden–Julian Oscillation. *Journal of the Atmospheric Sciences*, **62**, 1694–1721.

Bony, S. and K. A. Emanuel, 2001: A parameterization of the cloudiness associated with cumulus convection; evaluation using TOGA COARE data. *Journal of the Atmospheric Sciences*, **58**, 3158–3183.

Bony, S. and K. A. Emanuel, 2005: On the role of moist processes in tropical intraseasonal variability: Cloud–radiation and moisture–convection feedbacks. *Journal of the Atmospheric Sciences*, **62**, 2770–2789.

Bretherton, C. S., 2003: Wave-CISK. *Encyclopedia of Atmospheric Sciences,* J. R. Holton, J. A. Curry, and J. A. Pyle, Eds., Academic Press, 1019–1022.

Bretherton, C. S., in press: Challenges in numerical modeling of tropical circulations. *The General Circulation of the Atmosphere,* T. Schneider and A. H. Sobel, Eds., Princeton University Press.

Bretherton, C. S., P. N. Blossey, and M. Khairoutdinov, 2005: An energy-balance analysis of deep convective self-aggregation above uniform SST. *Journal of the Atmospheric Sciences*, **62**, 4273–4292.

Bretherton, C. S., M. E. Peters, and L. E. Back, 2004: Relationships between water vapor path and precipitation over the tropical oceans. *Journal of Climate*, **17**, 1517–1528.

Bretherton, C. S. and P. K. Smolarkiewicz, 1989: Gravity waves, compensating subsidence and detrainment around cumulus clouds. *Journal of the Atmospheric Sciences*, **46**, 740–759.

Bretherton, C. S. and A. H. Sobel, 2002: A simple model of a convectively coupled walker circulation using the weak temperature gradient approximation. *Journal of Climate*, **15**, 2907–2920.

Bretherton, C. S. and A. H. Sobel, 2003: The Gill model and the weak temperature gradient approximation. *Journal of the Atmospheric Sciences*, **60**, 451–460.

Brown, R. G. and C. S. Bretherton, 1995: Tropical wave instabilities: Convective interaction with dynamics using the Emanuel convective parameterization. *Journal of the Atmospheric Sciences*, **52**, 67–82.

Brown, R. G. and C. Zhang, 1997: Variability of midtropospheric moisture and its effect on cloud-top height distribution during TOGA COARE. *Journal of the Atmospheric Sciences*, **54**, 2760–2774.

Burns, S. P., A. H. Sobel, and L. M. Polvani, 2006: Asymptotic solutions of the axisymmetric moist Hadley circulation in a model with two vertical modes. *Theoretical and Computational Fluid Dynamics*, **20**, 443–467.

Chao, W. C. and L. Deng, 1996: On the role of wind-induced surface heat exchange in a two-dimensional model of super cloud clusters. *Journal of Geophysical Research.*, **101**, 16931–16937.

Chao, W. C. and S.-J. Lin, 1994: Tropical intraseasonal oscillation, super cloud clusters, and cumulus convection schemes. *Journal of the Atmospheric Sciences*, **51**, 1282–1297.

Charney, J. G., 1963: A note on large-scale motions in the tropics. *Journal of the Atmospheric Sciences*, **20**, 607–609.

Charney, J. G. and A. Eliassen, 1964: On the growth of the hurricane depression. *Journal of the Atmospheric Sciences*, **21**, 68–75.

Charney, J. G. and M. E. Stern, 1962: On the stability of internal baroclinic jets in a rotating atmosphere. *Journal of the Atmospheric Sciences*, **19**, 159–172.

Chiang, J. C. H. and A. H. Sobel, 2002: Tropical tropospheric temperature variations caused by ENSO and their influence on the remote tropical climate. *Journal of Climate*, **15**, 2616–2631.

Cronin, M. F. and M. J. McPhaden, 1997: The upper ocean heat balance in the western equatorial Pacific warm pool during September–December 1992. *Journal of Geophysical Research*, **102**, 8533–8553.

Crum, F. X. and T. J. Dunkerton, 1992: Analytic and numerical models of wave-CISK with conditional heating. *Journal of the Atmospheric Sciences*, **49**, 1693–1708.

Derbyshire, S. H., I. Beau, P. Bechtold, J.-Y. Grandpeix, J.-M. Piriou, J.-L. Redelsperger, and P. M. M. Soares, 2004: Sensitivity of moist convection to environmental humidity. *Quarterly Journal of the Royal Meteorological Society*, **130**, 3055–3079.

Donald, A., H. Meinke, B. Power, A. H. N. Maia, M. C. Wheeler, N. White, R. C. Stone, and J. Ribbe, 2006: Near-global impact of the Madden-Julian oscillation on rainfall. *Geophysical Research Letters*, **33**, L09704, doi:10.1029/2005GL025155.

Durran, D. R., 1999: *Numerical Methods for Wave Equations in Geophysical Fluid Dynamics*. Texts in Applied Mathematics Series, Vol. 32, Springer, 465 pp.

Emanuel, K. A., 1986: An air-sea interaction theory for tropical cyclones. Part I: Steady-state maintenance. *Journal of the Atmospheric Sciences*, **43**, 585–604.

Emanuel, K. A., 1987: An air-sea interaction model of intraseasonal oscillations in the tropics. *Journal of the Atmospheric Sciences*, **44**, 2324–2340.

Emanuel, K. A., 1991: A scheme for representing cumulus convection in large-scale models. *Journal of the Atmospheric Sciences*, **48**, 2313–2335.

Emanuel, K. A., 1993: The effect of convective response time on WISHE modes. *Journal of the Atmospheric Sciences*, **50**, 1763–1775.

Emanuel, K. A., J. D. Neelin, and C. S. Bretherton, 1994: On large-scale circulations in convecting atmospheres. *Quarterly Journal of the Royal Meteorological Society*, **120**, 1111–1143.

Emanuel, K. A. and R. T. Pierrehumbert, 1996: Microphysical and dynamical control of tropospheric water vapor. *Clouds, Chemistry and Climate,* P. J. Crutzen and V. Ramanathan, Eds., Springer-Verlag, 17–28.

Emanuel, K. A. and M. Živković-Rothman, 1999: Development and Evaluation of a Convection Scheme for Use in Climate Models. *Journal of the Atmospheric Sciences*, **56**, 1766–1782.

Ferranti, L., T. N. Palmer, F. Molteni, and E. Klinker, 1990: Tropical-extratropical interaction associated with the 30-60 day oscillation and its impact on medium and extended range prediction. *Journal of the Atmospheric Sciences*, **47**, 2177–2199.

Fouquart, Y. and B. Bonnel, 1980: Computations of solar heating of the earth's atmosphere: A new parameterization. *Beitraege zur Physik der Atmosphaere*, **53**, 35–62.

Fuchs, Ž. and D. J. Raymond, 2002: Large-Scale Modes of a Nonrotating Atmosphere with Water Vapor and Cloud–Radiation Feedbacks. *Journal of the Atmospheric Sciences*, **59**, 1669–1679.

Fuchs, Ž. and D. J. Raymond, 2005: Large-Scale Modes in a Rotating Atmosphere with Radiative–Convective Instability and WISHE. *Journal of the Atmospheric Sciences*, **62**, 4084–4094.

Fuchs, Ž. and D. J. Raymond, 2006: A simple, vertically resolved model of tropical disturbances with a humidity closure. *Extended Abstracts, 27th Conference on Hurricanes and Tropical Meteorology,* Monterey, CA, American Meteorological Society, 1–2.

Fuchs, Ž. and D. J. Raymond, 2007: A simple, vertically resolved model of tropical disturbances with a humidity closure. *Tellus*, **59A**, 344–354.

Fulton, S. R. and W. H. Schubert, 1985: Vertical normal mode transforms: Theory and application. *Monthly Weather Review*, **113**, 647–658.

Gill, A. E., 1980: Some simple solutions for heat-induced tropical circulation. *Quarterly Journal of the Royal Meteorological Society*, **106**, 447–462.

Goswami, B. N., 2005: South Asian monsoon. *Intraseasonal Variability in the Atmosphere-Ocean Climate System,* W. K. M. Lau and D. E. Waliser, Eds., Praxis, 19–61.

Grabowski, W., 2004: An improved framework for superparameterization. *Journal of the Atmospheric Sciences*, **61**, 1940–1952.

Grabowski, W. and M. W. Moncrieff, 2004: Moisture-convection feedback in the tropics. *Quarterly Journal of the Royal Meteorological Society*, **130**, 3081–3104.

Grabowski, W. W. and M. W. Moncrieff, 2001: Large-scale organization of tropical convection in two-dimensional explicit numerical simulations. *Quarterly Journal of the Royal Meteorological Society*, **127**, 445–468.

Grabowski, W. W. and M. W. Moncrieff, 2002: Large-scale organization of tropical convection in two-dimensional explicit numerical simulations: Effects of interactive radiation. *Quarterly Journal of the Royal Meteorological Society*, **128**, 2349–2375.

Grandpeix, J.-Y., V. Phillips, and R. Tailleux, 2004: Improved mixing representation in Emanuel's convection scheme. *Quarterly Journal of the Royal Meteorological Society*, **130**, 3207–3222.

Hayashi, Y., 1970: A theory of large-scale equatorial waves generated by condensation heat and accelerating the zonal wind. *Journal of the Meteorological Society of Japan*, **48**, 140–160.

Hayashi, Y. and D. G. Golder, 1993: Tropical 40-50- and 25-30-day oscillations appearing in realistic and idealized GFDL climate models and the ECMWF dataset. *Journal of the Atmospheric Sciences*, **50**, 464–494.

Hayashi, Y.-Y. and A. Sumi, 1986: The 30-40-day oscillation simulated in an "aqua-planet" model. *Journal of the Meteorological Society of Japan*, **64**, 451–467.

Held, I. M., R. S. Hemler, and V. Ramaswamy, 1993: Radiative-convective equilibrium with explicit two-dimensional moist convection. *Journal of the Atmospheric Sciences*, **50**, 3909–3927.

Held, I. M. and A. Y. Hou, 1980: Nonlinear axially symmetric circulations in a nearly inviscid atmosphere. *Journal of the Atmospheric Sciences*, **37**, 515–533.

Held, I. M. and B. J. Soden, 2000: Water vapor feedback and global warming. *Annual Review of Energy and the Environment*, **25**, 441–475.

Hendon, H. H., 1988: A simple model of the 40-50 day oscillation. *Journal of the Atmospheric Sciences*, **45**, 569–584.

Hendon, H. H., 2005: Air-sea interaction. *Intraseasonal Variability in the Atmosphere-Ocean Climate System,* W. K. M. Lau and D. E. Waliser, Eds., Praxis, 223–246.

Hendon, H. H. and J. Glick, 1997: Intraseasonal air-sea interaction in the tropical Indian and Pacific Oceans. *Journal of Climate*, **10**, 647–661.

Hendon, H. H. and M. L. Salby, 1994: The life cycle of the Madden-Julian oscillation. *Journal of the Atmospheric Sciences*, **51**, 2225–2237.

Holton, J. R., 2004: *An Introduction to Dynamic Meteorology*. 4th ed. Academic Press, 535 pp.

Hu, Q. and D. A. Randall, 1994: Low-frequency oscillations in radiative-convective systems. *Journal of the Atmospheric Sciences*, **51**, 1089–1099.

Kalnay, E., M. Kanamitsu, R. Kistler, W. Collins, D. Deaven, L. Gandin, M. Iredell, S. Saha, G. White, J. Woollen, Y. Zhu, M. Chelliah, W. Ebisuzaki, W. Higgins, J. Janowiak, K. C. Mo, C. Ropelewski, J. Wang, A. Leetmaa, R. Reynolds, R. Jenne, and D. Joseph, 1996: The NCEP/NCAR 40-year reanalysis project. *Bulletin of the American Meteorological Society*, **77**, 437–471.

Kemball-Cook, S. R. and B. C. Weare, 2001: The onset of convection in the Madden–Julian oscillation. *Journal of Climate*, **14**, 780–793.

Khairoutdinov, M., D. Randall, and C. DeMott, 2005: Simulations of the atmospheric general circulation using a cloud-resolving model as a superparameterization of physical processes. *Journal of the Atmospheric Sciences*, **62**, 2136–2154.

Khouider, B. and A. J. Majda, 2006: A simple multicloud parameterization for convectively coupled tropical waves. Part I: Linear analysis. *Journal of the Atmospheric Sciences*, **63**, 1308–1323.

Kikuchi, K. and T. N. Takayabu, 2004: The development of organized convection associated with the MJO during TOGA COARE IOP: Trimodal characteristics. *Geophysical Research Letters*, **31**, L10101, doi:10.1029/2004GL019601.

Kiladis, G. N., K. H. Straub, and P. T. Haertel, 2005: Zonal and vertical structure of the Madden–Julian oscillation. *Journal of the Atmospheric Sciences*, **62**, 2790–2809.

Kiladis, G. N. and K. M. Weickmann, 1992: Circulation anomalies associated with tropical convection during Northern winter. *Monthly Weather Review*, **120**, 1900–1923.

Knutson, T. R. and K. M. Weickmann, 1987: 30-60 day atmospheric oscillations: Composite life cycles of convection and circulation anomalies. *Monthly Weather Review*, **115**, 1407–1436.

Krishnamurti, T. N. and D. Subrahmanyam, 1982: The 30-50 day mode at 850mb during MONEX. *Journal of the Atmospheric Sciences*, **39**, 2088–2095.

Kuang, Z., 2007: A moisture-stratiform instability for convectively coupled waves. *Journal of the Atmospheric Sciences*, accepted.

Kuang, Z., P. N. Blossey, and C. S. Bretherton, 2005: A new approach for 3D cloud-resolving simulations of large-scale atmospheric circulation. *Geophysical Research Letters*, **32**, L02809, doi:10.1029/2004GL021024.

Kuang, Z. and C. S. Bretherton, 2006: A mass-flux scheme view of a high-resolution simulation of a transition from shallow to deep cumulus convection. *Journal of the Atmospheric Sciences*, **63**, 1895–1909.

Kuo, H. L., 1974: Further studies of the parameterization of the influence of cumulus convection on large-scale flow. *Journal of the Atmospheric Sciences*, **31**, 1232–1240.

Lau, K.-M. and L. Peng, 1987: Origin of low-frequency (intraseasonal) oscillations in the tropical atmosphere. Part I: Basic theory. *Journal of the Atmospheric Sciences*, **44**, 950–972.

Lau, K.-M. and C.-H. Sui, 1997: Mechanisms of short-term sea surface temperature regulation: Observations during TOGA COARE. *Journal of Climate*, **10**, 465–472.

Lau, W. K. M., 2005: El Niño Sourthern Oscillation connection. *Intraseasonal Variability in the Atmosphere-Ocean Climate System,* W. K. M. Lau and D. E. Waliser, Eds., Praxis, 271–305.

Lau, W. K. M. and D. E. Waliser, 2005: *Intraseasonal Variability in the Atmosphere-Ocean Climate System*. Springer and Praxis Books, 436 pp.

Lee, M.-I., I.-S. Kang, J.-K. Kim, and B. E. Mapes, 2001: Influence of cloud-radiation interaction on simulating tropoical intraseasonal oscillation with an atmospheric general circulation model. *Journal of Geophysical Research*, **106**, 14219–14233.

Lee, M.-I., I.-S. Kang, and B. E. Mapes, 2003: Impacts of cumulus convection parameterization on aqua-planet AGCM simulations of tropical intraseasonal variability. *Journal of the Meteorological Society of Japan*, **81**, 963–992.

Liebmann, B. and D. L. Hartmann, 1984: An observational study of tropical-midlatitude interaction on intraseasonal time scales druing winter. *Journal of the Atmospheric Sciences*, **41**, 3333–3350.

Lin, J., B. Mapes, M. Zhang, and M. Newman, 2004: Stratiform precipitation, vertical heating profiles, and the Madden-Julian oscillation. *Journal of the Atmospheric Sciences*, **61**, 296–309.

Lin, J.-L., G. N. Kiladis, B. E. Mapes, K. M. Weickmann, K. R. Sperber, W. Lin, M. C. Wheeler, S. D. Schubert, A. D. Genio, L. J. Donner, S. Emori, J.-F. Gueremy, F. Hourdin, P. J. Rasch, E. Roeckner, and J. F. Scinocca, 2006: Tropical intraseasonal variability in 14 IPCC AR4 climate models. Part I: Convective signals. *Journal of Climate*, **19**, 2665–2690.

Lin, J.-L., M. Zhang, and B. Mapes, 2005: Zonal momentum budget of the Madden–Julian oscillation: The source and strength of equivalent linear damping. *Journal of the Atmospheric Sciences*, **62**, 2172–2188.

Lin, W.-B. J., J. D. Neelin, and N. Zeng, 2000: Maintenance of tropical intraseasonal variability: Impact of evaporation-wind feedback and midlatitude storms. *Journal of the Atmospheric Sciences*, **57**, 2793–2823.

Lin, X. and R. H. Johnson, 1996: Kinematic and thermodynamic characteristics of the flow over the western Pacific warm pool during TOGA COARE. *Journal of the Atmospheric Sciences*, **53**, 695–715.

Lindzen, R. S., 1974: Wave-CISK in the Tropics. *Journal of the Atmospheric Sciences*, **31**, 156–179.

Lindzen, R. S., 1990: *Dynamics in Atmospheric Physics*. Cambridge University Press, 320 pp.

Lindzen, R. S. and S. Nigam, 1987: On the role of sea surface temperature gradients in forcing low-level winds and convergence in the tropics. *Journal of the Atmospheric Sciences*, **44**, 2418–2436.

Madden, R. A. and P. R. Julian, 1971: Detection of a 40-50 day oscillation in the zonal wind in the tropical Pacific. *Journal of the Atmospheric Sciences*, **28**, 702–708.

Madden, R. A. and P. R. Julian, 1972: Description of global-scale circulation cells in the tropics with a 40-50 day period. *Journal of the Atmospheric Sciences*, **29**, 1109–1123.

Madden, R. A. and P. R. Julian, 1994: Observations of the 40-50 day tropical oscillation – a review. *Monthly Weather Review*, **122**, 814–837.

Majda, A. J., 2007: New multiscale models and self-similarity in tropical convection. *Journal of the Atmospheric Sciences*, **64**, 1393–1404.

Majda, A. J. and J. A. Biello, 2004: A multiscale model for tropical intraseasonal oscillations. *Proceedings of the National Academy of Sciences*, **101**, 4736–4741.

Majda, A. J. and R. Klein, 2003: Systematic multiscale models for the tropics. *Journal of the Atmospheric Sciences*, **60**, 393–408.

Majda, A. J., S. N. Stechmann, and B. Khouider, 2007: Madden-Julian Oscillation analog and intraseasonal variability in a multicloud model above the equator. *Proceedings of the National Academy of Sciences*, **104**, 9919–9924.

Maloney, E. D. and D. L. Hartmann, 1998: Frictional moisture convergence in a composite life cycle of the Madden–Julian oscillation. *Journal of Climate*, **11**, 2387–2403.

Maloney, E. D. and D. L. Hartmann, 2000: Modulation of hurricane activity in the Gulf of Mexico by the Madden-Julian oscillation. *Science*, **287**, 2002–2004.

Maloney, E. D. and D. L. Hartmann, 2001: The sensitivity of intraseasonal variability in the NCAR CCM3 to changes in convective parameterization. *Journal of Climate*, **14**, 2015–2034.

Maloney, E. D. and A. H. Sobel, 2004: Surface fluxes and ocean coupling in the tropical intraseasonal oscillation. *Journal of Climate*, **17**, 4368–4386.

Manabe, S. and R. F. Strickler, 1964: Thermal equilibrium of the atmosphere with a convective adjustment. *Journal of the Atmospheric Sciences*, **21**, 361–385.

Mapes, B. E., 2000: Convective inhibition, subgrid-scale triggering energy, and stratiform instability in a toy tropical wave model. *Journal of the Atmospheric Sciences*, **57**, 1515–1535.

Masunaga, H., T. S. L'Ecuyer, and C. D. Kummerow, 2006: The Madden–Julian oscillation recorded in early observations from the Tropical Rainfall Measuring Mission (TRMM). *Journal of the Atmospheric Sciences*, **63**, 2777–2794.

Matsuno, T., 1966: Quasi-geostrophic motions in the equatorial area. *Journal of the Meteorological Society of Japan*, **44**, 25–43.

Morcrette, J.-J., 1991: Radiation and cloud radiative properties in the ECMWF operational weather forecast model. *Journal of Geophysical Research*, **96**, 9121–9132.

Moskowitz, B. M. and C. S. Bretherton, 2000: An analysis of frictional feedback on a moist equatorial Kelvin mode. *Journal of the Atmospheric Sciences*, **57**, 2188–2206.

Murakami, T. and T. Nakazawa, 1985: Tropical 45 day oscillation during the 1979 Northern Hemisphere summer. *Journal of the Atmospheric Sciences*, **42**, 1107–1122.

Myers, D. S. and D. E. Waliser, 2003: Three-dimensional water vapor and cloud variations associated with the Madden-Julian oscillation during Northern Hemisphere winter. *Journal of Climate*, **16**, 929–950.

Nakazawa, T., 1988: Tropical super clusters within intraseasonal variations over the western Pacific. *Journal of the Meteorological Society of Japan*, **66**, 823–839.

Natsuno, T., H. Tomita, S. Iga, H. Miura, and M. Satoh, 2007: Multiscale organization of convection simulated with explicit cloud processes on an aquaplanet. *Journal of the Atmospheric Sciences*, **64**, 1902–1921.

Neelin, J. D., 1989: On the intepretation of the Gill model. *Journal of the Atmospheric Sciences*, **46**, 2466–2468.

Neelin, J. D. and I. M. Held, 1987: Modeling tropical convergence based on the moist static energy budget. *Monthly Weather Review*, **115**, 3–12.

Neelin, J. D., I. M. Held, and K. H. Cook, 1987: Evaporation-wind feedback and low-frequency variability in the tropical atmosphere. *Journal of the Atmospheric Sciences*, **44**, 2341–2348.

Neelin, J. D. and J. Y. Yu, 1994: Modes of tropical variability under convective adjustment and the Madden–Julian oscillation. Part I: Analytical theory. *Journal of the Atmospheric Sciences*, **51**, 1876–1894.

Neelin, J. D. and N. Zeng, 2000: A quasi-equilibrium tropical circulation model–Formulation. *Journal of the Atmospheric Sciences*, **57**, 1741–1766.

Neggers, R. A. J., J. D. Neelin, and B. Stevens, 2007: Impact mechanisms of shallow cumulus convection on tropical climate dynamics. *Journal of Climate*, **20**, 2623–2642.

Numaguti, A., R. Oki, K. Nakamura, K. Tsuboki, N. Misawa, T. Asai, and Y.-M. Kodama, 1995: 4-5-day-period variation and low-level dry air observed in the equatorial western Pacific during the TOGA-COARE IOP. *Journal of the Meteorological Society of Japan*, **73**, 267–290.

Pauluis, O., D. M. W. Frierson, S. T. Garner, I. M. Held, and G. K. Vallis, 2006: The hypohydrostatic rescaling and its impacts on modeling of atmospheric convection. *Theoretical and Computational Fluid Dynamics*, **20**, 485–499.

Peters, M. and C. Bretherton, 2006: Structure of tropical variability from a vertical mode perspective. *Theoretical and Computational Fluid Dynamics*, **20**, 501–524.

Peters, M. E. and C. S. Bretherton, 2005: A simplified model of the Walker circulation with an interactive ocean mixed layer and cloud-radiative feedbacks. *Journal of Climate*, **18**, 4216–4234.

Peters, M. E., Z. Kuang, and C. Walker, in review: Analysis of atmospheric energy transport in ERA40 and implications for simple models of the mean tropical circulation. *Journal of Climate*.

Peters, O. and J. D. Neelin, 2006: Critical phenomena in atmospheric precipitation. *Nature Physics*, **2**, 393–396.

Polvani, L. M. and A. H. Sobel, 2002: The Hadley circulation and the weak temperature gradient approximation. *Journal of the Atmospheric Sciences*, **59**, 1744–1752.

Raymond, D. J., 1995: Regulation of moist convection over the west Pacific warm pool. *Journal of the Atmospheric Sciences*, **52**, 3945–3959.

Raymond, D. J., 2000: Thermodyanmic control of tropical rainfall. *Quarterly Journal of the Royal Meteorological Society*, **126**, 889–898.

Raymond, D. J., 2001: A new model of the Madden-Julian oscillation. *Journal of the Atmospheric Sciences*, **58**, 2807–2819.

Raymond, D. J., 2007: Testing a cumulus parameterization with a cumulus ensemble model in weak-temperature-gradient mode. *Quarterly Journal of the Royal Meteorological Society*, **133**, 1073–1085.

Raymond, D. J. and A. M. Blyth, 1986: A stochastic mixing model for nonprecipitating cumulus clouds. *Journal of the Atmospheric Sciences*, **43**, 2708–2718.

Raymond, D. J. and X. Zeng, 2000: Instability and large-scale circulations in a two-column model of the tropical troposphere. *Quarterly Journal of the Royal Meteorological Society*, **126**, 3117–3135.

Redelsperger, J.-L., F. Guichard, and S. Mondon, 2000: A parameterization of mesoscale enhancement of surface fluxes for large-scale models. *Journal of Climate*, **13**, 402–421.

Redelsperger, J.-L., D. B. Parsons, and F. Guichard, 2002: Recovery processes and factors limiting cloud-top height following the arrival of a dry intrusion observed during TOGA COARE. *Journal of the Atmospheric Sciences*, **59**, 2438–2457.

Rennó, N. O., K. A. Emanuel, and P. H. Stone, 1994: Radiative-convective model with an explicit hydrologic cycle 1. Formulation and sensitivity to model parameters. *Journal of Geophysical Research*, **99**, 14429–14441.

Reynolds, R. W. and T. M. Smith, 1994: Improved global sea surface temperature analyses using optimum interpolation. *Journal of Climate*, **7**, 929–948.

Rodwell, M. J. and B. J. Hoskins, 1996: Monsoons and the dynamics of deserts. *Quarterly Journal of the Royal Meteorological Society*, **122**, 1385–1404.

Rodwell, M. J. and B. J. Hoskins, 2001: Subtropical anticyclones and summer monsoons. *Journal of Climate*, **14**, 3192–3211.

Rossow, W. B. and R. A. Schiffer, 1991: ISCCP Cloud Data Products. *Bulletin of the American Meteorological Society*, **72**, 2–20.

Salby, M. L., R. R. Garcia, and H. H. Hendon, 1994: Planetary-scale circulations in the presence of climatological and wave-induced heating. *Journal of the Atmospheric Sciences*, **51**, 2344–2367.

Salby, M. L. and H. H. Hendon, 1994: Intraseasonal behavior of clouds, temperature, and motion in the Tropics. *Journal of the Atmospheric Sciences*, **51**, 2207–2224.

Schneider, E. K., 1977: Axially symmetric steady-state models of the basic state for instability and climate studies. Part II. Nonlinear calculations. *Journal of the Atmospheric Sciences*, **34**, 280–296.

Sherwood, S. C., 1999: Convective precursors and predictability in the tropical western Pacific. *Monthly Weather Review*, **127**, 2977–2991.

Sherwood, S. C. and R. Wahrlich, 1999: Observed evolution of tropical deep convective events and their environment. *Monthly Weather Review*, **127**, 1777–1795.

Shinoda, T., H. H. Hendon, and J. Glick, 1998: Intraseasonal variability of surface fluxes and sea surface temperature in the tropical western Pacific and Indian oceans. *Journal of Climate*, **11**, 1685–1702.

Slingo, J. M., P. M. Inness, and K. R. Sperber, 2005: Modeling. *Intraseasonal Variability in the Atmosphere-Ocean Climate System,* W. K. M. Lau and D. E. Waliser, Eds., Praxis, 361–388.

Slingo, J. M. and R. A. Madden, 1991: Characteristics of the tropical intraseasonal oscillation in the NCAR community climate model. *Quarterly Journal of the Royal Meteorological Society*, **117**, 1129–1169.

Slingo, J. M., K. R. Sperber, J. S. Boyle, J.-P. Ceron, M. Dix, B. Dugas, W. Ebisuzaki, J. Fyfe, D. Gregory, J.-F. Gueremy, J. Hack, A. Harzallah, P. Inness, A. Kitoh, W. K.-M. Lau, B. McAvaney, R. Madden, A. Matthews, T. N. Palmer, C.-K. Park, D. Randall, and N. Renno, 1996: Intraseasonal oscillations in 15 atmospheric general circulation models: results from an AMIP diagnostic subproject. *Climate Dynamics*, **12**, 325–357.

Sobel, A. H., 2002: Water vapor as an active scalar in tropical atmospheric dynamics. *Chaos*, **12**, 451–459.

Sobel, A. H. and C. S. Bretherton, 2000: Modeling tropical precipitation in a single column. *Journal of Climate*, **13**, 4378–4392.

Sobel, A. H. and H. Gildor, 2003: A simple time-dependent model of SST hot spots. *Journal of Climate*, **16**, 3978–3992.

Sobel, A. H. and J. D. Neelin, 2006: The boundary layer contribution to intertropical convergence zones in the quasi-equilibrium tropical circulation model framework. *Theoretical and Computational Fluid Dynamics*, **20**, 323–350.

Sobel, A. H., J. Nilsson, and L. M. Polvani, 2001: The weak temperature gradient approximation and balanced tropical moisture waves. *Journal of the Atmospheric Sciences*, **58**, 3650–3665.

Sobel, A. H., S. E. Yuter, C. S. Bretherton, and G. N. Kiladis, 2004: Large-scale meteorology and deep convection during TRMM KWAJEX. *Monthly Weather Review*, **132**, 422–444.

Sperber, K. R., 2003: Propagation and the vertical structure of the Madden–Julian oscillation. *Monthly Weather Review*, **131**, 3018–3037.

Sperber, K. R., J. M. Slingo, P. M. Inness, and W. K.-M. Lau, 1997: On the maintenance and initiation of the intraseasonal oscillation in the NCEP/NCAR reanalysis and in the GLA and UKMO AMIP simulations. *Climate Dynamics*, **13**, 769–795.

Straus, D. M. and R. S. Lindzen, 2000: Planetary-scale baroclinic instability and the MJO. *Journal of the Atmospheric Sciences*, **57**, 3609–3626.

Strogatz, S. H., 1994: *Nonlinear Dynamics and Chaos: With Applications to Physics, Biology, Chemistry, and Engineering*. Addison-Wesley, 498 pp.

Su, H. and J. D. Neelin, 2002: Teleconnection mechanisms for tropical Pacific descent anomalies during El Niño. *Journal of the Atmospheric Sciences*, **59**, 2694–2712.

Suzuki, T., Y. N. Takayabu, and S. Emori, 2006: Coupling mechanisms between equatorial waves and cumulus convection in an AGCM. *Dynamics of Atmospheres and Oceans*, **42**, 81–106.

Swinbank, R., T. N. Palmer, and M. K. Davey, 1988: Numerical simulations of the Madden and Julian oscillation. *Journal of the Atmospheric Sciences*, **45**, 774–788.

Takayabu, Y. N., 1994: Lage-scale cloud disturbances associated with equatorial waves. Part I: spectral features of the cloud disturbances. *Journal of the Meteorological Society of Japan*, **72**, 433–449.

Takayabu, Y. N., T. Iguchi, M. Kachi, A. Shibata, and H. Kanzawa, 1999: Abrupt termination of the 1997-98 El Niño in response to a Madden-Julian oscillation. *Nature*, **402**, 279–282.

Takemi, T., O. Hirayama, and C. Liu, 2004: Factors responsible for the vertical development of tropical oceanic cumulus convection. *Geophysical Research Letters*, **31**, L11109, doi:10.1029/2004GL020225.

Tian, B., D. E. Waliser, E. J. Fetzer, B. H. Lambrigtsen, Y. L. Yung, and B. Wang, 2006: Vertical moist thermodynamic structure and spatial–temporal evolution of the MJO in AIRS observations. *Journal of the Atmospheric Sciences*, **63**, 2462–2485.

Tokioka, T., K. Yamazaki, A. Kitoh, and T. Ose, 1988: The equatorial 30-60 day oscillation and the Arakawa-Schubert penetrative cumulus parameterization. *Journal of the Meteorological Society of Japan*, **66**, 883–901.

Tomita, H., H. Miura, S. Iga, T. Nasuno, and M. Satoh, 2005: A global cloud-resolving simulation: Preliminary results from an aqua planet experiment. *Geophysical Research Letters*, **32**, L08805, doi:10.1029/2005GL022459.

Tompkins, A. M., 2001: Organization of tropical convection in low vertical wind shears: The role of water vapor. *Journal of the Atmospheric Sciences*, **58**, 529–545.

Tuyl, A. H. V., 1987: Nonlinearities in low-frequency equatorial waves. *Journal of the Atmospheric Sciences*, **44**, 2478–2492.

Wang, B., 1988: Comments on "An air-sea interaction model of intraseasonal oscillation in the tropics". *Journal of the Atmospheric Sciences*, **45**, 3521–3525.

Wang, B., 2005: Theory. *Intraseasonal Variability in the Atmosphere-Ocean Climate System,* W. K. M. Lau and D. E. Waliser, Eds., Praxis, 307–360.

Wang, B. and H. Rui, 1990: Dynamics of the coupled moist Kelvin-Rossby wave on an equatorial β-plane. *Journal of the Atmospheric Sciences*, **47**, 397–413.

Weare, B. C., 2005: Composite singular value decomposition analysis of moisture variations associated with the Madden–Julian oscillation. *Journal of Climate*, **18**, 4329–4335.

Webster, P. J. and R. Lukas, 1992: TOGA COARE: The Coupled Ocean–Atmosphere Response Experiment. *Bulletin of the American Meteorological Society*, **73**, 1377–1416.

Wheeler, M. and G. N. Kiladis, 1999: Convectively coupled equatorial waves: Analysis of clouds and temperature in the wavenumber-frequency domain. *Journal of the Atmospheric Sciences*, **56**, 374–399.

Wheeler, M., G. N. Kiladis, and P. J. Webster, 2000: Large-scale dynamical fields associated with convectively coupled equatorial waves. *Journal of the Atmospheric Sciences*, **57**, 613–640.

Wheeler, M. C. and H. H. Hendon, 2004: An all-season real-time multivariate MJO index: Development of an index for monitoring and prediction. *Monthly Weather Review*, **132**, 1917–1932.

Wheeler, M. C. and J. L. McBride, 2005: Australian-Indonesian monsoon. *Intraseasonal Variability in the Atmosphere-Ocean Climate System,* W. K. M. Lau and D. E. Waliser, Eds., Praxis, 125–173.

Williams, E. and N. Rennó, 1993: An analysis of the conditional instability of the tropical atmosphere. *Monthly Weather Review*, **121**, 21–36.

Woolnough, S. J., J. M. Slingo, and B. J. Hoskins, 2000: The relationship between convection and sea surface temperature on intraseasonal timescales. *Journal of Climate*, **13**, 2086–2104.

Woolnough, S. J., J. M. Slingo, and B. J. Hoskins, 2001: The organization of tropical convection by intraseasonal sea surface temperature anomalies. *Quarterly Journal of the Royal Meteorological Society*, **127**, 887–907.

Xie, P. and P. A. Arkin, 1997: Global precipitation: A 17-year monthly analysis based on gauge observations, satellite estimates, and numerical model outputs. *Bulletin of the American Meteorological Society*, **78**, 2539–2558.

Xie, S.-P., A. Kubokawa, and K. Hanawa, 1993: Evaporation-wind feedback and the organizing of tropical convection on the planetary scale. Part I: Quasi-linear instability. . *Journal of the Atmospheric Sciences*, **50**, 3873–3883.

Xu, K.-M. and K. A. Emanuel, 1988: Is the tropical atmosphere conditionally unstable? . *Monthly Weather Review*, **117**, 1471–1479.

Yamagata, T. and Y. Hayashi, 1984: A simple diagnostic model for the 30–50 day oscillation in the tropics. *Journal of the Meteorological Society of Japan*, **62**, 709–717.

Yano, J.-I., R. Blender, C. Zhang, and K. Fraedrich, 2004: $1/f$ noise and pulse-like events in the tropical atmospheric surface variabilities. *Quarterly Journal of the Royal Meteorological Society*, **130**, 1697–1721.

Yano, J.-I. and K. A. Emanuel, 1991: An improved model of the equatorial troposphere and its coupling with the stratosphere. *Journal of the Atmospheric Sciences*, **48**, 377–389.

Yano, J.-I., J. C. McWilliams, M. W. Moncrieff, and K. A. Emanuel, 1995: Hierarchical tropical cloud systems in an analog shallow-water model. *Journal of the Atmospheric Sciences*, **52**, 1723–1742.

Yasunari, T., 1979: Cloudiness fluctuations associated with the Northern Hemisphere summer monsoon. *Journal of the Meteorological Society of Japan*, **57**, 227–242.

Yu, J.-Y. and J. D. Neelin, 1994: Modes of tropical variability under convective adjustment and the Madden-Julian oscillation. Part II: Numerical results. *Journal of the Atmospheric Sciences*, **51**, 1895–1914.

Zhang, C., 1996: Atmospheric intraseasonal variability at the surface in the tropical western Pacific ocean. *Journal of the Atmospheric Sciences*, **53**, 739–758.

Zhang, C., 2005: Madden-Julian Oscillation. *Reviews of Geophysics*, **43**, RG2003, doi:10.1029/2004RG000158.

Zhang, C. and M. J. McPhaden, 2000: Intraseasonal surface cooling in the equatorial western Pacific. *Journal of Climate*, **13**, 2261–2276.

Zurovac-Jevtić, D., S. Bony, and K. A. Emanuel, 2006: On the role of clouds and moisture in tropical waves: A two-dimensional model study. *Journal of the Atmospheric Sciences*, **63**, 2140–2155.